



Titre: Numerical and Experimental Investigation of Solid Mixing and Segregation in Tumbling Blenders
Title:

Auteur: Ebrahim Alizadeh
Author:

Date: 2013

Type: Mémoire ou thèse / Dissertation or Thesis

Référence: Alizadeh, E. (2013). Numerical and Experimental Investigation of Solid Mixing and Segregation in Tumbling Blenders [Thèse de doctorat, École Polytechnique de Montréal]. PolyPublie. <https://publications.polymtl.ca/1079/>
Citation:

 **Document en libre accès dans PolyPublie**
Open Access document in PolyPublie

URL de PolyPublie: <https://publications.polymtl.ca/1079/>
PolyPublie URL:

Directeurs de recherche: Jamal Chaouki, & François Bertrand
Advisors:

Programme: Génie chimique
Program:

UNIVERSITÉ DE MONTRÉAL

NUMERICAL AND EXPERIMENTAL INVESTIGATION OF SOLID MIXING AND
SEGREGATION IN TUMBLING BLENDERS

EBRAHIM ALIZADEH

DÉPARTEMENT DE GÉNIE CHIMIQUE
ÉCOLE POLYTECHNIQUE DE MONTRÉAL

THÈSE PRÉSENTÉE EN VUE DE L'OBTENTION
DU DIPLÔME DE PHILOSOPHIÆ DOCTOR
(GÉNIE CHIMIQUE)

AVRIL 2013

UNIVERSITÉ DE MONTRÉAL

ÉCOLE POLYTECHNIQUE DE MONTRÉAL

Cette thèse intitulée :

NUMERICAL AND EXPERIMENTAL INVESTIGATION OF SOLID MIXING AND
SEGREGATION IN TUMBLING BLENDERS

présentée par : ALIZADEH Ebrahim

en vue de l'obtention du diplôme de : Philosophiæ Doctor

a été dûment acceptée par le jury d'examen constitué de :

M. PATIENCE, Gregory S., Ph.D., président

M. CHAOUKI, Jamal, Ph.D., membre et directeur de recherche

M. BERTRAND, François, Ph.D., membre et codirecteur de recherche

M. DOUCET, Jocelyn, Ph.D., membre

M. ABATZOGLOU, Nicolas, Ph.D., membre

- *To my family.*

ACKNOWLEDGMENTS

My years of graduate study are finally nearing completion. This is the opportune moment to acknowledge all who have crossed my path throughout this journey and contributed directly or indirectly to my reaching the light at the end of the tunnel.

I would like to express my deep and sincere gratitude to my supervisors, Dr. Jamal Chaouki and Dr. François Bertrand. Their wide knowledge and their logical way of thinking have been of great value to me. Their understanding, encouragement and personal guidance have provided a solid foundation for the present thesis. I learnt from them ; not only scientific matters, but much knowledge that will inevitably encompass all aspects of my life. I would also like to convey my gratitude to all my committee members for accepting to be a member of the jury.

I would like to extend my thanks to my colleagues and friends for sharing their friendship and knowledge with me. I am thankful to Mr. Habibollah Hajhashemi and Mr. Olivier Dubé for helping me to fulfill the experimental work. My thanks also goes to Mr. Hamed Bashiri, Mr. Majid Rasouli and Mr. Jonathan Bouffard for helpful discussions. Special thanks to Dr. Rouzbeh Jafari and Dr. Babak Esmaeili for their generous nature. For their kind assistance in preparing radioactive tracers and activating them, I would like to thank Dr. Gregory Kennedy, Ms. Cornelia Chilian, and Mr. Jean St. Pierre.

Special thanks go to all secretaries and technical staff of the chemical engineering department and R&D laboratory of Ratiopharm operations. In particular, I wish to thank Mr. Yazid Belkhir and Mr. Jean Huard for their technical support.

I would like to extend my thanks to all members of our group and everybody I have worked and had discussions with. I made a number of friends in Montreal and my best memories are the times I have spent with them.

Also, I would like to acknowledge the R&D Center of Ratiopharm operations, Teva Canada, Praxair Inc. and Natural Sciences and Engineering Research Council of Canada, which

have funded most of this work. All simulations were made possible thanks to the computational resources of Compute Canada.

I could not have accomplished this without the loving support of my parents, sister and brother. They are the driving force behind all of my successes. To them I express my fervent thanks.

Last, but most importantly, I would like to thank my wife, Atefeh. She showed me the light when darkness loomed, motivated and encouraged me when depression was the order of the day and provided warmth and support during difficult times. She is the coauthor of this thesis.

Ebrahim ALIZADEH

École Polytechnique de Montréal,

Spring 2013

RÉSUMÉ

Les mélangeurs rotatifs (surtout les mélangeurs en V et les mélangeurs à tambour) sont parmi les équipements les plus utilisés pour les besoins de mélange de granules. Un des aspects dont il faut considérer lors de la conception de tels mélangeurs est la faible efficacité de brassage axial, ce qui peut entraîner des mélanges non homogènes, en particulier lorsque les propriétés physiques et d'écoulement des particules sont différentes. L'existence de granules ayant des propriétés différentes peut mener à la création de patrons de ségrégation importants. Afin de surmonter ces limitations, nous nous sommes intéressés à un appareil dénommé mélangeur tétrapodal, breveté en 1964 (États-Unis, bureau de brevets, 3,134,578). Ce mélangeur est constitué de deux paires de bras en forme de V reliées dans bas de l'appareil et où l'un des deux est tourné à 90° .

L'objectif principal de cette étude est d'examiner (autant de façon expérimentale que numérique), le mélange solide et la ségrégation à l'intérieur des mélangeurs suivants : mélangeur à tambour, mélangeur en V et le mélangeur tétrapodal. Selon la littérature, plusieurs études ont été effectuées pour investiguer la performance des mélangeurs à tambour et des mélangeurs en V. Malgré l'apparente efficacité de la forme du mélangeur tétrapodal pour le mélange solide, aucune étude n'a été effectuée pour déterminer la performance de ce type de mélangeur. Par conséquent, débiter l'étude de ce mélangeur à partir d'une version mise à l'échelle pour le laboratoire est risquée et il est essentiel de caractériser son efficacité via des outils numériques et obtenir les paramètres de conception. Parmi les techniques courantes pour simuler l'écoulement de granules, la méthode des éléments discrets (DEM) a récemment été appliquée pour étudier l'écoulement de granules dans plusieurs domaines. Cette technique de simulation s'est avérée efficace et capable d'offrir un aperçu des phénomènes qui ont lieu dans des lits de granules aussi bien que les détails sur l'écoulement et le mélange de granules. Cependant, cette technique possède des limitations dont il faut tenir compte et il faut être prudent lorsque les résultats de cette méthode de simulation sont utilisés. Donc, afin de

tenir compte de ces limitations, la première étape de ce travail a été de vérifier la validité de la méthode des éléments discrets par la comparaison de ses résultats avec des données expérimentales lagrangiennes. Ensuite, en se basant sur les résultats de cette première étape, des paramètres appropriés ont été sélectionnés pour la simulation numérique afin d'étudier le mélange et la ségrégation de granules non adhésives à l'intérieur des mélangeurs rotatifs. Finalement, les données de simulation obtenues pour le mélange et la ségrégation à l'intérieur de ce mélangeur ont été validées à l'aide de données expérimentales et d'autres investigations ont été faites afin de caractériser l'effet des conditions de fonctionnement sur son efficacité.

En général, la validité de la méthode des éléments discrets est vérifiée par la comparaison avec des données eulériennes à cause du manque de résultats expérimentaux lagrangiens. Par conséquent, le but de la première étape était de comparer les résultats DEM aux données expérimentales obtenues à l'aide de la technique lagrangienne non intrusive RPT (Radioactive Particle Tracking). Des résultats de simulations ont été fournis pour la ségrégation selon la taille de granules polydispersés dans un mélangeur à tambour rotatif en mode de fonctionnement dit de roulement. Cette étape a été limitée à la géométrie simple d'un tambour rotatif et, par conséquent, ne traite pas des effets géométriques sur le comportement de l'écoulement. De plus, dans ce travail et contrairement à la littérature où, en général, un mélange binaire est étudié, un mélange polydispersé de billes de verre avec une distribution précise de la taille a été employé (quatre particules de tailles différentes). Étant donné que la méthode des éléments discrets est sensible aux paramètres de simulation, des propriétés mécaniques et physiques précises de granules ont été soit mesurées par des expériences en laboratoire ou extraites de la littérature. À fin d'évaluer la capacité de la méthode des éléments discrets de prédire des phénomènes différents à l'intérieur du tambour, plusieurs comportements de granules ont été examinés pour la première fois et les résultats numériques ont été validés à l'aide de données expérimentales. Par exemple, un modèle a été introduit afin de prédire le temps de résidence le long des lignes d'écoulements dynamiques et d'évaluer le taux auquel le matériel se renouvelle à la surface libre et au niveau des couches intérieures du lit de

granules. Une analyse de sensibilité du modèle basée sur la méthode des éléments discrets en fonction des paramètres d'entrées est aussi présentée, mettant l'accent sur le module de Young et sur les coefficients de frottement. Afin de faire une comparaison raisonnable entre les données expérimentales et les résultats numériques, des équations adimensionnelles du mouvement des particules dans les directions normale et tangentielle ont été établies et analysées. De plus, des nombres adimensionnels efficaces ont été introduits pour expliquer la meilleure façon de choisir les paramètres de la méthode d'éléments distincts. Les résultats de l'investigation expérimentale de l'écoulement granulaire à l'intérieur du mélangeur à tambour sont présentés dans le premier article et la comparaison entre les résultats obtenus par DEM et par ceux par RPT, ainsi qu'une analyse de sensibilité du modèle basé sur la DEM sont présentés dans le second article.

Selon l'analyse effectuée pour valider les résultats de la méthode des éléments discrets, des paramètres adéquats ont été sélectionnés et plusieurs simulations ont été réalisées afin d'étudier le mélange et la ségrégation à l'intérieur du mélangeur tétrapodal et du mélangeur en V et pour comparer leur performance. Les résultats sont comparés selon le temps de mélange et l'uniformité du mélange pour divers profils de chargement, niveaux de remplissage, et vitesses de rotation. Par rapport aux mélangeurs en V, le mélangeur tétrapodal fournit une efficacité de mélange (axial et radial) meilleure, surtout lorsque les parties supérieure et inférieure du mélangeur sont tournées à 45° , ce qui rend le mélange axial aussi efficace que le mélange radial. De plus, les mécanismes qui contrôlent la ségrégation à l'intérieur du mélangeur tétrapodal ont été examinés en profondeur et des critères ont été tirés pour adapter cet équipement à l'échelle commerciale. Ce critère pour la mise à l'échelle peut être utilisé pour le mélangeur en V puisque dans les deux géométries, les particules s'écoulent sur les surfaces inclinées des mélangeurs et que la ségrégation s'effectue de manière similaire. Une performance supérieure du mélangeur tétrapodal a été observée en ce qui concerne la ségrégation des particules de tailles différentes, en comparaison avec les données disponibles dans la littérature pour les mélangeurs en V. Cependant, il faudrait investiguer d'avantage

les pires scénarios, par exemple pour des particules dont le ratio de taille est très important et avec des densités différentes. L'analyse de tous les paramètres qui affectent la ségrégation requiert beaucoup de temps avec les ressources informatiques disponibles actuellement. Donc, il a été décidé d'étudier l'effet de tous ces paramètres expérimentalement et par la suite de valider les résultats numériques obtenus. Les résultats des simulations DEM pour le mélangeur tétrapodal et pour le mélangeur en V sont présentés dans le troisième article.

À la troisième étape, plus de 100 expériences sur le mélange et la ségrégation de granules non adhésives ont été réalisées avec le mélangeur en V et le mélangeur tétrapodal. Les expériences ont été caractérisées à l'aide d'échantillons prélevés avec une sonde voleuse. La ségrégation de granules de tailles et de densités différentes a été étudiée pour une large gamme de vitesses de rotation (5-30 *RPM*) et de niveaux de remplissages (35-65 %V). Il a été démontré que l'intensité de la ségrégation est de loin inférieure dans le mélangeur tétrapodal comparativement à celle du mélangeur en V conventionnel, qu'elle diminue significativement avec une augmentation de la vitesse de rotation et que l'effet du niveau de remplissage de particules n'est pas significatif. Les résultats de ces expériences et la mise à l'échelle des mélangeurs rotatifs font l'objet du quatrième article.

Bien que les résultats des simulations de la méthode des éléments discrets concordent avec les résultats expérimentaux pour la dynamique des granules, quelques divergences mineures ont été observées en ce qui concerne les taux de mélange. Une source importante d'erreurs dans les simulations DEM provient de la qualité des prédictions des modèles de forces de contact. Par exemple, les modèles sur la force de contact normale n'arrivent pas à prédire un comportement de restitution d'énergie adéquat lorsque la vitesse d'impact normale augmente. En particulier, la plupart des modèles non linéaires prédisent une force d'attraction nette vers la fin de la collision entre deux particules qui s'entrechoquent ; ceci n'est pas réaliste d'après les résultats de la littérature. Ces limitations ont donné un nouvel élan pour développer un modèle de force de contact normale capable de prédire le déroulement d'une collision entre deux particules. Ce modèle comprend une force élastique hertzienne et une

force dissipative évaluée par le mouvement d'un liquide non newtonien dans un amortisseur. Les paramètres du modèle sont déterminés à l'aide de données de restitution expérimentales pour des contacts particule/particule et particule/mur. Dans le travail actuel, les mesures de restitution d'énergie pour les collisions particule/mur ont été réalisées à l'aide de plusieurs matériaux avec une large gamme de vitesses d'impact, contrairement aux données de collision particule/particule qui ont été obtenues dans la littérature. Des prédictions de modèles pour des quantités microscopiques (*i.e.* vitesse de particule) et macroscopiques (*i.e.* temps de collision) ont été présentées et comparées avec celles d'autres modèles non linéaires et de données expérimentales. Il a été observé que le modèle prédit adéquatement le coefficient de restitution et il diminue la force d'attraction à la fin d'une collision. Notre nouveau modèle pour la force de contact est présenté dans le cinquième article.

En conclusion, les résultats scientifiques de ce travail ont mené à quatre types de contributions. En premier, les découvertes de cette recherche dans le cas de mélangeurs rotatifs peuvent faciliter une conception efficace des procédés de mélanges solides. Deuxièmement, la performance du mélangeur tétrapodal fut investiguée pour la première fois. Il est recommandé d'utiliser un mélangeur tétrapodal, lorsqu'il y a des problèmes avec les mélangeurs conventionnels concernant le temps de mélange ou lorsqu'il y a la présence de produits non homogènes causés par des mécanismes de mélange moins efficaces ou par la ségrégation. Troisièmement, il a été montré originalement pourquoi la méthode des éléments discrets génère des résultats acceptables, même si des paramètres physiques erronés sont utilisés. Finalement, notre modèle précis de force de contact peut être appliqué dans des simulations basées sur la méthode des éléments discrets afin d'obtenir des résultats plus fiables.

ABSTRACT

Tumbling blenders (especially V-blenders and rotating drums) are among the most commonly used equipment for granular mixing purposes. One aspect that must be addressed when designing such mixing devices is low axial mixing efficiency, which can lead to non-homogeneous mixtures, especially when the physical and flow properties of the particles brought into play are different. Existence of granules with different properties inside tumbling blenders could lead to significant segregation. To overcome these limitations, we recently undertook an interest in the so-called tetrapodal mixing device, patented in 1964 (USA patent office, 3,134,578). This blender can be described as two V-shaped pairs of arms connected at the bottom whereby one is twisted by 90° .

The main objective of this study is to investigate (both numerically and experimentally) solid mixing and segregation in the following tumbling blenders: rotating drum, V-blender and tetrapodal blender. There are several studies in the literature that have been performed to investigate the performance of rotating drums and V-blenders. However, despite the seemingly effective shape of the tetrapodal blender for solid mixing, there have not been any studies to investigate the performance of this blender. Therefore, investing in manufacturing a lab-scale version of such a blender at first step is risky and it is of interest to characterize its efficiency via numerical tools and obtain design parameters. Among the common techniques for simulating granular flow, the discrete element method (DEM) has recently been applied to investigate the granular flow in many applications. This simulation technique has been proven to be efficient in providing insight into phenomena occurring in granular beds as well as details about the flow and mixing of granules. However, this technique suffers from some limitations that one should be vigilant when using the results of this simulation method. Therefore, to offset these limitations the first step of this work was to check the validity of DEM-based model by comparing its results with Lagrangian experimental data. Next, based on the results of first step, appropriate parameters were chosen for DEM-based model to investigate

the mixing and segregation of non-adhesive granules inside the tumbling blenders. Finally, the simulation findings of mixing and segregation were validated using experimental data and further investigations were performed to characterize the effect of operating conditions on blender efficiency.

Generally, the validity of DEM-based model has been checked by comparing it with Eulerian data due to the lack of Lagrangian experimental results. Accordingly, the aim of the first step of current work is to compare DEM results to experimental data obtained using Lagrangian non-intrusive radioactive particle tracking (RPT) technique. The simulation results are reported for the size segregation of polydisperse granules in a rotating drum when operating in rolling mode. This step was restricted to a simple geometry of a rotating drum and, as a consequence, does not look into geometrical effects of flow behavior. Moreover, contrary to the literature where a binary mixture has generally been the subject of study, in this work a polydisperse mixture of glass beads with a precise particle size distribution was employed (four different sized particles). Given that the DEM is sensitive to simulation parameters, accurate mechanical and physical properties of granules were either measured experimentally or extracted from the literature. To capture the ability of DEM in predicting different phenomena inside the drum, using these numerical results, several granular behaviors were investigated for the first time and validated through the experimental data. For instance, a model was introduced to predict the residence times along streamlines and evaluate the rate at which the material renews at the free surface and within the inner layers of the bed. A sensitivity analysis of the DEM-based model with respect to the input parameters is then presented, with an emphasis on the Young's modulus and the friction coefficients. To enable a fair comparison between the experimental data and the numerical results, dimensionless motion equations for the particles in normal and tangential directions were subsequently derived and analyzed. In addition, effective dimensionless numbers were introduced to explain how best to choose DEM parameters. The results of the experimental investigation of granular flow inside the rotating drum is the subject of the first research paper and the comparison

between DEM and RPT results as well as the sensitivity analysis of the DEM-based model are presented in the second paper.

Based on the analysis performed for the validation of DEM-based model, adequate parameters were chosen and several simulations were carried out to investigate the mixing and segregation of granules inside the tetrapodal blender and V-blender to compare their performances. The results are compared on the basis of mixing time and mixture uniformity for different loading profiles, fill levels and rotational speeds. Compared to the V-blender, the tetrapodal blender provides better (axial and radial) mixing efficiency, especially when the upper or lower part of the blender is twisted by 45° making the axial mixing as efficient as the radial mixing. Moreover, mechanisms that govern the segregation inside the tetrapodal blender were thoroughly investigated and a criterion was derived for the scaling-up of this device. Such a criterion for scale-up could be extended to the V-blender since in both blenders, particles slide on the inclined surfaces of the blender arms and segregation happens in a similar manner. Superior performance of the tetrapodal blender was observed in the case of size segregating granules when compared with the data reported in the literature for V-blenders. However, additional investigation was needed for unfavorably worst-case scenarios such as granules with large size and/or density ratios. Investigation of all affecting parameters on the segregation intensity with the DEM-based model is time-consuming with current computing facilities. Therefore, it was decided to study the effect of all these parameters experimentally and in addition validate the obtained numerical findings. The results of DEM simulations in the tetrapodal blender and the V-blender are presented in the third research paper.

In the third step, more than 100 experiments were carried out on mixing and segregation of non-adhesive granules in both the tetrapodal blender and the V-blender. The experiments were characterized using thief sampling. Segregation of granules with different sizes and densities were investigated over a wide range of rotational speeds ($5\text{-}30\text{RPM}$) and fill levels ($35\text{-}65\%V$). It was observed that the segregation intensity is far less important in the

tetrapodal blender than in the V-blender and it decreases significantly with an increase in the rotational speed, while the effect of the fill level is insignificant. The results of these experiments and scale-up of the tumbling blenders are presented in the fourth paper.

Although good agreements were observed between the DEM simulation results and experimental data especially when the dynamics of granules were considered, some minor discrepancies were observed regarding the mixing rates. Most of such errors arise mainly from inappropriate simulation parameters as well as weak predictions of contact force models. The former was discussed in the first step of this work, but the latter indeed requires more investigation. Contact force models suffer from some limitations. For instance, normal contact force models regularly fail to predict an adequate energy restitution behavior with increasing normal impact velocity. In particular, most non-linear models predict a net attraction force between two impacting particles near the end of a collision; this is unrealistic according to reported results. Such limitations have provided the impetus for the development of a normal contact force model that better predicts the unfolding of a collision between two particles. This model comprises a Hertz elastic force and a dissipative force that is evaluated by the motion of a non-Newtonian liquid in a dashpot. The model parameters are set using experimental restitution data for particle/particle and particle/wall contacts. In the current work, the measurement of energy restitution for particle/wall collision was carried out using several materials over a wide range of impact velocities, whereas particle/particle collision data were obtained from the literature. Model predictions for microscopic (*e.g.* particle velocity) and macroscopic (*e.g.* collision time) quantities were presented and compared with those from other non-linear models and experimental data. The model was observed to adequately predict the coefficient of restitution and to decrease the attraction force at the end of a collision. Our new contact force model is presented in the fifth paper.

As a conclusion, the scientific findings of this work contribute to four categories of applications. Firstly, the deep findings of this work in the case of tumbling blenders may facilitate the design and scale-up of more efficient solid mixing processes. Secondly, the performance

of the tetrapodal blender was investigated for the first time. It is recommended to use a tetrapodal blender, where there are issues with conventional mixers regarding mixing time or non-homogenous products that may be a result of less efficient mixing mechanisms or segregation of ingredients. Thirdly, it was originally shown why the DEM-based model yields acceptable results even when wrong physical parameters are used. Lastly, our accurate contact force model could be applied in DEM-based simulations to obtain more reliable results.

TABLE OF CONTENTS

DEDICATION	iii
ACKNOWLEDGMENTS	iv
RÉSUMÉ	vi
ABSTRACT	xi
TABLE OF CONTENTS	xvi
LIST OF TABLES	xxi
LIST OF FIGURESxxiv
LIST OF APPENDICES	xxxiv
LIST OF ABBREVIATIONS	xxxv
CHAPTER 1 INTRODUCTION	1
1.1 References	5
CHAPTER 2 LITERATURE REVIEW	9
2.1 Solid mixing	9
2.1.1 Mixtures types	10
2.1.2 Measuring the homogeneity of a mixture	10
2.2 Mixing equipment	13
2.2.1 Tumbling drum	13
2.2.2 Double cone, V-blender and bin blender	15
2.2.3 New configurations	22

2.3	Mixing in tumbling blenders and its mechanisms	24
2.4	Segregation in tumbling blenders and its mechanisms	25
2.4.1	Segregation Mechanisms	26
2.4.2	Segregation in rotating drum	29
2.4.3	Segregation in V-blender	31
2.5	Solid mixing characterization	32
2.5.1	Thief sampling	32
2.5.2	Radioactive particle tracking	33
2.5.3	Discrete element method	36
2.6	Problem identification and specific objectives	44
2.7	References	45
CHAPTER 3	COHERENCE OF THE ARTICLES	56
CHAPTER 4	Characterization of Mixing and Size Segregation in a Rotating Drum by a Particle Tracking Method	58
4.1	Introduction	60
4.2	Methodology	63
4.2.1	RPT	63
4.2.2	RPT with ^{24}Na	64
4.3	Experiments	65
4.3.1	Material	65
4.3.2	Details of the experiments	66
4.4	Results	66
4.4.1	Occupancy plots	67
4.4.2	Velocity profiles	67
4.4.3	Active layer thickness	72
4.4.4	Residence time	76

4.4.5	Segregation	79
4.4.6	Axial dispersion	82
4.5	Concluding remarks	85
4.6	References	86
 CHAPTER 5 Comparison of DEM Results and Lagrangian Experimental Data for the		
	Mixing and Segregation of Granules in a Rotating Drum	92
5.1	Introduction	94
5.2	Methodology	97
5.2.1	RPT experiments	97
5.2.2	DEM simulation	98
5.3	Results and discussion	101
5.3.1	DEM parameters	101
5.3.2	Velocity profiles and active layer thickness	106
5.3.3	Residence time	109
5.3.4	Mixing and segregation in the rotating drum	110
5.3.5	Quantification of axial dispersion	116
5.3.6	Sensitivity analysis of the DEM-based model	119
5.4	Conclusions	124
5.5	References	126
 CHAPTER 6 Discrete Element Simulation of Particle Mixing and Segregation in a Te-		
	trapodal Blender	134
6.1	Introduction	136
6.2	Methodology	140
6.2.1	DEM-based model	140
6.2.2	Details of the simulations	142
6.3	Results and discussion	145

6.3.1	Granular flow	145
6.3.2	Degree of mixing	146
6.3.3	Segregation	152
6.3.4	Dynamics of particles	157
6.4	Concluding remarks	161
6.5	References	163

CHAPTER 7 Experimental Investigation of Solid Mixing and Segregation in a Tetra-

podal Blender	168
7.1 Introduction	170
7.2 Methodology	172
7.2.1 Apparatus	172
7.2.2 Materials	173
7.2.3 Details of the experiments	175
7.2.4 Sampling method	177
7.2.5 Sample Analysis	179
7.3 Results and discussions	180
7.3.1 Degree of mixing	181
7.3.2 Segregation	185
7.4 Concluding remarks	198
7.5 References	199

CHAPTER 8 Development of a granular normal contact force model based on a non-

Newtonian liquid filled dashpot	204
8.1 Introduction	206
8.2 Contact forces	208
8.2.1 Collision of particles	208
8.2.2 Normal contact force models	209

8.3	Experimental setup and materials	213
8.4	Model development	215
8.5	Results and discussion	219
8.5.1	Macroscopic quantities	221
8.5.2	Microscopic quantities	227
8.6	Conclusion	229
8.7	References	231
CHAPTER 9	GENERAL DISCUSSION	237
9.1	References	242
CHAPTER 10	CONCLUSION AND RECOMMENDATIONS	243
10.1	Summary of the thesis	243
10.2	Contributions of the thesis	243
10.3	Limitations of the tetrapodal blender	244
10.4	Future work and recommendations	244
APPENDICES	246
A.1	Introduction	248
A.2	Methodology	250
A.2.1	RPT	250
A.2.2	Experiments	252
A.3	Results and discussion	255
A.3.1	Modeling of the residence time	257
A.3.2	Mixing and segregation	278
A.3.3	Axial dispersion	283
A.4	Conclusion	286
A.5	References	287

LIST OF TABLES

CHAPTER 1	1
CHAPTER 2	9
Table 2.1 Summary of specific studies performed to investigate performance of tumbling blenders.	17
Table 2.2 Summary of comparative studies performed to investigate performance of tumbling blenders. In addition to these studies, more studies can be found in Adams and Baker (1956); Carstensen and Patel (1977); Chowhan and Linn (1979); Gray (1957); Harnby (1967).	21
CHAPTER 3	56
CHAPTER 4	58
Table 4.1 Mixing experiments involving monodisperse and polydisperse particles.	67
Table 4.2 Depth of the active layer δ'_o	74
Table 4.3 Depth of the turning point active layer (δ_o). All data are in $[cm]$ (percentage of bed depth).	74
Table 4.4 Average residence time in the active layer. The range indicated for the experimental data corresponds to the standard deviation.	80
Table 4.5 Axial dispersion coefficient for the different experiments.	84
Table 4.6 Summary of the similarities and differences between the flow behavior of monodisperse, binary and polydisperse systems of particles.	85
CHAPTER 5	92
Table 5.1 RPT experiments and blend characteristics.	98

Table 5.2	DEM-based model parameters (measured and applied). The particle/wall impact properties were measured with the techniques mentioned and the particle/particle impact properties were extracted from the literature.	102
Table 5.3	Values of the Young's modulus (E) and friction coefficients used in DEM simulations from the literature that have led to acceptable results. When E is not given, the stiffness constant (k_n in Eq. 5.1) has been reported directly in the corresponding paper.	104
CHAPTER 6	134
Table 6.1	Physical and mechanical particle properties for the DEM-based model. P/P and P/W denote particle/particle and particle/wall collisions, respectively.	142
Table 6.2	Characteristics of the simulations.	144
Table 6.3	Mixing rate coefficient ($rev^{-1})(\times 10^{-2})$ for the TB and RL loading profiles of cases A-H.	150
CHAPTER 7	168
Table 7.1	Materials involved in the experiments.	174
Table 7.2	Characteristics of the experiments.	176
Table 7.3	Number of samples in each case of Table 7.2.	180
Table 7.4	Mixing rates ($rev^{-1})(\times 10^{-2})$ for different operating conditions.	182
Table 7.5	Average concentrations of big particles (MTL3) in the left (white) and right (blue) arms of the tetrapodal blender; these data were obtained by averaging the concentration of samples in each arm.	189
Table 7.6	Calculated values of $\overline{S_{r,t}}/k$ for different sized V-blenders. The blender sizes and experimental transition speeds were extracted from Alexander et al. (2004b)	198

CHAPTER 8	204
Table 8.1 Mechanical and geometrical properties of the spheres used in the particle/wall normal impact experiments. These properties were provided by the supplier (McMaster-Carr) and the literature (Bolz and Tuve, 1970; Gale, 2004; Kschinka et al., 1986).	215
Table 8.2 Model parameters for various materials in the case of particle/particle collisions. Mechanical and geometrical properties of these materials can be found in Kruggel-Emden et al. (2007).	220
Table 8.3 Model parameters for various materials in the case of particle/wall collisions. For abbreviations and material properties, see Table 8.1.	220
CHAPTER 9	237
CHAPTER 10	243
Table A.1 Tablet composition	253
Table A.2 Tablet properties	254
Table A.3 Design of experiments	256
Table A.4 Definition of the variables used	258
Table A.5 Primary observations	259
Table A.6 Values of the active layer thickness α_o based on the turning point line	272
Table A.7 Values of the active layer thickness δ_o based on the yield line	274
Table A.8 Blend characteristic ratios	280
Table A.9 Axial dispersion coefficient	285

LIST OF FIGURES

CHAPTER 1	1
Figure 1.1 Tetrapodal mixing device.	3
CHAPTER 2	9
Figure 2.1 Different types of free flowing mixtures : (a) perfect mixture, (b) ran- dom mixture and (c) segregated mixture.	11
Figure 2.2 Different transverse motions of solids in a rotating drum (Mellmann, 2001).	14
Figure 2.3 Rolling regime in a cylindrical drum.	15
Figure 2.4 Industrial blenders (a) double cone, (b) V-blender and (c) tote bin blender. The bin-blender is usually built in two geometrical configura- tions, one with a square cross section (tote bin blender) and one with a cylindrical cross section (bohle bin blender).	16
Figure 2.5 Different loading profiles for V-blender, (a) Front-Back (FB), (b) Right- Left (RL) and (c) Top-Bottom (TB) (Lemieux et al., 2007).	22
Figure 2.6 New geometries proposed for solid mixing.	23
Figure 2.7 (a) Bad convective and diffusive mechanisms, (b) good convective and bad diffusive mechanisms, (c) bad convective and good diffusive me- chanisms, (d) good convective and diffusive mechanisms.	25
Figure 2.8 Mechanisms of segregation (a) trajectory, (b) sifting (Schulze, 2008), (c) kinetic sieving (Schulze, 2008) and (d) elutriation (Rhodes, 2008).	27
Figure 2.9 (a) Segregation due to percolation in containers shaken vertically, (b) segregation on a pile due to avalanching (Schulze, 2008).	29
Figure 2.10 Segregation due to different repose angles resulting from (a) particle shape, and (b) particle size (Schulze, 2008).	30

Figure 2.11	Segregation patterns in V-blender (Alexander et al., 2003).	32
Figure 2.12	(a) Core sampler and (b) side-sampler.	33
Figure 2.13	Typical setup of RPT.	35
Figure 2.14	Nonlinear contact force model predictions for normal impact with different coefficients of restitution : (a) Kuwabara and Kono (KK) model, (b) Tsuji (TS) model and (c) normalized experimental results (Zhang and Whiten, 1996).	42
CHAPTER 3	56
CHAPTER 4	58
Figure 4.1	Rolling regime in a cylindrical drum.	61
Figure 4.2	Schematic of the setup.	65
Figure 4.3	Velocity vectors in the transverse plane of the drum for (a) monodisperse (case MD2) and (b) polydisperse (case PD2) glass beads.	68
Figure 4.4	Variation of the (a) transverse and (b) streamwise velocities for a rotational speed of $11.6RPM$ in the transverse plane of the drum along the line at $x = 0$. H is the distance from the free surface to the center of the drum, δ is the distance from the free surface to the depth at which glass beads change direction along the x axis, and δ' is the distance from the free surface to the depth at which the solid body rotation stops.	69
Figure 4.5	Streamwise velocity profiles for the polydisperse mixture of case PD2 for different positions in x	70
Figure 4.6	Streamwise velocity profiles along the x -direction ; (a) on the free surface and (b) in the inner layers, in the case of MD2. d stands for the distance from the free surface, $L = L(y)$ corresponds to half the length of the corresponding streamline in the active layer, and $L^* = L _{y=-H}$. u_{act} is the velocity at the middle of each streamline.	71

Figure 4.7	Variation of the residence time versus the angle of the streamlines for (a) cases MD1 and PD1, and (b) cases MD2 and PD2. The symbols correspond to experimental data.	77
Figure 4.8	Occupancy plots for the different tracers in the polydisperse mixtures; the upper and lower plots refer to cases PD1 and PD2, respectively. The white curve highlights the boundary between the passive and active layers on the basis of the turning point criterion.	80
Figure 4.9	Probability of the occurrence of the different tracers along the middle line at $x = 0$; (a) case PD1 and (b) case PD2.	81
Figure 4.10	Typical axial displacement distribution for the 3- <i>mm</i> tracer in the monodisperse case MD2.	83
Figure 4.11	Variation of the axial dispersion coefficient along the line at $x = 0$ in the transverse plane of the drum.	84
CHAPTER 5	92
Figure 5.1	Typical velocity vectors obtained by (a) the DEM simulations and (b) RPT experiments. (c) Differences in the velocity vectors displayed in (a) and (b).	107
Figure 5.2	Streamwise velocity profile at $x = 0$ as seen from the drum end wall. The vertical axis represents the distance from the center of the drum, and the horizontal axis represents the streamwise velocity. H is the distance from the center of the drum to the free surface of material, δ_o is the distance from the free surface to the depth at which the solid body rotation of the bed of particles stops, and δ'_o is the distance from the free surface to the depth at which these particles change direction along the x axis.	107

Figure 5.3	Surface velocity profiles : (a) normalized streamwise velocity vs the dimensionless distance along the surface, (b) velocity vectors at the free surface along the drum length, where the DEM (resp. RPT) results are used for the left (resp. right) side of the drum.	108
Figure 5.4	(a) A streamline making a full rotation in the active and passive layers ; (b) variations of the residence times in active and passive layers when the angle of the streamline increases.	110
Figure 5.5	Evolution of the (a) weak sense and (b) strong sense mixing indices along the radial and axial directions.	112
Figure 5.6	Occupancy plots for the different-sized particles of the polydisperse mixture : (a)-(d) and (e)-(h) were obtained from the DEM and RPT, respectively. The colors show the probabilities of occurrence of the corresponding particles. The RPT occupancy plots come from Alizadeh et al. (2013b)	113
Figure 5.7	(a) Time variation of $d_{i,t}$, and (b) variation of $d_{i,t}$ along the drum length for $t = 120s$ (DEM results only).	114
Figure 5.8	Axial segregation predicted by the DEM. The colors show the probabilities of occurrence of corresponding particles.	116
Figure 5.9	Concentration of the different-sized particles after 120 sec of DEM simulation. See Table 5.1 for the overall concentration of each species. . .	117
Figure 5.10	Axial dispersion coefficients determined from the displacements of the different-sized particles along a line perpendicular to the free surface at $x = 0$	118
Figure 5.11	Effect of the damping constant ($c_n = 0.3, c_t = 0.3, c_{n,w} = 0.3$ and $c_{t,w} = 0.3$) on the (a) time variation of $d_{i,t}$, and (b) variation of $d_{i,t}$ along the drum length for $t = 100s$ (DEM results only).	120

Figure 5.12	Effect of the friction coefficient $\mu_{w,s}$ on the simulation results when smaller values of the Young's modulus are used.	124
CHAPTER 6	134
Figure 6.1	Rotation of (a) the V-blender around two axes and (b) the standard tetrapodal blender.	138
Figure 6.2	Different configurations of the twisted tetrapodal blender considered in the current work.	144
Figure 6.3	Comparison of the RSD curves obtained from DEM simulations for the standard tetrapodal blender and the V-blender underlying different loading profiles and operating conditions.	148
Figure 6.4	Evolution of the weak sense mixing index for the V, standard tetrapodal and twisted tetrapodal blenders.	151
Figure 6.5	Evolution of the strong sense mixing index in the X, Y and Z directions for a bidisperse mixture in the standard tetrapodal blender. The simulations were run from (a) fully segregated (FB loading profile) and (b) fully mixed initial states.	153
Figure 6.6	Front (a and c) and side (b and d) views of the local segregation patterns in the standard tetrapodal blender (case J). When the granules flow over an inclined surface (region A), kinetic sieving and trajectory mechanisms separate the large (blue) and small (red) granules into regions B and C, respectively. When the flowing layer becomes thin enough, kinetic sieving separates the particles with respect to size into nearly pure layers (D and E). For similar reasons, the larger particles also accumulate in region F.	156
Figure 6.7	Percentage of particles crossing the axial plane of symmetry in a full revolution, for the different blenders and operating conditions.	158

Figure 6.8	Granular mean radial and axial velocities in a full revolution of the different blenders, for operating conditions given in Table 6.2 : (a), (b) standard tetrapodal blender and (c), (d) V-blender.	161
Figure 6.9	Granular (a) mean radial and (b) axial velocities in a full revolution of twisted configurations of the tetrapodal blender, for the operating conditions in Table 6.2.	162
CHAPTER 7	168
Figure 7.1	Dimensions of the blenders considered in this study ; (a) standard tetrapodal blender, and (b) V-blender.	173
Figure 7.2	Front view of the different configurations and loading profiles of the tetrapodal blender : (a) (45 0) and Top-Bottom (TB), (b) (0 0) and Front-Back (FB), (c) (90 45) and Right-Left (RL), (d) (90 90).	177
Figure 7.3	Applied (a) core sampler and (b) side sampler in the experiments involving the tetrapodal blender and the V-blender, respectively.	178
Figure 7.4	Sampling locations for (a) the tetrapodal blender and (b) the V-blender. The red dashed straight lines show the rotation axis of the blenders. . .	179
Figure 7.5	Comparison of the RSD curves obtained for the standard tetrapodal blender and the V blender in the case of TB and FB loading profiles under different operating conditions, as summarized in Table 7.2. . . .	183
Figure 7.6	Comparison of the RSD curves in the case of RL loading profile under different operating conditions, as summarized in Table 7.2 : (a) standard tetrapodal blender and (b) V-blender.	184
Figure 7.7	(a) Radial k_r and (b) axial k_a mixing rates obtained from the TB and RL loading profiles, respectively. The mixing rates are in $(rev^{-1})(\times 10^{-2})$. . .	184
Figure 7.8	Values of I_s for different configurations of the tetrapodal blender under several operating conditions, as summarized in Table 7.2.	187

Figure 7.9	Effect of density and simultaneous effects of density and size of granules on the segregation intensity in the twisted tetrapodal blender (-45 45) for various rotational speeds, as summarized in Table 7.2.	192
Figure 7.10	(a) Regular granular flow in the tetrapodal blender, (b) granular flow in the simplified model of this work for the scale-up of the blender. The red and blue colors correspond to the two types of particles in the system.	194
CHAPTER 8	204
Figure 8.1	Normalized RSD curves obtained from DEM simulations (Chapter 6) and thief sampling (Chapter 7) for a tetrapodal blender (fill level 35% V and rotating at 15 RPM).	205
Figure 8.2	Collision of two spheres.	209
Figure 8.3	Nonlinear contact force model predictions for normal impact with different coefficients of restitution : (a) Kuwabara and Kono (KK) model, (b) Tsuji (TS) model and (c) normalized experimental results (Zhang and Whiten, 1996).	213
Figure 8.4	The main components of the experimental setup.	214
Figure 8.5	Model proposed for the normal contact of two particles : (a) just before the collision, and (b) during the collision. The piston is partially immersed in the non-Newtonian liquid of the dashpot, and kR_D and R_D are the radii of the piston and cylinder, respectively.	217
Figure 8.6	Coefficient of restitution versus the impact velocity for different materials in the case of particle/particle collisions : (a) stainless steel (SS), (b) brass (BR) and (c) lead (LE).	222
Figure 8.7	Collision time versus the impact velocity for different materials in the case of particle/particle collisions : (a) stainless steel (SS), (b) brass (BR) and (c) aluminum (Al).	223

Figure 8.8	Coefficient of restitution versus the impact velocity for different materials in the case of particle/wall collisions : (a) metallic spheres and (b) non metallic spheres.	224
Figure 8.9	Variation of the coefficient of restitution for low carbon steel spheres when (a) the power law index is constant ($n_l = 1.72$) and μ varies, and (b) μ is constant ($\mu = 1.35 \times 10^5$) and n_l varies. The symbols in (a) refer to particle size.	225
Figure 8.10	Experimental variation of the power law index (n_l) versus the hardness of the materials.	226
Figure 8.11	Experimental variation of the coefficient of restitution with respect to the impact velocity for 4-mm polypropylene spheres. Error bars have been added to show the uncertainty for this type of measurements . . .	226
Figure 8.12	Comparison of non-linear models in the case of a particle/particle collision : (a) nearly elastic collision (stainless steel), (b) viscoelastic collision (brass) and (c) very viscoelastic collision (lead).	228
Figure 8.13	Graph of the normal impulse P^n versus the impact velocity when (a) repulsive and (b) attractive forces are considered for the collision of two brass spheres.	230
CHAPTER 9	237
Figure 9.1	Prediction of CoR for (a) brass spheres and (b) marble spheres using viscoelastic, hysteretic and proposed models. The symbols refer to the experimental data from (Goldsmith, 1960) and the predictions of hysteretic models are extracted from Kruggel-Emden et al. (2007).	242
CHAPTER 10	243
Figure A.1	Schematic representation of the five tablets used in this study.	254

Figure A.2	(a) Cross-section view of the rotating drum and (b) a close-up on the active layer.	257
Figure A.3	Typical velocity field for (a) tablet E and (b) blend AE (at 10RPM). .	260
Figure A.4	Streamwise velocity profiles at $x=0$ for (a) the individual tablets and (c) the different blends, and transverse velocity profiles at $x=0$ for (b) the individual tablets and (d) the different blends.	263
Figure A.5	Streamwise velocity profiles for (a) tablet C and (c) blend AE, and transverse velocity profiles for (b) tablet C and (d) blend AE, at $x = 0\text{m}$, $\pm 0.04\text{m}$ and $\pm 0.08\text{m}$	264
Figure A.6	Streamwise velocity profiles along the bed free surface for (a) the individual tablets and (b) the different blends, and the scaled streamwise velocity profiles along the bed free surface for (c) the individual tablets and (d) the different blends.	266
Figure A.7	Normalized streamwise velocity profiles at the bed surface for (a) the individual tablets and (b) the different blends, and under the bed surface for (c) tablet C and (d) tablet D.	267
Figure A.8	Normalized active layer depth profile $\alpha(x)/\alpha_o$ for tablets D and E, and 6mm glass bead.	269
Figure A.9	Mean residence time in cells of the Eulerian grid used for (a) tablet B and (b) tablet D.	275
Figure A.10	Residence times in the active and passive layers for all the tablets and blends tested. The symbols correspond to experimental data.	279
Figure A.11	Values of (a and c) the occupancy and (b and d) the location probability for blends AE, AE*, BC and the 5-6 mm glass beads. For (a) and (b), the smaller particle was used as a tracer. For (c) and (d), the larger particle was used as a tracer.	281

Figure A.12	Values of (a) the occupancy and (b) the location probability for blends CD and CE.	283
Figure A.13	Evolution of D_{axial} with respect to the active layer depth (ξ_o).	284

LIST OF APPENDICES

Annexe A	Dynamics of Non-Spherical Particles in a Rotating Drum	246
----------	--	-----

LIST OF ABBREVIATIONS

CoR	Coefficient of Restitution
DEM	Discrete ElementMethod
FEM	Finite Element Method
Fr	Froude Number
FB	Front-Back loading profile
KK	Kuwabara-Kono contact force model (Kuwabara and Kono, 1987)
LDA	Laser Doppler Anemometry
LH	Lee-Herrmann contact force model (Lee and Herrmann, 1993)
LSD	Linear Spring Dashpot force model
MD	Mindlin contact force model (Mindlin, 1949) ;
NIR	Near Infrared Spectroscopy
PEPT	Positron Emission Particle Tracking
PIV	Particle Image Velocimetry
RL	Right-Left loading profile.
RPT	Radioactive Particle Tracking
RSD	Relative Standard Deviation
RSD _r	Random Mixed State Relative Standard Deviation
TB	Top-Bottom loading profile.
TH	Thornton contact force model (Thornton and Ning, 1998)
TO	Tomas contact force model (Tomas, 2003)
TS	Tsuji contact force model (Tsuji et al., 1992)
WB	Walton and Braun contact force model (Walton and Braun, 1986)

CHAPTER 1

INTRODUCTION

Solid mixing is a key unit operation for many industries, including ceramic, metallurgical, chemical, food, cosmetics, coal, plastics and pharmaceutical. For an indication of the widespread applications of granular material, a 1993 study estimated that granule-based products contributed one trillion dollars to the US economy ([Scott, 2003](#)). In some processes, it is desirable to separate specific components of a mixture, while in most others, the ingredients should generally be mixed with each other and their concentration must be strictly maintained within very small intervals to meet quality and performance goals. Therefore, weak mixing may lead to the rejection of the final product due to poor quality. Despite the importance of the homogenous mixtures, obtaining the homogeneity in scrutiny scale is difficult, particularly when the granules have different physical or mechanical properties, which may result in segregation. This is the situation that is likely to prevail more and more with the formulation of new products.

Blenders are among the most commonly used equipment to obtain a homogenous mixture. They are divided into two main groups : convective and tumbling blenders. While convective blenders involve the use of moving parts; tumbling blenders apply gravity and blender rotation to mix granules. Convective blenders vary by ribbon type and/or bowl shape, and tumbling blenders differ mainly in their geometry ([Brone et al., 1998](#)). In comparison with the convective blenders, tumbling blenders are easy to operate and handle a variety of materials including shear sensitive granules. Among tumbling blenders, V-blenders and rotating drums are among the most frequently employed blenders in the industry. V-blender was first designed and patented by [Fischer \(1950\)](#) and, subsequently, found numerous applications in many industries. Tumbling blenders, also, show significant segregating behavior for granules with different properties ([Alexander et al., 2003, 2004](#)).

Mixing occurs in both axial and radial directions of tumbling blenders. The axial (resp. radial) direction is defined as parallel (resp. perpendicular) to the rotation axis of the blender. The governing mixing mechanism in the axial direction is diffusion and a combination of convection and diffusion in the radial direction. Convection moves large clusters of particles, while diffusion leads to individual movements of the particles. Since diffusion is a slower phenomenon than convection, tumbling blenders always suffer from weak axial mixing ([Arratia et al., 2006](#); [Brone et al., 1997](#); [Lemieux et al., 2007](#); [Moakher et al., 2000](#)). Some modifications have been patented to disturb the periodic and symmetric flow inside the bowl and increase axial mixing. In the case of V-blender, these ideas include using a controlled axial flow by installing an intensifier ([Fischer, 1983](#)), an offset rotating axis with respect to the plane of symmetry of the blender ([Peck, 1954](#)), and non-equal lengths of the blender arms. Such modifications do not result in remarkable improvement in the axial flow. Therefore, an alternative geometry is required to produce different granular flows inside the blender and alleviate the limitations of conventional tumbling blenders.

One solution may be to add another rotation axis perpendicular to the existing rotation axis. Such a rotation allows granules to flow in the axial direction. This method has been applied in the case of the double-cone and bin blenders whereby enhanced mixing was observed ([Manickam et al., 2010](#); [Mehrotra and Muzzio, 2009](#)). Simultaneous rotations around two axes are challenging due to mechanical limitations. In order to benefit the function of both rotation axes, we undertook an interest in the geometry shown in Fig. 1.1. This geometry, called the tetrapodal mixing device, was patented in 1964 (USA patent office, 3,134,578, [Anderson, 1964](#)). It consists of a container with one axis of rotation going through its center of gravity, one arm extending from it in one direction and three other arms organized like a tripod and extending in the opposite direction. In other words, it consists of a pair of V-blenders connected at the bottom with one twisted by 90° . The lower V-shaped part is like a conventional V-blender and the upper part is similar to a V-blender with the rotation axis perpendicular to the conventional one. Despite the seemingly effective shape of this blender

for granule mixing, no study has yet been conducted to investigate its performance. Apart from the complexity of the geometry and the cleaning process after the operation of the blender, larger dimensions of this blender other than the conventional V-blender, necessitate additional space and energy to operate the blender. In addition, the scaling-up of the device for industrial applications seems to be another limiting parameter to generalize the application of this blender. Regardless of such drawbacks, the limitations of conventional tumbling blenders provided the impetus to investigate solid mixing inside this device.

Designing more efficient solid mixing processes is mostly limited by poor knowledge of mixing and segregation behavior inside granular systems. This is mainly due to the complex behavior of granular dynamics. Therefore, the main objective of this work is to shed light on the granular behavior inside conventional tumbling blenders : the rotating drum, the V-blender as well as the tetrapodal blender.

Investigation of the mixing and dynamics of granules can be carried out via thief sampling ([Lemieux et al., 2007](#)) and non-intrusive techniques ([Doucet et al., 2008](#)). However, before investing in manufacturing a lab-scale version of the tetrapodal blender to investigate its performance experimentally, it is of interest to characterize the efficiency of the blender via

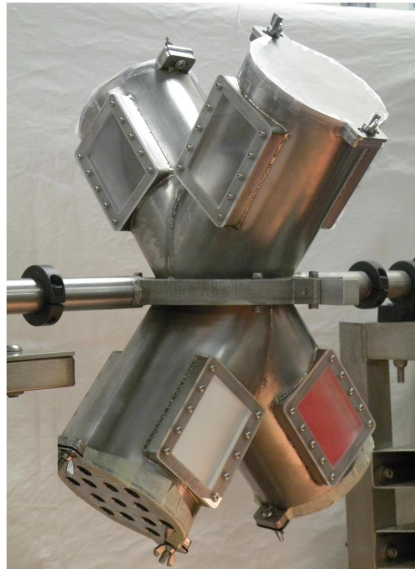


Figure 1.1: Tetrapodal mixing device.

numerical tools to verify its superiority against conventional tumbling blenders and obtain design parameters. Two approaches (both continuum models and particle dynamic simulations) have been employed to simulate granular flow in the literature. The first approach is Eulerian and assumes the continuity for the powders ([Aranson and Tsimring, 1999](#); [Khakhar et al., 1997, 2001](#)) and the second approach is Lagrangian, which considers each single particle as a system (*e.g.* particle dynamics). In the second approach the discrete element method (DEM), originally given by [Cundall and Strack \(1979\)](#), has been applied to investigate granule mixing and segregation inside the tumbling blenders ([Lemieux et al., 2007, 2008](#); [Rapaport, 2007](#)). The DEM method provides new insights into the phenomena occurring in the granular bed and affords extensive details about the flow and mixing of the granules.

Unresolved questions about the granular flow and the ability of DEM to predict these types of flow have generated considerable interest, resulting in extensive research works on this subject in recent years. However, few comparisons with experimental data have been performed to examine the validity of the DEM ([Lemieux et al., 2007](#); [Sudah et al., 2005](#); [Taberlet et al., 2006](#); [Yamane et al., 1998](#)). Such studies in the literature are mostly qualitative via visual comparison of flow patterns. For instance, [Moakher et al. \(2000\)](#) considered double-cone and V-blenders, and [Iwasaki et al. \(2001\)](#) studied a high-speed elliptical rotor-type powder mixer, both groups demonstrating that calculated flow patterns agreed with experimental observations. Since there is a limited number of techniques capable of providing Lagrangian data and mapping the velocity field inside opaque granular systems, studies that quantitatively validate the DEM at the particle scale are lacking. Such studies can be found in [Laurent and Cleary \(2012\)](#), [Kuo et al. \(2002\)](#) and [Stewart et al. \(2001\)](#). Despite the importance of previous investigations, comparisons of Lagrangian experimental data and DEM-based model continue to be inadequate. Indeed, in many studies, real values of particle properties have not been used for the DEM simulations and neither have they been experimentally measured. While these parameters demonstrate a high effect on the granular flow, authors have often adjusted them in order to obtain results that agree well with experimental observations.

According to what was mentioned earlier, the first challenge of this study is to provide a detailed and thorough comparison between Lagrangian numerical results of the DEM and experimental data of radioactive particle tracking (RPT) technique. This step is restricted to a simple geometry of a rotating drum and, as a consequence, does not look into geometrical effects on the flow behavior. To capture the ability of DEM in predicting different granular behavior, using RPT data, several phenomena are investigated for the first time and DEM prediction for such phenomena are checked. Then, effective dimensionless numbers are introduced to explain how DEM parameters should be chosen. Based on these analyses, adequate parameters could be chosen to conduct several simulations to investigate the mixing and segregation inside the tetrapodal blender and common V-blenders. In the next step, numerical findings should be validated through experimental data. In addition, further investigations are necessary to thoroughly consider the effect of several parameters on the blender efficiency, which could not be performed using the DEM-based model due to it being CPU-intensive.

1.1 References

- Alexander, A., Muzzio, F., and Shinbrot, T. (2003). Segregation patterns in V-blenders. *Chemical Engineering Science*, 58(2) :487–496.
- Alexander, A., Shinbrot, T., Johnson, B., and Muzzio, F. J. (2004). V-blender segregation patterns for free-flowing materials : effects of blender capacity and fill level. *International Journal of Pharmaceutics*, 269(1) :19–28.
- Anderson, M. (1964). Tetrapodal mixing device. US Patent :US 3,134,578.
- Aranson, I. and Tsimring, L. (1999). Dynamics of axial separation in long rotating drums. *Physical Review Letters*, 82(23) :4643–4646.
- Arratia, P., Duong, N.-h., Muzzio, F., Godbole, P., and Reynolds, S. (2006). A study of the mixing and segregation mechanisms in the bohle tote blender via DEM simulations. *Powder Technology*, 164(1) :50–57.

- Brone, D., Alexander, A., and Muzzio, F. (1998). Quantitative characterization of mixing of dry powders in V-blenders. *AIChE Journal*, 44(2) :271–278.
- Brone, D., Wightman, C., Connor, K., Alexander, A., Muzzio, F. J., and Robinson, P. (1997). Using flow perturbations to enhance mixing of dry powders in V-blenders. *Powder Technology*, 91(3) :165–172.
- Cundall, P. and Strack, O. (1979). Discrete numerical model for granular assemblies. *Geotechnique*, 29(1) :47–65.
- Doucet, J., Bertrand, F., and Chaouki, J. (2008). An extended radioactive particle tracking method for systems with irregular moving boundaries. *Powder Technology*, 181(2) :195–204.
- Fischer, J. (1950). Blending or mixing apparatus. US Patent :US 2,514,126.
- Fischer, J. (1983). Dual shell blender with intensifier. US Patent :US 4,368,986.
- Iwasaki, T., Satoh, M., and Koga, T. (2001). Analysis of collision energy of bead media in a high-speed elliptical-rotor-type powder mixer using the discrete element method. *Powder Technology*, 121(2-2) :239–248.
- Khakhar, D., McCarthy, J., and Ottino, J. (1997). Radial segregation of granular mixtures in rotating cylinders. *Physics of Fluids*, 9(12) :3600–3614.
- Khakhar, D., Orpe, A. V., and Ottino, J. (2001). Continuum model of mixing and size segregation in a rotating cylinder : Concentration-flow coupling and streak formation. *Powder Technology*, 116(2-3) :232–245.
- Kuo, H., Knight, P., Parker, D., Tsuji, Y., Adams, M., and Seville, J. (2002). The influence of DEM simulation parameters on the particle behaviour in a V-mixer. *Chemical Engineering Science*, 57(17) :3621 – 3638.
- Laurent, B. and Cleary, P. (2012). Comparative study by PEPT and DEM for flow and mixing in a ploughshare mixer. *Powder Technology*, 228 :171–186.

- Lemieux, M., Bertrand, F., Chaouki, J., and Gosselin, P. (2007). Comparative study of the mixing of free-flowing particles in a V-blender and a bin-blender. *Chemical Engineering Science*, 62(6) :1783–1802.
- Lemieux, M., Leonard, G., Doucet, J., Leclaire, L.-A., Viens, F., Chaouki, J., and Bertrand, F. (2008). Large-scale numerical investigation of solids mixing in a V-blender using the discrete element method. *Powder Technology*, 181(2) :205–216.
- Manickam, S., Shah, R., Tomei, J., Bergman, T., and Chaudhuri, B. (2010). Investigating mixing in a multi-dimensional rotary mixer : Experiments and simulations. *Powder Technology*, 201(1) :83–92.
- Mehrotra, A. and Muzzio, F. (2009). Comparing mixing performance of uniaxial and biaxial bin blenders. *Powder Technology*, 196(1) :1–7.
- Moakher, M., Shinbrot, T., and Muzzio, F. (2000). Experimentally validated computations of flow, mixing and segregation of non-cohesive grains in 3D tumbling blenders. *Powder Technology*, 109(1-3) :58–71.
- Peck, W. C. (1954). Improvements relating to apparatus for mixing discrete particles. GB Patent :GB 709,003.
- Rapaport, D. (2007). Radial and axial segregation of granular matter in a rotating cylinder : a simulation study. *Physical Review E*, 75(3) :31301–1–11.
- Scott, D. M. (2003). Characterizing particle characterization. *Particle and Particle Systems Characterization*, 20(5) :305–310.
- Stewart, R. L., Bridgwater, J., Zhou, Y. C., and Yu, A. B. (2001). Simulated and measured flow of granules in a bladed mixer—a detailed comparison. *Chemical Engineering Science*, 56(19) :5457–5471.
- Sudah, O. S., Arratia, P. E., Alexander, A., and Muzzio, F. J. (2005). Simulation and experiments of mixing and segregation in a tote blender. *AIChE Journal*, 51(3) :836–844.

Taberlet, N., Newey, M., Richard, P., and Losert, W. (2006). On axial segregation in a tumbler : an experimental and numerical study. *Journal of Statistical Mechanics : Theory and Experiment*, 2006(07) :17 pp.

Yamane, K., Nakagawa, M., Altobelli, S., Tanaka, T., and Tsuji, Y. (1998). Steady particulate flows in a horizontal rotating cylinder. *Physics of Fluids*, 10(6) :1419–27.

CHAPTER 2

LITERATURE REVIEW

As mentioned in the previous chapter, the main objective of this study is the investigation of granular flow as well as solid mixing and segregation behavior inside the rotating drum, the V-blender and the tetrapodal blender. Selecting and designing a proper mixer demands an understanding of process requirements as well as material properties. Therefore, in Section 2.1, concepts of the solid mixing in a “dry” state are covered. In Section 2.2, equipments that are commonly used to obtain a homogenous mixture are introduced and their limitations are investigated. The mechanisms of solid mixing and segregation in tumbling blenders are described in Sections 2.3 and 2.4, respectively. Finally, the techniques to characterize solid mixing, which are employed in this study, are explained in Section 2.5 and the gaps in the body of knowledge will be explained in Section 2.6.

2.1 Solid mixing

Solid mixing processes are widely used in many industries, including ceramic, metallurgical, chemical, food, cosmetics, coal, plastics and pharmaceutical. Solid mixing adheres to several objectives; some of them are summarized below :

- Mixing of a product for homogenization or reduction of variance (*e.g.* blending of polymer pellets) ;
- Mixing of active ingredients into a carrier material (*e.g.* pharmaceutical drugs) ;
- Mixing of multicomponent mixture (*e.g.* cereal mix) ;
- Coating of a cohesive component onto a carrier.

In most of these applications, homogeneity of the mixture is an objective. To have a clear idea about the definition of “homogeneity”, we should have an understanding of different kinds of

mixtures and the indices in which homogeneity can be measured.

2.1.1 Mixtures types

Definitions of mixtures may differ depending on the granules. Generally, granules are divided into two main groups regarding the magnitude of the inter-particle forces :

- *Free flowing (non-cohesive)* : In these granules, inter-particle forces are negligible and do not play a role in the granule motion ;
- *Cohesive* : Granules have non-negligible inter-particle forces and their motion is also subjected to inter-particle forces.

We have restricted the study to free flowing granules and, as a result, have simplified the case study. Indeed, the mixing of cohesive material, especially in the case of tetrapodal blender, remains to be seen in future works.

Different types of free flowing mixtures are shown in Fig. 2.1. In a perfect mixture of two species, any randomly taken sample from the mixture has the same properties as the whole of the mixture (Fig. 2.1a). Such perfect mixtures are rarely found in nature and may be obtained by placing each particle one at a time. A random mixture is obtained when two non-interactive components with similar properties are mixed in an ideal blender (Fig. 2.1b). If the particles have different properties (shape, size, density, etc.) a textured (segregated) mixture will be obtained, as shown in 2.1c. Henceforth in this paper a homogenous mixture will denote randomly mixed one.

2.1.2 Measuring the homogeneity of a mixture

Many indices were developed to measure the homogeneity of mixtures. A good review of these indices can be found in Poux et al. (1991) and Fan et al. (1970). Common methods are based on the sampling and measuring of the concentration of a key component at various locations over time, in order to determine how fast the variance of the samples concentration approaches an expected value. Among these indices, relative standard deviation (RSD) has

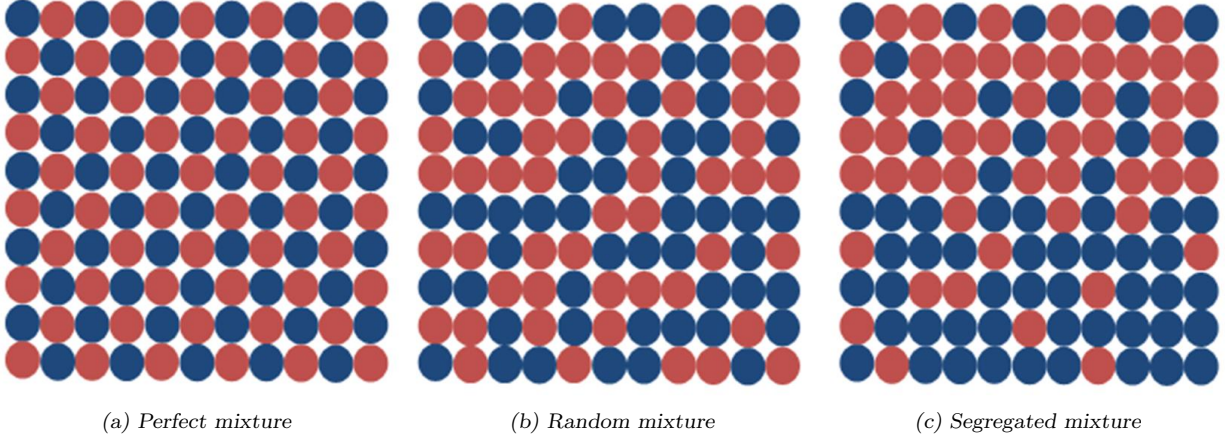


Figure 2.1: Different types of free flowing mixtures : (a) perfect mixture, (b) random mixture and (c) segregated mixture.

many applications. It evaluates the variance of the concentration of a given species in a system :

$$RSD = \frac{\sigma}{\bar{x}}, \quad (2.1)$$

with

$$\sigma = \sqrt{\frac{\sum_{i=1}^M (x_i - \bar{x})^2}{M - 1}}, \quad (2.2)$$

where M is the number of taken samples, x_i the concentration of one species in sample i and \bar{x} the mean concentration of that species in the whole blender. To obtain mixing time, the RSD of a system should be compared with the RSD of a random mixture, RSD_r (Paul et al., 2004) :

$$RSD_r = \frac{\sigma_r}{\bar{x}}, \quad (2.3)$$

$$\sigma_r = \sqrt{\frac{\bar{x}(1 - \bar{x})}{m}}, \quad (2.4)$$

where m denotes the number of the particles in one sample and depends on the level of scrutiny¹.

Indices like RSD, which measure the homogeneity of a mixture from samples, suffer from some limitations. For instance :

- Mixing measurements are not connected to a special coordinate ;
- Many of indices are based on the concentration of a given species that is one single property. Other properties (*e.g.* temperature, particle size, particle density) could be considered ;
- These indices depend on the number, size and location of the samples as discussed by [Lemieux et al. \(2008\)](#).

Considering these limitations, [Doucet et al. \(2008c\)](#) proposed a new mixing index to bridge the global mixing properties and local viewpoint of chaotic theory, with applications to granular and fluid flow systems. The index is based on the Lagrangian trajectory of particles obtained either numerically through computer simulation (*e.g.* discrete element method) or experimentally by means of non-intrusive methods (*e.g.* radioactive particle tracking). This index has been applied to assess the quality of mixing in pharmaceutical equipment ([Bouffard et al., 2013](#); [Doucet et al., 2008a](#)). More details on the mathematical formulation of this index can be found in [Doucet et al. \(2008c\)](#).

Two different indices were in fact defined by [Doucet et al. \(2008c\)](#), which characterize the concept of mixing in the weak and strong senses. Mixing in the weak sense considers the correlation between the current and initial positions of the particles without respect to their properties, such as size or density. More precisely, a system is mixed in the weak sense if the position of the particles at time t is not correlated to their initial position. In such a case, the particles distribute themselves uniformly in the blender and the index levels off to zero with respect to time. However, this index fails to capture the occurrence of segregation with respect to the particle properties. For this reason, a more strict definition of mixing

1. The level of scrutiny is the smallest amount of a mixture (volume or number of particles) which the homogeneity needs to be investigated.

was introduced, which considers properties of the material and is called mixing in the strong sense. A system is said to be mixed in the strong sense if the position of the particles at time t is not correlated to their initial position and other given properties. The corresponding strong sense mixing index then levels off to zero with respect to time. Note that, from these definitions, a system that is mixed in the strong sense is also mixed in the weak sense. It is also possible to define and use similar indices to investigate the intensity of mixing (or segregation) along specific directions.

2.2 Mixing equipment

Generally, blenders are used to obtain a homogenous mixture from granular material. Other options are fluidized beds, hoppers and etc. Blenders are divided into two main groups : convective and tumbling blenders. Whereas convective blenders involve the use of moving parts, tumbling blenders apply gravity and blender rotation to mix granules. Convective blenders vary by ribbon type and/or bowl shape, while tumbling blenders differ mainly in their geometry ([Brone et al., 1998](#)). In comparison with the convective blenders, tumbling blenders are easy to operate and handle a variety of materials including shear sensitive granules. The most common tumbling blenders are introduced in the following sections.

2.2.1 Tumbling drum

The simplest tumbling blender is a rotating drum that is known as a low shear equipment and has lots of applications such as a granular mixer, a dryer, a coater or a gas/solid reactor. Since the simple geometry of this blender does not disturb granular flow, it attracts many academic research interests on granular flow behavior. In this study, this blender was considered to check the validity of the results of employed numerical technique.

In the rotating drum, depending on the range of Froude numbers (Fr), the fill levels and the frictions coefficients between the particles and the drum, different types of transverse bed motions can be observed, as illustrated in Fig. 2.2 ([Meier et al., 2007](#); [Mellmann, 2001](#)),

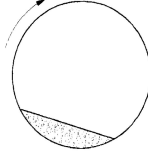
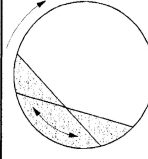
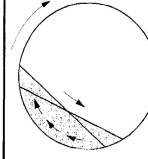
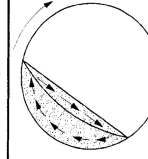
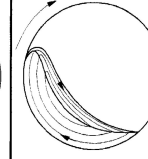
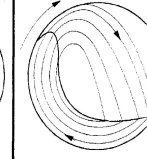
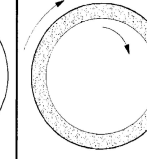
Subtype	Sliding	Surging	Slumping	Rolling	Cascading	Catacting	Centrifuging
Schematic							
Physical process	Slipping		Mixing			Crushing	Centrifuging
Froude number Fr [-]	$0 < Fr < 10^{-4}$		$10^{-5} < Fr < 10^{-3}$	$10^{-4} < Fr < 10^{-2}$	$10^{-3} < Fr < 10^{-1}$	$0.1 < Fr < 1$	$Fr \geq 1$
Filling degree f [-]	$f < 0.1$	$f > 0.1$	$f < 0.1$	$f > 0.1$		$f > 0.2$	
Wall friction coeff. μ_w [-]	$\mu_w < \mu_{w,c}$	$\mu_w \geq \mu_{w,c}$	$\mu_w > \mu_{w,c}$			$\mu_w > \mu_{w,c}$	
Application	no use		Rotary kilns and reactors; rotary dryers and coolers; mixing drums			Ball mills	no use

Figure 2.2: Different transverse motions of solids in a rotating drum ([Mellmann, 2001](#)).

$$Fr = \frac{\omega^2 R}{g}, \quad (2.5)$$

where ω , R and g stand for the rotational speed, the drum radius and the gravitational acceleration. Rolling regime, happens in $10^{-4} < Fr < 10^{-2}$, is common for mixing purpose. This regime is characterized by a flat surface layer, where the particles flow at a given dynamic repose angle with respect to the horizontal. This dynamic repose angle depends on granule properties such as size and surface roughness, as well as on the tumbler dimensions and rotational speed ([Meier et al., 2007](#)).

As shown in Fig. 2.3, the granular bed in the rolling mode can be divided into two distinct regions : 1) a thin lens-like flowing or active layer, and 2) a larger passive layer beneath the active layer. In the passive region, the particles flow as a solid body and rotate with the drum at fixed axial and radial positions. When particles reach the surface, they slide down within the active layer and eventually rejoin the passive layer.

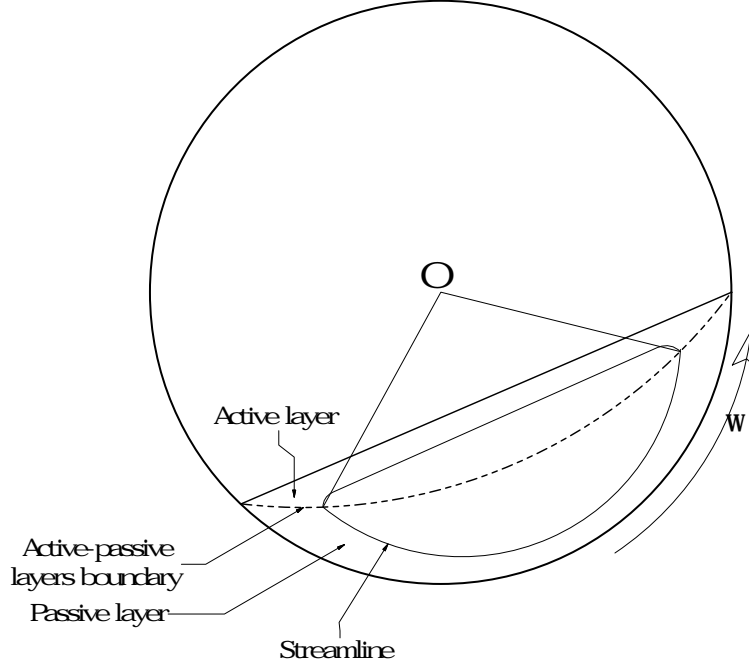


Figure 2.3: Rolling regime in a cylindrical drum.

2.2.2 Double cone, V-blender and bin blender

Apart from the tumbling drum, there are other types of blenders that have many applications in different industries; namely the V-blender (see Fig. 2.4b), also called the twin shell blender. It was first designed and patented by Fischer (1950) and has found many applications in many industries. After 1950, this apparatus was produced under the trade mark of Patterson-Kelley Co., (East Stroudsburg, Pa 18301). V-blenders consist of two hollow cylindrical shells, jointed at an angle in the range of $70^\circ - 90^\circ$. The mixing vessel is typically connected to a rotating shaft causing a tumbling motion. There are some trends in industries which rely on the bin-blender. The main advantage of the bin-blender over the V-blender is material contamination. Contrary to the industrial scale V-blenders that are permanently fixed to the blender shaft, bin-blenders can usually be moved, eliminating one discharge operation and thereby reducing powder exposure to the operator and cleaning time as well as segregation during discharge (Carson et al., 1996).

Extensive works (both numerically and experimentally) have been carried out in the

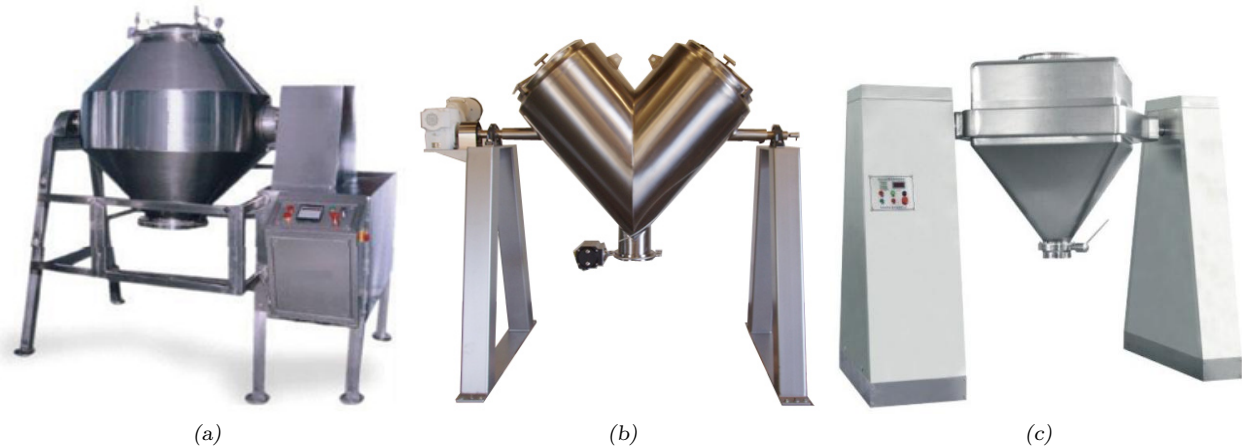


Figure 2.4: Industrial blenders (a) double cone, (b) V-blender and (c) tote bin blender. The bin-blender is usually built in two geometrical configurations, one with a square cross section (tote bin blender) and one with a cylindrical cross section (bohle bin blender).

literature to investigate mixing inside the different tumbling blenders. These works could be divided into specific and comparative studies. The specific studies only consider investigation of mixing inside one specific type of the blender, while comparative studies compare the performance of at least two types of blenders. A summary of the specific and comparative studies are provided in Tables 2.1 and 2.2, respectively. The main observations of these studies can be summarized as below :

- Generally, performance of tumbling blenders decrease with increasing fill level ;
- The effect of rotational speed on the performance of the blenders is not as significant as fill level ;
- Segregation patterns of granules in blenders depend on the fill level and rotational speed ;
- There are more difficulties in the mixing of cohesive materials than free flowing granules.

In these studies, different loading profiles have been considered. The main profiles are : Top-Bottom (TB), Front-Back (FB) and Right-Left (RL) (as seen in Fig. 2.5). The most common profile in the industry is TB. It has been shown that TB and FB profiles are more efficient than RL profiles ; this will be further discussed later.

Table 2.1: Summary of specific studies performed to investigate performance of tumbling blenders.

Blender type	Method of characterization	Fill level (%) Rotation [<i>RPM</i>]	Material	Reference	Objective of study
V-blender	Experimental (γ ray detection)	30,50,70 [%] 26,41 [<i>RPM</i>]	MgSt, MCC ^a PH101 and lactose	(Perrault et al., 2010)	To study the mixing of MgSt into a mixture of MCC and lactose
V-blender	Numerical (DEM ^b)	45 [%] 15,30 [<i>RPM</i>]	3mm granules (monodisperse) 3, 6mm granules (bidisperse)	(Lemieux et al., 2008)	Large scale DEM simulations in V-blender
V-blender	Experimental (qualitative visualization)	30-80 [%] 4-30 [<i>RPM</i>]	780 and 200 μ m bidisperse mixture of glass beads	(Alexander et al., 2003, 2004b)	Obtaining of segregation patterns inside different sized V-blender
V-blender	Experimental (visualization and bed solidification)	50 [%] 16 [<i>RPM</i>]	600 μ m red and blue glass beads	(Brone et al., 1997)	Using flow perturbations (rocking motion) to enhance mixing
V-blender	Experimental (bed solidification & image analysis)	40,50,60 [%] 8-24 [<i>RPM</i>]	66 μ m red and green glass beads	(Brone et al., 1998)	Determining the effect of rotation rate, fill level and total number of revolutions on the mixing performance
					<i>Continued on next page</i>

a. Microcrystalline Cellulose (Avicel)

b. Discrete Element Method

Table 2.1 : continued from previous page

Blender type	Method of characterization	Fill level (%) Rotation [<i>RPM</i>]	Material	Reference	Objective of study
V-blender	Experimental (sampling)	— [%] 30 [<i>RPM</i>]	1% sodium salicylate in 99% MCC PH102	(Chang et al., 1995)	To investigate the performance of modified V-blender (uneven leg or offset angle)
V-blender	Experimental (PEPT ^a)	20,28,34,46 [%] 15-60 [<i>RPM</i>]	3mm glass beads	(Kuo et al., 2005)	To study the dynamics of granules and axial dispersion
V-blender	Numerical (DEM) and experimental (PEPT)	20 [%] 15-60 [<i>RPM</i>]	3mm granules	(Kuo et al., 2005)	To study the influence of DEM parameters on the particles flow behavior ; validity of results have been checked through PEPT data.
Tote bin blender (rectangular)	Experimental (core sampling)	40,60,80 [%] 6,10,14 [<i>RPM</i>]	25w% 100μm acetaminophen in a mixture of MgSt, MCC PH102, mannitol, aspartame	(Alexander et al., 2004d)	To study the effect of rotation rate, fill level, baffle and loading profile on the performance of different sized blenders in the case of mixing of free flowing granules
		20,40,60,80 [%] 6,10,14 [<i>RPM</i>]	50/50w% 400μm black and white sand		

Continued on next page

a. Positron Emission Particle Tracking

Table 2.1 : continued from previous page

Blender type	Method of characterization	Fill level (%) Rotation [<i>RPM</i>]	Material	Reference	Objective of study
Tote bin blender (rectangular)	Experimental (groove sampling and NIR ^a)	50-70 [%] 8-14 [<i>RPM</i>]	Acetaminophen and lactose	(Portillo et al., 2008)	To design and scale-up of a batch mixing process
Bin blender	Experimental (sampling & NIR)	60,70,80 [%] 15,20,25 [<i>RPM</i>]	Acetaminophen in MCC PH102 and lactose	(Mehrotra and Muzzio, 2009)	Comparing of mixing performance in uniaxial and biaxial bin blenders
Bohle bin blender (cylindrical)	Numerical (DEM)	40,60,80 [%] 10 [<i>RPM</i>]	7mm (monodisperse) 5, 8mm (bidisperse)	(Arratia et al., 2006b)	Numerical simulations of mixing and segregation of free flowing granules
Bohle bin blender (cylindrical)	Experimental (core sampling)	20,40,60,80 [%] 6,10,14 [<i>RPM</i>]	3% of 30 μ m acetaminophen in 50/50w% MCC PH102 and lactose KCl (360 μ m) or NaCl (95 μ m or 360 μ m) mixed with the blend of MgSt and MCC PH102 1w% MgSt in a blend of 64/35w% MCC PH102 and lactose	(Alexander et al., 2004c)	To study the effect of rotation rate, fill level, baffle and loading profile on the performance of different sized blenders for cohesive granules

Continued on next page

^a. Near Infrared Spectroscopy

Table 2.1 : continued from previous page

Blender type	Method of characterization	Fill level (%) Rotation [<i>RPM</i>]	Material	Reference	Objective of study
Bohle bin blender (cylindrical)	Experimental (NIR)	40,60,85 [%] 6,10,14 [<i>RPM</i>]	1 <i>w</i> % MgSt in a 64/35 <i>w</i> % blend of MCC PH101 and lactose	(Arratia et al., 2006a)	To study the effects of fill level, rotational speed and presence of baffles on the mixing quality
Tote bin blender (rectangular)	Experimental (core sampling)	20,40,60 [%] 6,10,14 [<i>RPM</i>]	330 μm and 390 μm white and black sand (free flowing) MgSt (11 μm), NaCl (56 μm), MCC (53 μm) (cohesive)	(Sudah et al., 2002a)	To study the roles of rotational speed and discharge on the homogeneity of free flowing and cohesive granules using image analysis and solution conductivity, respectively
Tote bin blender (rectangular)	Experimental (core sampling and image analysis)	20,40,60,80 [%] 10 [<i>RPM</i>]	330 μm and 390 μm white and black sand	(Sudah et al., 2002b)	To determine the effects of fill level, mixing time and use of baffles on the mixing performance
Tote bin blender (rectangular)	Numerical (DEM) and experimental (core sampling)	40,60 [%] 10 [<i>RPM</i>]	12 <i>mm</i> (monodisperse) 6, 12 <i>mm</i> (bidisperse)	(Sudah et al., 2005)	Experimental and numerical investigation of mixing and segregation of granules

Table 2.2: Summary of comparative studies performed to investigate performance of tumbling blenders. In addition to these studies, more studies can be found in [Adams and Baker \(1956\)](#); [Carstensen and Patel \(1977\)](#); [Chowhan and Linn \(1979\)](#); [Gray \(1957\)](#); [Harnby \(1967\)](#).

Blender type	Method of characterization	Fill level (%) Rotation [<i>RPM</i>]	Material	Reference	Objective of study
V-blender, Bin blender	Numerical (DEM), and experimental (thief sampling)	35,50,65 [%] 15,30,45 [<i>RPM</i>]	2mm granules (numerical) 500μm MCC PH101 (experimental)	(Lemieux et al., 2007)	Comparison of performance of two type of blenders and effect of the different operating conditions
V-blender, Double cone	Numerical (DEM),	44 [%] 15,30 [<i>RPM</i>]	2, 3.2mm monodisperse 6, 12 and 2.5, 5mm bi- disperse	(Moakher et al., 2000)	Comparison of performance of two types of blenders in the case of mixing and segregation
	Experimental	50 [%] 16 [<i>RPM</i>]	1.6mm monodisperse 1.6, 4mm bidisperse		

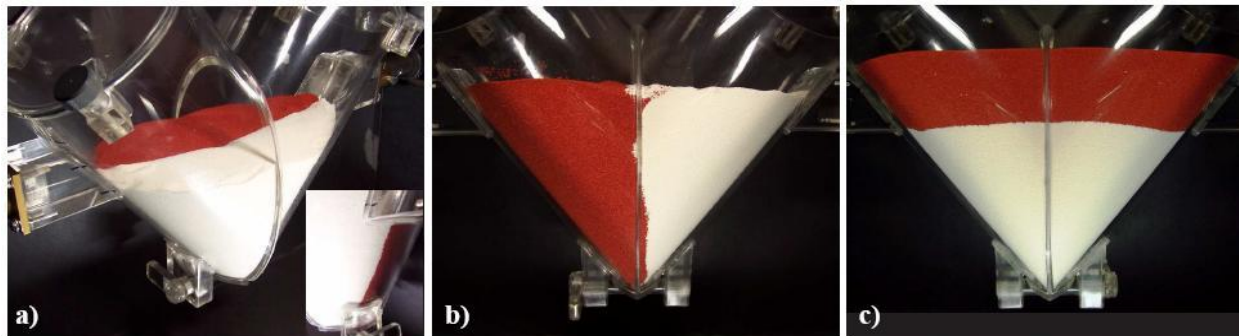


Figure 2.5: Different loading profiles for V-blender, (a) Front-Back (FB), (b) Right-Left (RL) and (c) Top-Bottom (TB) (Lemieux et al., 2007).

2.2.3 New configurations

In addition to the above mentioned common blenders, there have been some attempts to improve the performance of current blenders or propose new geometries. In this section, we focus on such attempts.

Modifications : Fischer (1954) modified the V-blender for cohesive material by installing an internal intensifier shaft in the axial direction thus moving the material in the radial direction and thereby impeding the flow of material from one arm to the other. To increase material axial flow, Fischer (1983) proposed a non-symmetrical intensifier. He also modified the stub shaft to inject hot gas into the blender thereby simultaneously agitating and drying the material (Fischer, 1957). Another improvement to the standard V-blender was disclosed by Fischer (1979), where one arm of the blender differed in length from the other. Such disparity reduced the mixing time over that normally experienced with standard V-blenders.

New geometries : Some of the patented innovative geometries are presented in Fig. 2.6. Peterson (1981) proposed a Y-shaped blender and Locke (1965) suggested a new configuration of two V-blenders connected together at their arms. This blender has a non-symmetric rotation axis. Russum (1959) proposed another combination of two V-shapes, connected at the bottom. In this geometry, two V-shapes are at the same plane and the blender can be as-

sumed as a “X-blender”. An alternate geometry was provided by [Anderson \(1964\)](#), consisting of a container with one axis of rotation going through its center of gravity, one arm extending from it in one direction and three other arms organized like a tripod extending in the opposite direction. In other words, it consists of a pair of V-blenders connected at the bottom with one twisted by 90° . The bottom V-shape resembles a conventional V-blender and the upper part is similar to a V-blender with the rotation axis perpendicular to the conventional one (also see Fig. 1.1).

Despite the seemingly effective shape of this blender for granule mixing, no study has yet been conducted to investigate its performance. Apart from the complexity of the geometry and the cleaning process after the operation of the blender, larger dimensions of this blender other than the conventional V-blender, necessitate additional space and energy to operate

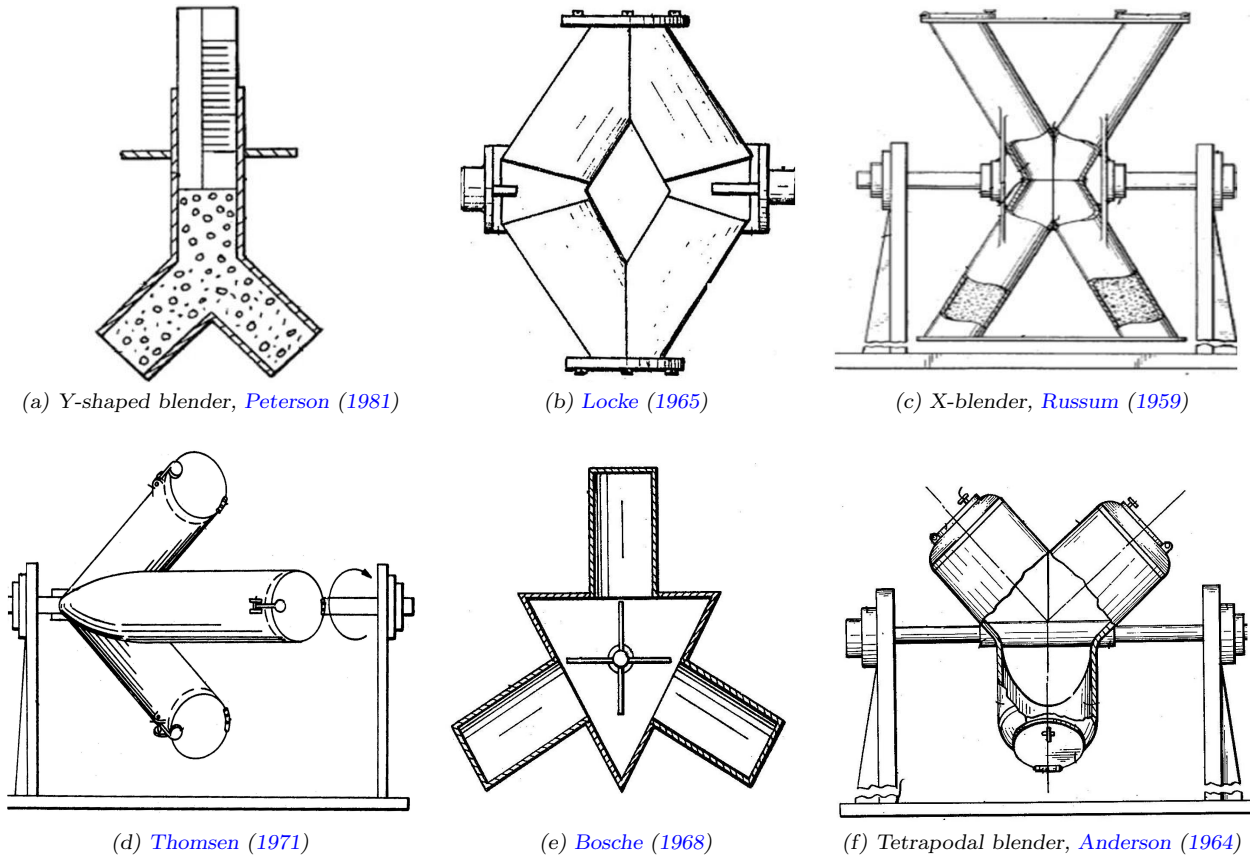


Figure 2.6: New geometries proposed for solid mixing.

the blender. In addition, the scaling-up of the device for industrial applications seems to be another limiting parameter to generalize the application of this blender. Regardless of such drawbacks, the limitations of conventional tumbling blenders provided the impetus to investigate mixing of solids inside this device. No application of this device despite having an effective geometry is somehow similar to the videocassette recorder (VCR) business, where a superior Sony Betamax system came second to the more prevalent video home system (VHS) system in the standard battle and this was not due to technological superiority ([Wonglimpiyarat, 2005](#)).

2.3 Mixing in tumbling blenders and its mechanisms

According to [Lacey \(1954\)](#), there are three main mechanisms for granule mixing in all types of tumbling blender :

- *Convective mixing* : In this mechanism, groups of particles are moved from one region of the blender to the other one. This mechanism occurs due to the rotation of the blender and gravity force on the particles. Convection is a fast phenomenon and distributes the groups of the particles across the whole blender volume ;
- *Diffusive mixing* : This mechanism rearranges the position of the particles in the scale of a few particles. It is slow when compared with the convective mixing ;
- *Shear mixing* : When a layer of particles is moving in contact with other layers, some particles are exchanged between layers.

Convective and diffusive mechanisms, respectively, are responsible for the distribution and dispersion of granules inside a blender. In order to have a homogenous mixture, both mechanisms are required and absence of each of them will affect the quality of the final product. Fig. 2.7 illustrates cases, where one or both mechanisms are working in a granular media. In tumbling blenders, the mixing mechanism in the axial direction is diffusion and a combination of convection and diffusion in the radial direction. Axial direction is along the rotation axis of the blender and radial direction is perpendicular to the rotation axis.

Given that diffusive mixing is an order of magnitude slower than convective mixing, tumbling blenders invariably suffer from weak mixing in the axial direction ([Arratia et al., 2006b](#); [Brone et al., 1997](#); [Lemieux et al., 2007](#); [Moakher et al., 2000](#)). This is mainly investigated via comparing the performance of RL with TB and FB loading profiles. The governing mechanism for the RL loading profile is diffusion, whereas for TB and FB profiles it is a combination of convection and diffusion.

2.4 Segregation in tumbling blenders and its mechanisms

One of the phenomena that makes the mixing of granules difficult is segregation (de-mixing). This may arise when particles have different physical or mechanical properties such as size, density, shape and roughness. Most segregating materials are free-flowing or slightly

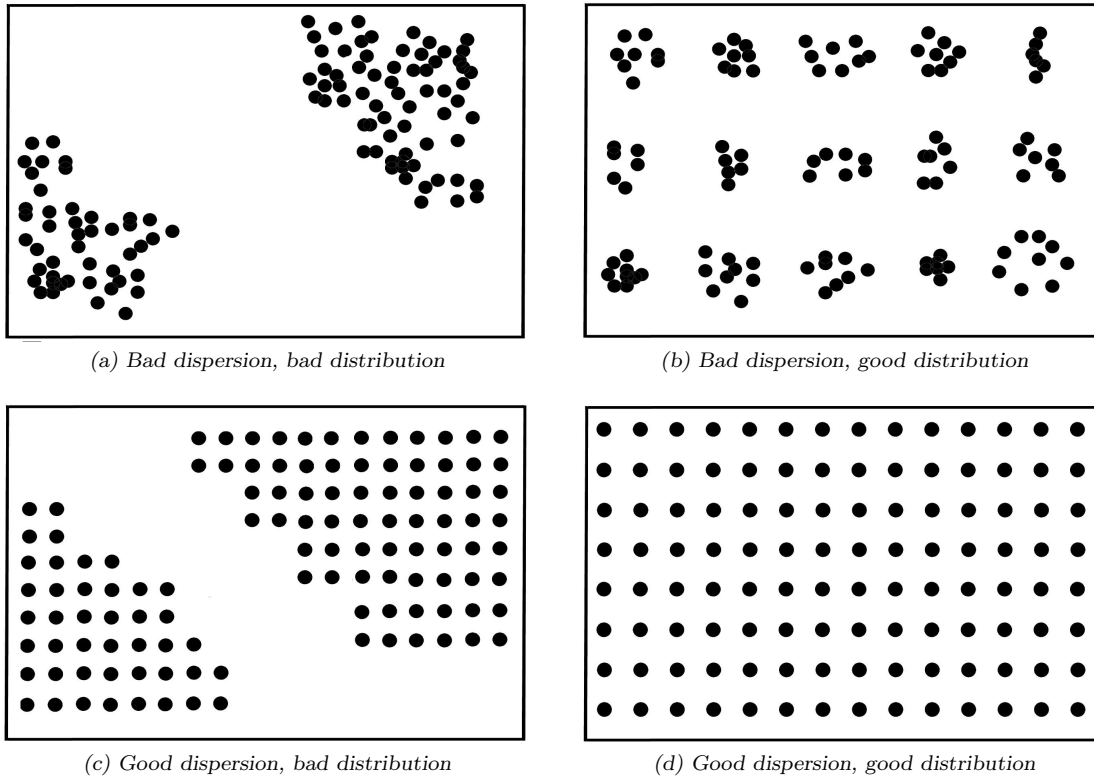


Figure 2.7: (a) Bad convective and diffusive mechanisms, (b) good convective and bad diffusive mechanisms, (c) bad convective and good diffusive mechanisms, (d) good convective and diffusive mechanisms.

cohesive whereby the particles can easily separate from each other. From a manufacturing point of view, it is vital to identify how segregation affects the performance of the processes and equipments that are designed to blend granular materials. Segregation is one of the problems that exist with tumbling blenders, but its mechanisms are not clearly understood and all given theories have exceptions. Segregation can appear in the following patterns :

- Axial segregation ;
- Radial segregation ;
- Competitive patterns.

Axial and radial segregation patterns can be clearly seen in simple geometries such as tumbling cylinder, while competitive patterns are mostly observed in the complex geometries such as V-blender. In the rest of this section, we will describe the main segregation mechanisms and then summarize the main findings regarding the segregation in the tumbling cylinder and V-blender.

2.4.1 Segregation Mechanisms

There are several mechanisms which govern segregation. They will be discussed below.

Trajectory :

As shown in Fig. 2.8a, if a particle of diameter d and density ρ_p , whose drag force is governed by Stokes' law, is forced to move horizontally with an initial velocity u into a fluid of viscosity μ and density ρ_f , the distance X that the particle can travel horizontally is (Rhodes, 2008) :

$$X = \frac{u\rho_p d^2}{18\mu}. \quad (2.6)$$

Therefore, a particle of diameter $2d$ would travel four times as far before coming to a stop. This mechanism can cause segregation where particles move through the air. This also occurs when powders fall from the end of a conveyor belt or an inclined surface.

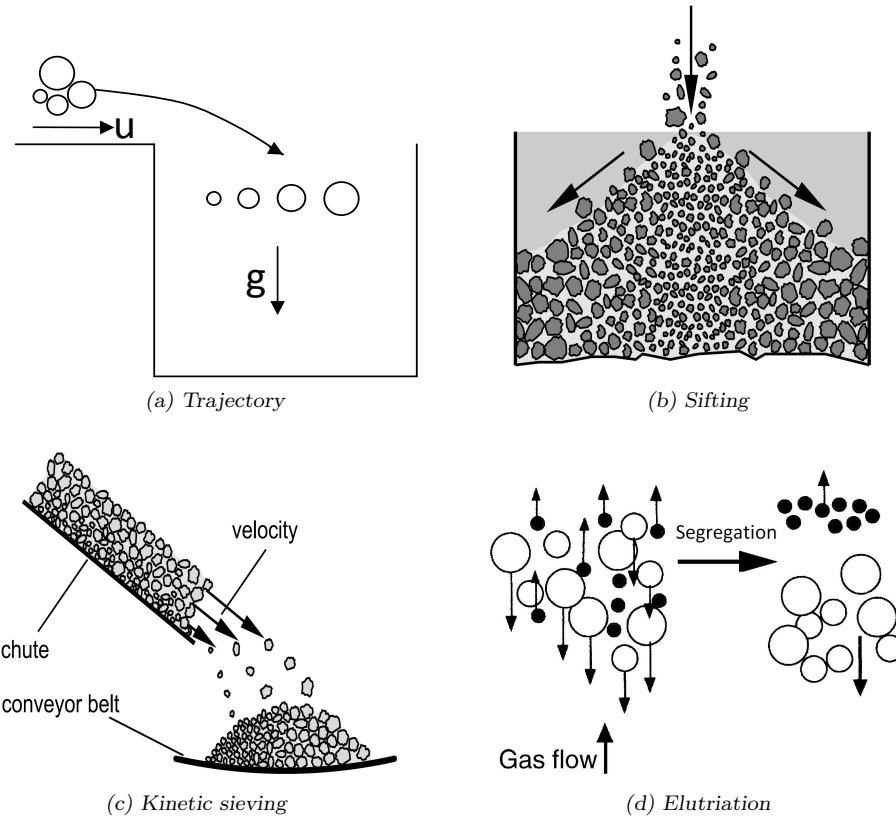


Figure 2.8: Mechanisms of segregation (a) trajectory, (b) sifting (Schulze, 2008), (c) kinetic sieving (Schulze, 2008) and (d) elutriation (Rhodes, 2008).

Sifting :

If a polydisperse mixture of particles slide downwards on the surface of bulk solids or any inclined surface of a granular bed, there is a higher probability for smaller particles to be caught by a sufficiently large cavities on the surface than larger particles. Thus, smaller particles stay in the cavities whereas the larger particles slide down to the base of the heap (Fig. 2.8b). The surface of the heap acts similarly to a sieve through which the smaller particles fall. Thus, this effect is called sifting.

Kinetic sieving :

Kinetic sieving is the dominant segregation mechanism in dense granular free-surface flows and separates big and small particles (Savage and Lun, 1988). If particles slide on the surface

of a bulk solid or any inclined surface of a granular bed, the local void ratio fluctuates, thereby a higher probability for smaller particles to be caught by sufficiently large cavities on the surface than larger particles. The small particles migrate towards the bottom of the flow and push the large particles upwards (Fig. 2.8c). The kinetic sieving process is utterly efficient that zones with nearly pure large and small particles may develop and separate by a sharp concentration jump.

Elutriation :

A gas flow against a mixture of different sized particles (Fig. 2.8d), could separate the particles. The upward gas velocity changes the free fall terminal velocity of the finer particles, which may then remain in suspension after the settling of larger particles.

Percolation :

If a granular bed is deformed, the particles move relative to each other. Thereby, small cavities are formed between individual granules whereby smaller particles may penetrate. Since the gravity force is the dominant external force in most processes, the small particles migrate preferentially downward within moving bulk solid layers. Segregation due to the percolation takes place in different situations, such as vibration (Fig. 2.9a) or avalanche (Fig. 2.9b). The latter is also called kinetic sieving.

Different repose angle :

If some particles form a larger angle of repose than other particles, segregation may arise in some parts of the heap. Particles with larger repose angles generally gather in the upper and steeper part of the heap, while particles with lower repose angles will remain further downward (see Fig. 2.10). Different repose angles may be a result of the following reasons :

- *Shape of the particles* : sharp edged particles form a steeper angle of repose than rounded particles (Fig. 2.10a) ;

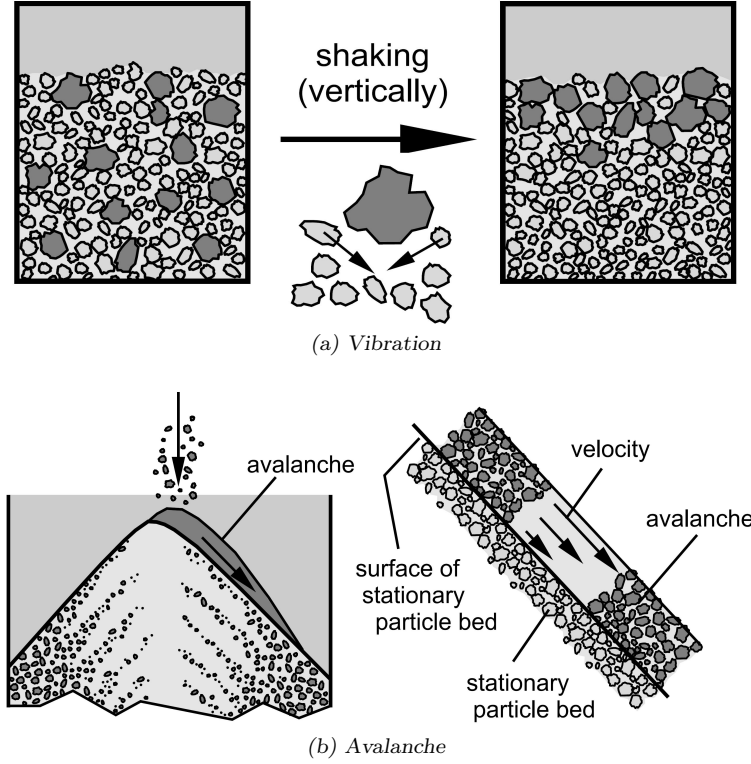


Figure 2.9: (a) Segregation due to percolation in containers shaken vertically, (b) segregation on a pile due to avalanching (Schulze, 2008).

- *Size of the particles* : fine bulk solids flow poorly due to the strong influence of adhesive forces and form high repose angle heaps (Fig. 2.10b).

2.4.2 Segregation in rotating drum

Segregation can happen in both radial (transverse) and axial directions of a tumbling drum. Since the radial mixing mechanism is mainly convective, radial segregation appears rapidly in the first few revolutions (Cantelaube and Bideau, 1995). Depending on the particle size distribution and the fraction of large particles, fine and dense particles generally migrate to the core region of the material bed near the rotation axis (Cantelaube and Bideau, 1995; Rapaport, 2007; Thomas, 2000; Wightman and Muzzio, 1998). Since the particle axial and radial positions do not change in the passive layer owing to the solid-like motion, segregation starts in the active layer near the free surface and only a very slow rearrangement of the

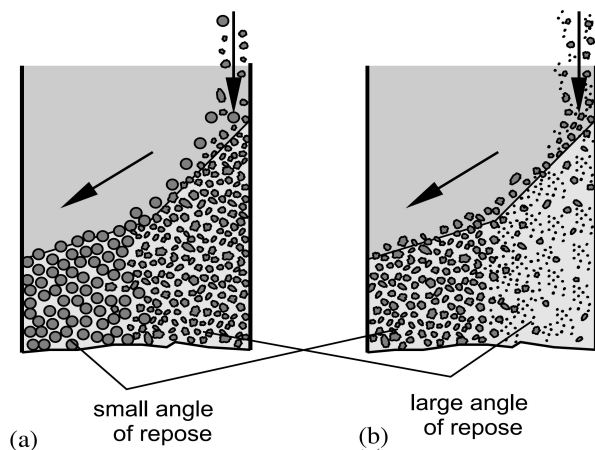


Figure 2.10: Segregation due to different repose angles resulting from (a) particle shape, and (b) particle size (Schulze, 2008).

particles occurs below this flowing layer (Aranson and Tsimring, 1999; Zik et al., 1994). Segregation in the transverse plane (that parallel to the drum ends) mainly results from the downward movement of small (or dense) particles within a thin surface layer, which displace larger (or lighter) particles upward (Meier et al., 2007). After a long enough period of the time, axial bands of coarse and fine particles are often formed. These bands are generally rich in one type of particles, but not necessarily pure. Axial banding segregation has been the topic of numerical and experimental works (Alexander et al., 2004a; Choo et al., 1998; Hill and Kakalios, 1995; Huang and Kuo, 2012; Rapaport, 2007; Taberlet et al., 2006; Zik et al., 1994). In particular, Hill and Kakalios (1995) showed that blends that appear mixed at low rotational speed, may form bands at higher speeds. The governing mechanism for such axial segregation is not clear. However, it has been shown that differences in the dynamic repose angle of the components of a blend may trigger the formation of these axial bands (Bridgwater et al., 1985; Hill and Kakalios, 1995). Recently, Chen et al. (2010) showed the effect of the end walls of the cylindrical drum on axial segregation. Since the governing mixing mechanism in the axial direction is dispersion, axial segregation occurs more slowly than radial segregation and may require hundreds or even thousands of revolutions. In the most of the studies that mentioned above, generally a binary mixtures of the granules were considered and the studies

that consider a poly-disperse blend is rare (Ingram et al., 2005).

2.4.3 Segregation in V-blender

Adams and Baker (1956) compared the efficiencies of different types of tumbling blenders (V-blender, double cone and rotocube) using a segregating mixture of polyethylene cubes. They observed segregation in the discharge stream of all blenders, and concluded that tumbling blenders are not adequate for mixing of granules with segregating tendencies. Harnby (1967) performed experiments with a mixture of millet and salt (size ratio of 4 :1) and observed that the mixture remained significantly unmixed after many revolutions of operation of a V-blender and a rotocube. The same results have been shown by Gray (1957) and Samyn and Murthy (1974), where the authors reported that V-blenders are not effective for mixing of materials that show segregating tendencies. Perhaps the most complete study was carried out by Alexander et al. (2003, 2004b). They used a 50/50 binary mixture (by volume) of spherical glass beads with two sizes : nominally 780 and $200\mu m$ in diameter. In their experiments, rigorous segregation patterns were observed for different sized V-blenders depending on the blender fill level and rotational speed (see Fig. 2.11). First behavior is “small-out”, where a core of the larger particles arises with smaller particles at the periphery next to the outer shell. Second segregation pattern, where a stripe of smaller particles develops in each arm, is named “stripes”. The rigorous segregation happened at “left-right” profile, where a structure was formed with the larger particles to the one side of the vertical central plane and the smaller particles to the other one. This pattern occurs at higher rotational speeds and may take hundreds of revolutions to develop. In the left-right pattern, small particles appearing on either the left or the right arm of the blender with nearly equal frequency. In this pattern, one shell may contain $\sim 80\%$ of the small particles while the other holds $\sim 80\%$ of the large particles.

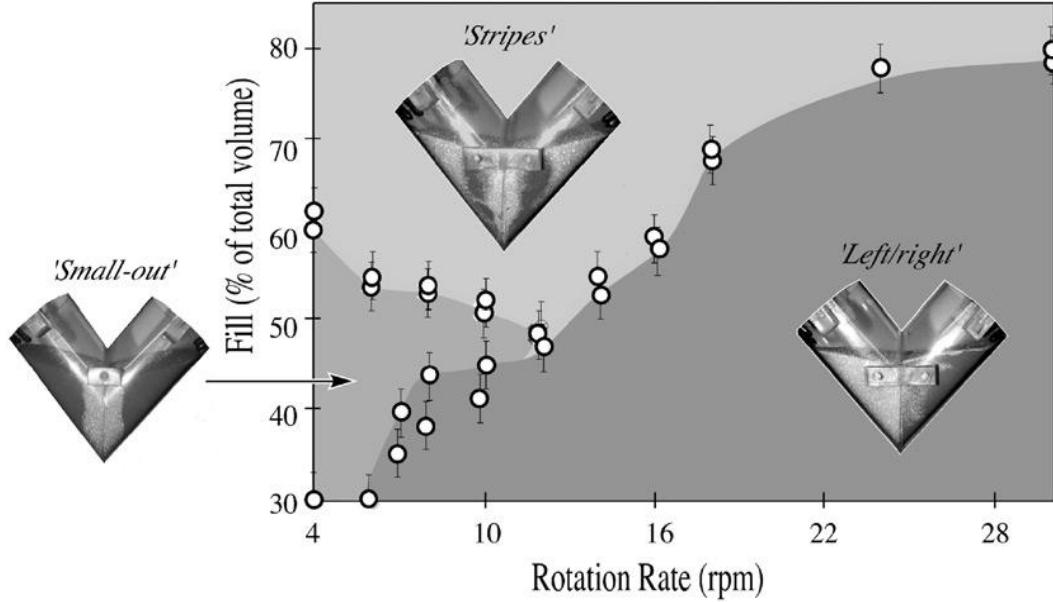


Figure 2.11: Segregation patterns in V-blender ([Alexander et al., 2003](#)).

2.5 Solid mixing characterization

The difficulties involved in reliably characterizing the granular mixtures are the main reason for the lack of accurate experimental data on the performance of powder mixers. In this section, some of these methods will be described, which were employed in the current work to characterize the granular flow and mixing quality.

2.5.1 Thief sampling

The opaque nature of the particulate materials makes it difficult to readily measure the quality of a mixture. Generally, some discrete samples are extracted from the granular bed and analyzed. There are two “golden rules” for powder sampling ([Allen, 1981](#)) :

- A powder should be sampled only when in motion ;
- A sample should be collected uniformly from the entire process stream.

The most common technique for granule sampling is thief sampling, where the use of thief probes violates both of these rules. Parameters such as sample size, number of samples and location of sampling points may affect measurement accuracy. Recently, perturbations of thief

sampling and its accuracy have been investigated ([Muzzio et al., 1997, 2003](#)).

Thief samplers mainly belong to one of two main groups : end-samplers and side-samplers. End-samplers consist of a hollow tube with an internal plugger that could be positioned in different locations to control sample size. The plugger prevents the flow of particles into the sampler during insertion. When the sampler reaches a desired location, it can be opened thus allowing granules to flow inside the sampler (Fig. 2.12a). A typical side-sampler has one or more cavities stamped in a hollow cylinder enclosed by an outer rotating sleeve. The sleeve has holes that align with the cavities, allowing adjacent powder to flow into the cavities (Fig. 2.12b).

2.5.2 Radioactive particle tracking

Thief sampling interferes with the matter and may affect the measurement itself ([Muzzio et al., 1997, 2003](#)). In addition, analyzing samples containing many species is tedious and takes a long time. To overcome these limitations, non-invasive methods such as laser doppler anemometry (LDA) and particle image velocimetry (PIV) are appealing at first sight, but the opaque nature of granular media renders such methods useless. Another possibility is to resort to characterization methods based on radioactive measurements. Two such methods have been applied in the field of solid mixing. The first one relies on positron annihilation and is called positron emission particle tracking (PEPT) ([Hawkesworth et al., 1991](#); [Parker et al.,](#)

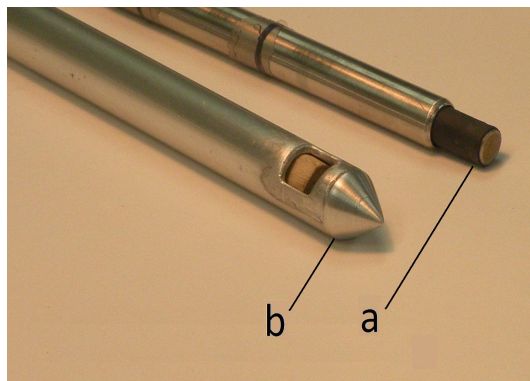


Figure 2.12: (a) Core sampler and (b) side-sampler.

1993), mainly applied in the University of Birmingham. The second method, which is applied in this work, uses gamma rays emitted from a single radioactive tracer (Larachi et al., 1994) containing activated element such as ^{46}Sc , ^{198}Au , ^{24}Na . This technique is known as radioactive particle tracking (RPT) and, in comparison with PEPT, is inexpensive, compact and can be used for large mixing vessels. This method is mainly used by the groups of prof. Chaouki (Doucet et al., 2008b; Larachi et al., 1995; Mostoufi and Chaouki, 2001) and prof. Dudukovic (Degaleesan et al., 2002). Our group has extended RPT so that it can be used in blenders (Doucet et al., 2008b).

RPT algorithm

RPT tracks the position of a single radioactive tracer with respect to time using an array of scintillation detectors located around the vessel to capture gamma rays emitted by this tracer. The set of recorded gamma ray counts depends on the position of the tracer. The position of this tracer is in fact reconstructed by minimizing the discrepancy between the recorded and calculated counts using a model proposed by Beam et al. (1978). This method uses Monte Carlo simulation to generate a dictionary that contains the number of gamma rays expected to be intercepted by the detectors when the tracer is in a given position. A typical setup for RPT experiments is shown in Fig. 2.13. Detection system consists of more than three NaI-Tl scintillation detectors.

RPT with ^{24}Na

One important step of the RPT method is the preparation of the tracer. In particular, this tracer should match the inert particles in size, density and shape. One way to achieve this consists of radioactivating particles that are identical to those in the granular bed. For instance, the glass beads contain 13-14% soda lime, which includes ^{23}Na that can be converted to ^{24}Na isotope using the nuclear reactor. In practice, only one particle in the vessel is radioactive, the tracer, and the others are inert. ^{24}Na emits gamma rays with two levels of

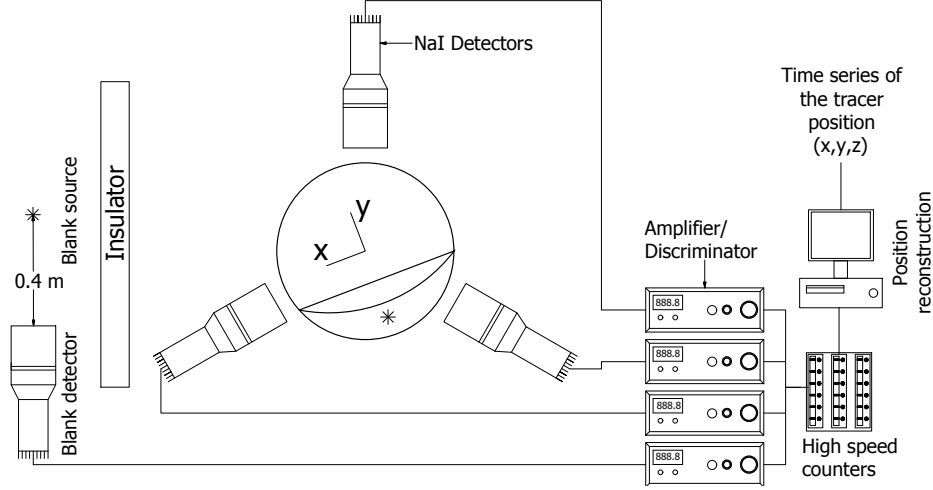


Figure 2.13: Typical setup of RPT.

energy (1.368 and 2.754 MeV). The problem of ^{24}Na is its short half-life (~ 15 hr). Depending on the duration of an experiment, the dictionaries that are valid at the beginning of such an experiment may then become inaccurate due to the decay of the ^{24}Na isotope, which may lead to large errors in the reconstruction of the tracer trajectory. To overcome this problem, recorded events must be corrected. To do so, a second tracer, which is similar to the first one, is used as a sentinel outside the vessel to monitor with the help of a dedicated NaI-Tl detector the loss of activity with time and then correct the number of events captured by the detectors around the vessel. Note that this so-called blank source is shielded in such a way that it does not affect the measurements made by these detectors. Recorded events can be corrected using the decay curve of ^{24}Na by means of Eq. 2.7.

$$C_{t,cor}^i = C_{t,rec}^i \times \frac{c_o^{blank}}{c_t^{blank}}, \quad (2.7)$$

where $C_{t,cor}^i$: corrected count for detector i ($i = 1, \dots, N$) at time t ,

$C_{t,rec}^i$: recorded count for detector i at time t ,

c_o^{blank} : recorded count from blank source at $t = 0$,

c_t^{blank} : recorded count from blank source at time t .

RPT limitations

Although RPT is a very strong tool to characterize flow inside opaque systems, it suffers from some limitations when applied to granular beds :

- Depending on isotope, there is a lower limit for tracer size (say $500\mu m$) ;
- The tracer should match in density, size and shape with inert particles ;
- Inert particles have a particle size distribution, but the tracer has only one unique size.

Due to segregation, the tracer can only follow the trajectories of particles that have the same size as the tracer, not all of them.

2.5.3 Discrete element method

Apart from efforts to develop non-intrusive techniques, numerical methods have progressed, and both continuum models and particle dynamics simulations have been developed. The first approach is Eulerian, which considers powders as a fluid ([Khakhar et al., 2001](#)), and the second approach is Lagrangian, which treats particles in the discrete domain including Monte Carlo method, cellular automata and discrete element method (DEM) ([Zhu et al., 2007](#)). In the latter approach, DEM, originally proposed by [Cundall and Strack \(1979\)](#), has been applied to investigate granular flow in many applications ([Dury and Ristow, 1997](#); [Lemieux et al., 2008](#); [Rapaport, 2007](#); [Taberlet et al., 2004](#); [Yamane et al., 1998](#)). This simulation technique is a soft particle method and has proven efficient in providing insight into phenomena occurring in granular beds as well as details about the flow and mixing of granules.

Validation of DEM-based model

Unresolved questions about granular flow and the ability of DEM to predict these types of flow have generated considerable interest, resulting in extensive research works on the subject in recent years. However, few comparisons with experimental data have been performed to examine the validity of the DEM ([Lemieux et al., 2007](#); [Sudah et al., 2005](#); [Taberlet et al.,](#)

2006; Yamane et al., 1998). Such studies in the literature are mostly qualitative via visual comparison of flow patterns. For instance, Moakher et al. (2000) considered double-cone and V-blenders, and Iwasaki et al. (2001) studied a high-speed elliptical rotor-type powder mixer, both groups demonstrating that calculated flow patterns agreed with experimental observations. While there is a limited number of techniques capable of providing Lagrangian data and mapping the velocity field inside opaque granular systems, studies that quantitatively validate the DEM at the particle scale are limited. Such studies can be found in Laurent and Cleary (2012), Kuo et al. (2002) and Stewart et al. (2001). Despite the importance of previous investigations, comparisons of Lagrangian experimental and DEM-based model continue to be inadequately thorough. Indeed, in many studies, real values of particle properties have not been used for the DEM simulations and neither have they been experimentally measured. While these parameters demonstrate a high effect on the granular flow, authors have often adjusted them in order to obtain results that agree well with experimental observations.

DEM algorithm

DEM simulation gives the position of each particle in a granular system by applying Newton's equation of motion for all particles in a granular bed (Bertrand et al., 2005; Lemieux et al., 2007, 2008) :

$$m_i \frac{d^2 x_i}{dt^2} = F_i^{total}, \quad (2.8)$$

$$I_i \frac{d\omega_i}{dt} = T_i^{total}, \quad (2.9)$$

where m_i and I_i represent, respectively, the mass and the moment of inertia of particle i , $v_i = (v_{i,x}, v_{i,y}, v_{i,z})$ and $\omega_i = (\omega_{i,x}, \omega_{i,y}, \omega_{i,z})$ its linear and angular velocities, F_i^{total} and T_i^{total} the total force and torque acting on this particle. In this study, total force includes gravity as well as particle interactions with wall and other particles through contact forces. Drag and buoyant forces can be neglected due to low density of fluid phase (generally air). Due

to particle size in DEM simulations (at the order of millimeters), colloidal force can also be neglected. Thus :

$$F_i^{total} = F_{gravity,i} + F_{contact,ij}. \quad (2.10)$$

A model is required to estimate contact force term $F_{contact,ij}$. Generally, contact forces are decomposed into normal (head-on) and tangential (shear) components :

$$F_{contact,ij} = F^n + F^t. \quad (2.11)$$

Normal contact force models

Normal force schemes can be divided into several groups depending on the way the impact of the normal force on the particle overlap and the relative particle velocities is modeled. Four main groups are defined : the *continuous potential models* (Aoki and Akiyama, 1995; Langston et al., 1994), the *linear viscoelastic models* (Walton, 1983), the *non-linear viscoelastic models* (Brilliantov et al., 1996; Kuwabara and Kono, 1987; Lee and Herrmann, 1993; Tsuji et al., 1992) and the *hysteretic models* (Sadd et al., 1993; Thornton, 1997; Thornton and Ning, 1998; Walton and Braun, 1986). Further details on force models can be found in Kruggel-Emden et al. (2007). Given their widespread application in DEM simulations, we focus here on the linear and non-linear viscoelastic models that are found in the literature. In these models, the contact force between two colliding particles includes two parts, one for the elastic repulsion modeled by a spring and the other for the viscous dissipation via a dashpot (Ji and Shen, 2006) :

$$F^n = F_{el}^n + F_{diss}^n = -K_n \delta_n^\alpha - C_n \delta_n^\beta v_{ij,n}^\gamma, \quad (2.12)$$

where K_n is the stiffness of a Hookean spring and C_n is the damping coefficient. When $\alpha = 1$, $\beta = 0$ and $\gamma = 1$, the model is referred to as the linear spring dashpot (LSD) model. In a

linear contact force model, the damping coefficient is given by :

$$C_n = 2\xi_n \sqrt{m_{eff} K_n}, \quad (2.13)$$

where m_{eff} is the mean mass of particles i and j ($\frac{1}{m_{eff}} = \frac{1}{m_i} + \frac{1}{m_j}$) and ξ_n depends on the coefficient of restitution (CoR)² (Thornton et al., 2013) :

$$\ln(CoR) = -\sqrt{\frac{K_n}{m_{eff}}} \xi_n t_c, \quad (2.14)$$

where t_c is contact duration. For LSD following equation has been mostly used (Ji and Shen, 2006; Mishra and Murty, 2001) :

$$\xi_n = \frac{-\ln(CoR)}{\sqrt{\pi^2 + \ln^2(CoR)}}. \quad (2.15)$$

This equation is inappropriate for DEM simulations since it assumes that the contact ends when displacement first returns to zero at which point the normal force is attractive (Schwager and Poschel, 2007; Thornton et al., 2013). The situations, where contact force switches into attractive will be discussed later. The use of a linear contact model in Newton's second law of motion leads to a differential equation that has an analytical solution with constant CoR and collision time (independent of the initial impact velocity) (Schäfer et al., 1996), whereas experimental and theoretical studies have shown that the CoR and the contact duration depend sensitively on the impact velocity (Bridges et al., 1984; Gorham and Kharaz, 2000; Hrenya and Stevens, 2005; Kuwabara and Kono, 1987; Ramirez et al., 1999). In the case of LSD, the damping force is independent of the overlap and depends linearly on the particle relative velocities. In such a model, the initial force is not zero despite the absence of the particle overlap δ_n , which is non-physical (Zhang and Whiten, 1996). To overcome this limitation of LSD, particle overlap δ_n can be added to the dissipative term that is the case for most of the non-linear viscoelastic models that have been developed based on the

2. CoR is defined as the ratio of the relative velocities after and before collision.

Hertz theory. Hertzian contacts are pure elastic ($C_n = 0$ in Eq. 2.12) and the spring stiffness (K_n) with this model ($\alpha = 3/2$) is a function of the particle geometry and its mechanical properties :

$$K_n = \frac{4}{3} E^* \sqrt{R^*}, \quad (2.16)$$

where R^* is the reduced radius ($\frac{1}{R^*} = \frac{1}{R_i} + \frac{1}{R_j}$) and E^* is the effective Young's modulus ($\frac{1}{E^*} = \frac{1-\nu_i^2}{E_i} + \frac{1-\nu_j^2}{E_j}$). ν_i and ν_j are the Poisson's ratios and E_i and E_j the Young's modulus of particles i and j , respectively. The drawback of such model is that it cannot resolve adequately inelastic collisions because of the absence of a damping term. [Lee and Herrmann \(1993\)](#) (LH) proposed a non-linear viscoelastic model ($\alpha = 3/2$, $\beta = 0$ and $\gamma = 1$) in which the elastic term is based on Hertz theory and the damping term depends linearly on the particle velocities. However, due to the absence of the overlap δ_n in the dissipative term, this model yields a non zero force at the beginning of the contact between two particles. [Kuwabara and Kono \(1987\)](#) (KK) proposed a non-linear viscoelastic model with $\alpha = 3/2$, $\beta = 1/2$, and $\gamma = 1$. This model was also independently derived by [Brilliantov et al. \(1996\)](#). In the KK model, C_n is an adjustable parameter. Results have shown that it leads to a decrease of the CoR and collision time when there is an increase in the impact velocity. Another non-linear model was derived heuristically by [Tsuji et al. \(1992\)](#) (TS) ($\alpha = 3/2$, $\beta = 1/4$, and $\gamma = 1$). This model gives a constant CoR and a velocity-dependent collision time. It appears that all these non-linear models for normal contact forces only differ in the exponent β in the dissipative term. Moreover, this exponent has a strong effect on the behavior of the model. [Ramirez et al. \(1999\)](#) proved that the dependency of the terminal velocity on the initial velocity vanishes if

$$2(\beta - \alpha) + \gamma(1 + \alpha) = 0. \quad (2.17)$$

This is the case for the LSD and the TS models. In practice, it appears that this dependency of the terminal velocity on the initial velocity has often been overlooked or ignored.

Another drawback of the non-linear viscoelastic models is encountered when there is an inelastic impact between two particles. Fig. 2.14 shows the variation of the normal contact force versus the contact duration both numerically (2.14a and 2.14b) and experimentally (2.14c). The numerical data are typical results that have been obtained for stainless steel spheres using a MATLAB implementation of the KK and TS models. One may notice that the repulsive contact force decreases from zero to a minimum, then increases back to zero. For nearly elastic collisions (CoR=1), the contact force profile is symmetric, whereas for inelastic collisions (CoR< 1) it is not. In this latter case, the numerical models fail to predict accurately the contact force at the end of the collision. This can be seen in Figs. 2.14a and 2.14b where the force switches from repulsive to attractive, whereby pulling the particles back towards each other instead of forcing them to split. Indeed, this attractive force at the end of the collision is unrealistic as shown in Fig. 2.14c (Zhang and Whiten, 1996) and discussed in the literature (Ji and Shen, 2006; Stevens and Hrenya, 2005). To overcome this limitation, some researchers have suggested that particles should be forced to separate when the force goes to zero, even though this corresponds to a non-zero overlap (Ji and Shen, 2006).

Tangential contact force models

The most pioneering work on the tangential force models was carried out by Mindlin (1949) and Mindlin and Deresiewicz (1954) (MD model). According to the MD model, the tangential force is obtained (Di Renzo and Di Maio, 2005) :

$$F_{el}^t = \mu F_{el}^n \left[1 - \left(1 - \frac{K}{\mu} \frac{\delta_t}{\delta_n} \right)^{3/2} \right], \quad (2.18)$$

where K is the ratio of tangential to normal stiffness :

$$K = \frac{K_t}{K_n}. \quad (2.19)$$

For identical particles :

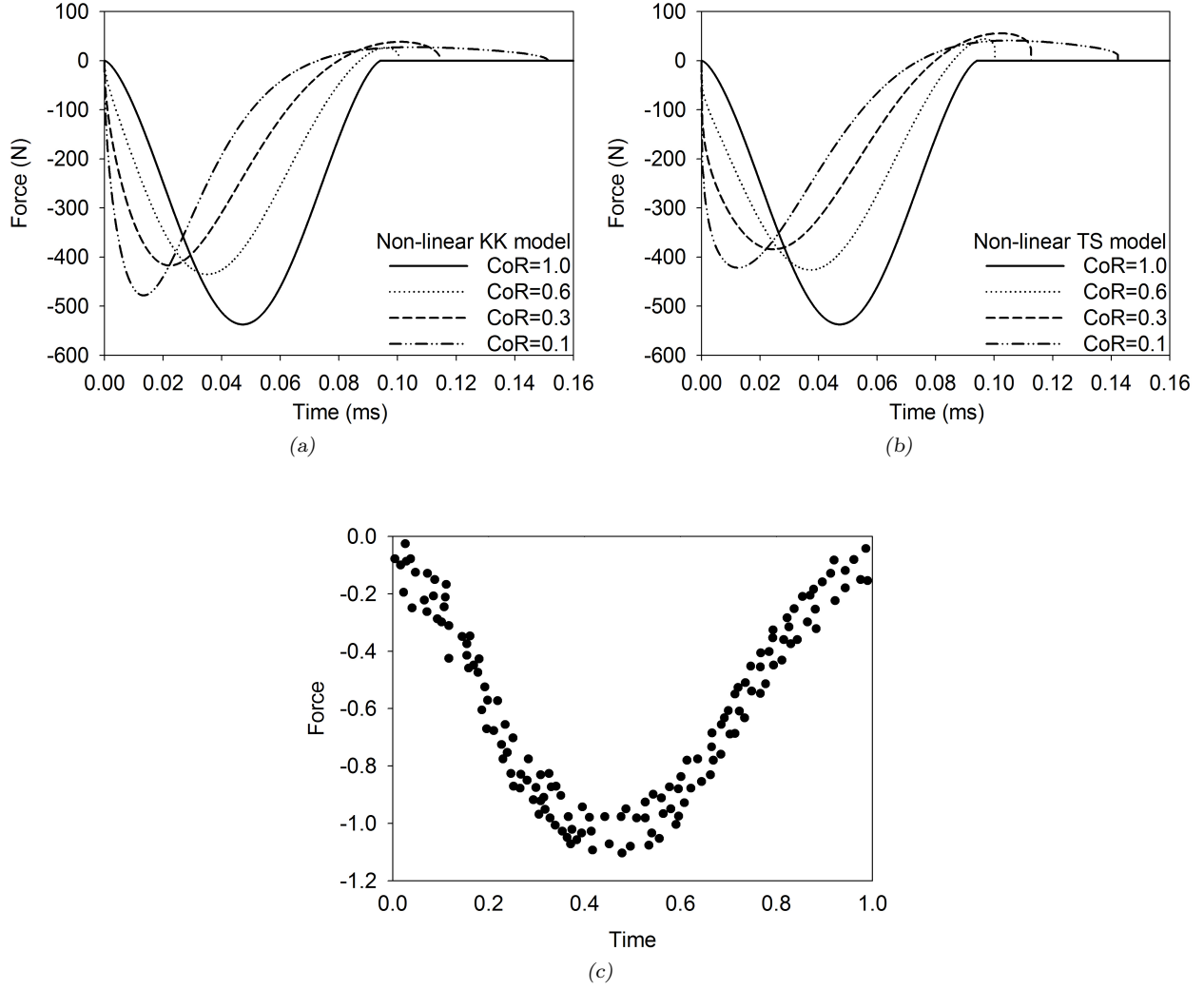


Figure 2.14: Nonlinear contact force model predictions for normal impact with different coefficients of restitution : (a) Kuwabara and Kono (KK) model, (b) Tsuji (TS) model and (c) normalized experimental results (Zhang and Whiten, 1996).

$$K = \frac{2(1 - v)}{(2 - v)}. \quad (2.20)$$

Tangential contact force is bounded up by Coulomb's friction force. Therefore, they can be coupled :

$$F_{el}^t = -\mu |F_{el}^n| \left[1 - \left(1 - \frac{\min(\delta_t, \delta_{t,max})}{\delta_{t,max}} \right)^{3/2} \right], \quad (2.21)$$

where $\delta_{t,max}$ is first obtained by [Langston et al. \(1994\)](#) and corresponds to the maximum tangential deformation :

$$\delta_{t,max} = \mu \frac{(2 - \nu)}{2(1 - \nu)} \delta_n. \quad (2.22)$$

Tangential damping coefficient is the arbitrary fraction of the critical damping value $C_t = 2[2m_{eff}K_t(\delta_t)]^{1/2}$ ([Baxter et al., 1997](#)). $K_t(\delta_t)$ is the derivative of the F_{el}^t with respect to the tangential overlap δ_t . Therefore, the tangential damping force is given by ([Zhou et al., 1999, 2002](#)) :

$$F_{diss}^t = c_t \left(6\mu m_{eff} |F_{el}^n| \frac{\sqrt{1 - \frac{|\delta_t|}{\delta_{t,max}}}}{\delta_{t,max}} \right)^{1/2} v_{ij,t}. \quad (2.23)$$

Time step in DEM simulations

Choosing a proper time step for a DEM simulation is generally a trade-off between the CPU time, the numerical error and the stability of the integration scheme. The time step should be smaller than the characteristic time, τ_c , which corresponds to a typical contact time between two colliding particles ([Li et al., 2005](#)) :

$$\tau_c = \frac{\pi \bar{R}}{\varepsilon} \sqrt{\frac{\rho}{G}}, \quad (2.24)$$

where ρ is the particle density, \bar{R} the average particle radius, $G = \frac{E}{2(1+\nu)}$ the particle shear modulus and ε can be approximated from :

$$\varepsilon = 0.8766 + 0.163 \nu. \quad (2.25)$$

In systems with smaller characteristic times (small particles, hard material or high velocities) a DEM simulation can maintain its stability if a small enough time step is used. (typically less than $10\mu s$) ([Lemieux et al., 2008](#)).

Limitations of DEM

The DEM-based model may be applied for a variety of geometries and different granular situations, where it provides detailed information. However, DEM suffers from some limitations :

- The maximum number of particles is limited by the power of computational facilities ;
- Simulations are CPU intensive ;
- Most simulations are limited to spherical particles and some known shapes ;
- “Why good results can be obtained by DEM-based model even if non-real values of particle properties are used ?” is still challenging.

2.6 Problem identification and specific objectives

According to the literature, tumbling blenders suffer from some limitations ; the main issues are summarized as below :

- Significant segregation occurs when granules with different properties play a role ;
- Obtaining a homogenous mixture may be difficult due to the weak axial mixing mechanism.

The main objective of this study is to investigate the mixing and segregation of free flowing granules inside tumbling blenders. The conventional blenders considered in this work are the V-blender and the rotating drum. To alleviate the limitations of conventional tumbling blenders, we undertook an interest in the so-called tetrapodal mixing device. Before investing in manufacturing a lab-scale version of the tetrapodal blender to investigate its performance experimentally, it is of interest to characterize the efficiency of the blender via numerical tools to verify its superiority against conventional tumbling blenders and obtain design parameters. For this purpose, the DEM-based model was chosen, notwithstanding some challenging issues regarding this method :

- How to measure granules properties to feed DEM code ?
- Why good results are obtained even if non-physical values of input parameters are

applied ?

- There is limited validation of DEM with Lagrangian experimental data ;
- Contact force models are not accurate.

Therefore, in the first step of this study, it is of interest to validate the DEM-based model. To do so, different phenomena inside a rotating drum are predicted by DEM and validated through experimental Lagrangian data obtained by RPT. Generally, in the literature, binary mixtures are used inside a rotating drum, while a polydisperse mixture is chosen in this study. Considering these steps, the specific objectives of this work are as follows :

1. To validate the DEM-based model and conduct a sensitivity analysis with respect to simulation parameters ;
2. To introduce the tetrapodal blender and compare its performance to that of the V-blender ;
3. To validate the numerical simulation results of solid mixing and segregation in the tetrapodal blender and the V-blender, and investigate the effect of operating parameters on their efficiencies.

2.7 References

- Adams, J. and Baker, A. (1956). Assessment of dry blending equipment. *Institution of Chemical Engineers Transactions*, 34(1) :91–99.
- Alexander, A., Muzzio, F., and Shinbrot, T. (2003). Segregation patterns in V-blenders. *Chemical Engineering Science*, 58(2) :487–496.
- Alexander, A., Muzzio, F. J., and Shinbrot, T. (2004a). Effects of scale and inertia on granular banding segregation. *Granular Matter*, 5(4) :171–175.
- Alexander, A., Shinbrot, T., Johnson, B., and Muzzio, F. J. (2004b). V-blender segregation patterns for free-flowing materials : Effects of blender capacity and fill level. *International Journal of Pharmaceutics*, 269(1) :19–28.

- Alexander, A., Sudah, O., Arratia, P., Duong, N.-H., and Muzzio, S. R. F. (2004c). Characterization of the performance of bin blenders, part 3 of 3 :cohesive powders. *Pharmaceutical Technology*, 28(9) :54–74.
- Alexander, A., Sudah, O., Arratia, P., Goodridge, C., Alani, L., and Muzzio, F. (2004d). Characterization of the performance of bin blenders, part 2 of 3 : Free-flowing mixtures. *Pharmaceutical Technology*, 28(7) :56–67.
- Allen, T. (1981). *Particle size measurment, 3rd Edition*. Chapman and Hall, London, UK.
- Anderson, M. (1964). Tetrapodal mixing device. US Patent :US 3,134,578.
- Aoki, K. and Akiyama, T. (1995). Simulation studies of pressure and density wave propagations in vertically vibrated beds of granules. *Physical Review E*, 52(3) :3288–3291.
- Aranson, I. and Tsimring, L. (1999). Dynamics of axial separation in long rotating drums. *Physical Review Letters*, 82(23) :4643–4646.
- Arratia, P., Duong, N., Muzzio, F., Godbole, P., Lange, A., and Reynolds, S. (2006a). Characterizing mixing and lubrication in the bohle bin blender. *Powder Technology*, 161(3) :202–208.
- Arratia, P., Duong, N.-h., Muzzio, F., Godbole, P., and Reynolds, S. (2006b). A study of the mixing and segregation mechanisms in the bohle tote blender via DEM simulations. *Powder Technology*, 164(1) :50–57.
- Baxter, J., Tuzun, U., Burnell, J., and Heyes, D. (1997). Granular dynamics simulations of two-dimensional heap formation. *Physical Review E*, 55(3) :3546–3554.
- Beam, G. B., Wielopolski, L., Gardner, R. P., and Verghese, K. (1978). Monte Carlo calculation of efficiencies of right-circular cylindrical nai detectors for arbitrarily located point sources. *Nuclear Instruments and Methods*, 154,(3) :501–508.
- Bertrand, F., Leclaire, L., and Levecque, G. (2005). DEM-based models for the mixing of granular materials. *Chemical Engineering Science*, 60(8-9) :2517–2531.
- Bosche, G. (1968). Mixer for particulate material. US Patent :US 3,387,828.

- Bouffard, J., Bertrand, F., Chaouki, J., and Dumont, H. (2013). Discrete element investigation of flow patterns and segregation in a spheronizer. *Computers and Chemical Engineering*, 49 :170–182.
- Bridges, F., Hatzes, A., and Lin, D. (1984). Structure, stability and evolution of saturn's rings. *Nature*, 309(5966) :333–335.
- Bridgwater, J., Foo, W., and Stephens, D. J. (1985). Particle mixing and segregation in failure zones-theory and experiment. *Powder Technology*, 41(2) :147–158.
- Brilliantov, N., Spahn, F., Hertzsch, J.-M., and Poschel, T. (1996). Model for collisions in granular gases. *Physical Review E*, 53(5) :5382–5392.
- Brone, D., Alexander, A., and Muzzio, F. (1998). Quantitative characterization of mixing of dry powders in V-blenders. *AIChE Journal*, 44(2) :271–278.
- Brone, D., Wightman, C., Connor, K., Alexander, A., Muzzio, F. J., and Robinson, P. (1997). Using flow perturbations to enhance mixing of dry powders in V-blenders. *Powder Technology*, 91(3) :165–172.
- Cantelaube, F. and Bideau, D. (1995). Radial segregation in a 2D drum : an experimental analysis. *Europhysics Letters*, 30(3) :133–138.
- Carson, J., Royal, T., and Troxel, T. (1996). Mix dry bulk solids properly and maintain blend integrity. *Chemical Engineering Progress*, 92 :72–80.
- Carstensen, J. and Patel, M. (1977). Blending of irregularly shaped particles. *Powder Technology*, 17(3) :273–282.
- Chang, R. K., Badawy, S., Hussain, M. A., and Buehle, J. D. (1995). A comparison of free-flowing, segregating and non-free-flowing, cohesive mixing systems in assessing the performance of a modified V-shaped solids mixer. *Drug Development and Industrial Pharmacy*, 21(3) :361–368.
- Chen, P., Ottino, J. M., and Lueptow, R. M. (2010). Onset mechanism for granular axial band formation in rotating tumblers. *Physical Review Letters*, 104(18) :188002.

- Choo, K., Baker, M., Molteno, T., and Morris, S. (1998). Dynamics of granular segregation patterns in a long drum mixer. *Physical Review E*, 58(5) :6115–6123.
- Chowhan, Z. and Linn, E. (1979). Mixing of pharmaceutical solids. I. effect of particle size on mixing in cylindrical shear and V-shaped tumbling mixers. *Powder Technology*, 24(2) :237–244.
- Cundall, P. and Strack, O. (1979). Discrete numerical model for granular assemblies. *Geotechnique*, 29(1) :47–65.
- Degaleesan, S., Dudukovic, M. P., and Pan, Y. (2002). Application of wavelet filtering to the radioactive particle tracking technique. *Flow Measurement and Instrumentation*, 13(1-2) :31–43.
- Di Renzo, A. and Di Maio, F. P. (2005). An improved integral non-linear model for the contact of particles in distinct element simulations. *Chemical Engineering Science*, 60 :1303–1312.
- Doucet, J., Bertrand, F., and Chaouki, J. (2008a). Experimental characterization of the chaotic dynamics of cohesionless particles : Application to a V-blender. *Granular Matter*, 10(2) :133–138.
- Doucet, J., Bertrand, F., and Chaouki, J. (2008b). An extended radioactive particle tracking method for systems with irregular moving boundaries. *Powder Technology*, 181(2) :195–204.
- Doucet, J., Bertrand, F., and Chaouki, J. (2008c). A measure of mixing from lagrangian tracking and its application to granular and fluid flow systems. *Chemical Engineering Research and Design*, 86(12) :1313–1321.
- Dury, C. M. and Ristow, G. H. (1997). Radial segregation in a two-dimensional rotating drum. *Journal de physique. I*, 7(5) :737–745.
- Fan, L., Chen, S., and Watson, C. (1970). Solids mixing. *Industrial and Engineering Chemistry*, 62(7) :53–69.
- Fischer, J. (1950). Blending or mixing apparatus. US Patent :US 2,514,126.

- Fischer, J. (1954). Blender. US Patent :US 2,677,534.
- Fischer, J. (1957). Heat exchanger mixing mill. US Patent :US 2,816,371.
- Fischer, J. (1979). Blendeing apparatus. US Patent :US 4,141,657.
- Fischer, J. (1983). Dual shell blender with intensifier. US Patent :US 4,368,986.
- Gorham, D. and Kharaz, A. (2000). The measurement of particle rebound characteristics. *Powder Technology*, 112(3) :193–202.
- Gray, J. (1957). Performance of dry solids mixing equipment. *Chemical Engineering Progress*, 53(1) :25–32.
- Harnby, N. (1967). A comparison of the performance of industrial solids mixers using segregating materials. *Powder Technology*, 1(2) :94–102.
- Hawkesworth, M., Parker, D., Fowles, P., Crilly, J., Jefferies, N., and Jonkers, G. (1991). Nonmedical applications of a positron camera. *Nuclear Instruments & Methods in Physics Research. Section A, Accelerators, Spectrometers, Detectors and Associated Equipment*, A310(1-2) :423–434.
- Hill, K. and Kakalios, J. (1995). Reversible axial segregation of rotating granular media. *Physical Review E*, 52(4) :4393–4400.
- Hrenya, C. and Stevens, A. (2005). Comparison of soft-sphere models to measurements of collision properties during normal impacts. *Powder Technology*, 154(2-3) :99–109.
- Huang, A. and Kuo, H. (2012). A study of the three-dimensional particle size segregation structure in a rotating drum. *AIChE Journal*, 58(4) :1076–1083.
- Ingram, A., Seville, J., Parker, D., Fan, X., and Forster, R. (2005). Axial and radial dispersion in rolling mode rotating drums. *Powder Technology*, 158(1-3) :76–91.
- Iwasaki, T., Satoh, M., and Koga, T. (2001). Analysis of collision energy of bead media in a high-speed elliptical-rotor-type powder mixer using the discrete element method. *Powder Technology*, 121(2-2) :239–248.

- Ji, S. and Shen, H. H. (2006). Effect of contact force models on granular flow dynamics. *Journal of Engineering Mechanics*, 132(11) :1252–1259.
- Khakhar, D., Orpe, A. V., and Ottino, J. (2001). Continuum model of mixing and size segregation in a rotating cylinder : Concentration-flow coupling and streak formation. *Powder Technology*, 116(2-3) :232–245.
- Krugger-Emden, H., Simsek, E., Rickelt, S., Wirtz, S., and Scherer, V. (2007). Review and extension of normal force models for the discrete element method. *Powder Technology*, 171(3) :157–173.
- Kuo, H., Knight, P., Parker, D., and Seville, J. (2005). Solids circulation and axial dispersion of cohesionless particles in a V-mixer. *Powder Technology*, 152(1-3) :133–140.
- Kuo, H., Knight, P., Parker, D., Tsuji, Y., Adams, M., and Seville, J. (2002). The influence of DEM simulation parameters on the particle behaviour in a V-mixer. *Chemical Engineering Science*, 57(17) :3621 – 3638.
- Kuwabara, G. and Kono, K. (1987). Restitution coefficient in a collision between two spheres. *Japanese Journal of Applied Physics*, 26(8) :1230–1233.
- Lacey, P. (1954). Developments in the theory of particle mixing. *Journal of Applied Chemistry*, 4(5) :257–268.
- Langston, P., Tüzün, U., and Heyes, D. (1994). Continuous potential discrete particle simulations of stress and velocity fields in hoppers : transition from fluid to granular flow. *Chemical Engineering Science*, 49(8) :1259–1275.
- Larachi, F., Chaouki, J., and Kennedy, G. (1995). 3-D mapping of solids flow-fields in multiphase reactors with rpt. *AIChE Journal*, 41(2) :439–443.
- Larachi, F., Kennedy, G., and Chaouki, J. (1994). A gamma ray detection system for 3-D particle tracking in multiphase reactors. *Nuclear Instruments & Methods in Physics Research Section a-Accelerators Spectrometers Detectors and Associated Equipment*, A338(2-3) :568–576.

- Laurent, B. and Cleary, P. (2012). Comparative study by PEPT and DEM for flow and mixing in a ploughshare mixer. *Powder Technology*, 228 :171–186.
- Lee, J. and Herrmann, H. (1993). Angle of repose and angle of marginal stability : molecular dynamics of granular particles. *Journal of Physics A*, 26(2) :373–83.
- Lemieux, M., Bertrand, F., Chaouki, J., and Gosselin, P. (2007). Comparative study of the mixing of free-flowing particles in a V-blender and a bin-blender. *Chemical Engineering Science*, 62(6) :1783–1802.
- Lemieux, M., Leonard, G., Doucet, J., Leclaire, L.-A., Viens, F., Chaouki, J., and Bertrand, F. (2008). Large-scale numerical investigation of solids mixing in a V-blender using the discrete element method. *Powder Technology*, 181(2) :205–216.
- Li, Y., Xu, Y., and Thornton, C. (2005). A comparison of discrete element simulations and experiments for 'sandpiles' composed of spherical particles. *Powder Technology*, 160(3) :219–228.
- Locke, H. (1965). Mixing apparatus. US Patent :US 3,188,058.
- Mehrotra, A. and Muzzio, F. (2009). Comparing mixing performance of uniaxial and biaxial bin blenders. *Powder Technology*, 196(1) :1–7.
- Meier, S., Lueptow, R., and Ottino, J. (2007). A dynamical systems approach to mixing and segregation of granular materials in tumblers. *Advances in Physics*, 56(5-6) :757–827.
- Mellmann, J. (2001). The transverse motion of solids in rotating cylinders-forms of motion and transition behavior. *Powder Technology*, 118(3) :251–270.
- Mindlin, R. (1949). Compliance of elastic bodies in contact. *Journal of Applied Mechanics*, 16 :259–268.
- Mindlin, R. and Deresiewicz, H. (1954). Thickness-shear and flexural vibrations of a circular disk. *Journal of Applied Physics*, 25 :1329–1332.
- Mishra, B. and Murty, C. (2001). On the determination of contact parameters for realistic DEM simulations of ball mills. *Powder Technology*, 115(3) :290–297.

- Moakher, M., Shinbrot, T., and Muzzio, F. (2000). Experimentally validated computations of flow, mixing and segregation of non-cohesive grains in 3D tumbling blenders. *Powder Technology*, 109(1-3) :58–71.
- Mostoufi, N. and Chaouki, J. (2001). Local solid mixing in gas-solid fluidized beds. *Powder Technology*, 114(1-3) :23–31.
- Muzzio, F., Robinson, P., Wightman, C., and Dean, B. (1997). Sampling practices in powder blending. *International Journal of Pharmaceutics*, 26(2) :153–178.
- Muzzio, F. J., Goodridge, C. L., Alexander, A., Arratia, P., Yang, H., Sudah, O., and Mergen, G. (2003). Sampling and characterization of pharmaceutical powders and granular blends. *International Journal of Pharmaceutics*, 250(1) :51–64.
- Parker, D., Broadbent, C., Fowles, P., Hawkesworth, M., and Mcneil, P. (1993). Positron emission particle tracking - A technique for studying flow within engineering equipment. *Nuclear Instruments & Methods in Physics Research Section A-Accelerators Spectrometers Detectors and Associated Equipment*, 326(3) :592–607.
- Paul, E., Atiemo-Obeng, V., and Kresta, S. (2004). *Handbook of industrial mixing : science and practice*. John Wiley & Sons.
- Perrault, M., Bertrand, F., and Chaouki, J. (2010). An investigation of magnesium stearate mixing in a V-blender through gamma-ray detection. *Powder Technology*, 200(3) :234–45.
- Peterson, R. W. (1981). Apparatus and method for solid particle bulk density measurements. US Patent :US 4,283,148.
- Portillo, P., Ierapetritou, M., Tomassone, S., Mc Dade, C., Clancy, D., Avontuur, P., and Muzzio, F. (2008). Quality by design methodology for development and scale-up of batch mixing processes. *Journal of Pharmaceutical Innovation*, 3(4) :258–270.
- Poux, M., Fayolle, P., Bertrand, J., Bridoux, D., and Bousquet, J. (1991). Powder mixing. some practical rules applied to agitated systems. *Powder Technology*, 68(3) :213–234.

- Ramirez, R., Poschel, T., Brilliantov, N., and Schwager, T. (1999). Coefficient of restitution of colliding viscoelastic spheres. *Physical Review E*, 60(4) :4465–4472.
- Rapaport, D. (2007). Radial and axial segregation of granular matter in a rotating cylinder : a simulation study. *Physical Review E*, 75(3) :31301–1–11.
- Rhodes, M. (2008). *Introduction to particle technology, 2nd edition*. John Wiley and sons.
- Russum, G. (1959). Mixing apparatus. US Patent :US 2,901,227.
- Sadd, M. H., Tai, Q., and Shukla, A. (1993). Contact law effects on wave propagation in particulate materials using distinct element modeling. *International Journal of Non-Linear Mechanics*, 28(2) :251–265.
- Samyn, J. C. and Murthy, K. S. (1974). Experiments in powder blending and unblending. *Journal of Pharmaceutical Sciences*, 63(3) :370–375.
- Savage, S. and Lun, C. (1988). Particle size segregation in inclined chute flow of dry cohesionless granular solids. *Journal of Fluid Mechanics*, 189 :311–325.
- Schäfer, J., Dippel, S., and Wolf, D. (1996). Force schemes in simulations of granular materials. *Journal De Physique, I*, 6(1) :5–20.
- Schulze, D. (2008). *Powders and bulk solids : Behavior, Characterization, Storage and Flow*. Springer.
- Schwager, T. and Poschel, T. (2007). Coefficient of restitution and linear-dashpot model revisited. *Granular Matter*, 9(6) :465–469.
- Stevens, A. and Hrenya, C. (2005). Comparison of soft-sphere models to measurements of collision properties during normal impacts. *Powder Technology*, 154(2-3) :99–109.
- Stewart, R. L., Bridgwater, J., Zhou, Y. C., and Yu, A. B. (2001). Simulated and measured flow of granules in a bladed mixer—a detailed comparison. *Chemical Engineering Science*, 56(19) :5457–5471.

- Sudah, O., Coffin-Beach, D., and Muzzio, F. (2002a). Effects of blender rotational speed and discharge on the homogeneity of cohesive and free flowing mixtures. *International Journal of Pharmaceutics*, 247(1) :57–68.
- Sudah, O. S., Arratia, P. E., Alexander, A., and Muzzio, F. J. (2005). Simulation and experiments of mixing and segregation in a tote blender. *AIChE Journal*, 51(3) :836–844.
- Sudah, O. S., Coffin-Beach, D., and Muzzio, F. (2002b). Quantitative characterization of mixing of free-flowing granular material in tote bin blenders. *Powder Technology*, 126(2) :191–200.
- Taberlet, N., Losert, W., and Richard, P. (2004). Understanding the dynamics of segregation bands of simulated granular material in a rotating drum. *Europhysics Letters*, 68(4) :522–528.
- Taberlet, N., Newey, M., Richard, P., and Losert, W. (2006). On axial segregation in a tumbler : an experimental and numerical study. *Journal of Statistical Mechanics : Theory and Experiment*, 2006(07) :17 pp.
- Thomas, N. (2000). Reverse and intermediate segregation of large beads in dry granular media. *Physical Review E*, 62(1) :961–974.
- Thomsen, J. G. (1971). Powder blender. US Patent :US 3,552,724.
- Thornton, C. (1997). Coefficient of restitution for collinear collisions of elastic-perfectly plastic spheres. *Journal of Applied Mechanics, Transactions ASME*, 64(2) :383–386.
- Thornton, C., Cummins, S. J., and Cleary, P. W. (2013). An investigation of the comparative behaviour of alternative contact force models during inelastic collisions. *Powder Technology*, 233(0) :30–46.
- Thornton, C. and Ning, Z. (1998). A theoretical model for the stick/bounce behaviour of adhesive, elastic-plastic spheres. *Powder Technology*, 99(2) :154–162.
- Tsuji, Y., Tanaka, T., and Ishida, T. (1992). Lagrangian numerical simulation of plug flow of cohesionless particles in a horizontal pipe. *Powder Technology*, 71(3) :239–250.

- Walton, O. and Braun, R. (1986). Viscosity, granular-temperature, and stress calculations for shearing assemblies of inelastic, frictional disks. *Journal of Rheology*, 30(5) :949–980.
- Walton, O. R. (1983). Application of molecular dynamics to macroscopic particles. *International Journal of Engineering Science*, 22(8-10) :1097–1107.
- Wightman, C. and Muzzio, F. J. (1998). Mixing of granular material in a drum mixer undergoing rotational and rocking motions II. segregating particles. *Powder Technology*, 98(2) :125–134.
- Wonglimpiyarat, J. (2005). Standard competition : Is collaborative strategy necessary in shaping the smart card market ? *Technological Forecasting and Social Change*, 72(8) :1001–1010.
- Yamane, K., Nakagawa, M., Altobelli, S., Tanaka, T., and Tsuji, Y. (1998). Steady particulate flows in a horizontal rotating cylinder. *Physics of Fluids*, 10(6) :1419–27.
- Zhang, D. and Whiten, W. (1996). Calculation of contact forces between particles using spring and damping models. *Powder Technology*, 88(1) :59–64.
- Zhou, Y., Wright, B., Yang, R., Xu, B., and Yu, A. (1999). Rolling friction in the dynamic simulation of sandpile formation. *Physica A*, 269(2-4) :536–553.
- Zhou, Y., Xu, B., Yu, A., and Zulli, P. (2002). An experimental and numerical study of the angle of repose of coarse spheres. *Powder Technology*, 125(1) :45–54.
- Zhu, H., Zhou, Z., Yang, R., and Yu, A. (2007). Discrete particle simulation of particulate systems : Theoretical developments. *Chemical Engineering Science*, 62(13) :3378–3396.
- Zik, O., Levine, D., Lipson, S., Shtrikman, S., and Stavans, J. (1994). Rotationally induced segregation of granular materials. *Physical Review Letters*, 73(5) :644–647.

CHAPTER 3

COHERENCE OF THE ARTICLES

Chapters 4 to 8 include the main body of this work and corresponding scientific findings. They include the simulations results of discrete element method (DEM) and experimental data of thief sampling for a tetrapodal blender and a V-blender as well as radioactive particle tracking (RPT) for a rotating drum. Each chapter consists of an individual scientific article. A brief description of each chapter is as follows :

- Chapter 4 presents the experimental data obtained by RPT inside a rotating drum. Further details of phenomena occurring inside the drum were investigated in this chapter. These results were applied in the next chapter to validate the DEM-based model ;
- In Chapter 5, DEM results were checked against Lagrangian RPT data. Dimensionless motion equations for the particles in normal and tangential directions were subsequently derived and analyzed. In addition, effective dimensionless numbers were introduced to explain how DEM parameters should be chosen. Chapters 4 and 5 cover the first specific objective of this work ;
- Using the results of Chapter 5, a proper set of DEM parameters were employed to simulate granular flow inside the tetrapodal blender and the V-blender in Chapter 6. The objective is to investigate the mixing and segregation of non-adhesive granules inside the tetrapodal blender and compare its performance with that of conventional V-blender. This chapter covers the second specific objective of this work ;
- In Chapter 7, several experiments were performed to validate the findings of Chapter 6 and investigate the effect of different parameters on the efficiencies of the tetrapodal blender and the V-blender regarding the mixing and segregation of granules. This chapter covers the third specific objective of this work ;
- Considering the minor discrepancies between DEM results and experimental data of

thief sampling for the tetrapodal blender and the V-blender as well as RPT data for the rotating drum, a model was developed in Chapter 8 to accurately predict the contact force term in DEM simulations. This model is examined using experimental data.

Chapter 9 is a general discussion and summary of the results and, finally, the conclusion and recommendations for future works are presented in Chapter 10.

CHAPTER 4

Characterization of Mixing and Size Segregation in a Rotating Drum by a Particle Tracking Method

Ebrahim Alizadeh, Olivier Dubé, François Bertrand, Jamal Chaouki

Department of Chemical Engineering, École Polytechnique de Montréal, C.P. 6079 succ.

Centre-Ville, Montréal, Québec, Canada, H3C 3A7

(Accepted in *AIChE Journal* - <http://dx.doi.org/10.1002/aic.13982>.)

Presentation of the article : It is desirable to check the ability of the DEM-based model in predicting several phenomena. Therefore, more details of such phenomena, occurring inside a rotating drum, are presented in this chapter and they will be used in the next chapter to check the DEM predictions.

Abstract : The mechanisms of segregation in solids mixing, even in simple rotating drums, are not clearly understood. While most past studies have focused on binary mixtures, this work investigates the effect of polydispersity on granular flow, mixing and segregation in a rotating drum operated in rolling regime through particle trajectories obtained from the radioactive particle tracking technique. Velocity profiles, radial segregation and axial dispersion coefficients for monodisperse and polydisperse systems of glass beads are analyzed with respect to rotational speed and particle size. A model is introduced to predict the residence times along streamlines and evaluate the rate at which the material renews at the free surface and within the inner layers of the bed. Our results reveal similar velocity profiles and residence times for monodisperse and polydisperse systems. They also indicate that the particles distribute along the radial direction of the drum, although not necessarily in a core/shell configuration.

Keyword : Solid mixing, Segregation, Rotating drum, Radioactive particle tracking, Velocity profile, Residence time, Axial dispersion

4.1 Introduction

Particulate materials are present in many industries, including ceramic, metallurgical, chemical, food, cosmetics, coal, plastics and pharmaceutical. In some of them, it is preferable to separate species of a mixture, while in many others, the final product is obtained by mixing the ingredients so that their final concentrations meet specific requirements within a given level of scrutiny. Blenders are commonly used in such industries to obtain a homogeneous mixture. Despite the wide applications reported for these blenders, their mechanisms of mixing are still poorly understood ([Jain et al., 2005](#)), so much that the dynamics of granular materials was identified as one of the 125 questions (Can we develop a general theory of the dynamics of turbulent flows and the motion of granular materials?) that point to critical knowledge gaps in science ([So much more to know, 2005](#)). In fact, during the last few decades, a large body of work has focused on the flow of granules and powders. However, more investigations are needed. Here, we restrict ourselves to the simple rotating drum, which is used, for instance, as a granular mixer, a dryer, a coater or a gas/solid reactor. In the rotating drum, different types of flow regimes are obtained by increasing the Froude number, $Fr = \frac{\omega^2 R}{g}$, where ω , R and g stand for the rotational speed, the drum radius and the gravitational acceleration ([Meier et al., 2007](#); [Mellmann, 2001](#)). In this paper, we focus on the rolling regime that is common for mixing purposes. It is characterized by a flat surface layer, where the particles flow at a given dynamic repose angle with respect to the horizontal. This dynamic repose angle depends on granule properties such as size and surface roughness, as well as on the tumbler dimensions and rotational speed ([Meier et al., 2007](#)).

As shown in [Fig. 4.1](#), the granular bed in the rolling mode can be divided into two distinct regions : 1) a thin lens-like flowing or active layer, and 2) a larger passive layer beneath the active layer. In the passive region, the particles flow as a solid body and rotate with the drum at fixed axial and radial positions. When particles reach the surface, they slide down within the active layer and eventually rejoin the passive layer.

One of the phenomena that makes mixing of granules difficult is segregation (demixing).

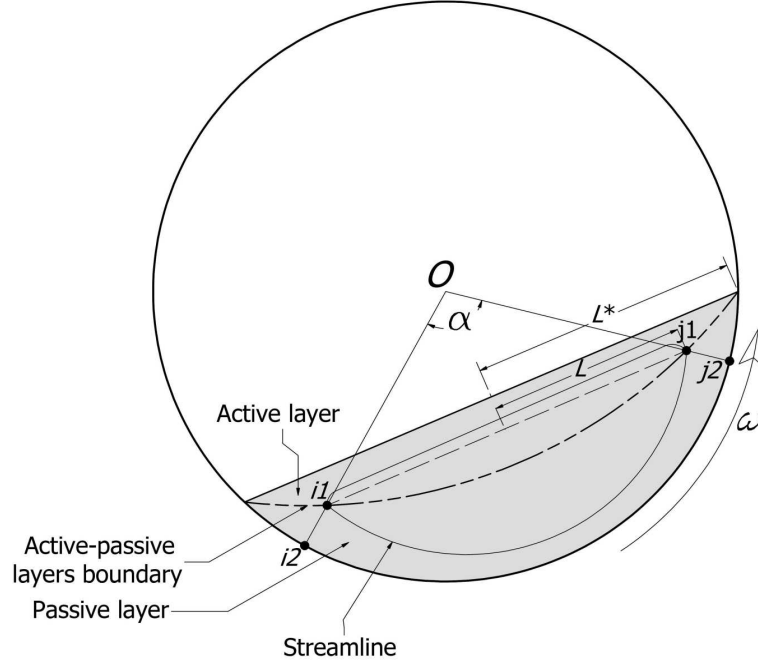


Figure 4.1: Rolling regime in a cylindrical drum.

In mixers, segregation happens when particles have different properties, such as size, density, shape, and roughness. While segregation occurs in tumbling blenders, its mechanisms are not clearly understood and all known theories or explanations have exceptions. Segregation can happen in both radial (transverse) and axial directions in a tumbling drum. Since the radial mixing mechanism is mainly convective, radial segregation appears rapidly in the first few revolutions ([Cantelaube and Bideau, 1995](#)). Depending on the particle size distribution and the fraction of large particles, fine and dense particles generally migrate to the core region of the material bed near the rotation axis ([Cantelaube and Bideau, 1995](#); [Rapaport, 2007](#); [Thomas, 2000](#); [Wightman and Muzzio, 1998](#)). Since the particle axial and radial positions do not change in the passive layer owing to the solid-like motion, segregation starts in the active layer near the free surface and only a very slow rearrangement of the particles occurs below this flowing layer ([Aranson and Tsimring, 1999](#); [Zik et al., 1994](#)). Segregation in the transverse plane (that parallel to the drum ends) mainly results from the downward movement of small (or dense) particles within a thin surface layer, which displace larger (or lighter) particles

upward (Meier et al., 2007). After a long enough period of the time, axial bands of coarse and fine particles are often formed. These bands are generally rich in one type of particles, but not necessarily pure. Axial banding segregation has been the topic of numerical and experimental works (Alexander et al., 2004; Choo et al., 1998; Hill and Kakalios, 1995; Huang and Kuo, 2012; Rapaport, 2007; Taberlet et al., 2006; Zik et al., 1994). In particular, Hill and Kakalios (1995) showed that blends that appear mixed at low rotational speed, may form bands at higher speed. The governing mechanism for such axial segregation is not clear. However, it has been shown that differences in the dynamic repose angle of the components of a blend may trigger the formation of these axial bands (Bridgwater et al., 1985; Hill and Kakalios, 1995). Recently, Chen et al. (2010) showed the effect of the end walls of the cylindrical drum on axial segregation. Since the governing mixing mechanism in the axial direction is dispersion, axial segregation occurs more slowly than radial segregation and may require hundreds or even thousands of revolutions.

In the studies mentioned above, binary mixtures of granules were considered. In fact, investigations on the flow of polydisperse blends are rare, one example being the work of Ingram et al. (2005). Therefore, it is of interest to investigate the effect on granular flow of a distribution of particle sizes inside the bed. This would help to find out whether theories and correlations that have been developed for monodisperse and binary mixtures are valid for more complex polydisperse systems.

The aim of this study is to gain insight into the flow dynamics of polydisperse particles in a cylindrical drum as well as the underlying mixing and segregation mechanisms. Parameters such as the residence time, active layer thickness and axial dispersion are discussed in detail. Understanding of these parameters is important as it may provide guidelines for the design of efficient mixing processes and other unit operations involving particles. In this work, only free flowing particles are considered so that non-contact forces such as cohesive forces are neglected. Radioactive particle tracking (RPT), which was used to capture the flow of particles inside the rotating drum, is described in next section. These RPT experiments differ

from previous studies because the tracers used and the particles in the drum have identical properties. The methodology and RPT experiments are then fully described, and the results obtained are presented thoroughly discussed.

4.2 Methodology

Characterizing the flow and the arrangement of the particles inside the drum can be done by extracting samples from it. However, such methods interfere with the matter and may affect the measurement itself (Muzzio et al., 1997, 2003). In addition, analyzing samples containing many species is tedious and takes a long time. To overcome these limitations, non-invasive methods such as laser doppler anemometry (LDA) and particle image velocimetry (PIV) are appealing at first sight, but the opaque nature of granular media renders such methods useless. Another possibility is to resort to characterization methods based on radioactive measurements. Two such methods have been applied in the field of solid mixing. The first one relies on positron annihilation and is called positron emission particle tracking (PEPT) (Hawkesworth et al., 1991; Parker et al., 1993). The second method, which is applied in this work, uses gamma rays emitted from a single radioactive tracer (Larachi et al., 1994). This technique is known as radioactive particle tracking (RPT) and, in comparison with PEPT, is inexpensive, compact and can be used for large mixing vessels. Our group has extended RPT so that it can be used in blenders (Doucet et al., 2008).

4.2.1 RPT

RPT tracks the position of a single radioactive tracer with respect to time using an array of scintillation detectors located around the vessel to capture gamma rays emitted by this tracer. The set of recorded gamma ray counts depends on the position of the tracer. The position of this tracer is in fact reconstructed by minimizing the discrepancy between the recorded and calculated counts using a model proposed by Beam et al. (1978). This method uses Monte Carlo simulation to generate a dictionary that contains the number of gamma

rays expected to be intercepted by the detectors when the tracer is in a given position. More details on this method can be found in [Larachi et al. \(1994\)](#) and [Doucet et al. \(2008\)](#). The RPT method has a resolution of $2 - 3\text{mm}$ in all three directions (x, y and z) under the conditions of this work.

4.2.2 RPT with ^{24}Na

One important step of the RPT method is the preparation of the tracer. In particular, this tracer should match the inert particles in size, density and shape. One way to achieve this consists of radioactivating particles that are identical to those in the vessel. For instance, the glass beads used in this work contain 13-14% soda lime, which includes ^{23}Na that can be converted to ^{24}Na isotope using the Slowpoke reactor of École Polytechnique de Montréal. In practice, only one particle in the vessel is radioactive, the tracer, and the others are inert. The activation time of the tracers depends on their size and may vary from 30 to 90 minutes. ^{24}Na emits gamma rays with two levels of energy (1.368 and 2.754 MeV). In this study, only events related to the gamma rays with the higher energy are captured in order to prevent recording diffracted rays. The problem of ^{24}Na is its short half-life (~ 15 hr). Depending on the duration of an experiment, the dictionaries that are valid at the beginning of such an experiment may then become inaccurate due to the decay of the ^{24}Na isotope, which may lead to large errors in the reconstruction of the tracer trajectory. To overcome this problem, recorded events must be corrected. To do so, a second tracer, which is similar to the first one, is used as a sentinel outside the vessel to monitor with the help of a dedicated NaI-Tl detector the loss of activity with time and then correct the number of events captured by the detectors around the vessel. Note that this so-called blank source is shielded in such a way that it does not affect the measurements made by these detectors.

4.3 Experiments

4.3.1 Material

The RPT technique was applied to investigate flow behavior and mixing inside a horizontal rotating drum made from plexiglass. The drum has a 24cm inner diameter and is 36cm long. The drum was filled up to $35\text{vol}\%$ with glass beads ($\rho = 2.5\text{kg/l}$) of varying diameter between 3 and 6 mm . The rotational speed of the drum was set to 11.6RPM , which is the maximum velocity for the rolling mode. To study the effect of the rotational speed on the granular flow behavior, other sets of experiments were carried out at about 50% of the maximum rolling regime velocity (5.4RPM). A schematic of the setup used for the experiments is given in Fig. 4.2. Eight $3'' \times 3''$ NaI-Tl scintillation detectors were installed around the drum. Six detectors were strategically placed at 120° from each other around the drum and two other detectors were positioned at both its ends. The distance between the detectors and the drum was fixed in such a way to avoid the saturation of gamma rays. The dwell time, let alone the time for each measurement by a detector, was set to 10ms to minimize event fluctuations and track the tracer with adequate accuracy with respect to the maximum particle velocity inside the drum.

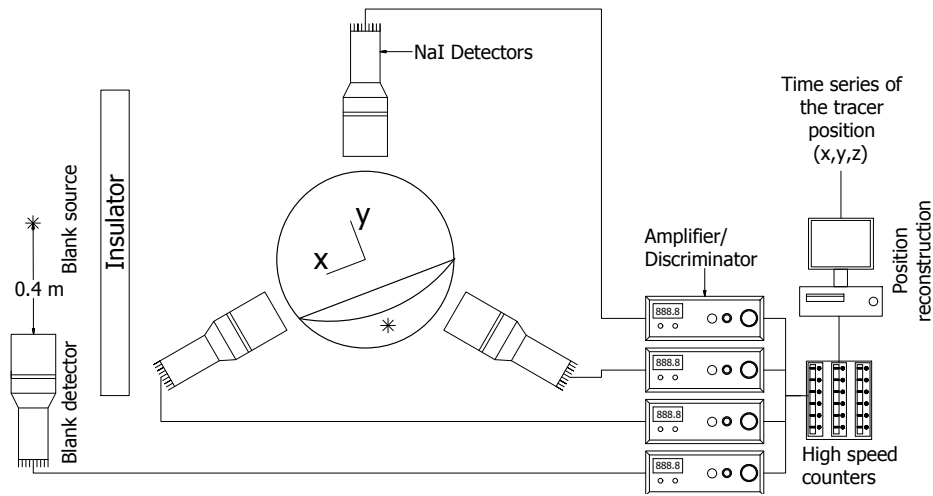


Figure 4.2: Schematic of the setup.

The approximate activity level was $60 \mu\text{ci}$ initially. To eliminate the effects of the other isotopes (*e.g.* antimony), which have a shorter half-life, the tracers were used 1-2 hours after their activation in the Slowpoke reactor. The only change in the properties of a tracer after its activation was a darkening of its original color. The darker color of the tracer helps find it inside the bed after an experiment. Because chipping or erosion of the tracer may affect its properties as well as the RPT accuracy, the inner surface of the drum was checked for contamination with accurate germanium detectors after each experiment. It confirmed that the tracers did remain sealed and their surface and physical properties remained identical to those of the other particles in the drum.

4.3.2 Details of the experiments

Mixing experiments were performed with 3-*mm* monodisperse glass beads and polydisperse mixtures of glass beads, the diameter of which were 3,4,5, or 6 *mm*. The composition of the polydisperse systems was chosen to ensure a rapid segregation in the drum (Table 4.1). Overall, 10 different experiments were performed. In each one, the radioactive tracer was tracked using RPT for a period of 210 minutes to make sure it travels everywhere inside the drum. Details of the experiments are given in Table 4.1. The RPT data were then post-processed to reconstruct the trajectory of the tracer.

4.4 Results

The RPT data can be exploited to gain insight into the flow behavior and mixing performance in the drum. First, velocity profiles on a transverse plane are presented. A model is then proposed to characterize the residence time of the glass beads in the active and passive layers, and its validity is assessed with experimental data. Finally, the radial segregation and the axial dispersion of the polydisperse mixtures with respect to the drum rotational speed and tracer size are analyzed.

Table 4.1: Mixing experiments involving monodisperse and polydisperse particles.

Case	Type	Rotational speed [RPM]	Tracer size [mm]
MD1	Monodisperse ($3mm$)	5.4	3
MD2	Monodisperse ($3mm$)	11.6	3
PD1.3	Polydisperse ($3mm(15vol\%), 4mm(35vol\%),$ $5mm(35vol\%), 6mm(15vol\%)$)	5.4	3
PD1.4		5.4	4
PD1.5		5.4	5
PD1.6		5.4	6
PD2.3	Polydisperse ($3mm(15vol\%), 4mm(35vol\%),$ $5mm(35vol\%), 6mm(15vol\%)$)	11.6	3
PD2.4		11.6	4
PD2.5		11.6	5
PD2.6		11.6	6

4.4.1 Occupancy plots

As mentioned in the previous section, the particles retain their properties when they are irradiated. This can also be assessed indirectly by checking that the occupancy plot of a tracer in a monodisperse system is homogenous, which means that it appears the same amount of time everywhere in the volume of the drum and that no segregation therefore takes place. Obtaining occupancy plots using the RPT technique is straightforward since this method collects large amounts of tracer positions during an experiment. These positions can be projected onto transverse planes of the drum to yield occupancy profiles (see Fig. 4.8 for an example). Occupancy plots for monodisperse cases MD1 and MD2 indeed indicate (not shown here) that the tracer travels homogenously inside the drum.

4.4.2 Velocity profiles

The velocity of the tracer can be obtained by differentiating its position with respect to time. To obtain an average value of the velocity profile in a transverse plane, all of the reconstructed tracer positions and their corresponding velocities are projected onto it. Fig. 4.3 shows typical velocity profiles in the transverse plane of the drum for cases MD2 (mono-

disperse) and PD2 (polydisperse). The velocity profile of the polydisperse mixture has been obtained by averaging the velocity profiles of all particles, irrespective of their size. Similar qualitative patterns can be observed for the monodisperse and polydisperse systems, and it seems a priori that the velocity profile is independent of the particle size distribution.

A qualitative comparison of the monodisperse and polydisperse cases can be done by looking at the corresponding velocity profiles in the streamwise (x) and transverse (y) directions. Coordinate $(0,0,0)$ is located at the center of the drum, x is parallel to the free surface in the direction of the flow while y is perpendicular to the free surface and points outward. The z axis is aligned with the axial direction. Only the streamwise and transverse velocities for a rotational speed of $11.6RPM$ are presented since the results at the lower speed show the same trend. Fig. 4.4 presents the transverse (v) and streamwise velocity (u) variations along the line at $x = 0$. These data were obtained by projecting the full data on the transverse plane of the drum by means of $2mm \times 2mm$ cells. On average, the tracer passes in each cell more than 400 times in each experiment, thus providing statistically reliable data.

It is commonly assumed in the literature that there is no transverse velocity (v) at $x = 0$. Recently, [Jain et al. \(2004\)](#) performed experiments with steel balls and showed that the

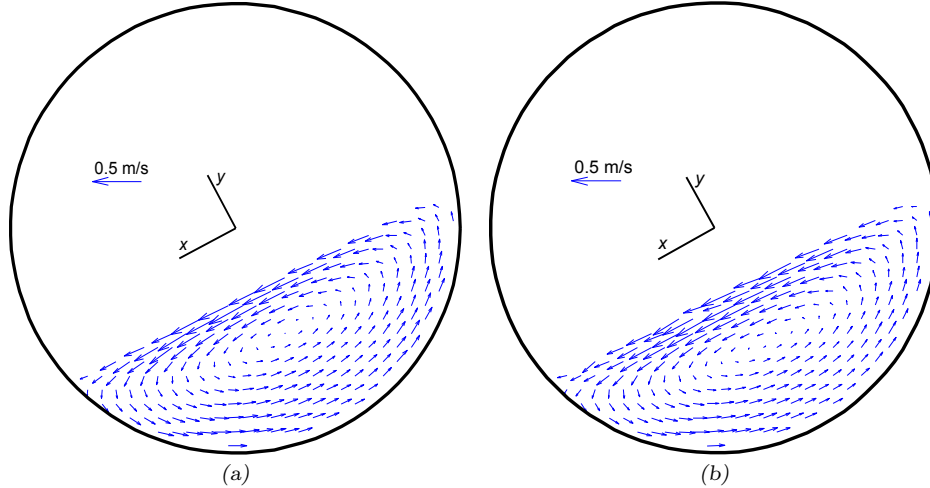


Figure 4.3: Velocity vectors in the transverse plane of the drum for (a) monodisperse (case MD2) and (b) polydisperse (case PD2) glass beads.

transverse velocity varies slightly around zero. Our results show that the mean transverse velocity along the depth of the granular bed at $x = 0$ is $-1.46 \times 10^{-3} \text{ m/s}$ (standard deviation $= 6.4 \times 10^{-3}$) and $2.2 \times 10^{-3} \text{ m/s}$ (standard deviation $= 6.9 \times 10^{-3}$) for the polydisperse and monodisperse cases, respectively. In the passive layer, the glass beads flow as a solid body, whereas in the active layer, these particles can slightly move in the y -direction.

As regards the streamwise velocity (u), one may observe that :

- Despite the occurrence of radial segregation for the polydisperse cases, as will be discussed later, there are no significant differences in the streamwise velocity profiles with respect to particle size ;
- There are no significant differences between the velocity profiles of the polydisperse and monodisperse systems. The only small difference is that the velocity profile of the monodisperse mixture is slightly above those of the polydisperse mixtures, indicating a slightly thinner active layer in the former case ;
- The streamwise velocity varies approximately linearly with respect to y in the active

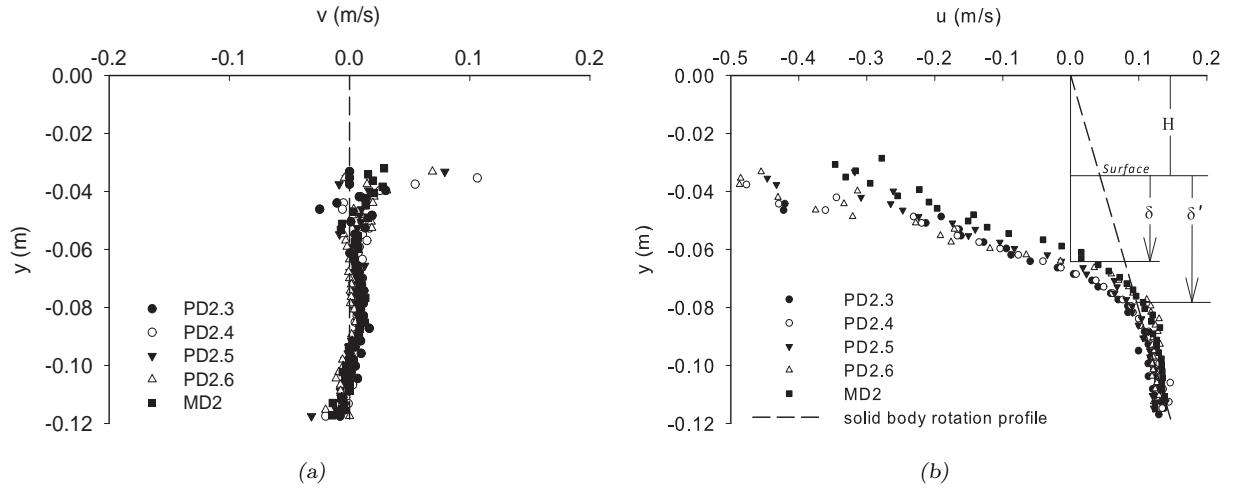


Figure 4.4: Variation of the (a) transverse and (b) streamwise velocities for a rotational speed of 11.6 RPM in the transverse plane of the drum along the line at $x = 0$. H is the distance from the free surface to the center of the drum, δ is the distance from the free surface to the depth at which glass beads change direction along the x axis, and δ' is the distance from the free surface to the depth at which the solid body rotation stops.

and passive layers, although with different slopes.

The linear behavior of the streamwise velocity is a well-known phenomenon and similar results, based on either numerical simulation or experimentation, have been reported in the literature (Bonamy et al., 2002; Jain et al., 2002; Meier et al., 2007; Nakagawa et al., 1993; Taberlet et al., 2006). Each of the two regions (active and passive), is characterized by a line and a slope. This behavior remains valid for other positions in x , as can be seen in Fig. 4.5. The solid lines are the best fitted lines in the active layer for different positions in x , and the dashed line is what is expected in the passive layer and the solid body rotation found therein. The slope of the solid lines in the active layer increases with increasing x . When $x = 0$, the linear velocity profiles in the active and passive layers were obtained from the following correlations :

$$u_{act} = u_{max} \left(1 + \frac{y + H}{\delta_o} \right), \quad (4.1)$$

$$u_{pas} = \omega y, \quad (4.2)$$

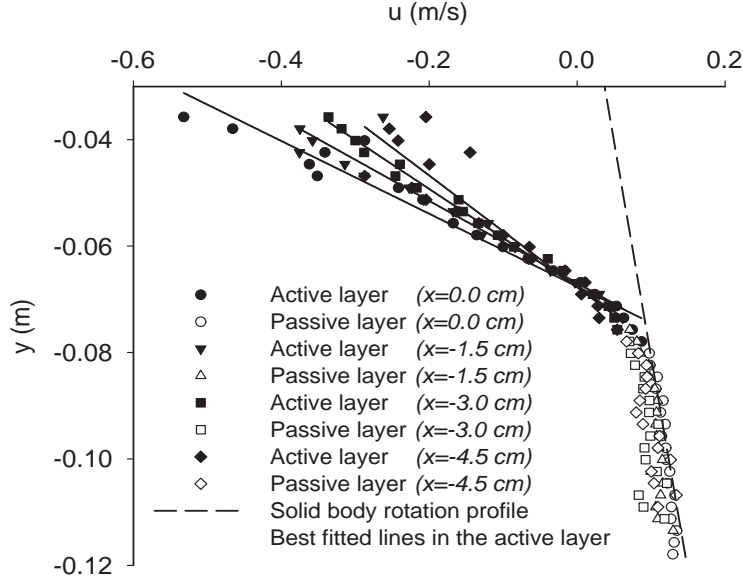


Figure 4.5: Streamwise velocity profiles for the polydisperse mixture of case PD2 for different positions in x .

where u_{max} is the maximum value of the streamwise velocity on the free surface, H the distance from the free surface to the center of the drum, and δ_o the distance from the surface to the depth at which the glass beads change direction along the x axis, hereafter called the active layer thickness.

Another important aspect involves the variation of the streamwise velocity along the free surface. For example, [Chen et al. \(2010\)](#) evidenced the effect of the surface flow on axial segregation. To show the surface flow, normalized velocities for the monodisperse and polydisperse cases were evaluated from the RPT data. The results are reported in Fig. 4.6a. Note that, due to the probability of particles jumping off the surface, the data are shown a few millimeters beneath the top of the bed. The streamwise velocities were normalized with respect to the maximum value (u_{max}) attained at the middle of the surface when $x = 0$. Along the free surface, the particles accelerate until they reach the middle point and then decelerate as they proceed toward the downstream endpoint. It can be shown that the particle velocity profile along the free surface can be expressed as ([Khakhar et al., 1997](#)) :

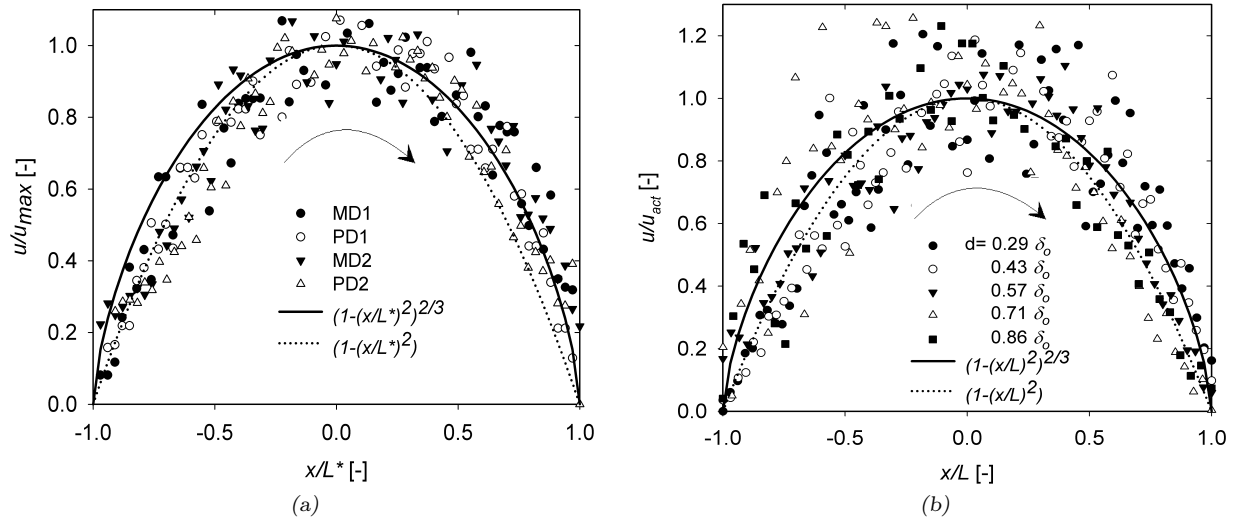


Figure 4.6: Streamwise velocity profiles along the x -direction; (a) on the free surface and (b) in the inner layers, in the case of MD2. d stands for the distance from the free surface, $L = L(y)$ corresponds to half the length of the corresponding streamline in the active layer, and $L^* = L|_{y=-H}$. u_{act} is the velocity at the middle of each streamline.

$$\frac{u}{u_{max}} = 1 - \frac{x^2}{L^{*2}}, \quad (4.3)$$

$$u_{max} = \omega L^{*2} / \delta_o, \quad (4.4)$$

where $L^* = L|_{y=-H}$ corresponds to half the length of the free surface and, more generally, L corresponds to half the length of the corresponding streamline (see Fig. 4.1). As illustrated in Fig. 4.6a, the experimental data of the velocity profiles along the upstream half of the free surface can be adequately modeled by Eq. 4.3 (dashed curve). The downstream half is better approximated by a change in the exponent of Eq. 4.3 (solid curve), as has been reported by Ding et al. (2002b). It can also be seen that one single curve is needed to represent the streamwise velocity profile along the free surface for all monodisperse and polydisperse cases. The same model (with L^* replaced by L) can be applied for the streamlines in the inner layers of the bed. In this case, the velocity is normalized with respect to u_{act} , which is the maximum streamwise velocity evaluated from Eq. 4.1. Similar conclusions can be drawn, as can be seen in Fig. 4.6b. Despite a slightly better fit of the solid curve in the downstream half of the graph of Fig. 4.6b, the following expression, similar to Eq. 4.3, will be used in the rest of the paper :

$$u = u_{act}(1 - (x/L)^2). \quad (4.5)$$

4.4.3 Active layer thickness

The active layer thickness is an important parameter in models used for the material transport in rotating drums (Mu and Perlmutter, 1980). In fact, the thickness of the active layer has an impact on the mixing and segregation phenomena occurring in the drum. As a result, its determination is key to a better understanding of the kinetic and the extent of such phenomena. For instance, in a kiln operated in rolling regime, it has been shown that

the thermal efficiency is proportional to the fraction of the mixing zone (Kelbert and Royere, 1991). In direct-fired rotary kilns, the heat is mainly transferred into the bulk of the material bed through the active layer (Liu and Specht, 2010).

The intersection point of the velocity profiles in the active and passive layers is known as the active layer lower boundary where the particles stop rotating as a solid body and start free flowing. This is indicated by δ' in Fig. 4.4b. In other studies, this boundary is defined as the point where the particles change direction ($u = 0$) along the x axis, as defined by δ in Fig. 4.4b (Ingram et al., 2005). This second definition, called the “turning point criterion”, is associated with a parabolic representation of the boundary :

$$y = ax^2 - (H + \delta_o), \quad (4.6)$$

where $\delta_o = \delta|_{x=0}$. Parameter $a = \delta_o/L^{*2}$ is the parabolic constant, where $L^* = 11.5\text{cm}$, the value of which depends on the fill level and the radius of the drum. The depth of the active layer at $x = 0$ (as expressed by $\delta'_o = \delta'|_{x=0}$ and δ_o) for the different experiments is given in Tables 4.2 and 4.3. Note that PD1 and PD2 correspond to average values obtained for the four corresponding polydisperse cases. Contrary to the belief that the active layer is a rather thin layer, it can be around 30 to 40% of the total bed depth, based on these two definitions. As can be seen in the tables, the depth of the active layer is thicker for a polydisperse mixture and increases when the rotational speed is increased. This is in agreement with most of the data reported in the literature (Boateng and Barr, 1997; Henein et al., 1983; Van Puyvelde et al., 2000; Woodle and Munro, 1993).

Being able to evaluate the active layer thickness is important because it affects the particle velocity profile. There are correlations in the literature that predict the thickness of the active layer as a function of x . Unfortunately, many of them include parameters (for example, the maximum surface velocity) that are difficult to measure, mostly in industrial scale unit operations (Khakhar et al., 1997). We propose here to resort to a model that predicts the depth of the active layer based only on the operating conditions, the material properties, and

Table 4.2: Depth of the active layer δ'_o .

Case	Type	ω [RPM]	δ'_o (measured) [cm](%) ¹	δ'_o (Eq. 4.7) [cm](%) ¹
MD1	Monodisperse	5.4	2.6(30)	2.6(30)
MD2		11.6	3.8(43)	3.8(43)
PD1	Polydisperse	5.4	3.5(40)	2.9(33)
PD2		11.6	4.2(48)	4.2(48)

¹ percentage of bed depth

Table 4.3: Depth of the turning point active layer (δ_o). All data are in [cm](percentage of bed depth).

Case	ω [RPM]	Measured	Eq. 4.11	Cheng et al.	Ding et al.	Liu et al.	Weir et al.
MD1	5.4	2.1(24)	2.4(27)	1.9(21)	2.5(28)	1.5(18)	2.1(24)
MD2	11.6	2.8(32)	3.3(37)	2.1(24)	2.3(27)	2.0(23)	2.6(30)
PD1	5.4	2.6(30)	2.6(30)	1.8(21)	3.0(34)	1.6(18)	2.4(28)
PD2	11.6	2.9(33)	3.5(40)	1.7(20)	2.8(32)	2.1(24)	3.0(34)
Average error (%)			13	27	13	30	4

the geometrical characteristics of the rotating drum (Khakhar et al., 2001; Meier et al., 2007; Orpe and Khakhar, 2001). It is given by :

$$\delta'(x) = \sqrt{\frac{\omega}{\dot{\gamma}}(L^{*2} - x^2)}, \quad (4.7)$$

where the shear rate $\dot{\gamma}$ depends on the material properties :

$$\dot{\gamma}(x) = \sqrt{\frac{g \cos\beta(x) \sin(\beta_d - \beta_s)}{d_p \cos\beta_d \cos\beta_s}}, \quad (4.8)$$

with d_p the particle size and $\beta(x)$ the angle between the horizontal axis and the boundary between the active and passive layers. β_s and β_d are the measured static and dynamic angles of repose, are equal to 25° and 27°, respectively. At $x = 0$, $\beta(0) \rightarrow \beta_d$ and the calculated values of δ'_o are given in Table 4.2. As can be seen, this model predicts accurately the thickness of the active layer except for the case PD1, where a reasonable 17% discrepancy is obtained.

Recently, Cheng et al. (2011) applied an incomplete similarity theory for estimating δ_o .

when the drum was half-filled. They extended their correlation to cover various fill fractions and fitted the underlying constants using experimental data of [Felix et al. \(2002, 2007\)](#), where glass beads have been used. Other expressions have been developed by [Ding et al. \(2002a, 2001\)](#), [Weir et al. \(2005\)](#) and [Liu and Specht \(2010\)](#); [Liu et al. \(2006\)](#). Since these models suffer from weak predictions or need fitting constants, in the current work, a new correlation is proposed for δ_o . Given that the linear streamwise velocity profiles in the active (Eq. 4.1) and passive (Eq. 4.2) layers meet at $y = -(\delta'_o + H)$ (see Figs. 4.4 and 4.5), it follows that :

$$u_{act}|_{y=-(\delta'_o+H)} = u_{pas}|_{y=-(\delta'_o+H)}, \quad (4.9)$$

$$\delta_o = \frac{\delta'_o u_{max}}{u_{max} + \omega(H + \delta'_o)}, \quad (4.10)$$

and, from Eq. 4.4,

$$1 - \frac{L^{*2}}{\delta_o^2} \frac{\delta'_o - \delta_o}{H + \delta'_o} = 0. \quad (4.11)$$

The values of δ_o using Eq. 4.11 and those obtained with the correlations from the literature are presented in Table 4.3. A good agreement with the experimental data is obtained in all cases when Eq. 4.11 is used. This shows the ability of this expression to predict the active layer thickness, which can then be used to derive velocity profiles by means of Eqs. 4.1 and 4.4. Among the correlations from the literature, the one by [Weir et al. \(2005\)](#) yields the best results. Their model predicts that δ_o increases with increasing particle size or rotational speed. However, it brings into play an author-dependent coefficient (λ), the value of which depends on particle properties, the geometrical characteristics of the drum and the operating conditions. They used $\lambda = 1$ for glass beads based on the experimental data of [Felix et al. \(2002\)](#), which was used in the last column of Table 4.3 to predict the value of δ_o with their expression. Since the operating conditions in [Felix et al. \(2002\)](#) are close to the conditions of the experiments of the current work ($d_p < 2mm$, $\omega = 2.0 - 10.4 RPM$ and $R = 0.06 - 0.20m$), very small discrepancies are observed between the values predicted by this model and the

measured values of δ_o . However, a larger error could be obtained for operating conditions far from those considered to fit coefficient λ . The advantages of Eq. 4.11 comes from the fact that its parameters are easy to obtain : H and L^* from geometrical conditions and δ' using Eqs. 4.7 and 4.8. The predictions from the models of Liu and Specht (2010); Liu et al. (2006) and Cheng et al. (2011) underestimate the thickness of the active layer, although the former does predict the behavior of δ_o when the rotational speed increases or the mixture changes from MD to PD. Finally, the model by Ding et al. (2002a, 2001) performs rather well as regards the thickness of active layer (average error of 13%) and succeeds to predict the behavior of δ_o when the type of mixture changes, but fails to correctly predict the trend when the rotational speed changes.

4.4.4 Residence time

In the cylindrical drum, the transverse motion of the particles is the primary factor that controls the renewal of the material at the exposed bed surface. In particular, the rate of surface renewal affects the heat/mass transfer from the freeboard to the bed (Boateng, 1998). For example, in industrial pan coaters, where a nozzle sprays the surface of the bed, the coating time is related to the residence (cycling) time of the granules on the free surface (Ottino and Khakhar, 2002). Another example is the granulation process with rotating drums, where the determination of the residence time in the different layers of the granular bed could help estimate local rates of granulation and then the granulation time. These facts have provided the impetus to model the residence time of the particles on the free surface as well as in the inner layers of the granular bed.

In Fig. 4.7, the total residence time of the glass beads along streamlines (t_t), as evaluated from RPT data, is shown versus the angle α of these streamlines (Fig. 4.1) for the monodisperse and polydisperse cases. It corresponds to the time taken by these particles to make one full circulation along a closed streamline. As can be noticed, there is a linear increase in the residence time when the angle of the streamlines increases. To analyze these results in more

detail, the residence time can be divided into two components corresponding to the active and passive layers. In the passive layer, because of the solid body motion, a linear increase of the residence time is expected when α increases. This can be shown for an arbitrary streamline that displaces particles from $i1 \rightarrow j1$ (see Fig. 4.1). Due to the solid body rotation in the passive layer, the traveling time along this streamline from $i1$ to $j1$ is equal to the traveling time from $i2$ to $j2$, along the drum wall :

[!tb]

$$t_{i1 \rightarrow j1} = t_{i2 \rightarrow j2} = \frac{\text{distance}_{i2 \rightarrow j2}}{\text{velocity}_{i2 \rightarrow j2}}. \quad (4.12)$$

The velocity along the drum wall is related to the angular velocity (ω) of the rotating drum so that

$$t_{pas} = t_{i2 \rightarrow j2} = \frac{R\alpha}{R\omega} = \frac{1}{\omega}\alpha, \quad (4.13)$$

which means that the residence time t_{pas} along any streamline in the passive layer is propor-

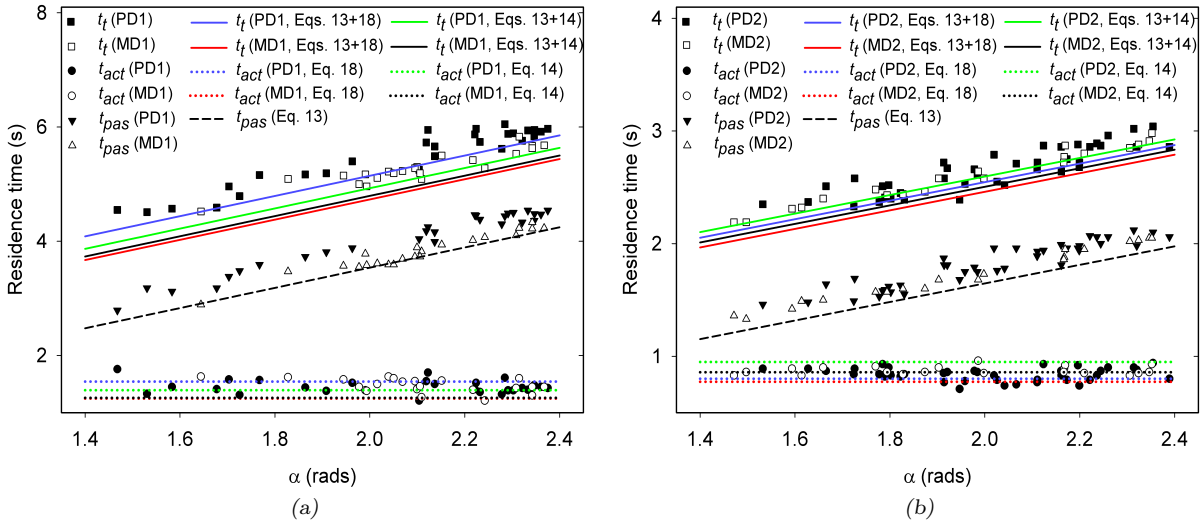


Figure 4.7: Variation of the residence time versus the angle of the streamlines for (a) cases MD1 and PD1, and (b) cases MD2 and PD2. The symbols correspond to experimental data.

tional to α .

The residence time in the active layer has been modeled in the literature by [Sturman et al. \(2008\)](#) :

$$t_{act} = \frac{\pi}{\sqrt{\omega\dot{\gamma}}}. \quad (4.14)$$

Here, another point of view is proposed and compared to Eq. 4.14. To do so, it is assumed that the glass beads travel along a straight line in this region (dashed line $j1 - i1$ in Fig. 4.1). This assumption neglects the curvature at the beginning and end of this streamline where the particles flow rapidly in the transverse direction. The consequence is that it increases the particle residence time, especially for small angles α where higher curvature is found. The streamwise velocity profile u along a streamline in the active layer obeys Eq. 4.5. The residence time in the active layer is $t_{act} = 2 \int_0^L \frac{dx}{u}$, which can be approximated by $2L/\bar{u}$, where $\bar{u} = \frac{1}{L} \int_0^L u dx = \frac{2}{3}u_{act}$. By combining these expressions, it follows that :

$$t_{act} = \frac{3L}{u_{max}(1 + \frac{y+H}{\delta_o})}. \quad (4.15)$$

The value of L for a given streamline can be obtained from the location of the boundary between the active and passive layers, by setting $x = L$ in Eq. 4.6 :

$$L = \sqrt{\frac{y + \delta_o + H}{a}}. \quad (4.16)$$

Substituting Eq. 4.16 and u_{max} from Eq. 4.4 into Eq. 4.15, and recalling that $a = \delta_o/L^{*2}$ yield :

$$t_{act} = \frac{3 \delta_o}{\omega L^*} \frac{1}{\sqrt{1 + \frac{y+H}{\delta_o}}}. \quad (4.17)$$

This equation shows that the residence time in the active layer should increase with an increase of the depth y . Introducing $\zeta = \frac{y+H}{\delta_o}$ and considering that in most of the reported

data (as can be seen from Fig. 4.7) $\zeta \in (-0.8, 0)$, $\frac{1}{\sqrt{1+\zeta}}$ can be approximated by its value at middle point $\zeta = -0.4$. Eq. 4.17 then becomes :

$$t_{act} = \frac{3.87 \delta_o}{\omega L^*}. \quad (4.18)$$

According to Eq. 4.18, the residence time in the active layer depends only on the operating conditions (ω) as well as the geometrical characteristics of the drum (L^*) and the thickness of the active layer δ_o .

To asses the validity of Eqs. 4.13, 4.14 and 4.18, the residence times of the glass beads in the active and passive layers versus the angle of the streamline are given in Fig. 4.7. It can be readily seen that there are no significant differences between the monodisperse and polydisperse cases. One may notice that the residence time in the passive layer varies linearly when the angle of the streamlines increases, whereas it is constant in the active layer. Consequently, the total residence time (t_t , the summation of the residence times in both layers) also varies linearly. Moreover, there is a good agreement between the experimental data and what is expected from the short dashed lines (solid body rotation according to Eq. 4.13) in the passive layer, the dotted lines (Eqs. 4.14 and 4.18) in the active layer and the solid lines (total residence time from the sum of Eqs. 4.13+4.14 or 4.13+4.18). Average values of the the residence time in the active layer from Eqs. 4.14 and 4.18 are compared to those deduced from RPT data in Table 4.4. Note that these experimental data were obtained by averaging the residence times of many randomly selected streamlines in the active layer. A good agreement can be noticed in all cases between the measured and predicted values.

4.4.5 Segregation

The difference in the size of the glass beads in the polydisperse cases (see Table 4.1) is large enough for radial segregation in the cylindrical drum to manifest itself in the first few drum rotations. In order to characterize the particle segregation, occupancy plots obtained from RPT data can be used. In Fig. 4.8, the red and blue colors correspond to the higher and

Table 4.4: Average residence time in the active layer. The range indicated for the experimental data corresponds to the standard deviation.

Case	ω [RPM]	\bar{t}_{act} [s] (Experiment)	t_{act} (Eq. 4.14) [s] (measured δ_o -Table 4.3)	t_{act} (Eq. 4.18) [s] (measured δ_o -Table 4.3)
MD1	5.4	1.47 ± 0.12	1.26	1.25
PD1	5.4	1.46 ± 0.12	1.39	1.54
MD2	11.6	0.87 ± 0.04	0.86	0.77
PD2	11.6	0.84 ± 0.06	0.95	0.80

lower probabilities of occurrence of the tracer at a given position, respectively. Note that the blends of glass beads were mixed initially. The small particles end up in the central core of the bed whereas the large particles concentrate mainly in the surrounding shell section. More precisely, 3-*mm* particles are present in the core, 4-*mm* particles are present everywhere in the granular bed but mainly in the inner layers, while large 5-*mm* and 6-*mm* particles surround the small particles.

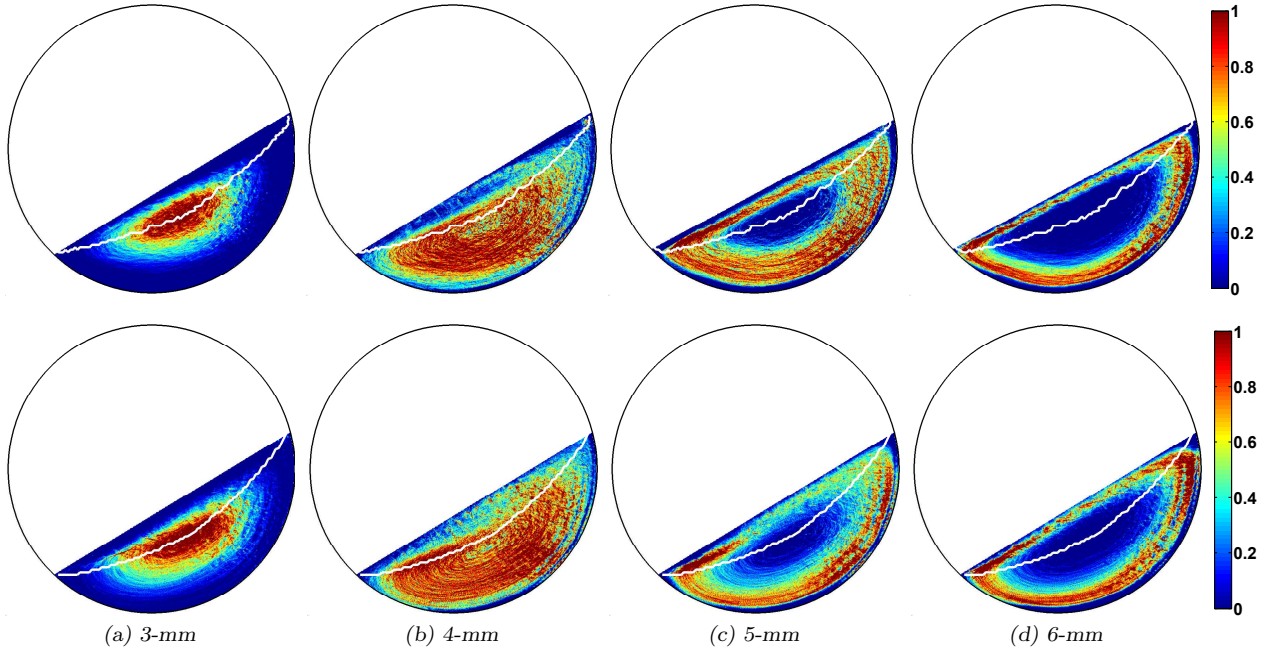


Figure 4.8: Occupancy plots for the different tracers in the polydisperse mixtures ; the upper and lower plots refer to cases PD1 and PD2, respectively. The white curve highlights the boundary between the passive and active layers on the basis of the turning point criterion.

To provide a more quantitative analysis, the occurrence probabilities of the different tracers along the middle line at $x = 0$ are presented in Fig. 4.9 for the PD1 (5.4RPM) and PD2 (11.6RPM) cases. First, it can be readily noticed that the impact of the drum rotational speed is not significant. More precisely, it can be observed that, for both cases, the small 3-*mm* particles are located in the core of the granular bed, while the large 5-*mm* and 6-*mm* particles surround these small particles. Moreover, the 4-*mm* particles can be found everywhere in the granular bed and it seems that they do not accumulate in the core region close to the material axis of rotation. This is contrary to the literature where it is always assumed that small particles are mainly present in the core (Rapaport, 2007). Thus, in an operation where one or more species need to be distributed across the radial direction of the drum, inert granules of different sizes could be added to the granular media to regulate the species concentrations along this direction.

As mentioned before, differences in the dynamic repose angle of the components of a mixture are believed to be the main reason for the occurrence of axial segregation and the formation of axial bands (Bridgwater et al., 1985; Hill and Kakalios, 1995). In our experiments, there were no measurable differences in the dynamic repose angle of the monodisperse and

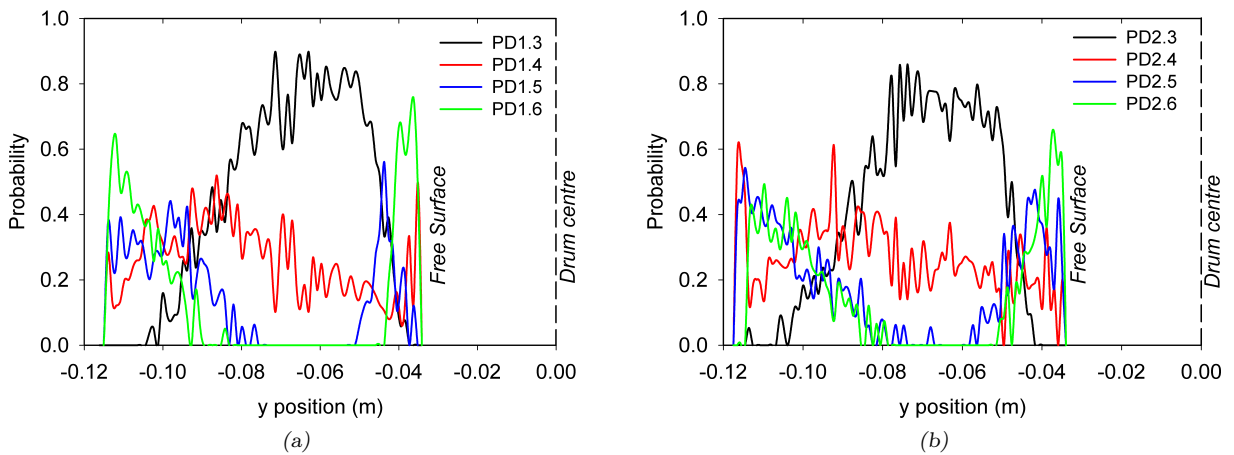


Figure 4.9: Probability of the occurrence of the different tracers along the middle line at $x = 0$; (a) case PD1 and (b) case PD2.

polydisperse mixtures ($\sim 27^\circ$), and the glass beads of different sizes did not form axial bands, even after around 2500 revolutions. Similar results for glass beads were reported by Zik et al. (1994).

4.4.6 Axial dispersion

To be efficient, mixing must take place in both the axial and radial directions of the cylindrical drum. The governing mechanisms are dispersion in the axial direction and a combination of convection and dispersion in the radial direction. Since dispersion is slower than convection, tumbling blenders always suffer from weak axial mixing (Lemieux et al., 2007). Therefore, the axial dispersion coefficient, D_{axial} , is a useful index to quantify the relative motion of the particles and thereby assess mixing efficiency in the axial direction.

Particles slowly drift along the drum axis of rotation so that, in our experiments, they could only travel the full blender length a few times during 2500 revolutions. In particular, this indicates that the axial dispersion of the glass beads inside the drum was indeed very slow. It has been shown that the distribution of particle axial displacements is similar to a normal distribution (Ingram et al., 2005). The axial displacement distribution for the 3-mm tracer, measured for each cycle, is given in Fig. 4.10 for case MD2. The dispersion coefficient in the axial direction can be approximated by means of Einstein's law (Einstein, 1905) :

$$D_{axial} = \frac{\sum_i^n (\Delta z_i - \overline{\Delta z})^2 / \Delta t_i}{2n}, \quad (4.19)$$

where Δz_i is the axial displacement of the tracer during the i th cycle ($i = 1, \dots, n$), Δt_i the time interval, and $\overline{\Delta z}$ the mean axial displacement, which should be 0 for a large number n of cycles.

D_{axial} corresponds to the variance of the measured displacements, and is in fact the sum of two variances that come from the tracer displacement and the measurement error. Large time intervals generally lead to a high variance due to large displacements, while the variance related to the measurement error remains constant. The latter can then be made negligible

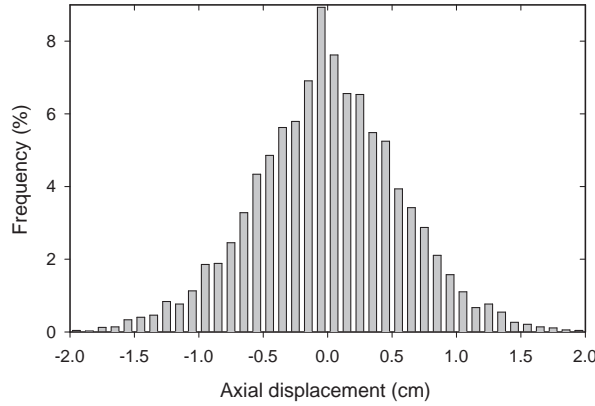


Figure 4.10: Typical axial displacement distribution for the 3-*mm* tracer in the monodisperse case MD2.

by increasing the time interval. In this study, the residence time of granules along streamlines was chosen as the time interval, which guarantees that the measurement error does not alter significantly the dispersion coefficients, as discussed by [Sherritt et al. \(2003\)](#).

D_{axial} is a function of the glass beads properties as well as the drum geometry and the operating conditions. Fig. 4.11 shows the variation of the axial dispersion coefficient along the line $x = 0$ in the transverse plane of the drum. To obtain these results, this transverse plane has been divided into thin annuli, and an axial dispersion coefficient has been calculated in each section. The figure shows that the axial dispersion coefficient is nearly constant in the inner layers and slightly increases near the drum wall. This trend is shown with solid and dashed lines for the low and high rotational speeds, respectively. These lines were obtained by averaging the experimental data points in each rotational speed. These results are reasonable since, in the layers close to the wall, the particles have more freedom to move axially because they eventually reach the free surface. Consequently greater values of the axial dispersion coefficient are expected for the large particles that are in the outer layers. Rather similar results have been obtained by [Ingram et al. \(2005\)](#) who showed an increase in axial dispersion with an increase of the particle size except for very large particles that ended up in the core of the bed. Values of D_{axial} for the different tracers are given in Table 4.5. First, these values

are comparable to those reported in the literature. Ding et al. (2002b) obtained an axial dispersion coefficient of $3 \times 10^{-6} m^2/s$ for 3-mm glass beads and a drum rotational speed of $9.6 RPM$, whereas Sherritt et al. (2003) reported values of the order of $10^{-5} m^2/s$ for rotational speeds of 5 to 25 RPM . Next, it can be noticed that D_{axial} is proportional to the drum rotational speed and that its value slightly increases with an increasing particle size.

Finally, Table 4.6 summarizes most of the findings of the current work in the case of monodisperse and polydisperse systems of glass beads.

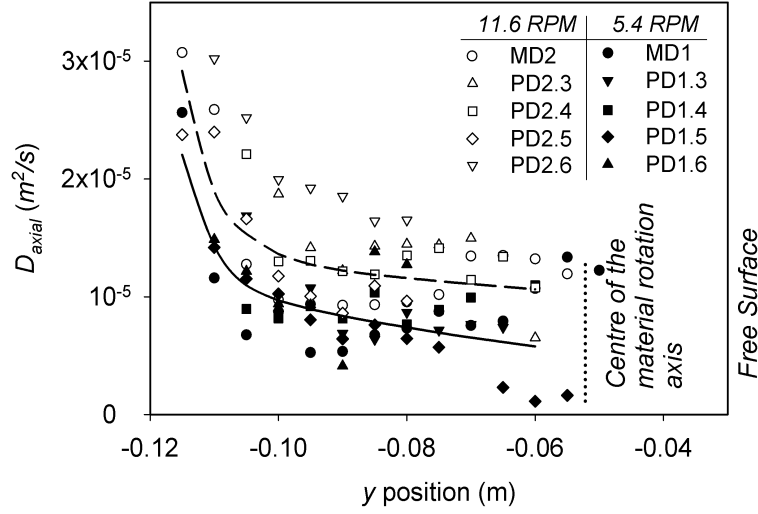


Figure 4.11: Variation of the axial dispersion coefficient along the line at $x = 0$ in the transverse plane of the drum.

Table 4.5: Axial dispersion coefficient for the different experiments.

Case	Tracer size	$D_{axial}(m^2/s)$	
		5.4RPM	11.6RPM
Monodisperse	3mm	8.3×10^{-6}	15×10^{-6}
	3mm	7.0×10^{-6}	16×10^{-6}
Polydisperse	4mm	9.2×10^{-6}	18×10^{-6}
	5mm	10.9×10^{-6}	19×10^{-6}
	6mm	12.2×10^{-6}	21×10^{-6}
Average value		9.5×10^{-6}	18×10^{-6}

Table 4.6: Summary of the similarities and differences between the flow behavior of monodisperse, binary and polydisperse systems of particles.

Issue	Polydisperse	Binary	Monodisperse
Segregation	Species distribute with respect to size in the transverse plane of the bed (see Figs. 4.8 and 4.9).	A core/shell configuration is formed (Wightman and Muzzio, 1998).	—
Dynamics of granules	Same velocity profiles in the streamwise and transverse directions (see Fig. 4.4).		
Active layer thickness	Thickness of the active layer is around 30-40% of the granular bed and it is thicker for the polydisperse case than for the monodisperse case (see Tables 4.2 and 4.3).		
Residence time	Residence times in passive and active layers can be obtained via $t_{pas} = \frac{1}{\omega}\alpha$ (Eq. 4.13) and $t_{act} = \frac{3.87}{\omega L^*} \frac{\delta_o}{\omega}$ (Eq. 4.18), respectively.		
Axial dispersion coefficient	The axial dispersion coefficients are small $O(10^{-5})$ for the monodisperse and polydisperse cases and are proportional to the drum rotational speed and particle size (see Fig. 4.11 and Table 4.5).		

4.5 Concluding remarks

In this work, the flow of monodisperse and polydisperse systems of glass beads were investigated inside a rotating cylindrical drum when operated in rolling mode. Radioactive particle tracking (RPT), a powerful tool for characterizing the granular flow of opaque systems, was used to track a single radioactive tracer. ^{24}Na was used as the radioactive isotope, thanks to the presence of ^{23}Na in the glass beads. This resulted in a tracer with physical properties (size and density) identical to those of the non-radioactive glass beads. No significant differences were observed for the flow behavior of the monodisperse and polydisperse mixtures considered in this work. Note that different behaviors might be observed for large particle size ratios (Ingram et al., 2005). The following findings were obtained :

- There are only small differences between the velocity profiles and the active layer thicknesses of the monodisperse and polydisperse cases. This was confirmed by both experimental data as well as predictive models developed within the scope of this work ;

- Small particles (3-*mm*) are present in the core section of the bed while large particles (5-*mm* and 6-*mm*) surround them. Particles with an average size (4-*mm*) are found in the whole volume of the drum. This is true for the two rotational speeds considered (5.4 and 11.6 *RPM*);
- Particles do not have a lot of freedom when flowing in the axial direction and the axial dispersion coefficient was found to be small in all cases. It was observed to increase slightly with an increase of radial position and to be proportional to the drum rotational speed;
- A model was developed to predict the residence time of granules in the active layer, and its validity was tested against RPT data. It was shown to predict correctly that the residence time is nearly constant in the active layer, whereas it varies linearly with an increase in the angle of the streamlines in the passive layer.

Acknowledgments

The authors would like to thank the Research and Development Center of Ratiopharm operations (Mirabel, Québec) and the Natural Sciences and Engineering Research Council of Canada for financial support. The authors are grateful to Jean St-Pierre and Cornelia Chilian from the Institute of Nuclear Engineering for the activation of tracers, and Majid Rasouli for helpful discussion regarding residence time.

4.6 References

- Alexander, A., Muzzio, F. J., and Shinbrot, T. (2004). Effects of scale and inertia on granular banding segregation. *Granular Matter*, 5(4) :171–175.
- Aranson, I. and Tsimring, L. (1999). Dynamics of axial separation in long rotating drums. *Physical Review Letters*, 82(23) :4643–4646.

- Beam, G. B., Wielopolski, L., Gardner, R. P., and Verghese, K. (1978). Monte carlo calculation of efficiencies of right-circular cylindrical nai detectors for arbitrarily located point sources. *Nuclear Instruments and Methods*, 154,(3) :501–508.
- Boateng, A. and Barr, P. (1997). Granular flow behaviour in the transverse plane of a partially filled rotating cylinder. *Journal of Engineering and Applied Science*, 330 :233–249.
- Boateng, A. A. (1998). Boundary layer modeling of granular flow in the transverse plane of a partially filled rotating cylinder. *International Journal of Multiphase Flow*, 24(3) :499–521.
- Bonamy, D., Daviaud, F., and Laurent, L. (2002). Experimental study of granular surface flows via a fast camera : A continuous description. *Physics of Fluids*, 14(5) :1666–1673.
- Bridgwater, J., Foo, W., and Stephens, D. J. (1985). Particle mixing and segregation in failure zones-theory and experiment. *Powder Technology*, 41(2) :147–158.
- Cantelaube, F. and Bideau, D. (1995). Radial segregation in a 2D drum : an experimental analysis. *Europhysics Letters*, 30(3) :133–138.
- Chen, P., Ottino, J. M., and Lueptow, R. M. (2010). Onset mechanism for granular axial band formation in rotating tumblers. *Physical Review Letters*, 104(18) :188002.
- Cheng, N.-S., Zhou, Q., Tan, S. K., and Zhao, K. (2011). Application of incomplete similarity theory for estimating maximum shear layer thickness of granular flows in rotating drums. *Chemical Engineering Science*, 66(12) :2872–2878.
- Choo, K., Baker, M., Molteno, T., and Morris, S. (1998). Dynamics of granular segregation patterns in a long drum mixer. *Physical Review E*, 58(5) :6115–6123.
- Ding, Y., Forster, R., Seville, J., and Parker, D. (2002a). Granular motion in rotating drums : bed turnover time and slumping-rolling transition. *Powder Technology*, 124(1-2) :18–27.
- Ding, Y., Forster, R., Seville, J., and Parker, D. (2002b). Segregation of granular flow in the transverse plane of a rolling mode rotating drum. *International Journal of Multiphase Flow*, 28(4) :635–663.

- Ding, Y., Seville, J., Forster, R., and Parker, D. (2001). Solids motion in rolling mode rotating drums operated at low to medium rotational speeds. *Chemical Engineering Science*, 56(5) :1769–1780.
- Doucet, J., Bertrand, F., and Chaouki, J. (2008). An extended radioactive particle tracking method for systems with irregular moving boundaries. *Powder Technology*, 181(2) :195–204.
- Einstein, A. (1905). Über die von der molekularkinetischen theorie der wärme geforderte bewegung von in ruhenden flüssigkeiten suspendierten teilchen (on the movement of small particles suspended in a stationary liquid demanded by the molecular-kinetic theory of heat). *Annalen der Physik*, 322(8) :549–560.
- Felix, G., Falk, V., and D’Ortona, U. (2002). Segregation of dry granular material in rotating drum : Experimental study of the flowing zone thickness. *Powder Technology*, 128(2-3) :314–319.
- Felix, G., Falk, V., and D’Ortona, U. (2007). Granular flows in a rotating drum : the scaling law between velocity and thickness of the flow. *European Physical Journal E*, 22(1) :25–31.
- Hawkesworth, M., Parker, D., Fowles, P., Crilly, J., Jefferies, N., and Jonkers, G. (1991). Nonmedical applications of a positron camera. *Nuclear Instruments & Methods in Physics Research. Section A, Accelerators, Spectrometers, Detectors and Associated Equipment*, A310(1-2) :423–434.
- Henein, H., Brimacombe, J., and Watkinson, A. (1983). Experimental study of transverse bed motion in rotary kilns. *Metallurgical Transactions B (Process Metallurgy)*, 14 B(2) :191–205.
- Hill, K. and Kakalios, J. (1995). Reversible axial segregation of rotating granular media. *Physical Review E*, 52(4) :4393–4400.
- Huang, A. and Kuo, H. (2012). A study of the three-dimensional particle size segregation structure in a rotating drum. *AIChE Journal*, 58(4) :1076–1083.

- Ingram, A., Seville, J., Parker, D., Fan, X., and Forster, R. (2005). Axial and radial dispersion in rolling mode rotating drums. *Powder Technology*, 158(1-3) :76–91.
- Jain, N., Ottino, J., and Lueptow, R. (2002). An experimental study of the flowing granular layer in a rotating tumbler. *Physics of Fluids*, 14(2) :572–582.
- Jain, N., Ottino, J., and Lueptow, R. (2004). Effect of interstitial fluid on a granular flowing layer. *Journal of Fluid Mechanics*, 508 :23–44.
- Jain, N., Ottino, J. M., and Lueptow, R. M. (2005). Regimes of segregation and mixing in combined size and density granular systems : An experimental study. *Granular Matter*, 7(2-3) :69–81.
- Kelbert, F. and Royere, C. (1991). Lateral mixing and heat transfer in a rolling bed. *International Chemical Engineering*, 31(3) :441–449.
- Khakhar, D., McCarthy, J., and Ottino, J. (1997). Radial segregation of granular mixtures in rotating cylinders. *Physics of Fluids*, 9(12) :3600–3614.
- Khakhar, D., Orpe, A. V., and Ottino, J. (2001). Surface granular flows : two related examples. *Advances in Complex Systems*, 64(4) :407–417.
- Larachi, F., Kennedy, G., and Chaouki, J. (1994). A gamma ray detection system for 3-D particle tracking in multiphase reactors. *Nuclear Instruments & Methods in Physics Research Section a-Accelerators Spectrometers Detectors and Associated Equipment*, A338(2-3) :568–576.
- Lemieux, M., Bertrand, F., Chaouki, J., and Gosselin, P. (2007). Comparative study of the mixing of free-flowing particles in a V-blender and a bin-blender. *Chemical Engineering Science*, 62(6) :1783–1802.
- Liu, X. Y. and Specht, E. (2010). Predicting the fraction of the mixing zone of a rolling bed in rotary kilns. *Chemical Engineering Science*, 65(10) :3059–3063.

- Liu, X. Y., Specht, E., Gonzalez, O., and Walzel, P. (2006). Analytical solution for the rolling-mode granular motion in rotary kilns. *Chemical Engineering and Processing*, 45(6) :515–521.
- Meier, S., Lueptow, R., and Ottino, J. (2007). A dynamical systems approach to mixing and segregation of granular materials in tumblers. *Advances in Physics*, 56(5-6) :757–827.
- Mellmann, J. (2001). The transverse motion of solids in rotating cylinders - forms of motion and transition behavior. *Powder Technology*, 118(3) :251–270.
- Mu, J. and Perlmutter, D. D. (1980). The mixing of granular solids in a rotary cylinder. *AIChE Journal*, 26(6) :928–934.
- Muzzio, F., Robinson, P., Wightman, C., and Dean, B. (1997). Sampling practices in powder blending. *International Journal of Pharmaceutics*, 26(2) :153–178.
- Muzzio, F. J., Goodridge, C. L., Alexander, A., Arratia, P., Yang, H., Sudah, O., and Mergen, G. (2003). Sampling and characterization of pharmaceutical powders and granular blends. *International Journal of Pharmaceutics*, 250(1) :51–64.
- Nakagawa, M., Altobelli, S., Caprihan, A., Fukushima, E., and Jeong, E.-K. (1993). Non-invasive measurements of granular flows by magnetic resonance imaging. *Experiments in Fluids*, 16(1) :54–60.
- Orpe, A. V. and Khakhar, D. V. (2001). Scaling relations for granular flow in quasi-two-dimensional rotating cylinders. *Physical Review E*, 64 :031302.
- Ottino, J. and Khakhar, D. (2002). Scaling of granular flow processes : From surface flows to design rules. *AIChE Journal*, 48(10) :2157 – 2166.
- Parker, D., Broadbent, C., Fowles, P., Hawkesworth, M., and Mcneil, P. (1993). Positron emission particle tracking - A technique for studying flow within engineering equipment. *Nuclear Instruments & Methods in Physics Research Section A*, 326(3) :592–607.
- Rapaport, D. (2007). Radial and axial segregation of granular matter in a rotating cylinder : a simulation study. *Physical Review E*, 75(3) :31301.

Sherritt, R., Chaouki, J., Mehrotra, A., and Behie, L. (2003). Axial dispersion in the three-dimensional mixing of particles in a rotating drum reactor. *Chemical Engineering Science*, 58(2) :401–415.

So much more to know (2005). *Science*, 309(5731) :78–102.

Sturman, R., Meier, S., Ottino, J., and Wiggins, S. (2008). Linked twist map formalism in two and three dimensions applied to mixing in tumbled granular flows. *Journal of Fluid Mechanics*, 602 :129–174.

Taberlet, N., Newey, M., Richard, P., and Losert, W. (2006). On axial segregation in a tumbler : an experimental and numerical study. *Journal of Statistical Mechanics : Theory and Experiment*, 2006(07) :P07013.

Thomas, N. (2000). Reverse and intermediate segregation of large beads in dry granular media. *Physical Review E*, 62(1) :961–974.

Van Puyvelde, D., Young, B., Wilson, M., and Schmidt, S. (2000). Modelling transverse segregation of particulate solids in a rolling drum. *Chemical Engineering Research and Design*, 78(4) :643–650.

Weir, G., Krouse, D., and McGavin, P. (2005). The maximum thickness of upper shear layers of granular materials in rotating cylinders. *Chemical Engineering Science*, 60(7) :2027–2035.

Wightman, C. and Muzzio, F. J. (1998). Mixing of granular material in a drum mixer undergoing rotational and rocking motions II. segregating particles. *Powder Technology*, 98(2) :125–134.

Woodle, G. R. and Munro, J. M. (1993). Particle motion and mixing in a rotary kiln. *Powder Technology*, 76(3) :241–245.

Zik, O., Levine, D., Lipson, S., Shtrikman, S., and Stavans, J. (1994). Rotationally induced segregation of granular materials. *Physical Review Letters*, 73(5) :644–647.

CHAPTER 5

Comparison of DEM Results and Lagrangian Experimental Data for the Mixing and Segregation of Granules in a Rotating Drum

Ebrahim Alizadeh, François Bertrand, Jamal Chaouki

Department of Chemical Engineering, École Polytechnique de Montréal, C.P. 6079 succ.

Centre-Ville, Montréal, Québec, Canada, H3C 3A7

(Submitted to *AIChE Journal*.)

Presentation of the article : DEM results for granular flow inside a rotating drum will be presented and their validity will be checked through the experimental data from the previous chapter. A sensitivity analysis of DEM-based model with respect to its parameters will be provided.

Abstract : The discrete element method (DEM) has proven efficient to investigate solids mixing. So far, its accuracy has been tested against Eulerian data because of the lack of Lagrangian experimental results. This work compares DEM results to experimental data obtained using the Lagrangian non-intrusive radioactive particle tracking technique. The results concern the size segregation of polydisperse granules in a rotating drum operated in rolling mode. Given that the DEM is sensitive to simulation parameters, granule properties were measured experimentally or extracted from the literature. Several granular behaviors are investigated for the first time both numerically and experimentally. A sensitivity analysis of the DEM model is then presented, with an emphasis on the Young's modulus and friction coefficients. To enable a fair comparison between the experimental data and numerical results, dimensionless motion equations are next derived and analyzed. Finally, effective dimensionless numbers are introduced to explain how DEM parameters should be chosen.

Keyword : Discrete element method, Radioactive particle tracking, Lagrangian method, Solids mixing, Size segregation, Rotating drum, Physical properties

5.1 Introduction

Granular materials are widely used in processes found for instance in the mineral, ceramic, cement, metallurgical, food and pharmaceutical industries. A common device for handling granular materials is the rotating drum utilized for various purposes. Regardless of the geometrical simplicity of such drums, the flow of material within these devices is quite complex. Depending on the range of Froude numbers ($Fr = \frac{\omega^2 R_D}{g}$), the fill levels and the frictions coefficients between the particles and the drum, different types of transverse bed motions can be observed (Mellmann, 2001), where ω , R_D and g stand for the rotational speed, the drum radius and the gravitational acceleration. The most critical regime for the purpose of mixing is rolling (Henein et al., 1983). This type of motion is characterized by a uniform flow of particles on a free flowing layer (active layer) located at the top of the bed, while the particles in the large underneath layer (passive layer) are transported upwards by the solid body motion of the drum wall. It is well known that in rolling mode, the bed has a flat surface inclined at a dynamic repose angle (Alizadeh et al., 2013b; Dury et al., 1998; Ingram et al., 2005).

Understanding and controlling the granular flow and mixing behavior in a rotating drum (as well as in other tumbling blenders) is of paramount importance for many industries. Inadequate mixing may result in rejection of the finished product due to poor quality. Unfortunately, there is insufficient knowledge concerning the mixing of granular materials. Therefore, further understanding of granular flow is required to better grasp the mixing mechanisms as well as to design more efficient installations. In the past 25 years, excessive attempts have been made to comprehend the flow, handling, and characterization of granular materials. In spite of such efforts, the mixing of granular solids is still not well understood as fluid mixing, due to the complex dynamic behavior involved.

To determine mixing time or measure blend uniformity, several measurement techniques have been proposed. Light induced fluorescence (LIF), near-infrared reflectance spectroscopy (NIR) and effusivity are some of the techniques that are currently available (Leonard et al.,

2008). Characterizing granular mixing is also possible via physical sampling (*e.g.* thief sampling), which however interferes with the matter and affects the measure itself (Muzzio et al., 2003). To overcome the limitations of physical sampling and to measure granular flow dynamics, several non-intrusive methods have been developed. Unfortunately, the granular media is opaque, thereby limiting most of these measurement techniques (including optical and visual methods) inside the granular assembly. Moreover, the available optical experimental methods are limited to visualizing the granular surface. Among these methods, particle image velocimetry (PIV) (Jain et al., 2002) and particle tracking velocimetry (PTV) (Lueptow et al., 2000) are primarily applied. Magnetic resonance imaging (MRI) is another technique, capable of visualizing the bulk of the granular bed (Nakagawa et al., 1993). However, difficulty in obtaining MRI signals from solid samples restricts this method, thereby rendering it generally inapplicable to a wide range of granules (Yamane et al., 1998). MRI cannot be used to examine the flow of granules in any type or size of geometry since the apparatus must fit within the MRI machine. Its high cost is another issue.

There are two radioactive-based methods, which follow a single labeled tracer in the granular bed. One is known as positron emission particle tracking (PEPT) and uses positron annihilation. This method was developed by Hawkesworth et al. (1991) and applied to the rotating drum a few years later (Parker et al., 1997). The other method, the results of which are used in this work, is known as radioactive particle tracking (RPT) and is based on the attenuation of gamma rays in the material. This technique was originally developed by Lin et al. (1985) and applied by Larachi et al. (1994). It has been used for the rotating drum (Alizadeh et al., 2013b; Sheritt et al., 2003) and extended for geometries with irregular moving boundaries, such as the V-blender (Doucet et al., 2008b). The RPT in comparison with the PEPT is less costly, compact, and can be used for larger vessels, whereas PEPT is more efficient for investigating systems with complicated free surfaces.

Apart from efforts to develop non-intrusive techniques, numerical methods have progressed, and both continuum models and particle dynamics simulations have been developed.

The first approach is Eulerian, which considers powders as a fluid ([Khakhar et al., 2001](#)), and the second approach is Lagrangian, which treats particles in the discrete domain. In the latter approach, the discrete element method (DEM), originally proposed by [Cundall and Strack \(1979\)](#), has been applied to investigate granular flow in many applications. This simulation technique is a soft particle method and has proven efficient in providing insight into phenomena occurring in granular beds as well as details about the flow and mixing of granules.

Unresolved questions about granular flow and the ability of DEM to predict these types of flow have generated considerable interest, resulting in extensive research works on the subject in recent years. However, few comparisons with experimental data have been performed to examine the validity of the DEM ([Lemieux et al., 2007](#); [Sudah et al., 2005](#); [Taberlet et al., 2006](#); [Yamane et al., 1998](#)). Such studies in the literature are mostly qualitative via visual comparison of flow patterns. For instance, [Moakher et al. \(2000\)](#) considered double-cone and V-blenders, and [Iwasaki et al. \(2001\)](#) studied a high-speed elliptical rotor-type powder mixer, both groups demonstrating that calculated flow patterns agreed with experimental observations. While there is a limited number of techniques capable of providing Lagrangian data and mapping the velocity field inside opaque granular systems, studies that quantitatively validate the DEM at the particle scale are limited. Such studies can be found in [Laurent and Cleary \(2012\)](#), [Kuo et al. \(2002\)](#) and [Stewart et al. \(2001\)](#). Despite the importance of previous investigations, comparisons of Lagrangian experimental and DEM-based model continue to be inadequately thorough. Indeed, in many studies, real values of particle properties have not been used for the DEM simulations and neither have they been experimentally measured. While these parameters demonstrate a high effect on the granular flow, authors have often adjusted them in order to obtain results that agree well with experimental observations.

The challenge of this study is to provide a detailed and thorough comparison between Lagrangian experimental data of the RPT and numerical results of the DEM. To do so, the granular properties were measured experimentally or extracted from the literature. This work

is restricted to the simple geometry of a rotating drum and, as a consequence, does not look into geometrical effects on the flow behavior. The granules are glass beads and the drum was operated in rolling mode. Moreover, contrary to the literature where a binary mixture has generally been the subject of study (Cantelaube and Bideau, 1995; Dury and Ristow, 1997), in this work a polydisperse mixture with a precise particle size distribution is considered (four different size particles). First, details of the phenomena occurring inside the rotating drum are investigated including radial and axial segregation, velocity profiles, residence times of granules and axial dispersion. Next, to evidence the sensitivity of DEM results to the particle mechanical and physical properties, thereby pointing out the importance of using real values for these properties, dimensionless motion equations of particles in normal and tangential directions are derived and analyzed. Finally, effective dimensionless numbers are introduced to explain how the DEM parameters should be chosen.

5.2 Methodology

5.2.1 RPT experiments

The RPT technique follows a radioactively marked particle having similar physical and mechanical properties as the inert particles in the bed, to provide a 3D position of this tracer with respect to time. The tracers were activated in the Slowpoke nuclear reactor of École Polytechnique de Montréal, and the activity level was initially approximately 60 μci thanks to presence of ^{24}Na . Eight $3'' \times 3''$ NaI scintillation detectors were installed around the drum made of Plexiglas with a 24cm internal diameter and 36cm length. The drum was filled up to 35vol% with soda lime glass beads and its rotational speed was 11.6RPM.

Experiments and blend characteristics are shown in Table 5.1. Two sets of RPT experiments were performed. In the first one that comes from our previous work (Alizadeh et al., 2013b), each case lasted 210 minutes. Due to the occurrence of segregation in these experiments, the ergodic hypothesis did not hold and the flow of one single tracer could not be used to represent the trajectories of many particles (Ruelle, 1976). As a result, segregation

was only assessed in a global manner by means of occupancy plots. In the current work, the goal was to look into segregation more deeply by resorting to mixing indices were developed in our group (Doucet et al., 2008c), as will be further discussed later. Therefore, a second set of experiments was carried out, where each case lasted 2 minutes and was repeated 50 times with a randomly chosen initial position for the corresponding tracer. Further details of the experimental procedure can be found in Alizadeh et al. (2013b).

5.2.2 DEM simulation

A DEM simulation tracks the position of the particles of a granular system by solving Newton's equation of motion on each of it. In this study, the total acting force on each particle includes gravity as well as a contact force term that accounts for the particle/particle and particle/wall interactions. Drag and buoyant forces can be neglected because of the low density of the fluid phase (air). Due to the rather large particle size (in the order of millimeters), colloidal forces can be also neglected. A model is required to estimate the contact force term. In this work, the contact force acting on particle i when it is colliding with another particle j is decomposed in normal (head-on) and tangential (shear) components, and the following non-linear viscoelastic model is used :

Table 5.1: RPT experiments and blend characteristics.

Case	Type	Rotational speed [RPM]	Tracer size [mm]	Experiment duration [min]	
				1 st set (Alizadeh et al., 2013b)	2 nd set (New data)
A	Polydisperse	11.6	3	210	2 ($\times 50$)
B	$\left(3mm(15vol\%), \right.$ $\left. 4mm(35vol\%), \right.$ $\left. 5mm(35vol\%), \right.$ $\left. 6mm(15vol\%) \right)$	11.6	4	210	2 ($\times 50$)
C		11.6	5	210	2 ($\times 50$)
D		11.6	6	210	2 ($\times 50$)

$$\begin{aligned}
F^n &= F_{el}^n + F_{dis}^n \\
&= k_n \xi_n^\alpha + C_n \xi_n^\beta \dot{\xi}_n,
\end{aligned} \tag{5.1}$$

$$\begin{aligned}
F^t &= F_{el}^t + F_{dis}^t \\
&= k_t f_1(\xi_t) + C_t f_2(\xi_t) \dot{\xi}_t.
\end{aligned} \tag{5.2}$$

The first and second terms in this model correspond to repulsion and dissipation forces, respectively. ξ_n and ξ_t are the normal and tangential components of the overlap between contacting particles i and j , k_n and k_t stiffness coefficients, C_n and C_t damping coefficients, and α and β non-linear constants that depend on the model. A review of the normal and tangential contact force models can be found in [Kruggel-Emden et al. \(2007, 2008\)](#). In the current study, the contact force model is similar to those of [Zhou et al. \(2002\)](#) and [Baxter et al. \(1997\)](#). In particular, $\alpha = \frac{3}{2}$ and $\beta = \frac{1}{4}$ are set to evaluate the normal elastic force with the Hertz theory and the normal dissipative term with a model proposed by [Tsuji et al. \(1992\)](#). The stiffness (k_n and k_t) and damping coefficients ($C_n = -c_n \sqrt{6m^* E^* \sqrt{R^*}}$ and $C_t = -c_t \sqrt{\frac{6\mu_s m^* |F_{el}^n|}{\xi_{t,m}}}$) are functions of the Young's modulus E , Poisson's ratio ν , damping constants (c_n and c_t) as well as static and dynamic friction coefficients (μ_s and μ) :

$$F_{el}^n = -\frac{4}{3} E^* \sqrt{R^*} \xi_n^{\frac{3}{2}}, \tag{5.3}$$

$$F_{dis}^n = -c_n (6m^* E^* \sqrt{R^*})^{\frac{1}{2}} \xi_n^{\frac{1}{4}} \dot{\xi}_n, \tag{5.4}$$

$$F_{el}^t = -\mu_s |F_{el}^n| f_1(\xi_t), \tag{5.5}$$

$$F_{dis}^t = -c_t \left(6\mu_s m^* |F_{el}^n| \frac{f_2(\xi_t)}{\xi_{t,m}} \right)^{1/2} \dot{\xi}_t, \tag{5.6}$$

where R^* is the reduced radius ($\frac{1}{R^*} = \frac{1}{R_i} + \frac{1}{R_j}$), E^* is the effective Young's modulus ($\frac{1}{E^*} = \frac{1-\nu_i^2}{E_i} + \frac{1-\nu_j^2}{E_j}$), m^* is the mean mass of particles i and j ($\frac{1}{m^*} = \frac{1}{m_i} + \frac{1}{m_j}$), and $\xi_{t,m} = \mu \frac{(2-\nu)}{2(1-\nu)} \xi_n$ is the maximum tangential deformation. $f_1(\xi_t)$ and $f_2(\xi_t)$ in Eq. 5.2 are defined as $f_1(\xi_t) = 1 - \left(1 - \frac{\min(\xi_t, \xi_{t,m})}{\xi_{t,m}}\right)^{3/2}$ and $f_2(\xi_t) = \sqrt{1 - |\xi_t|/\xi_{t,m}}$. The tangential force is bounded by $(\mu|F_{el}^n|)$, following the Coulomb law of friction.

Choosing a proper time step for a DEM simulation is generally a trade-off between the CPU time, the numerical error and the stability of the integration scheme. The time step should be smaller than the characteristic time, τ_c , which corresponds to a typical contact time between two colliding particles (Li et al., 2005) :

$$\tau_c = \frac{\pi \bar{R}}{\varepsilon} \sqrt{\frac{\rho}{G}}, \quad (5.7)$$

where ρ is the particle density, \bar{R} is the average particle radius, $G = \frac{E}{2(1+\nu)}$ is the particle shear modulus and ε can be approximated from :

$$\varepsilon = 0.8766 + 0.163 \nu. \quad (5.8)$$

In systems with smaller characteristic times (small particles, high stiffness or high velocities) a DEM simulation can maintain its stability if a small enough time step is used. In the current study, this time step corresponds to $1.2\mu s$, which explains why corresponding DEM simulations are CPU-intensive. The detailed particle information (position and velocity) was stored at $0.033s$ intervals. To reduce the CPU time, the computational domain was decomposed into subdomains and the code was run in parallel through the MPI communication library using 32 cores of parallel clusters of Compute Canada.

For the polydisperse system of this work, the simulation comprised 83,000 particles, the size of which complied with the distributions used for the RPT experiments (see Table 5.1). Each simulation started with an initially homogenous mixed state and the total simulated time was $120s$. The total computation time of each simulation was 35 days.

5.3 Results and discussion

This section discusses the DEM parameters and how they were measured. Next, the DEM simulation results are compared to the experimental RPT data. To this end, results concerning the velocity profiles, the residence times of granules, the segregation, and the axial dispersion of granules are analyzed. Finally, a sensitivity analysis of the DEM is performed to demonstrate the effects of simulation parameters on the results. Note that the results of the first set of RPT experiments are applied unless otherwise mentioned.

5.3.1 DEM parameters

Here, the focus is on the properties of granules used for the DEM simulations. The measured properties of the soda lime glass beads in the case of particle/particle and particle/wall impacts are presented in the second column of Table 5.2. Some properties were measured experimentally, while others were extracted from the literature. The third column of the table illustrates the parameters used for a DEM simulation to obtain results that best agree with the RPT experimental data. As can be seen, real values of the glass beads properties were applied except for the Young's modulus and the friction coefficients. Explanations are given below as more details are given on the properties of the glass beads and how they were measured.

Physical and mechanical properties The particles used in this work are commercially available soda-lime glass beads from Fisher Scientific with a density of $2.5g/cm^3$, a Young's modulus of $6.8 \times 10^{10} Pa$, and Poisson's ratio of 0.24 (Bolz and Tuve, 1970). Such a high value of the Young's modulus indicates that the glass beads are very hard material. A collision between two such granules has a short contact duration time (see Eq. 5.7) and, consequently, DEM simulations involving this type of solid particles require small time steps and large computational times. To overcome this limitation, the Young's modulus of such granules or its equivalent (stiffness coefficient in Eq. 5.1) is generally reduced to increase the duration of a collision and allow for a bigger time step (Kruggel-Emden et al., 2007). This is indeed

Table 5.2: DEM-based model parameters (measured and applied). The particle/wall impact properties were measured with the techniques mentioned and the particle/particle impact properties were extracted from the literature.

Properties	Measured	DEM simulation	Measurement technique or reference
Particle/particle	Density $\rho[g/cm^3]$	2.5	Bolz and Tuve (1970)
	Young's modulus $E[MPa]$	68900	Bolz and Tuve (1970)
	Poisson's ratio ν	0.24	Bolz and Tuve (1970)
	Normal damping constant c_n	0.0075	Foerster et al. (1994)
	Tangential damping constant c_t	— — —	Same as particle/wall
	Dynamic friction coefficient μ	0.092 \pm 0.006	Foerster et al. (1994)
	Static friction coefficient μ_s	0.16 — 0.29	Amstock (1997)
Particle/wall	Normal damping constant $c_{n,w}$	0.06 — 0.075	High speed camera
	Tangential damping constant $c_{t,w}$	0.02	High speed camera
	Dynamic friction coefficient μ_w	0.083 \pm 0.012 (fresh glass)	High speed camera
		0.135 \pm 0.009 (scratched glass)	+ force balance
	Static friction coefficient $\mu_{w,s}$	0.179 \pm 0.016 (fresh glass)	Inclined plate
		0.208 \pm 0.026 (scratched glass)	+ force balance
Rolling friction coefficient		2.5 $\times 10^{-5}$	Zhou et al. (1999)

common in the literature, and the first column of Table 5.3 indicates the typical values of the Young's modulus that have been applied in the cited investigations. Note that some recent investigations have considered real values of the Young's modulus (González-Montellano et al., 2011a,b; Guo et al., 2012; Hartl and Ooi, 2008; Persson and Frenning, 2012; Zobel et al., 2012). However, these studies have pertained to very soft material (*e.g.* microcrystalline cellulose or agricultural seeds) or very small numbers of particles, sometimes in two-dimensional systems. Therefore, in this study, the Young's modulus is set at 200MPa , which is relatively high in comparison with the values used in the literature (Table 5.3). This point will be further discussed in Section 5.3.6 where a sensitivity analysis of the DEM results with respect to the granule physical properties is presented.

Coefficients of restitution Given that particles collide with the blender wall and other particles, characterizing particle/particle and particle/wall impacts is essential. The velocity of the particles after each contact can be found via the coefficient of restitution (CoR), which is the particle velocity ratio after and before a collision in both normal and tangential directions.

To obtain the normal CoR of glass beads against a solid wall, their impact during free fall under gravity was considered. The impact was perpendicular and against a horizontal Plexiglas plate (same material as that used for the drum). Before the impact, the particle was held at an appropriate height by a vacuum nozzle. The particle was then released, without any spin or initial velocity. A high speed camera was used to record the details of the impact at a rate of 200 frames per second. The initial height of the particles was varied ($0.10-0.23\text{m}$) in order to cover a wide range of impacting velocities ($1.2-2.1\text{m/s}$). The impact velocity was calculated using the conservation of mechanical energy. More details about the experimental procedure can be found in Alizadeh et al. (2013a). The measured normal CoR was 0.82 ± 0.02 for this velocity range. Next, particle/particle normal CoR values were obtained directly from the literature : 0.97 ± 0.01 for a velocity range of $0.64-1.2\text{m/s}$ (Foerster et al., 1994). Damping constants $c_n = 0.0075$ and $c_{n,w} = 0.065$ were then backed out from DEM simulations involving

Table 5.3: Values of the Young's modulus (E) and friction coefficient used in DEM simulations from the literature that have led to acceptable results. When E is not given, the stiffness constant (k_n in Eq. 5.1) has been reported directly in the corresponding paper.

E [MPa]	Friction coefficient	Real particles and their properties (E in [GPa])	Reference
4.87	0.5	Glass beads ($E = 68.9, \mu = 0.092$)	Bouffard et al. (2013)
0.3	0.3, 0.6	Pure numerical simulation	Balevicius et al. (2008)
2	0.375 – 0.5	Avicel PH101 ($E = 7.4 - 10.3^1, \mu = 0.15 - 0.4^2$)	Lemieux et al. (2007, 2008)
– – –	0.3, 0.5	Glass beads ($E = 68.9, \mu = 0.092$) and steel beads ($E = 193, \mu = 0.23^3$)	Taberlet et al. (2004, 2006)
10-200	0.3, 0.5	Glass beads ($E = 68.9, \mu = 0.092$)	Yang et al. (2006, 2003)
– – –	0.5	Wheat grains ($E = 0.3 - 20^4, \mu = 0.35 - 0.6^5$) and green peas	Schutyser et al. (2003)
1-2.16	$\mu = 0.4, \mu_w = 0.7$	Glass beads ($E = 68.9, \mu = 0.092$)	Zhou et al. (1999, 2002)
2.16	0.3, 0.5	Glass beads ($E = 68.9, \mu = 0.092$)	Stewart et al. (2001)
– – –	0.3	Polypropylene ($E = 1.34, \mu = 0.1 - 0.3$)	Kaneko et al. (2000)
– – –	$\mu = 0.2, \mu_w = 0.4$	Vulcanite	Dury et al. (1998)
¹ Rowe and Roberts (1995)		⁴ Khodabakhshian and Emadi (2011)	
² Robinson (2009)		⁵ Sharan and Lee (1970)	
³ Li (2004)			

one single contact in the case of particle/particle and particle/wall collisions, respectively.

The same technique as for the normal CoR was applied to measure the tangential CoR on a plate. The initial height was fixed at $\sim 5\text{cm}$, leading to an impact velocity of $\sim 1\text{m/s}$. The impact angle was varied from $5^\circ - 55^\circ$ by adjusting the position of the plate. It was observed that the tangential CoR increases when the impact angle increases, which is in agreement with data reported in the literature (Kharaz et al., 2001). DEM simulations revealed that $c_{t,w} = 0.02$ fits best these experimental data. Moreover, it was found that damping constant c_t has no significant impact on the dynamics of granules, and only minor effects on the mixing behavior inside the drum. Therefore, no experiment was performed to measure its value for particle/particle impact and it was chosen to be the same as $c_{t,w}$.

Friction coefficients To measure the particle/wall static friction coefficient, three particles were glued onto a plate and then put in contact with a fresh Plexiglas sheet. This Plexiglas sheet was gradually inclined until the particles started to slide (Mueth et al., 1998). By means of a force balance, the static friction coefficient was calculated to be the tangent of the angle λ at which these particles started to slide ($\mu_{w,s} = \tan(\lambda)$). To obtain the dynamic friction coefficient μ_w , glued particles were allowed to slide on the inclined Plexiglas sheet from a zero initial velocity. The distance and time duration during an experiment were recorded by a high speed camera. Newton's second law of motion then yielded a value for this coefficient. The values of the dynamic and static friction coefficients of soda-lime glass beads on a fresh Plexiglas sheet obtained with this technique are 0.083 ± 0.012 and 0.179 ± 0.016 , respectively. The drum wall used for the experiments is made of Plexiglass but is not as smooth as a fresh Plexiglass sheet. Therefore, dynamic and static friction coefficients of soda-lime glass beads on a scratched Plexiglas were also measured using the same technique. The values obtained are 0.135 ± 0.009 and 0.208 ± 0.026 , respectively. The dynamic and static friction coefficients of particle/particle collision were obtained from the literature, 0.092 ± 0.006 and $0.16\text{-}0.29$, respectively (Amstock, 1997; Foerster et al., 1994). Note that it is common in the literature to use identical values of the dynamic and static friction coefficients, for both

particle/particle and particle/wall impacts, which in most cases are above 0.3 (see the second column of Table 5.3). In this study, different values of friction coefficients were chosen for the DEM simulations : $\mu = 0.06$, $\mu_s = 0.16$, $\mu_w = 0.35$ and $\mu_{w,s} = 0.45$. Why it was decided to use such values, which in the case of the particle/wall friction coefficients are different from the ones that were measured, will be justified in Section 5.3.6.

5.3.2 Velocity profiles and active layer thickness

The investigation of the particle dynamics inside the drum leads to a better understanding of mixing and segregation mechanisms, and ultimately helps design more efficient unit operations. Both the RPT method and DEM-based model were used to obtain particle velocity profiles. In the DEM simulations, the particle velocities were stored at each time interval (0.033s), whereas in RPT, they were derived from the tracer displacement. Figs. 5.1a and 5.1b show the velocity profiles in the transverse plane of the drum, respectively obtained by DEM and RPT, as well as their subtraction in Fig. 5.1c. As can be seen, there is good agreement between these DEM and RPT results with some differences near the free surface. Variations in streamwise velocity u (x -direction) along a line perpendicular to the bed surface at $x = 0$ is shown in Fig. 5.2. The x and y axes are shown in Fig. 5.1. A linear fit describes the flow of particles in the active layer (solid line) while a straight line from the drum center (dashed line) goes through the data points in the passive layer, complying with the solid body rotation, $u = -\omega y$, expected therein. Similar results (not presented) were obtained for other x -positions. Here again, a good agreement between the RPT data and the DEM results was observed.

The depth at which the particles stop moving as a solid body and start free flowing is the boundary between the active and passive layers (δ in Fig. 5.2). According to the RPT and DEM results, the maximum depth of the active layer ($\delta_o = \delta|_{x=0}$) was obtained at 4.2cm, which is 48% into the material bed. Many studies dealing with the active layer thickness exist (Cheng et al., 2011; Ding et al., 2001; Liu et al., 2006; Weir et al., 2005), although the

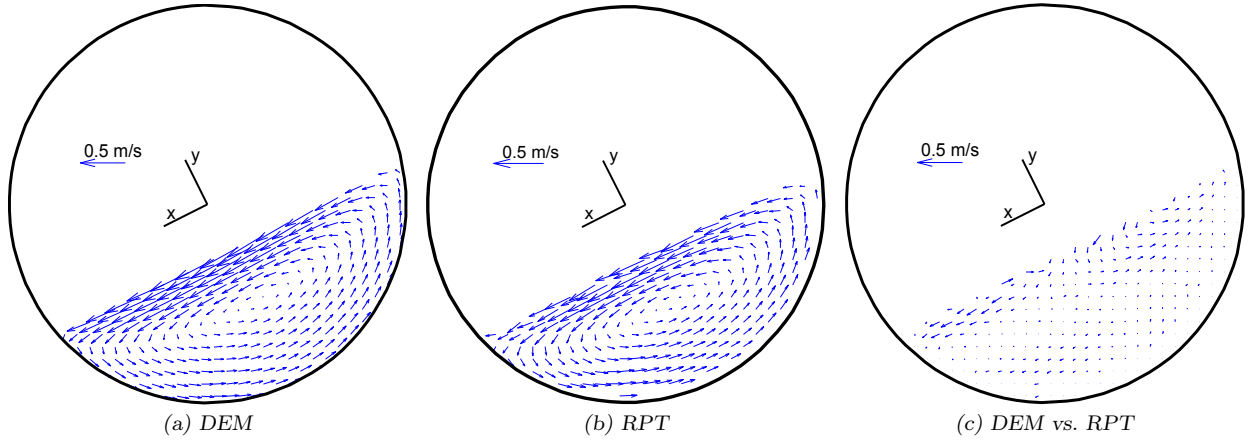


Figure 5.1: Typical velocity vectors obtained by (a) the DEM simulations and (b) RPT experiments. (c) Differences in the velocity vectors displayed in (a) and (b).

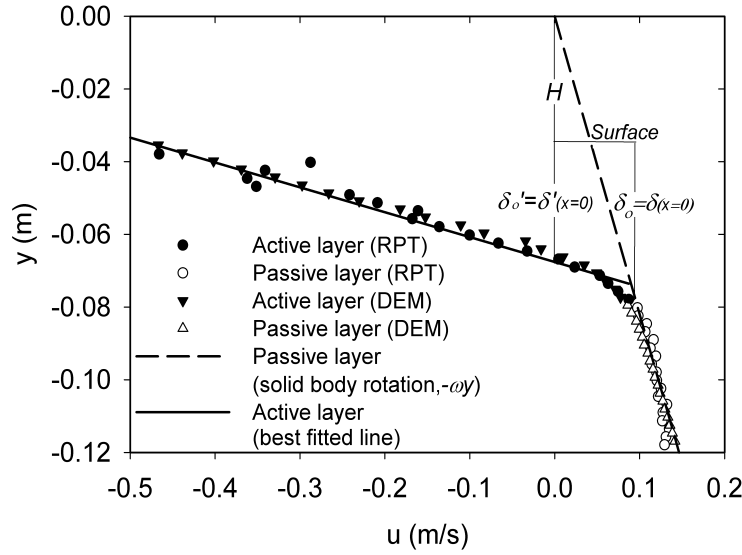


Figure 5.2: Streamwise velocity profile at $x = 0$ as seen from the drum end wall. The vertical axis represents the distance from the center of the drum, and the horizontal axis represents the streamwise velocity. H is the distance from the center of the drum to the free surface of material, δ_o is the distance from the free surface to the depth at which the solid body rotation of the bed of particles stops, and δ'_o is the distance from the free surface to the depth at which these particles change direction along the x axis.

definition of the thickness varies. It can also be defined as the point where the particles change direction ($u = 0$) along the x axis, as defined by δ'_o in Fig. 5.2. For both our experimental and simulation results, δ'_o ($= \delta'_{|x=0}$) was measured at 2.9cm , which is 33% into the material

bed.

The particle velocity profile at the free surface is plotted as a function of the normalized x position in Fig. 5.3a. The profiles have been normalized with respect to the velocity at mid-chord position ($u_{max} = u|_{(x=0,y=-H)}$). The solid line is a parabolic functions, $u/u_{max} = 1 - (x/L)^2$, where L is the half-length of the free surface. Similar results were previously shown by Ding et al. (2002) and Alizadeh et al. (2013b).

Fig. 5.3b shows the variation in surface velocity across the axial direction of the drum, as obtained by the DEM and the RPT. In both cases, the velocity vectors near the end walls ($|z| = +0.18m$) are different from those in the middle of the drum ($z = 0m$), with a small axial component. This has also been reported in the literature (Maneval et al., 2005) and can be attributed to the end-wall friction, which projects the particles above the free surface and away from the end-wall in the axial direction. The axial flow of the particles downstream towards the wall may then be explained by the conservation of mass.

End-wall friction also affects the dynamic repose angle of the granules, which is higher in regions near the end walls (34°) than in the middle of the cylinder (27°). The former was

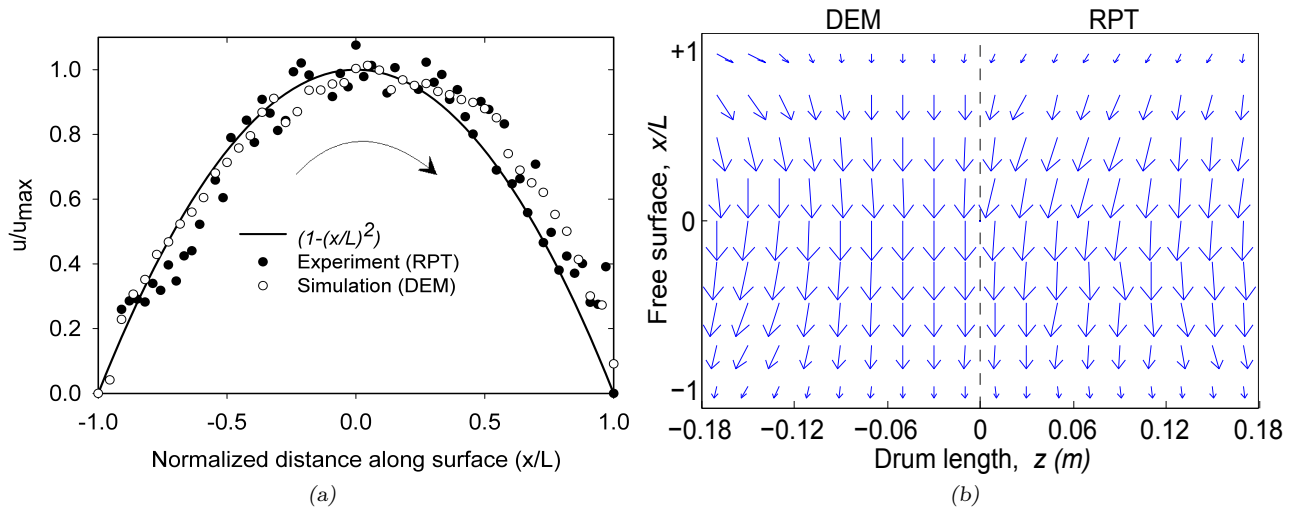


Figure 5.3: Surface velocity profiles : (a) normalized streamwise velocity vs the dimensionless distance along the surface, (b) velocity vectors at the free surface along the drum length, where the DEM (resp. RPT) results are used for the left (resp. right) side of the drum.

predicted by DEM simulations and the latter was obtained both from RPT data and DEM results. The influence of these walls seems to be short-ranged, and the dynamic repose angle drops rapidly within a few centimeters to its value in the middle of the drum. Note that this phenomenon was observed in the DEM simulations due to the use of particle/wall friction parameters larger than the real ones (see Table 5.2). Such behavior was reported by Dury et al. (1998) who measured the variations of the repose angle along the axial direction by means of DEM simulation. To obtain such results, these authors adjusted the particle/wall friction coefficients, the values of which are presented in Table 5.3.

5.3.3 Residence time

In the rotating drum, the transverse motion of the particles is the primary factor controlling the renewal of the material at the exposed bed surface. The residence times in the active and passive layers have an impact on the efficiency of many processes such as pan coating where a solution (*e.g.* binder) is top-sprayed on the surface of the bed of particles (Alizadeh et al., 2013b). It was shown in this earlier work, through RPT data, that the residence times in the active and passive layers can be evaluated through the following expressions :

$$t_{act} = \frac{3.87 \delta'_o}{\omega L}, \quad (5.9)$$

$$t_{pas} = \frac{1}{\omega} \gamma, \quad (5.10)$$

where γ is the angle of each streamline (see Fig. 5.4a). The residence times in the active and passive layers versus the angle of the streamlines is provided in Fig. 5.4b. First, it can be seen that the RPT results validates the DEM simulation results. In particular, the residence time in the passive layer is shown to vary linearly when the angle of the streamlines increases, whereas it is constant in the active layer. Consequently, the total residence time (the sum of the residence times in both layers) also varies linearly. These results are in agreement with

the short-dashed line (solid body rotation according to Eq. 5.10) in the passive layer, the long-dashed line (Eq. 5.9) in the active layer and the solid line (total residence time from the sum of Eqs. 5.9 and 5.10).

5.3.4 Mixing and segregation in the rotating drum

Lacey (1954) demonstrated the usefulness of many methods to assess the state of a mixture. A well-known one for solids mixing is the relative standard deviation (RSD) that measures the standard deviation in composition of a set of samples taken at a certain stage of the mixing operation. Recently, Doucet et al. (2008c) proposed a new mixing index to bridge the global mixing properties and local viewpoint of chaotic theory, with applications to granular and fluid flow systems. The index is based on the Lagrangian trajectory of particles obtained either numerically through computer simulation or experimentally by means of non-intrusive methods (such as PEPT and RPT). This index has been applied to assess the quality of mixing in pharmaceutical equipment (Bouffard et al., 2013; Doucet et al., 2008a).

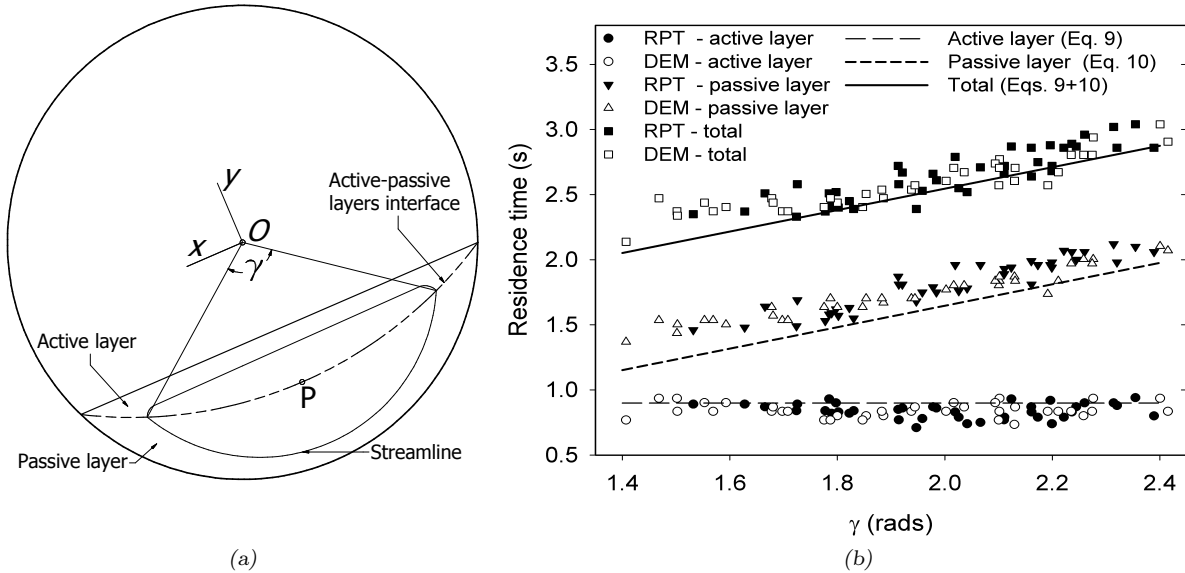


Figure 5.4: (a) A streamline making a full rotation in the active and passive layers; (b) variations of the residence times in active and passive layers when the angle of the streamline increases.

More details on the mathematical formulation of this index can be found in [Doucet et al. \(2008c\)](#).

Two different indices were in fact defined by [Doucet et al. \(2008c\)](#), which characterize the concept of mixing in the weak and strong senses. Mixing in the weak sense considers the correlation between the current and initial positions of the particles without respect to their properties, such as size or density. More precisely, a system is mixed in the weak sense if the position of the particles at time t is not correlated to their initial position. In such a case, the particles distribute themselves uniformly in the blender and the index levels off to zero with respect to time. However, this index fails to capture the occurrence of segregation with respect to the particle properties. For this reason, a more strict definition of mixing was introduced, which considers properties of the material and is called mixing in the strong sense. A system is said to be mixed in the strong sense if the position of the particles at time t is not correlated to their initial position and other given properties. The corresponding strong sense mixing index then levels off to zero with respect to time. Note that, from these definitions, a system that is mixed in the strong sense is also mixed in the weak sense. It is also possible to define and use similar indices to investigate the intensity of mixing (or segregation) along specific directions (here the radial and axial directions).

DEM simulations and the second set of experiments from Table 5.1 were used to assess mixing in the rotating drum based on these indices. Fig. 5.5a presents the evolution of the weak sense mixing indices in the radial and axial directions for the polydisperse system. As can be observed, there is an agreement between the RPT data and the simulation results. The radial direction curves decay to zero while the axial direction curves decrease slowly but remain near 1 even after 25 blender revolutions. This clearly indicates that overall mixing is limited by inefficient axial mixing, as has already been shown in the literature ([Lemieux et al., 2007](#)).

It should be noted that this system is known to lead to both axial and radial segregation ([Choo et al., 1997](#); [Hill and Kakalios, 1995](#)). To take into account segregation, the strong

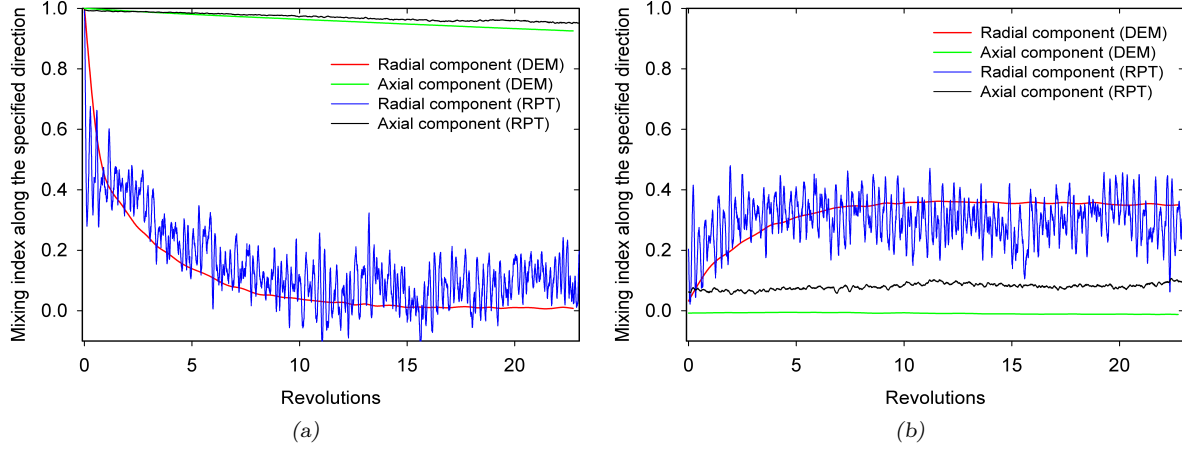


Figure 5.5: Evolution of the (a) weak sense and (b) strong sense mixing indices along the radial and axial directions.

sense definition of mixing must be considered. Fig. 5.5b shows that the strong sense mixing index in the radial direction levels off to an asymptotic value of around 0.35. This shows that the polydisperse mixture does not mix well in the radial direction. It can also be seen that the final radial segregation state is reached earlier for the RPT data than for the DEM results. Next, it seems that the index is not able to capture the segregation phenomenon that occurs slightly in the axial direction, as the values of this index remain near 0 (slightly larger for the RPT data) after many drum revolutions. The slightly non-zero value of this index when obtained from the RPT data is due to the non-homogenous initial axial distribution of the radioactive tracer positions in the 50 experiments, and does not imply axial segregation.

To gain more insight into the radial segregation pattern taking place in the drum, occupancy plots on a transverse plane located midway between both end walls are displayed in Fig. 5.6 for different-sized particles. These plots were obtained by projecting the particle positions onto the transverse plane. As evidenced by both the DEM results and the RPT data, the small 3-*mm* particles form a core along the material rotation axis and are surrounded by the larger 5-*mm* and 6-*mm* particles. The 4-*mm* particles are present in the entire volume of the drum, although mainly in inner layers.

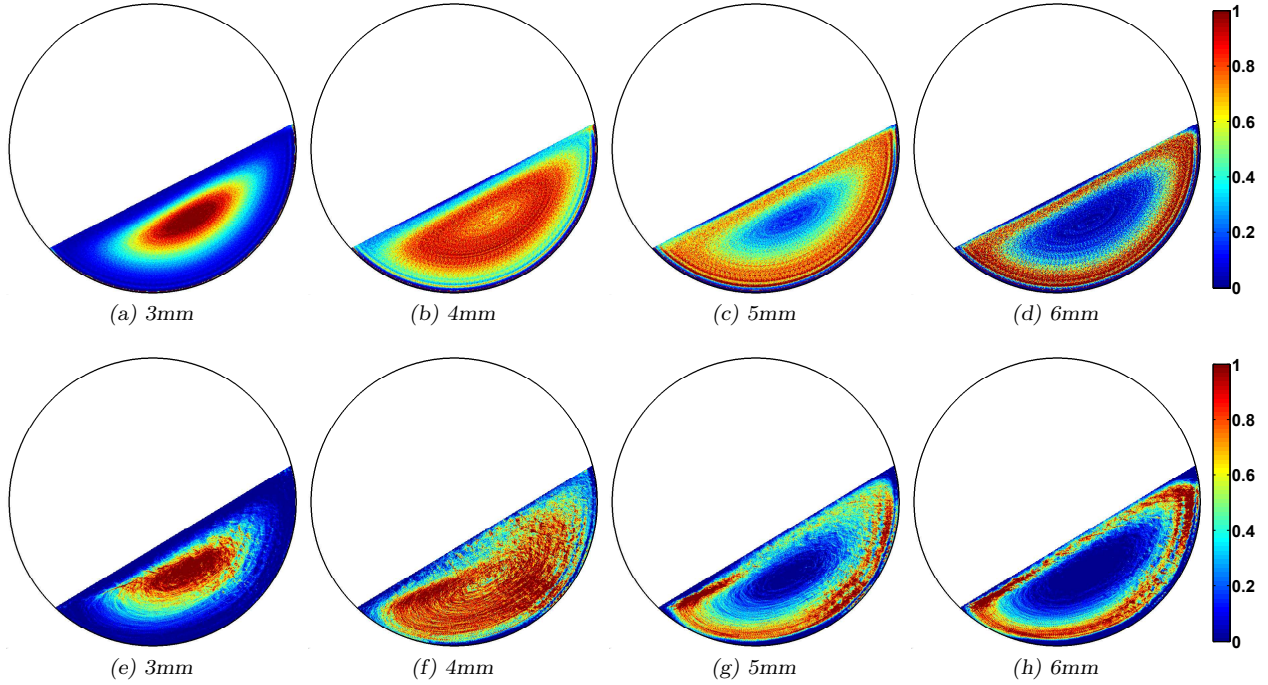


Figure 5.6: Occupancy plots for the different-sized particles of the polydisperse mixture : (a)-(d) and (e)-(h) were obtained from the DEM and RPT, respectively. The colors show the probabilities of occurrence of the corresponding particles. The RPT occupancy plots come from Alizadeh et al. (2013b).

Occupancy plots do not provide information about the rate at which radial segregation occurs. To do so, the average distance of the particles from the material rotation axis (point P in Fig. 5.4a) can be calculated for each revolution :

$$d_{i,t} = \frac{\sum_{j=1}^{n_i} |r_{j,t} - r_P|}{n_i}, i = 3, 4, 5, 6, \quad (5.11)$$

where $d_{i,t}$ is the average distance of the particles of size i at time t with respect to axis point P at radial position r_P , $r_{j,t}$ the radial position of the j th particle of size i at time t , and n_i the number of particles of size i . This quantity was calculated for both the DEM results and second set of RPT data. Fig. 5.7a shows the time variation of $d_{i,t}$ while Fig. 5.7b shows its variation along the drum length for $t = 120s$ (DEM results only). The following remarks can be made :

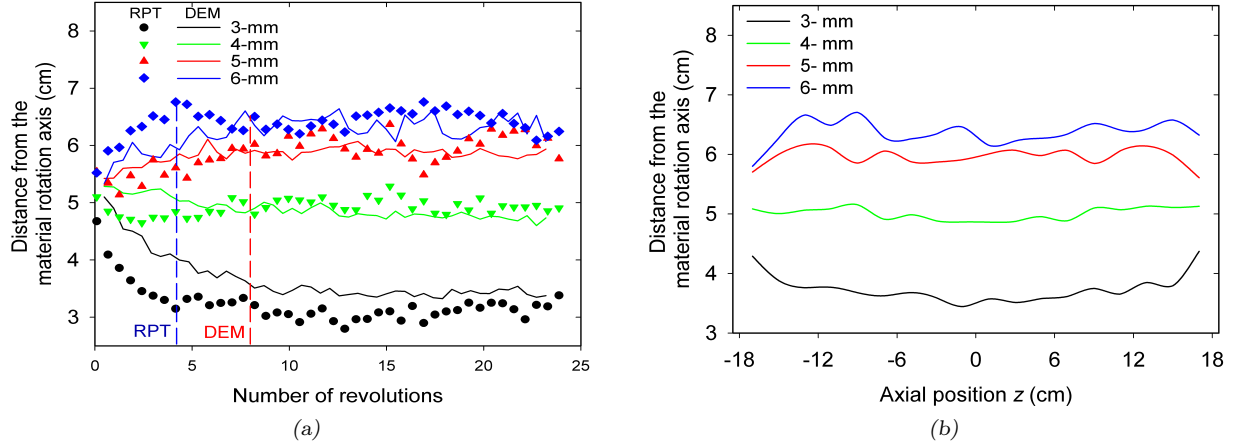


Figure 5.7: (a) Time variation of $d_{i,t}$, and (b) variation of $d_{i,t}$ along the drum length for $t = 120s$ (DEM results only).

1. In Fig. 5.7a, the agreement between the DEM results and RPT data is good, all the more so after 20 revolutions. However, as is shown in Fig. 5.5b, the rate at which radial segregation develops is different in these two cases. In Fig. 5.7a, radial segregation is complete in 5 and 7 revolutions with RPT and DEM, respectively ;
2. All curves start approximately from the same point in Fig. 5.7a, confirming that the particles were initially mixed ;
3. In Fig. 5.7a, the curves corresponding to the 3-mm and 4-mm particles exhibit a decreasing behavior whereas they increase in the case of the 5-mm and 6-mm particles. This means that the large (resp. small) particles migrate to outer (resp. inner) layers of the material bed. One would then expect a constant behavior for a particle size of 4.5-mm and, therefore, no radial segregation in such a case. This information could be used to adjust the particle size distribution in a mixture in order to preclude radial segregation for a selected species ;
4. Fig. 5.7b reveals that $d_{i,t}$ slightly varies along the axial direction of the drum. There seems to be less segregation in regions close to the end walls than in the middle of the drum. In particular, this shows that characterizing granular flow and mixing in

the transverse plane of the drum with techniques that can only visualize the material surface from the end walls (*e.g.* PIV) is limited. Alternative methods such as RPT are preferable in order to capture the particle motion inside the rotating drum.

Fig. 5.8 shows the evolution of the axial segregation as predicted by the DEM for the polydisperse mixture. To obtain such plots, the drum was divided into thin cylindrical discs perpendicular to the rotation axis, and the time variation in concentration of each species in every disk was calculated. The progress of the axial segregation can be divided into 3 steps. In step A, the radial segregation develops and no significant axial segregation is observed. After 7 revolutions ($\sim 30s$), the radial segregation reaches a stable profile (as shown in Figs. 5.5b and 5.7a) and the axial segregation continues (step B). After 60s, the axial bands that are formed in steps A and B become richer in small or large particles (step C). There are 2 narrow bands near the end walls (bands 1 and 5 when $|z| \in (0.15, 0.18)$) and a wide band in the middle of the drum (band 3 when $z \in (-0.1, 0.1)$) where 5-mm and 6-mm particles accumulate. Two bands of small particles are formed between these 3 bands (bands 2 and 4 when $|z| \in (0.10, 0.15)$), which are concentrated in 3-mm and 4-mm particles.

Fig. 5.9 shows the final concentration of the different-sized particles along the length of the drum after 120s of DEM simulation. The red and blue solid lines show the initial concentrations of the 3 & 6-mm and 4 & 5-mm particles, respectively. As can be noticed, the concentration of the small 3 & 4-mm particles decreases near the end walls (bands 1 and 5) whereas the concentration of the large 5 & 6-mm particles increases. This is in agreement with the reported data in the literature, which states that during the axial segregation of particles in a rotating drum, a band of large particles generally appears close to the end walls (Juarez et al., 2008). This can be explained by the end-wall effect as discussed in Section 5.3.2 and explained by Chen et al. (2010). Finally, in bands 2 and 4, the concentration of the small and large particles increases and decreases, respectively.

Note that after 210 minutes (around 2500 revolutions), no significant axial segregation could be visualized from outside the drum, contrary to the DEM results. This difference can

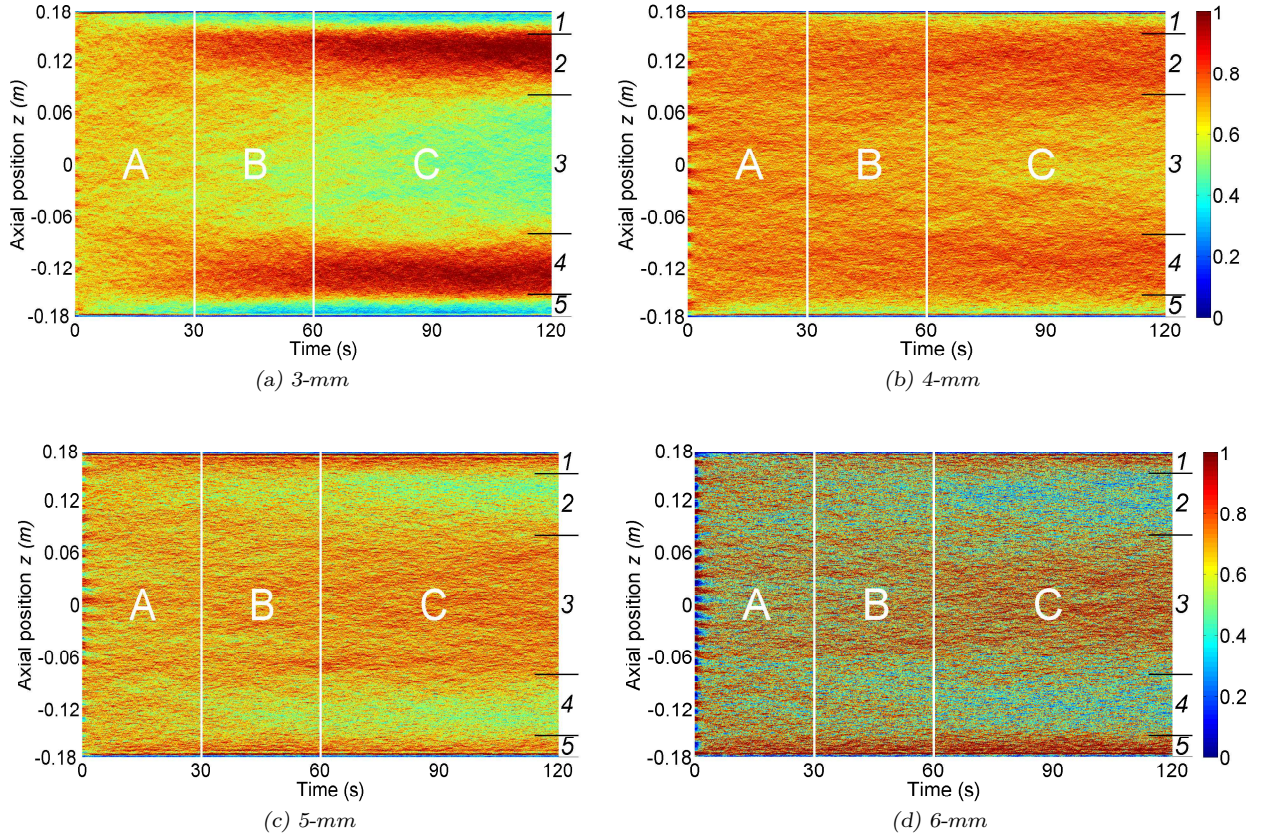


Figure 5.8: Axial segregation predicted by the DEM. The colors show the probabilities of occurrence of corresponding particles.

be explained by a larger friction coefficient used for the DEM simulations, thereby affecting the flow of particles near the end walls.

5.3.5 Quantification of axial dispersion

The DEM results may be utilized to quantify the dispersion of particles in the axial direction of the rotating drum (Kohring, 1995; Third et al., 2010). It can also be measured using the trajectories of a single particle inside the granular bed (Alizadeh et al., 2013b; Ingram et al., 2005; Parker et al., 1997; Sheritt et al., 2003). The axial dispersion coefficient (D_{axial}) is related to the variance of the axial displacement distribution :

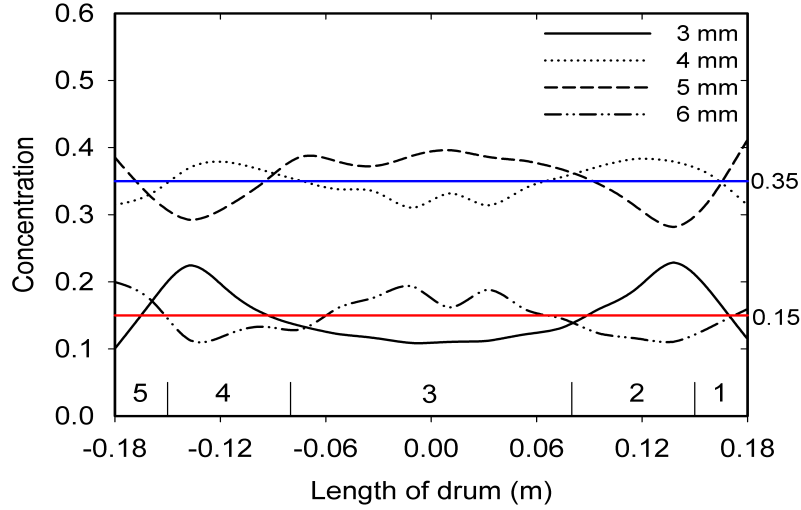


Figure 5.9: Concentration of the different-sized particles after 120 sec of DEM simulation. See Table 5.1 for the overall concentration of each species.

$$D_{axial} = \frac{\sum_i^n (\Delta z_i - \overline{\Delta z})^2 / \Delta t_i}{2n}. \quad (5.12)$$

For the DEM simulations and a simulation time of 2 minutes, Δz_i is the axial displacement of particle i in a full cycle, $\overline{\Delta z}$ the mean axial displacement, Δt_i the cycle time of particle i and n the number of particles. A cycle corresponds to the travel of a particle along a closed streamline. For the RPT experiments, which lasted 210 minutes, the initial trajectory of the single tracer is split into a series of new trajectories, each of which can be associated to the flow of a different particle along a closed streamline representing a cycle. These trajectories have non-equal lengths that are a fraction of that of the initial trajectory. Therefore, Δz_i is the axial displacement along trajectory i ($i = 1, \dots, n$), $\overline{\Delta z}$ the mean axial displacement, Δt_i the cycle time of trajectory i and n the number of trajectories.

Fig. 5.10 displays the variations of D_{axial} for the polydisperse system along a line perpendicular to the free surface at $x = 0$. As can be observed, the value of D_{axial} is of the order of $10^{-5} \text{m}^2/\text{s}$, which indicates that the axial motion of the particles is slow and the tumbling drum suffers from weak axial mixing. These values are comparable with those reported in

the literature. For instance, [Ding et al. \(2002\)](#) obtained an axial dispersion coefficient of $3 \times 10^{-6} \text{m}^2/\text{s}$ for 3-mm glass beads and a drum rotational speed of 9.6RPM , whereas [Sherritt et al. \(2003\)](#) reported values of the order of $10^{-5} \text{m}^2/\text{s}$ for rotational speeds of 5 to 25 RPM . Here, one may notice that D_{axial} is nearly constant along the y -direction although it increases near the wall where the granules eventually reach the free surface. This can be attributed to the fact that the closer the particles are to the free surface, the more freedom to move they have. The simulated results follow the same trends as the experimental measurements, yet the values predicted by the DEM are smaller than those obtained from the RPT. More precisely, the average value obtained from the RPT experiments is 1.54×10^{-5} , as opposed 0.52×10^{-5} with the DEM. This difference is due to the experimental error when tracking down the radioactive tracer in the drum and to the numerical error inherent to the DEM-based model. The impact of the particle properties used in the model is studied next.

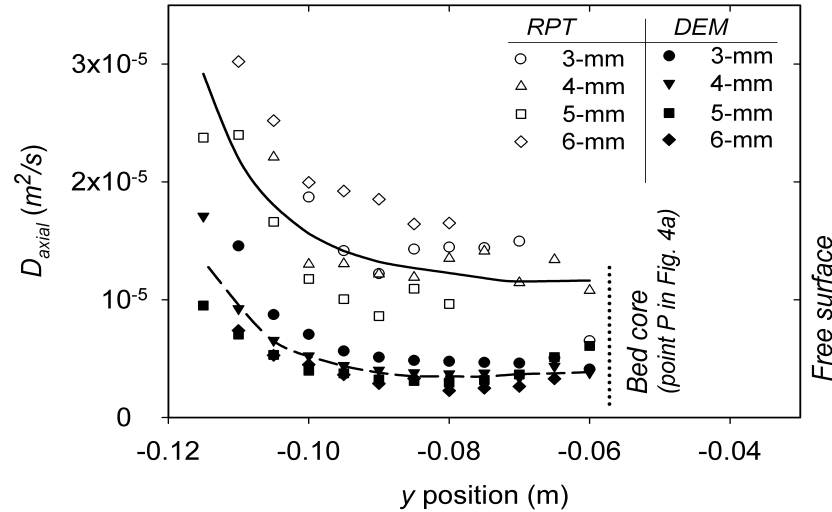


Figure 5.10: Axial dispersion coefficients determined from the displacements of the different-sized particles along a line perpendicular to the free surface at $x = 0$.

5.3.6 Sensitivity analysis of the DEM-based model

As it was shown in previous sections, there are discrepancies between the DEM and RPT results as regards axial dispersion and particle segregation in the drum. However, there is a good agreement in terms of the velocity profiles and the residence times of the granules, despite the use in the DEM simulations of smaller and higher values for the Young's modulus and the friction coefficients, respectively, in comparison with the measured values. Obtaining acceptable numerical results by using erroneous particle properties is indeed a challenging issue in the field of DEM modeling. In the literature, a common practice is to vary the value of several parameters until results that fit experimental data are obtained. In this section, a sensitivity analysis of the DEM-based model is provided with respect to the simulation parameters, in order to identify the most critical parameters and demonstrate how some parameters should be set to yield acceptable results when the value of one specific parameter is erroneous (*e.g.* Young's modulus).

The type of contact force model used in the DEM has been shown to affect the simulation results in the case of a single collision involving either two particles or one particle and the wall (Alizadeh et al., 2013a). In the case of the polydisperse system of this work, varying for instance the exponent in F_{el}^t (1 instead of $\frac{3}{2}$ in Eq. 5.5) leads to negligible differences in the predicted mixing behavior.

It was observed (results not shown here) that the Poisson's ratio does not have a significant effect on the simulation results. Similarly, applying different values of the damping constants in DEM simulations showed little influence on the dynamics of the granules and their velocity profiles but, interestingly, an observable impact on the mixing and segregation behavior (Fig. 5.11). Indeed, it can be noticed by comparing Fig. 5.11a and Fig. 5.7a (resp. Fig. 5.11b and Fig. 5.7b) that increasing the damping coefficient results in faster (resp. enhanced, near the end walls) radial segregation.

As mentioned in Section 5.3.1, smaller values of Young's modulus are generally chosen to avoid too large computational times. However, decreasing the value of the Young's modulus

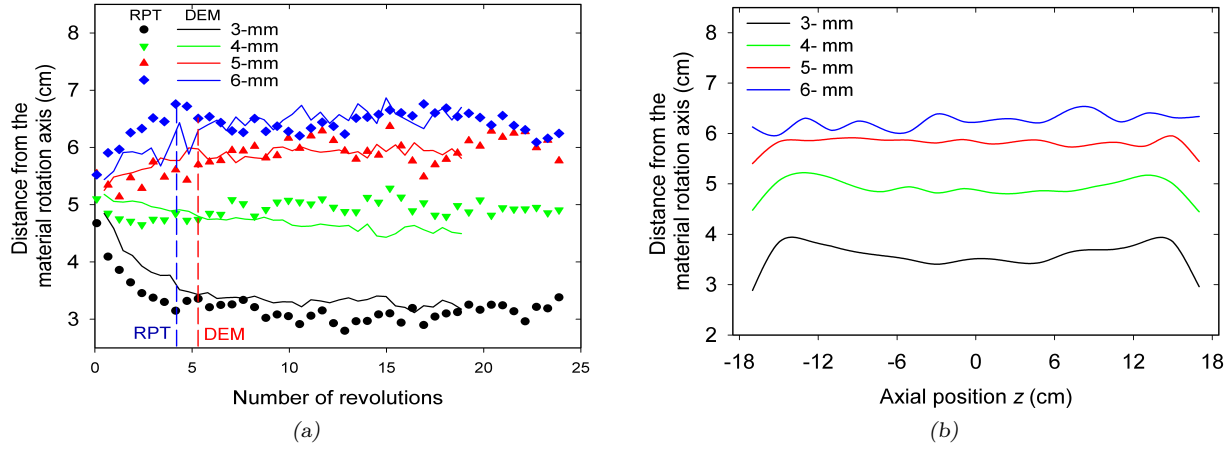


Figure 5.11: Effect of the damping constant ($c_n = 0.3, c_t = 0.3, c_{n,w} = 0.3$ and $c_{t,w} = 0.3$) on the (a) time variation of $d_{i,t}$, and (b) variation of $d_{i,t}$ along the drum length for $t = 100s$ (DEM results only).

affects the contact force (see Eqs. 5.3-5.6). Therefore, it is of interest to investigate how the motion equation is affected when a smaller Young's modulus is used. In the case of particles with the same properties, the normal component of this equation, when gravity is taken into account, can be written as :

$$m \frac{d\dot{\xi}_n}{dt} = k_n \xi_n^\alpha + C_n \xi_n^\beta \dot{\xi}_n - mg_n. \quad (5.13)$$

Following along the lines of Doucet (2008), dimensionless variables are next introduced :

$$\hat{\xi}_n = \frac{\xi_n}{\xi_{n,m}}, \quad 0 < |\hat{\xi}_n| < 1, \quad (5.14)$$

$$\hat{v}_n = \frac{\dot{\xi}_n}{v_{no}}, \quad \begin{cases} 0 < |\hat{v}_n| < 1, & \text{loading,} \\ 0 < |\hat{v}_n| < CoR_n, & \text{unloading,} \end{cases} \quad (5.15)$$

$$\hat{t} = \frac{v_{no}}{\xi_{n,m}} t, \quad (5.16)$$

where v_{no} is the initial normal impact velocity and $\xi_{n,m}$ is the maximum normal overlap

during a collision, the value of which can be shown by DEM simulations to be a function of the Young's modulus :

$$\xi_{n,m} \propto E^{-0.4}. \quad (5.17)$$

Substituting Eqs. 5.14-5.16 into Eq. 5.13 and considering that $k_n = -\frac{4}{3}E^*\sqrt{R^*}$ and $C_n = -c_n\sqrt{6m^*E^*\sqrt{R^*}}$ from Eqs. 5.3 and 5.4 leads the following dimensionless motion equation :

$$\frac{d\hat{v}_n}{d\hat{t}} - A^n \hat{\xi}_n^\alpha - B^n \hat{\xi}_n^\beta \hat{v}_n + C^n = 0, \quad (5.18)$$

where

$$A^n = \frac{-1}{\rho\pi\sqrt{8}} \frac{E}{R^{2.5}v_{no}^2} \frac{\xi_{n,m}^{\alpha+1}}{(1-\nu^2)}, \quad (5.19)$$

$$B^n = -c_n \left(-\frac{9}{2}A^n \right)^{\frac{1}{2}} \xi_{n,m}^{\beta-\frac{1}{2}(\alpha-1)}, \quad (5.20)$$

$$C^n = \frac{\xi_{n,m}g_n}{v_{no}^2}. \quad (5.21)$$

C^n is the inverse of the Froude number based on the maximum overlap during the collision ($\xi_{n,m}$) and the initial impact velocity (v_{no}). This term is small with respect to the contact force term and can be neglected as a first analysis for many collisions occurring in the bed, where gravity is not driving force for granular flow. We will back to this point below. Moreover, it can be noticed by considering Eq. 5.17 that dimensionless numbers A^n and B^n are independent of the Young's modulus when :

$$\beta = \frac{1}{2}(\alpha - 1). \quad (5.22)$$

This is the case for the model of this work ($\alpha = \frac{3}{2}$ and $\beta = \frac{1}{4}$). It is also true for the linear spring dashpot contact force model ($\alpha = 1$ and $\beta = 0$). In such a cases, the dimensionless equation of motion is independent of the Young's modulus.

A similar analysis can be made for the tangential equation of motion by considering

$$\hat{\xi}_t = \frac{\xi_t}{\xi_{t,m}}, \hat{v}_t = \frac{\dot{\xi}_t}{v_{to}} \text{ and } \hat{t} = \frac{v_{to}}{\xi_{t,m}} t :$$

$$\frac{d\hat{v}_t}{d\hat{t}} - A^t[1 - (1 - \hat{\xi}_t)^{\frac{3}{2}}] - B^t(1 - \hat{\xi}_t)^{\frac{1}{4}}\hat{v}_t + C^t = 0, \quad (5.23)$$

$$A^t = \frac{-1}{\rho\pi 4\sqrt{2}} \frac{\hat{\xi}_n^{\alpha+1}}{R^{\frac{5}{2}} v_{to}^2} \frac{2 - \nu}{(1 - \nu)^2(1 + \nu)} E \mu_s^2 \xi_{n,m}^{\alpha+1}, \quad (5.24)$$

$$B^t = -c_t \sqrt{-6A^t}, \quad (5.25)$$

$$C^t = \frac{2 - \nu}{2(1 - \nu)} \frac{\hat{\xi}_n}{v_{to}^2} g_t \mu_s \xi_{n,m}. \quad (5.26)$$

As C^n in the normal equation of motion, the term C^t can be neglected in Eq. 5.23 for many collisions in the granular bed, where gravity is not governing force. It is also straight forward to realize that both A^t and B^t are independent of the Young's modulus when $\alpha = \frac{3}{2}$ and $\beta = \frac{1}{4}$. In such a case, the tangential motion of two colliding objects is not affected by the Young's modulus. In particular, these properties signify that the CoR in both the normal and tangential directions can be predicted correctly with the corresponding DEM-based models even if wrong values of Young's modulus are used. More generally, it means that any value of Young's modulus can be used without the need to adjust other parameters to compensate for the use of an erroneous value. This explains why the use of a much smaller Young's modulus and close to real values of the particle/particle friction coefficients yielded acceptable results. Of course, in practice, gravity does play a non-negligible role for many collisions, which partly explains the minor discrepancies observed in the active layer of the bed with respect to the RPT data (Fig. 5.1c). For another example, C^t cannot be neglected when analyzing the particle/wall interactions in the passive layer of the rotating drum. In this case, one expects the tangential contact force to be strong enough to overcome the gravity force acting on the particles and thus create a solid body motion. Otherwise, the particles close to the drum wall would slide, thereby changing the flow regime from rolling to slipping. Since the particles and the drum wall have very small relative tangential velocities, the effect of the dissipative force

in Eq. 5.23 will become negligible so that B^t will not play a role. Therefore, the values of the physical parameters appearing in A^t should be chosen such that the ratio $\frac{A^t}{C^t}$ is the same as that obtained with real values :

$$\frac{A^t}{C^t} = K' E \mu_{w,s} \xi_{n,m}^\alpha, \quad (5.27)$$

where K' is independent of E and $\mu_{w,s}$. According to Eq. 5.17, $\xi_{n,m} \propto E^{-0.4}$, and for our Hertzian force model ($\alpha = \frac{3}{2}$) :

$$\frac{A^t}{C^t} = K \mu_{w,s} E^{0.4}, \quad (5.28)$$

where K includes a proportionality constant owing to the use of Eq. 5.17. The above equation can be applied as a criterion to choose $\mu_{w,s}$ when a smaller value of the Young's modulus is used in the DEM-based model to avoid too large computational time. This also explains why researchers have reported adequate simulation results despite the use of larger than real friction coefficients and smaller than real Young's modulus (see Table 5.3).

Considering the glass beads properties ($E = 68.9 GPa$ and $\mu_{w,s} = 0.208$ from Table 5.2) and the value of the Young's modulus for the current DEM simulations ($E = 200 MPa$), Eq. 5.28 gives $\mu_{w,s} = 2.15$. This value is larger than the value used for the DEM simulations ($\mu_{w,s} = 0.45$ from Table 5.2). However, the DEM results are in good agreement with the RPT data as discussed in previous sections. In fact, $\mu_{w,s}$ from Eq. 5.28 respects the minimum value for the rolling regime, which corresponds to $Fr = 10^{-4}$ according to Mellmann (2001). For larger value of this Froude number, $Fr = 0.018$ in this study, the rolling regime may persist if, for instance, a smaller friction coefficient $\mu_{w,s}$ is used. Fig. 5.12 shows the effect of the static friction coefficient $\mu_{w,s}$ on the simulation results of this work for varying values of the Young's modulus. The vertical axis corresponds to the average velocity of the particles in contact with the drum wall. As can be noticed, for small values of the Young's modulus, the use of a static friction coefficients larger than 0.35 guarantees that the velocity of these particles is close to $0.145 m/s$, the rotational speed of the drum (ωR_D), which is the expected value for the particles flowing in the rolling regime. Therefore, as it was expected, even with

a lower value of $\mu_{w,s}$ than what is predicted by Eq. 5.28, regime in drum is still rolling in higher rotational speed.

Fig. 5.12 also teaches us that the larger the value of the Young's modulus, the less important the value of the friction coefficient $\mu_{w,s}$. Of course, in practice, the value chosen for $\mu_{w,s}$ should guarantee that the resulting granular flow will be in the rolling regime. The extrapolated curve in this figure clearly shows that choosing the real value of E for a DEM simulation would generate results that do not depend on $\mu_{w,s}$.

5.4 Conclusions

The objective of this work was to assess the accuracy of a DEM-based model and explain why good results can be obtained by the DEM even when non-real values of particles properties are used. The validation was based on experimental radioactive particle tracking (RPT) data on the mixing behavior and size segregation of a polydisperse mixture of glass beads in a rotating drum operated in rolling mode. All the properties of glass beads were measured experimentally or extracted from the literature and used in the DEM simulations

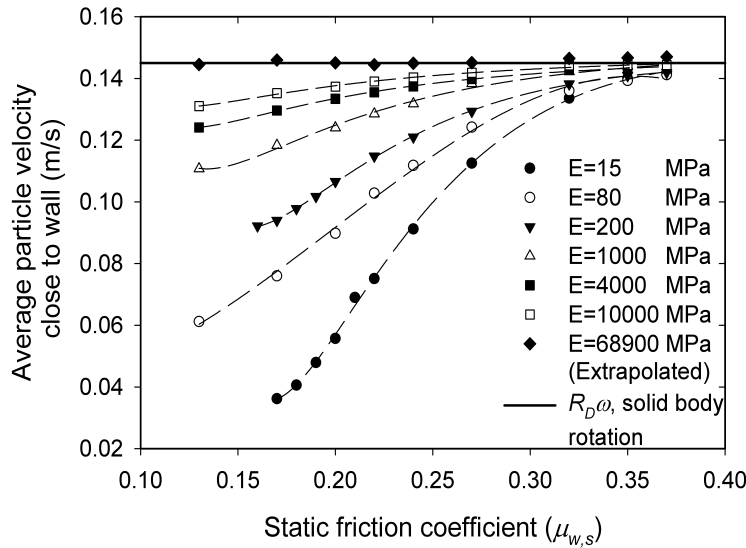


Figure 5.12: Effect of the friction coefficient $\mu_{w,s}$ on the simulation results when smaller values of the Young's modulus are used.

except the Young's modulus and the friction coefficients, where smaller and higher values were applied, respectively. Both techniques (DEM and RPT) provide Lagrangian particle trajectories. A comparison of RPT and DEM results was performed based on the velocity profiles and residence times of the granules in the active and passive layers as well as their axial dispersion and mixing/segregation behavior. A good agreement was obtained in terms of the velocity profile and residence time. The DEM prediction for the axial dispersion along the radial direction was observed to comply with the RPT data, although with smaller axial dispersion coefficients. In the case of mixing and segregation, the DEM simulations predicted axial segregation, a phenomenon that was not observed in the experiments. This can be explained by the large friction coefficients used in these simulations.

A sensitivity analysis of the DEM-based model was then performed with respect to the particle physical parameters. Dimensionless equations of motion were derived and analyzed in both the normal and tangential directions. They showed that when the gravity force on the particles can be neglected against the contact forces, the particle dynamics and the dimensionless motion equations are not affected by the Young's modulus. In cases where the gravity force on the particles is non-negligible, a correlation was derived, which could be used to set the values of the static friction coefficients for DEM simulations when a smaller value of the Young's modulus is applied.

Finally, the findings reported in this work have shed light on the importance of the Young's modulus and the static friction coefficients on the particle dynamics. Future work will focus on the effect of these parameters on the force exerted by the particles on each other and the wall of the computational domain.

Acknowledgments

The financial contribution of Teva Canada, Praxair Inc. and the Natural Sciences and Engineering Research Council of Canada (NSERC) is gratefully acknowledged. All simulations were made possible thanks to the computational resources of Compute Canada. The authors

are grateful to Majid Rasouli for helpful discussion on how to measure glass bead properties.

5.5 References

- Alizadeh, E., Bertrand, F., and Chaouki, J. (2013a). Development of a granular normal contact force model based on a non-newtonian liquid filled dashpot. *Powder Technology*, 237 :202–212.
- Alizadeh, E., Dubé, O., Bertrand, F., and Chaouki, J. (2013b). Characterization of mixing and size segregation in a rotating drum by a particle tracking method. *Accepted in AIChE Journal*, DOI 10.1002/aic.13982.
- Amstock, J. S. (1997). *Handbook of Glass in Construction*. McGraw-Hill.
- Balevicius, R., Kacianauskas, R., Mroz, Z., and Sielamowicz, I. (2008). Discrete-particle investigation of friction effect in filling and unsteady/steady discharge in three-dimensional wedge-shaped hopper. *Powder Technology*, 187(2) :159–174.
- Baxter, J., Tuzun, U., Burnell, J., and Heyes, D. (1997). Granular dynamics simulations of two-dimensional heap formation. *Physical Review E*, 55(3-B) :3546–3546.
- Bolz, R. and Tuve, G. (1970). *CRC handbook of tables for applied engineering science*. CRC Press, Boca Raton.
- Bouffard, J., Bertrand, F., Chaouki, J., and Dumont, H. (2013). Discrete element investigation of flow patterns and segregation in a spheronizer. *Computers and Chemical Engineering*, 49 :170–182.
- Cantelaube, F. and Bideau, D. (1995). Radial segregation in a 2D drum : an experimental analysis. *Europhysics Letters*, 30(3) :133–138.
- Chen, P., Ottino, J. M., and Lueptow, R. M. (2010). Onset mechanism for granular axial band formation in rotating tumblers. *Physical Review Letters*, 104(18) :188002.

- Cheng, N.-S., Zhou, Q., Tan, S. K., and Zhao, K. (2011). Application of incomplete similarity theory for estimating maximum shear layer thickness of granular flows in rotating drums. *Chemical Engineering Science*, 66(12) :2872–2878.
- Choo, K., Molteno, T., and Morris, S. (1997). Travelling granular segregation patterns in a long drum mixer. *Physical Review Letters*, 79(16) :2975–2978.
- Cundall, P. and Strack, O. (1979). Discrete numerical model for granular assemblies. *Geotechnique*, 29(1) :47–65.
- Ding, Y., Forster, R., Seville, J., and Parker, D. (2002). Segregation of granular flow in the transverse plane of a rolling mode rotating drum. *International Journal of Multiphase Flow*, 28(4) :635–663.
- Ding, Y., Seville, J., Forster, R., and Parker, D. (2001). Solids motion in rolling mode rotating drums operated at low to medium rotational speeds. *Chemical Engineering Science*, 56(5) :1769–1780.
- Doucet, J. (2008). *Mesure et caractérisation du mélange dans les systèmes granulaires denses*. PhD thesis, Polytechnique Montréal (in French).
- Doucet, J., Bertrand, F., and Chaouki, J. (2008a). Experimental characterization of the chaotic dynamics of cohesionless particles : Application to a V-blender. *Granular Matter*, 10(2) :133–138.
- Doucet, J., Bertrand, F., and Chaouki, J. (2008b). An extended radioactive particle tracking method for systems with irregular moving boundaries. *Powder Technology*, 181(2) :195–204.
- Doucet, J., Bertrand, F., and Chaouki, J. (2008c). A measure of mixing from lagrangian tracking and its application to granular and fluid flow systems. *Chemical Engineering Research and Design*, 86(12) :1313–1321.
- Dury, C. M. and Ristow, G. H. (1997). Radial segregation in a two-dimensional rotating drum. *Journal de physique. I*, 7(5) :737–745.

- Dury, C. M., Ristow, G. H., Moss, J. L., and Nakagawa, M. (1998). Boundary effects on the angle of repose in rotating cylinders. *Physical Review E*, 57(4) :4491–4497.
- Foerster, S., Louge, M., Chang, H., and Allia, K. (1994). Measurements of the collision properties of small spheres. *Physics of Fluids*, 6(3) :1108–1115.
- González-Montellano, C., Ayuga, F., and Ooi, J. (2011a). Discrete element modelling of grain flow in a planar silo : Influence of simulation parameters. *Granular Matter*, 13(2) :149–158.
- González-Montellano, C., Ramirez, A., Gallego, E., and Ayuga, F. (2011b). Validation and experimental calibration of 3D discrete element models for the simulation of the discharge flow in silos. *Chemical Engineering Science*, 66(21) :5116–5126.
- Guo, Y., Wassgren, C., Ketterhagen, W., Hancock, B., and Curtis, J. (2012). Some computational considerations associated with discrete element modeling of cylindrical particles. *Powder Technology*, 228(0) :193–198.
- Hartl, J. and Ooi, J. Y. (2008). Experiments and simulations of direct shear tests : Porosity, contact friction and bulk friction. *Granular Matter*, 10(4) :263–271.
- Hawkesworth, M., Parker, D., Fowles, P., Crilly, J., Jefferies, N., and Jonkers, G. (1991). Nonmedical applications of a positron camera. *Nuclear Instruments & Methods in Physics Research. Section A, Accelerators, Spectrometers, Detectors and Associated Equipment*, A310(1-2) :423–434.
- Henein, H., Brimacombe, J., and Watkinson, A. (1983). Experimental study of transverse bed motion in rotary kilns. *Metallurgical Transactions B*, 14(2) :191–205.
- Hill, K. and Kakalios, J. (1995). Reversible axial segregation of rotating granular media. *Physical Review E*, 52(4) :4393–4400.
- Ingram, A., Seville, J., Parker, D., Fan, X., and Forster, R. (2005). Axial and radial dispersion in rolling mode rotating drums. *Powder Technology*, 158(1-3) :76–91.

- Iwasaki, T., Satoh, M., and Koga, T. (2001). Analysis of collision energy of bead media in a high-speed elliptical-rotor-type powder mixer using the discrete element method. *Powder Technology*, 121(2-2) :239–248.
- Jain, N., Ottino, J., and Lueptow, R. (2002). An experimental study of the flowing granular layer in a rotating tumbler. *Physics of Fluids*, 14(2) :572–582.
- Juarez, G., Ottino, J., and Lueptow, R. (2008). Axial band scaling for bidisperse mixtures in granular tumblers. *Physical Review E*, 78(3) :031306.
- Kaneko, Y., Shiojima, T., and Horio, M. (2000). Numerical analysis of particle mixing characteristics in a single helical ribbon agitator using dem simulation. *Powder Technology*, 108(1) :55–64.
- Khakhar, D., Orpe, A. V., and Ottino, J. (2001). Continuum model of mixing and size segregation in a rotating cylinder : Concentration-flow coupling and streak formation. *Powder Technology*, 116(2-3) :232–245.
- Kharaz, A., Gorham, D., and Salman, A. (2001). An experimental study of the elastic rebound of spheres. *Powder Technology*, 120(3) :281–291.
- Khodabakhshian, R. and Emadi, B. (2011). Determination of the modulus of elasticity in agricultural seeds on the basis of elasticity theory. *Middle-East Journal of Scientific Research*, 7(3) :367–373.
- Kohring, G. (1995). Studies of diffusional mixing in rotating drums via computer simulations. *Journal De Physique, I*, 5(12) :1551–1561.
- Kruggel-Emden, H., Simsek, E., Rickelt, S., Wirtz, S., and Scherer, V. (2007). Review and extension of normal force models for the discrete element method. *Powder Technology*, 171(3) :157–173.
- Kruggel-Emden, H., Wirtz, S., and Scherer, V. (2008). A study on tangential force laws applicable to the discrete element method (DEM) for materials with viscoelastic or plastic behavior. *Chemical Engineering Science*, 63(6) :1523–1541.

- Kuo, H., Knight, P., Parker, D., Tsuji, Y., Adams, M., and Seville, J. (2002). The influence of DEM simulation parameters on the particle behaviour in a V-mixer. *Chemical Engineering Science*, 57(17) :3621–3638.
- Lacey, P. (1954). Development in the theory of particle mixing. *Journal of Applied Chemistry*, 4 :257–268.
- Larachi, F., Kennedy, G., and Chaouki, J. (1994). A gamma ray detection system for 3-D particle tracking in multiphase reactors. *Nuclear Instruments & Methods in Physics Research Section A-Accelerators Spectrometers Detectors and Associated Equipment*, A338(2-3) :568–576.
- Laurent, B. and Cleary, P. (2012). Comparative study by PEPT and DEM for flow and mixing in a ploughshare mixer. *Powder Technology*, 228 :171–186.
- Lemieux, M., Bertrand, F., Chaouki, J., and Gosselin, P. (2007). Comparative study of the mixing of free-flowing particles in a V-blender and a bin-blender. *Chemical Engineering Science*, 62(6) :1783–1802.
- Lemieux, M., Leonard, G., Doucet, J., Leclaire, L.-A., Viens, F., Chaouki, J., and Bertrand, F. (2008). Large-scale numerical investigation of solids mixing in a V-blender using the discrete element method. *Powder Technology*, 181(2) :205–216.
- Leonard, G., Bertrand, F., Chaouki, J., and Gosselin, P. (2008). An experimental investigation of effusivity as an indicator of powder blend uniformity. *Powder Technology*, 181(2) :149–59.
- Li, D. (2004). 25 - friction and wear. In Gale, W. and Totemeier, T., editors, *Smithells Metals Reference Book*, pages 1–26. Butterworth-Heinemann, Oxford, eighth edition.
- Li, Y., Xu, Y., and Thornton, C. (2005). A comparison of discrete element simulations and experiments for 'sandpiles' composed of spherical particles. *Powder Technology*, 160(3) :219–228.

- Lin, J., Chen, M., and Chao, B. (1985). A novel radioactive particle tracking facility for measurement of solids motion in gas fluidized beds. *AIChE Journal*, 31(3) :465–473.
- Liu, X. Y., Specht, E., Gonzalez, O., and Walzel, P. (2006). Analytical solution for the rolling-mode granular motion in rotary kilns. *Chemical Engineering and Processing*, 45(6) :515–521.
- Lueptow, R., Akonur, A., and Shinbrot, T. (2000). PIV for granular flows. *Experiments in Fluids*, 28(2) :183–186.
- Maneval, J., Hill, K., Smith, B., Caprihan, A., and Fukushima, E. (2005). Effects of end wall friction in rotating cylinder granular flow experiments. *Granular Matter*, 7(4) :199–202.
- Mellmann, J. (2001). The transverse motion of solids in rotating cylinders-forms of motion and transition behavior. *Powder Technology*, 118(3) :251–270.
- Moakher, M., Shinbrot, T., and Muzzio, F. J. (2000). Experimentally validated computations of flow, mixing and segregation of non-cohesive grains in 3D tumbling blenders. *Powder Technology*, 109(1-3) :58–71.
- Mueth, D., Jaeger, H., and Nagel, S. (1998). Force distribution in a granular medium. *Physical Review E*, 57(3) :3164–3169.
- Muzzio, F. J., Goodridge, C. L., Alexander, A., Arratia, P., Yang, H., Sudah, O., and Mergen, G. (2003). Sampling and characterization of pharmaceutical powders and granular blends. *International Journal of Pharmaceutics*, 250(1) :51–64.
- Nakagawa, M., Altobelli, S., Caprihan, A., Fukushima, E., and Jeong, E.-K. (1993). Non-invasive measurements of granular flows by magnetic resonance imaging. *Experiments in Fluids*, 16(1) :54–60.
- Parker, D., Dijkstra, A., Martin, T., and Seville, J. (1997). Positron emission particle tracking studies of spherical particle motion in rotating drums. *Chemical Engineering Science*, 52(13) :2011–2022.

- Persson, A.-S. and Frenning, G. (2012). An experimental evaluation of the accuracy to simulate granule bed compression using the discrete element method. *Powder Technology*, 219(0) :249–256.
- Robinson, B. J. (2009). Characterization of the viscoelastic behavior of pharmaceutical powders. Master’s thesis, Drexel University.
- Rowe, R. and Roberts, R. (1995). 1 - the mechanical properties of powders. In Ganderton, D., Jones, T., and McGinity, J., editors, *Advances in Pharmaceutical Sciences*, volume 7, pages 1–62. Academic Press.
- Ruelle, D. (1976). A measure associated with axiom a attractors. *American Journal of Mathematics*, 98 :619–654.
- Schutyser, M., Briels, W., Rinzema, A., and Boom, R. (2003). Numerical simulation and PEPT measurements of a 3D conical helical-blade mixer : A high potential solids mixer for solid-state fermentation. *Biotechnology and Bioengineering*, 84(1) :29–39.
- Sharan, G. and Lee, J. H. A. (1970). coefficient of friction of wheat grain on grain and steel. *Canadian Agricultural Engineering*, 12(1) :14–17.
- Sheritt, R. G., Chaouki, J., Mehrotra, A. K., and Behie, L. A. (2003). Axial dispersion in the three-dimensional mixing of particles in a rotating drum reactor. *Chemical Engineering Science*, 58(2) :401–415.
- Stewart, R. L., Bridgwater, J., Zhou, Y. C., and Yu, A. B. (2001). Simulated and measured flow of granules in a bladed mixer—a detailed comparison. *Chemical Engineering Science*, 56(19) :5457–5471.
- Sudah, O., Arratia, P., Alexander, A., and Muzzio, F. (2005). Simulation and experiments of mixing and segregation in a tote blender. *AIChE Journal*, 51(3) :836–844.
- Taberlet, N., Losert, W., and Richard, P. (2004). Understanding the dynamics of segregation bands of simulated granular material in a rotating drum. *Europhysics Letters*, 68(4) :522–528.

- Taberlet, N., Newey, M., Richard, P., and Losert, W. (2006). On axial segregation in a tumbler : an experimental and numerical study. *Journal of Statistical Mechanics : Theory and Experiment*, 2006(07) :1–17.
- Third, J., Scott, D., and Scott, S. (2010). Axial dispersion of granular material in horizontal rotating cylinders. *Powder Technology*, 203(3) :510–517.
- Tsuji, Y., Tanaka, T., and Ishida, T. (1992). Lagrangian numerical simulation of plug flow of cohesionless particles in a horizontal pipe. *Powder Technology*, 71(3) :239–250.
- Weir, G., Krouse, D., and McGavin, P. (2005). The maximum thickness of upper shear layers of granular materials in rotating cylinders. *Chemical Engineering Science*, 60(7) :2027–2035.
- Yamane, K., Nakagawa, M., Altobelli, S., Tanaka, T., and Tsuji, Y. (1998). Steady particulate flows in a horizontal rotating cylinder. *Physics of Fluids*, 10(6) :1419–27.
- Yang, R., Jayasundara, C., Yu, A., and Curry, D. (2006). DEM simulation of the flow of grinding media in isamill. *Minerals Engineering*, 19(10) :984–994.
- Yang, R., Zou, R., and Yu, A. (2003). Microdynamic analysis of particle flow in a horizontal rotating drum. *Powder Technology*, 130(1) :138–146.
- Zhou, Y., Wright, B., Yang, R., Xu, B., and Yu, A. (1999). Rolling friction in the dynamic simulation of sandpile formation. *Physica A*, 269(2) :536–553.
- Zhou, Y., Xu, B., Yu, A., and Zulli, P. (2002). An experimental and numerical study of the angle of repose of coarse spheres. *Powder Technology*, 125(1) :45–54.
- Zobel, N., Eppinger, T., Behrendt, F., and Kraume, M. (2012). Influence of the wall structure on the void fraction distribution in packed beds. *Chemical Engineering Science*, 71(0) :212–219.

CHAPTER 6

Discrete Element Simulation of Particle Mixing and Segregation in a Tetrapodal Blender

Ebrahim Alizadeh, François Bertrand, Jamal Chaouki

Department of Chemical Engineering, École Polytechnique de Montréal, C.P. 6079 succ.

Centre-Ville, Montréal, Québec, Canada, H3C 3A7

(Submitted to *Computers and Chemical Engineering*.)

Presentation of the article : In the previous chapter, it was demonstrated how DEM parameters should be chosen. Considering these findings, a proper set of DEM parameters will be used to simulate granular flow inside a tetrapodal blender and compare its performance with that of a conventional V-blender.

Abstract : One aspect that must be addressed when designing tumbling blenders is poor axial mixing, which can lead to non-homogeneous mixtures, especially when the particle physical and flow properties are different. To overcome these limitations, we recently undertook an interest in a tetrapodal mixing device patented in 1964. It can be described as two V-shaped pairs of arms connected at their bottoms, one of which is twisted by 90° . In this work, particle mixing and segregation are investigated using the discrete element method in both the V-blender and this tetrapodal blender. Results of mixing time and uniformity are compared for different loading profiles, fill levels and rotational speeds. Compared to the V-blender, this geometry is shown to provide better axial and radial mixing efficiency. Good behavior was also observed for size segregating granules, yet more investigation would be needed for worse cases involving granules with large size ratios and different densities.

Keyword : Tetrapodal blender, V-blender, Solid mixing, Segregation, Discrete element method

6.1 Introduction

Solid mixing is a key unit operation for many industries, including ceramic, metallurgical, chemical, food, cosmetics, coal, plastics and pharmaceutical. To attest to the widespread application of granular material, a 1993 study estimated that granule-based products contribute one trillion dollars to the US economy ([Scott, 2003](#)). In some processes, it is desirable to separate specific components of a mixture, whereas in most others, the ingredients should generally be mixed with each other, strictly maintaining their concentration within very small intervals to meet quality and performance goals. Therefore, weak mixing may lead to the rejection of the final product due to poor quality. Despite the importance of homogenous mixtures, obtaining homogeneity in very small scales is difficult, particularly when granules have different physical or mechanical properties possibly resulting in segregation. Such segregation, especially when portions of small particles are required to be mixed in a matrix of much larger particles, is most likely to prevail progressively with the formulation of new products ([Muzzio et al., 2002](#)).

Blenders are the most commonly used equipment to obtain a homogenous mixture. They are divided into two main groups : convective and tumbling blenders. While convective blenders involve the use of moving parts, tumbling blenders apply gravity and blender rotation to mix granules. Convective blenders vary by ribbon type and/or bowl shape, and tumbling blenders differ mainly in their geometry ([Brone et al., 1998](#)). In comparison with the convective blenders, tumbling blenders are easy to operate and handle a variety of materials, including shear sensitive granules. Among tumbling blenders, the V-blender is one of the most frequently employed in the industry. It was first designed and patented by [Fischer \(1950\)](#) and, subsequently, found numerous applications in many industries. However, such blenders show significant segregating behavior for granules with different properties ([Alexander et al., 2003, 2004](#)). Several applications in the industry rely on the bin-blender, in particular because this blender is less prone than the V-blender to material contamination. Contrary to industrial scale V-blenders, which are permanently fixed to the blender shaft, bin-blenders can usually

be moved, thus eliminating one discharge operation and thereby reducing powder exposure for the operator and cleaning time as well as segregation during extra discharge (Carson et al., 1996).

Mixing happens in both axial and radial directions of the tumbling blenders. The axial direction is defined as parallel to the axis of rotation (axis I in Fig. 6.1) and the radial direction is perpendicular to the rotation axis (YZ plane in Fig. 6.1). The governing mixing mechanism in the axial direction is diffusion and a combination of convection and diffusion in the radial direction. Convection moves large clusters of particles, while diffusion leads to individual movements of particles. Since diffusion is a slower phenomenon than convection, tumbling blenders invariably suffer from weak axial mixing (Arratia et al., 2006; Brone et al., 1997; Lemieux et al., 2007; Moakher et al., 2000). Some modifications have been patented to disturb the periodic and symmetric flow inside the bowl and increase axial mixing. These ideas include enhancing the axial flow by installing an intensifier (Fischer, 1983), an offset rotating axis with respect to the plane of symmetry of the blender (Peck, 1954), and non-equal lengths of the blender arms. However, these modifications do not result in remarkable improvement in the axial flow. Therefore, an alternative geometry is required to improve granular flow and alleviate the limitations of conventional tumbling blenders.

One solution may be to add another rotation axis (axis II in Fig. 6.1a) perpendicular to the existing rotation axis (axis I in Fig. 6.1a). Rotation around the axis II indeed allows granules to flow in the X direction. This method has been applied in the case of the double-cone and bin blenders whereby enhanced mixing was observed (Manickam et al., 2010; Mehrotra and Muzzio, 2009). Simultaneous rotations around two axes are challenging due to mechanical limitations. In order to benefit the function of both rotation axes, the geometry shown in Fig. 6.1b recently drew our attention. This geometry, called the tetrapodal mixing device, was patented in 1964 (USA patent office, 3,134,578, Anderson, 1964) and consists of a container with one axis of rotation going through its center of gravity, one arm extending from it in one direction and three other arms organized like a tripod and extending in the opposite direction.

In other words, it consists of a pair of V-blenders connected at their bottom with one twisted by 90° . To readily understand the different configurations of this blender considered in this study (see Fig. 6.2), the standard configuration shown in Fig. 6.1b is called the standard tetrapodal blender or (90-0), the latter indicating the upper twist angle (90°) and lower twist angle (0°) of the two V-shaped parts with respect to the rotation axis. Despite the seemingly effective shape of this blender for granule mixing, no study has yet been conducted to investigate its performance. In addition to its geometrical complexity and the effort needed to clean it after operation, the large size of the tetrapodal blender as compared to the V-blender and the fact that it requires more energy to operate are probably reasons why it has not been commercialized. Moreover, the scaling-up of this device for industrial applications seems to be another limiting factor that has hampered its use. Regardless of such drawbacks, the limitations of conventional tumbling blenders provided the impetus to investigate solid mixing inside this device. No application of this blender despite having an effective geometry is somehow similar to the videocassette recorder (VCR) business, where a technologically superior Sony Betamax system came second to the more prevalent video home system (VHS) in the standard battle ([Wonglimpiyarat, 2005](#)).

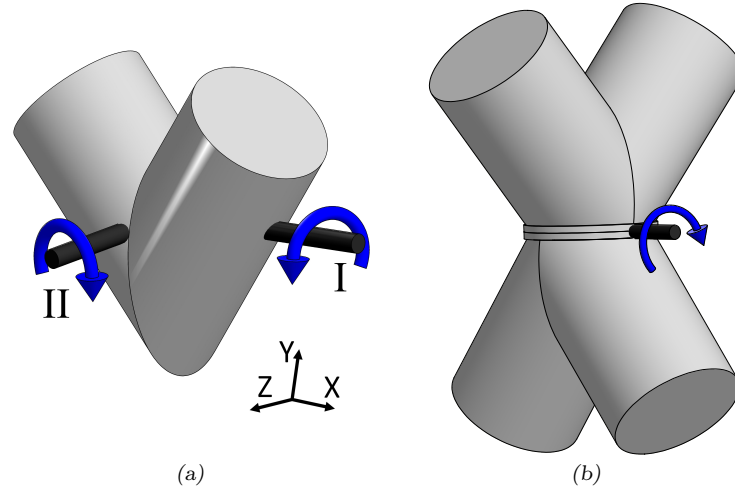


Figure 6.1: Rotation of (a) the V-blender around two axes and (b) the standard tetrapodal blender.

Investigation of the mixing and dynamics of granules can be carried out via thief sampling (Lemieux et al., 2007; Muzzio et al., 1997) and non-intrusive techniques (Doucet et al., 2008b), respectively. However, before investing in manufacturing a lab-scale version of the tetrapodal blender in order to investigate its performance experimentally, it is of interest to first characterize its efficiency via simulation to assess its performance against conventional tumbling blenders and obtain design parameters. Two approaches have been employed to simulate granular flow in the literature. The first approach is Eulerian and assumes the particles flow as a fluid (Aranson and Tsimring, 1999; Khakhar et al., 1997, 2001) while the second approach is Lagrangian and considers each single particle as a separate entity. In the second approach, the discrete element method (DEM), originally proposed by Cundall and Strack (1979), has been applied to investigate granular mixing and segregation inside tumbling blenders (Lemieux et al., 2007, 2008; Rapaport, 2007). The DEM method has shown to provide new insights into the phenomena occurring in granular systems and afford extensive details about the flow and mixing of granules.

The objective of this study is to investigate by means of DEM simulation the mixing and segregation of free-flowing granules in the tetrapodal blender and compare its performance to that of the V-blender. Several configurations of the tetrapodal blender (different twist angles of the top and bottom V-shaped parts) are considered and, in particular, the impacts of operating parameters, such as fill level, loading profile and rotational speed, are examined. This article is organized as follows. First, in Section 6.2, the DEM-based model for the simulations is introduced. Next, the mixing and segregation of free-flowing granules are investigated in both blenders and their performances are compared. Finally, Section 6.4 contains concluding remarks.

6.2 Methodology

6.2.1 DEM-based model

The DEM is a time-driven soft-particle method recognized as a reliable simulation tool to investigate the flow of particles inside a system. In the DEM, each particle is subjected to Newton's second law of motion and the position of every single particle is obtained by integrating it twice with respect to time. In this work, the total force acting on each particle includes gravity as well as particle/particle and particle/wall interactions by means of a contact force model. Due to the fluid phase properties (generally air in dry solid mixing), drag and buoyant forces are neglected. The size of the granules in the DEM simulations is in the order of millimeters so that colloidal forces can also be neglected.

In the DEM, the contact force acting on a particle i with radius R and density ρ , when it is colliding with an object j (a particle or the blender shell), is decomposed into normal and tangential components. These forces include a repulsion term f_{el} that depends on the overlap δ of the particle with the object, and a dissipative term f_{dis} that takes into account the energy dissipation due to the collision. Recently, new models have been developed to better represent the mechanics of contact deformation. A review of such models can be found in [Alizadeh et al. \(2013\)](#) and [Kruggel-Emden et al. \(2007, 2008\)](#). In the current work, a modified non-linear viscoelastic model is applied to predict the normal contact force, wherein a dissipative term is added to the standard Hertz formulation ([Zhou et al., 1999, 2002](#)) :

$$F_n = f_{n,el} + f_{n,dis} = k_n \delta_n^{3/2} + (C_n |\delta_n|^{1/4}) \dot{\delta}_n, \quad (6.1)$$

where δ_n is the normal component of the overlap, $k_n = -\frac{4}{3} E^* \sqrt{R^*}$ the normal stiffness constant and $C_n = -c_n (6m^* E^* \sqrt{R^*})^{1/2}$ the normal damping coefficient. In these expressions, c_n stands for the normal damping constant, $E^* = (\frac{1-\nu_i^2}{E_i} + \frac{1-\nu_j^2}{E_j})^{-1}$ the reduced Young's modulus where E stands for the Young's modulus and ν for the Poisson's ratio. $R^* = (\frac{1}{R_i} + \frac{1}{R_j})^{-1}$ is the reduced radius and $m^* = (\frac{1}{m_i} + \frac{1}{m_j})^{-1}$ the mean mass.

The tangential contact force models in the DEM are commonly based on the pioneering work of [Mindlin and Deresiewicz \(1953\)](#). Similar to the normal force models, the tangential force F_t acting on a particle is the sum of repulsive $f_{t,el}$ and dissipative $f_{t,dis}$ terms. The following expression, which is one of the most accepted formulations, have been applied in this work ([Baxter et al., 1997](#)) :

$$f_{t,el} = \mu_s |f_{n,el}| \left[1 - \left(1 - \frac{\delta_t}{\delta_{t,max}} \right)^{3/2} \right] \frac{\delta_t}{|\delta_t|}, \quad (6.2)$$

where μ_s is the static coefficient of friction, δ_t the tangential component of the overlap and $\delta_{t,max} = \mu \frac{2-\nu}{2(1-\nu)} \delta_n$ represents the maximum non-slipping tangential deformation ([Langston et al., 1995](#)). This force is bounded above by the Coulomb friction law ($f_{t,el} = \mu |f_{n,el}|$) resulting in $0 \leq \delta_t \leq \delta_{t,max}$, where μ is the dynamic friction coefficient. The tangential dissipative force is proportional to the tangential relative velocity $\dot{\delta}_t$:

$$f_{t,dis} = -c_t \left[6m^* \mu_s |f_{n,el}| \frac{\sqrt{1 - |\delta_t|/\delta_{t,max}}}{\delta_{t,max}} \right]^{1/2} \dot{\delta}_t, \quad (6.3)$$

where c_t stands for the tangential damping constant.

The rotation ζ of particle i can be obtained via an angular momentum balance :

$$I_i \frac{d\zeta_i}{dt} = T_i + T_r, \quad (6.4)$$

where I_i is the moment of inertia and T_i the torque that can be obtained by performing the cross product of the corresponding tangential force and particle radius. T_r represents the rolling friction force, which has shown to yield more accurate result for spherical particles ([Zhou et al., 1999](#)) :

$$T_r = -\mu_r |f_{n,el}| \frac{\zeta_i}{|\zeta_i|}, \quad (6.5)$$

where μ_r is the so-called rolling friction coefficient.

6.2.2 Details of the simulations

The above mentioned DEM-based model was used to investigate the mixing performance and flow behavior of granules inside a tetrapodal blender and V-blender (each 6.7 liters in volume). The dimensions of the V-blender were obtained by the scaling-down of typical V-blenders used in the pharmaceutical industry, while the dimensions of the tetrapodal blender were designed according to the equivalent volume of the V-blender. The applied physical and mechanical properties of the granules are given in Table 6.1. These parameters were set in a way to mimic the flow behavior of sucrose and starch spheres (common drug layering pellets in the pharmaceutical industry) inside a rotating drum. For more details on the methodology for choosing the DEM parameters, the reader is referred to [Alizadeh et al. \(2012\)](#), where it is shown that even for small values of the Young's modulus, which is common in the literature, a relatively large particle/wall static friction coefficient guarantees adequate particle dynamics. In the current study, a Young's modulus of 200MPa was selected, which is larger than the typical values used in the literature for DEM simulations. To compensate the effect of using a relatively small value for the Young's modulus, the particle/wall friction coefficient was chosen to be 0.3.

Three fill levels ($35\%V$, $50\%V$ and $65\%V$ with respect to the total volume of the blender)

Table 6.1: Physical and mechanical particle properties for the DEM-based model. P/P and P/W denote particle/particle and particle/wall collisions, respectively.

Properties	Value
Density (ρ)	1.5 g/cm^3
Young's Modulus (E)	200 MPa
Poisson's ratio (ν)	0.3
Normal damping constant (c_n)	0.3
Tangential damping constant (c_t)	0.3
P/P dynamic friction coefficient (μ)	0.09
P/P static friction coefficient (μ_s)	0.13
P/W dynamic friction coefficient (μ_w)	0.3
P/W static friction coefficient ($\mu_{w,s}$)	0.3
Rolling friction coefficient (μ_r)	$2.5 \times 10^{-4}\text{ m}$

and two rotational speeds ω ($15RPM$ and $30RPM$) were considered. Three loading profiles were also investigated : Front-Back (FB), Top-Bottom (TB) and Right-Left (RL). Note that the particles were colored after a simulation was completed to generate the FB, TB and RL loading profiles.

The characteristics of the simulations are given in Table 6.2. Four simulations (cases A-D) were carried out to compare the performance of the tetrapodal blender and the V-blender in various operating conditions (rotational speed and fill level). These simulations involved a monodisperse mixture of 3-mm particles. To investigate the effect of the geometry configuration on the efficiency of the tetrapodal blender, simulations E-H related to (45-0), (0-0), (90-45) and (90-90) configurations, respectively, were run. Recall that the first and second numbers respectively correspond to the twist angle of the upper and lower V-shaped parts with respect to the rotation axis. These configurations are shown in Fig. 6.2. In particular, configuration (0-0) is also called the X-blender and was patented in 1959 before the tetrapodal blender (USA patent office, 2,901,227, [Russum, 1959](#)). In addition to cases E-H, other sets of simulations were performed for the (30-0), (60-0), (90-30) and (90-60) configurations, but not presented here since they yielded similar results as cases E and G. Finally, to investigate the segregation of a bidisperse mixture in the standard tetrapodal blender (90-0), two simulations were carried out. The first simulation started from a fully segregated FB loading profile (case I), and the second simulation started from a fully mixed state (case J). The FB loading profile was chosen here to make sure that the final segregation pattern is obtained quickly and not limited by a weak axial mixing mechanism. The two different initial states for the bidisperse mixture were chosen to show that their final segregation patterns are similar. This indicates that no more segregation would occur if the simulation was continued over a long period.

In the current work, the time step was $0.6\mu s$ and the particle positions and velocities were stored at $0.033s$ intervals. In order to reduce the CPU time, a parallel version of the DEM was applied based on domain decomposition and parallel programming using the MPI communication library. The DEM is computationally intensive, even when run on many

Table 6.2: Characteristics of the simulations.

Case	Blender	$\omega[RPM]$	Fill level [%V]	System
A	(90-0) & V	15	35	Monodisperse mixture of 96,000 3- <i>mm</i> granules
B	(90-0) & V	15	50	Monodisperse mixture of 137,000 3- <i>mm</i> granules
C	(90-0) & V	30	50	Monodisperse mixture of 137,000 3- <i>mm</i> granules
D	(90-0) & V	15	65	Monodisperse mixture of 178,000 3- <i>mm</i> granules
E	(45-0)	15	50	Monodisperse mixture of 137,000 3- <i>mm</i> granules
F	(0-0)	15	50	Monodisperse mixture of 137,000 3- <i>mm</i> granules
G	(90-45)	15	50	Monodisperse mixture of 137,000 3- <i>mm</i> granules
H	(90-90)	15	50	Monodisperse mixture of 137,000 3- <i>mm</i> granules
I	(90-0)	15	50	Bidisperse mixture of 28,000 4- <i>mm</i> and 227,000 2- <i>mm</i> granules, with a fully segregated FB initial state
J	(90-0)	15	50	Bidisperse mixture of 28,000 4- <i>mm</i> and 227,000 2- <i>mm</i> granules, with a fully mixed initial state

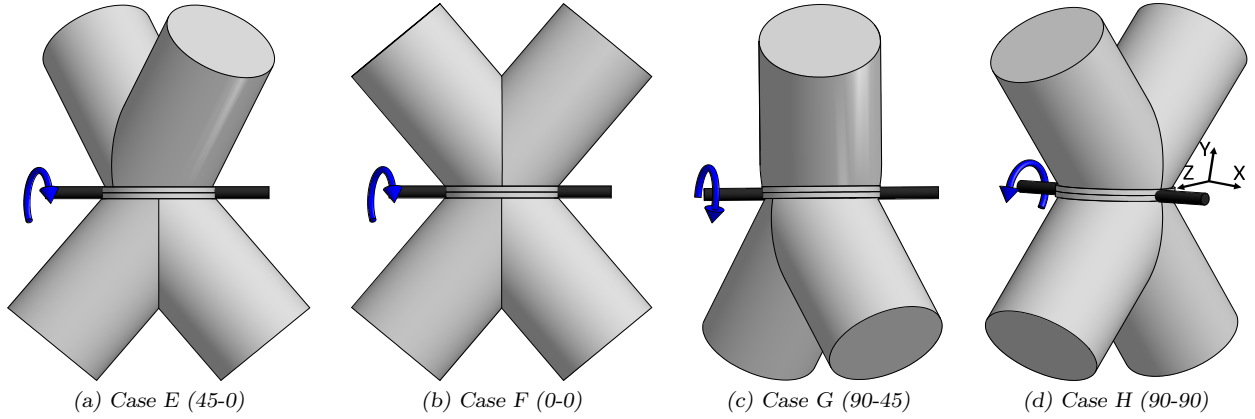


Figure 6.2: Different configurations of the twisted tetrapodal blender considered in the current work.

parallel cores. For instance, 1 second of simulation for case J took 36 hours with 48 cores of a parallel cluster of Compute Canada (Intel Xeon E5462 3 GHz quad-core processors). Simulations were run up to 120s in all cases except for the bidisperse mixtures (cases I and J), where segregation patterns were obtained after only 60s.

6.3 Results and discussion

First, the granular flow inside both blenders is investigated. Second, the mixing rate is analyzed for the different cases of Table 6.2 using relative standard deviation (RSD) curves and a mixing index that provides a local viewpoint. Next, the efficiency of the tetrapodal blender to mix bidisperse blends is investigated and compared to reported data from the literature in the case of V-blenders. Finally, the dynamics of granules in each blender is presented to figure out its effect on mixing performance.

6.3.1 Granular flow

The flow of the granules during one revolution of both blenders can be divided into two phases. The first phase corresponds to angular positions $\theta \in [0^\circ, 180^\circ]$ and the second phase to $\theta \in [180^\circ, 360^\circ]$. In the first phase of the V-blender, the granules separate and flow into its two arms, and subsequently recombine at its bottom in the second phase. In each phase of the tetrapodal blender, the particles combine and then flow and separate into the opposite arms. At the end of the first phase (angular position $\theta = 180^\circ$), separation occurs in the Z direction, whereas it does so in the X direction at the end of the second phase (angular position $\theta = 360^\circ$). Therefore, in each revolution of the tetrapodal blender, separation and recombination of the granules happen twice, yet it occurs but once in the V-blender. There are two quasi-static states in the Lagrangian frame of reference of the tetrapodal blender at angular positions $\theta \simeq 45^\circ$ and $\theta \simeq 225^\circ$. This can be confirmed by the zero velocity of the granules (see Section 6.3.4) and means that little mixing takes place around these positions. Other than convection and diffusion arising from the separation and recombination of the material, the rotation of the blender places the blender arms in inclined positions, thereby permitting granules to flow over the corresponding inclined surfaces and mix. The impact of such complex granular flow on the mixing and segregation of granules are investigated in next subsections.

6.3.2 Degree of mixing

Several criteria have been proposed in the literature to measure the homogeneity of a mixture from either a global viewpoint (RSD curves) or a local viewpoint, the latter of which takes into account the Lagrangian trajectories of the particles inside the blender. The degree of mixing in the tetrapodal blender and the V-blender are compared next using both viewpoints.

Global viewpoint : relative standard deviation

The relative standard deviation (RSD) is a well-known mixing index used in particular in the pharmaceutical industry. This method measures the standard deviation σ of the concentration of samples :

$$RSD = \frac{\sigma}{\bar{x}}, \quad (6.6)$$

$$\sigma = \sqrt{\frac{\sum_{i=1}^M (x_i - \bar{x})^2}{M - 1}}, \quad (6.7)$$

where M is the number of samples, x_i the concentration of one species in the i th sample and \bar{x} the mean concentration in the whole blender. As can be deduced from this definition, this index depends on the number, size and location of the samples, as discussed by [Lemieux et al. \(2008\)](#). Employing the RSD in the context of DEM simulations is effortless since the particle positions are available in each time interval and no perturbation occurs inside the granular bed during the sampling procedure ([Muzzio et al., 1997](#)). To obtain the mixing time, the RSD of each simulation should be compared to the RSD of a random mixture, RSD_r ([Paul et al., 2004](#)) :

$$RSD_r = \frac{\sigma_r}{\bar{x}}, \quad (6.8)$$

$$\sigma_r = \sqrt{\frac{\bar{x}(1 - \bar{x})}{m}}, \quad (6.9)$$

where m denotes the number of the particles in one sample and depends on the level of scrutiny. In this study, $m = 100$ particles was chosen ($RSD_r = 10\%$), corresponding to 0.1%, 0.07%, and 0.06% of granules for the 35%V, 50%V and 65%V fill levels, respectively. Such an amount of particles was deemed to represent a good level of scrutiny in this study according to the discussion provided by Lemieux et al. (2008). Samples were chosen from different locations to cover the whole volume of each blender. The number of samples varied between $M = 40$ and 70 for each revolution, depending on the blender type and fill level.

Fig. 6.3 reveals the effect of the fill level and rotational speed on the RSD curves of the standard tetrapodal blender and V-blender (cases A-D). Bear in mind all loading profiles are relevant since the TB and FB profiles are related to radial convective mixing while the RL profile needs axial diffusive mixing. In the case of the FB and TB loading profiles, the RSD curves of the tetrapodal blender decrease more rapidly to RSD_r than those of the V-blender. This suggests more efficient radial convective mixing in the standard tetrapodal blender. Depending on the fill level and the rotational speed, the corresponding mixing time varies between 7-15 and 12-30 revolutions for the standard tetrapodal and V-blender, respectively. For the RL loading profile, axial mixing in the standard tetrapodal blender is conclusively more efficient than the V-blender. Nonetheless, the prevalent mechanism is diffusion so that axial mixing is less efficient than radial mixing.

To compare the mixing rates of the different cases of Table 6.2, a more quantitative analysis was performed by applying a model proposed by Lacey (1954) and used by Lemieux et al. (2007, 2008) :

$$RSD = RSD_r + (RSD_0 - RSD_r)e^{-kN}, \quad (6.10)$$

where N is the number of revolutions, $RSD_0 = \sqrt{\bar{x}(1 - \bar{x})}/\bar{x}$ represents the RSD of a fully segregated mixture and k a coefficient associated with the mixing rate. For the TB and RL loading profiles, it is denoted k_r and k_a , since the relevant mixing mechanism applies in the radial and axial directions, respectively. The results of the FB loading profile are the

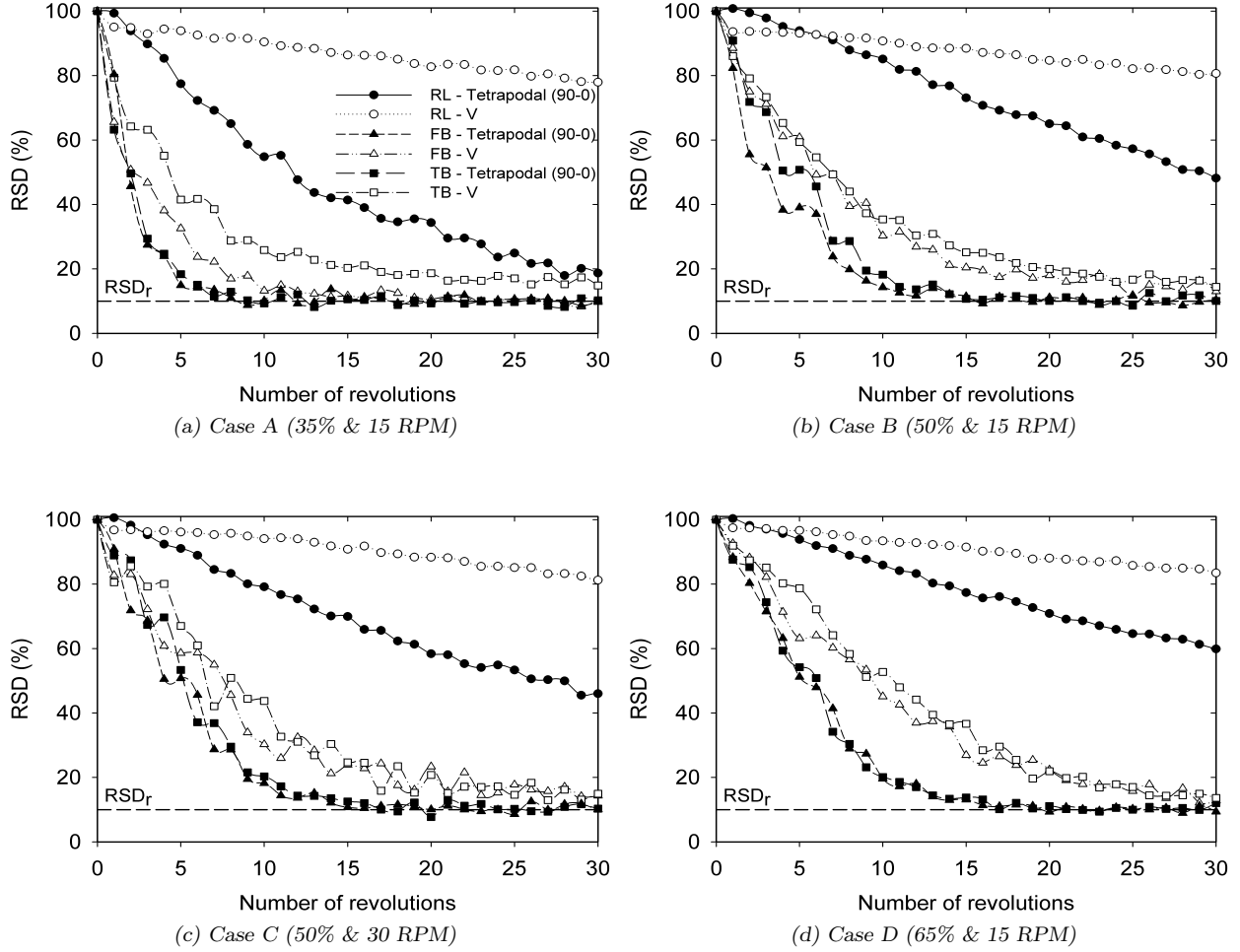


Figure 6.3: Comparison of the RSD curves obtained from DEM simulations for the standard tetrapodal blender and the V-blender underlying different loading profiles and operating conditions.

same as those of TB. The calculated values of these coefficients are presented in Table 6.3 for cases A-H. Comparing the mixing rates of cases A-D reveals that both convective radial and diffusive axial mixing mechanisms in standard tetrapodal blender are more efficient than those in the V-blender. In particular, k_r is twice as large for the standard tetrapodal blender than for the V-blender, which can be explained by the doubled frequency at which the tetrapodal blender pours, separates and recombines the material in one revolution, as was previously mentioned. Increasing the fill level decreases the free volume inside the blenders and, consequently, decreases both the radial and axial mixing rates (compare cases A, B and

D). This was previously reported for the V-blender by [Arratia et al. \(2006\)](#) and [Lemieux et al. \(2007\)](#). The effect of the rotational speed is not as significant as that of the fill level (compare cases B and C). An increase in the rotational speed makes the particles move faster, which then do not have enough time to mix with each other, thereby decreasing the radial mixing rate. At very high rotational speeds, particles may also stick to the blender wall due to the centrifugal force, significantly decreasing the radial mixing rate. The increased axial mixing rates in the tetrapodal blender when the rotational speed is increased can be explained by the higher particle mean axial velocities, as will be explained in Section 6.3.4. Regarding the effect of the geometrical configurations of the tetrapodal blender, the following comments can be made for a rotational speed of $15RPM$ and fill level of 50% :

- In cases E (45-0) and G (90-45) of the twisted tetrapodal blender, the axial mixing rate is of the order of the radial mixing rate. This is mainly due to the asymmetrical shape of this blender in the axial direction, which results in particle trajectories changing more significantly from one revolution to the other. This will be shown in Section 6.3.2 ;
- Compared to the standard tetrapodal blender (case B, 90-0), aligning the tetrapodal blender arms in the axial direction (case F, 0-0) results in a little increase of k_a but decreases k_r to the order of that of the V-blender (case B) ;
- When the blender arms are aligned in the radial direction (case H, 90-90), k_r slightly increases in comparison to the standard tetrapodal blender (case B, 90-0), but k_a is similar. For the same reason, k_r in case G (90-45) is higher than its value in case E (45-0).

These findings suggest that configurations E(45-0) and G(90-45) should be used when weak axial mixing efficiency is a limiting factor, for instance in a V-blender.

Local viewpoint : mixing index

To investigate the state of a mixture, [Doucet et al. \(2008c\)](#) proposed two new mixing indices using Lagrangian trajectories to connect global mixing properties and the local view-

Table 6.3: Mixing rate coefficient (rev^{-1})($\times 10^{-2}$) for the TB and RL loading profiles of cases A-H.

Case	V-blender		Standard tetrapodal blender		Case	Twisted tetrapodal blender	
	k_r	k_a	k_r	k_a		k_r	k_a
A	30	1.0	50	7.0	E	25	21
B	13	0.8	25	2.7	F	13	3.5
C	11	0.8	20	3.0	G	34	23
D	9	0.6	18	1.9	H	34	2.6

point of chaotic theory, for applications to granular and fluid flow systems. Lagrangian trajectories of particles can be obtained either numerically through computer simulation (*e.g.* DEM) or experimentally by means of non-intrusive methods (*e.g.* radioactive particle tracking, [Larachi et al., 1994](#)). These indices provide information as regards the main and secondary directions along which mixing occurs (here the radial and axial directions). They have been applied to assess the quality of mixing in pharmaceutical equipment ([Alizadeh et al., 2012](#); [Bouffard et al., 2013](#); [Doucet et al., 2008a](#)).

More precisely, these two indices are related to two definitions of mixing. First, mixing in the weak sense corresponds to the correlation between the current and initial positions of the particles without respect to their properties. According to this definition, a system is said to be well mixed when the positions of the particles at time t are independent on their initial positions. In other words, the two distributions are no longer correlated. In some systems with particles segregating due to differences in their properties, mixing in the weak sense is not satisfactory as it fails to capture this segregation. Therefore, a more strict definition of mixing was introduced, mixing in the strong sense, which also considers material properties (*e.g.* size, density, shape, etc.). According to this definition, a system is well mixed if the positions of the particles at time t are independent of their initial positions and some of their properties. Therefore, any system that is mixed in the strong sense is also mixed in the weak sense. For more details, the reader is referred to [Doucet et al. \(2008c\)](#). Suffice it to mention here that their values are expected to decay towards zero in a well-mixed system.

DEM results can be readily exploited to evaluate the correlation between the positions of the particles and their initial positions (weak sense) and properties (strong sense). Fig. 6.4 presents the evolution of the weak sense mixing index (β_{ws}) in the different blenders for the monodisperse mixture. The magnitude of this index is expected to decrease with the number of revolutions and, when it reaches a small enough value, for instance 5% of its initial value at $t = 0$ ($\beta_{ws}^o = 1$), it can be concluded that the positions of the particles are no longer correlated to their initial positions. In such a case, it can be inferred that the homogeneity of the mixture is close to that of a randomly mixed system. In the figure, one may observe that in the case of the standard tetrapodal blender and the V-blender, the index decays, but remains way above 0 even after many revolutions due to inefficient axial mixing. Nevertheless, the performance of the tetrapodal blender is significantly better than that of the V-blender. For the twisted tetrapodal blender (45-0), the weak sense mixing index rapidly decays to 0, mainly due to the strong axial mixing mechanism as can be deduced from Table 6.3.

The results above show the better performance of the tetrapodal blender over the conventional V-blender in the case of a monodisperse mixture. The performance of this blender in

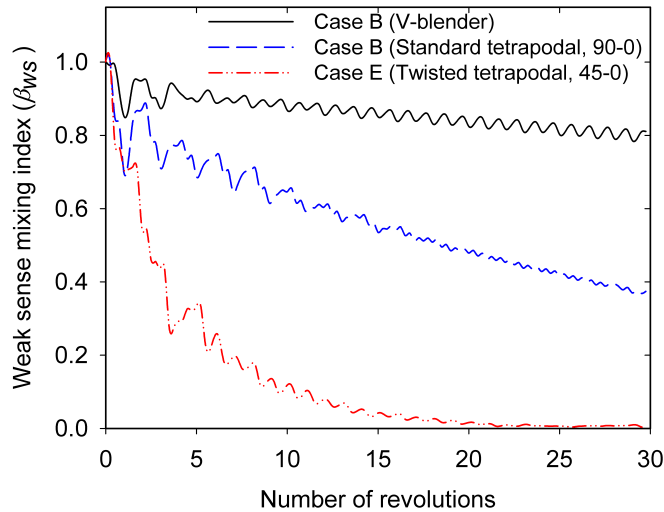


Figure 6.4: Evolution of the weak sense mixing index for the V, standard tetrapodal and twisted tetrapodal blenders.

the case of a binary mixture is considered next.

6.3.3 Segregation

Blender performance comparison

Two simulations were carried out to capture the importance of size segregation for a bidisperse mixture in the standard tetrapodal blender (cases I and J in Table 6.2). The strong sense mixing index, β_{ss} , described in Section 6.3.2 was applied to determine how the different sized granules distribute themselves along the X , Y and Z directions of the blender (see Fig. 6.5). Rather than taking into account the overall mixing index, its components in the X , Y and Z directions are considered. In case I, the granules were initially segregated along the Z direction, then their initial position was correlated to their size. As can be seen in Fig. 6.5a, the value of the Z component of β_{ss} starts at 1, oscillates, and eventually decays to zero. These oscillations of the index are due to the granules traveling from one region of the blender to another. A similar behavior is seen for the Y component of the index, which however starts at 0 due to no initial segregation in this direction. The X component of the index starts at 0 and remains nearly constant with a small amplitude, indicating that no major segregation occurs in the X -direction. In case J, the granules were initially mixed, thus all three components of the index start at 0. These components then oscillate around zero with a small amplitude (less than 0.05), which indicates that no significant segregation occurs in any direction. The fact that similar average values of the components of β_{ss} were asymptotically obtained for both cases I and J reveals that the expected segregation in the standard tetrapodal blender is weak. In all likelihood, continuing the simulations for more revolutions would not change these results.

Given that the mixing mechanisms are less efficient in the V-blender than the tetrapodal blender, obtaining final segregation patterns in this case would require considerable computational time. Therefore, simulations with the bidisperse mixture were not carried out for the V-blender. Instead, reported results from the literature were used to compare the per-

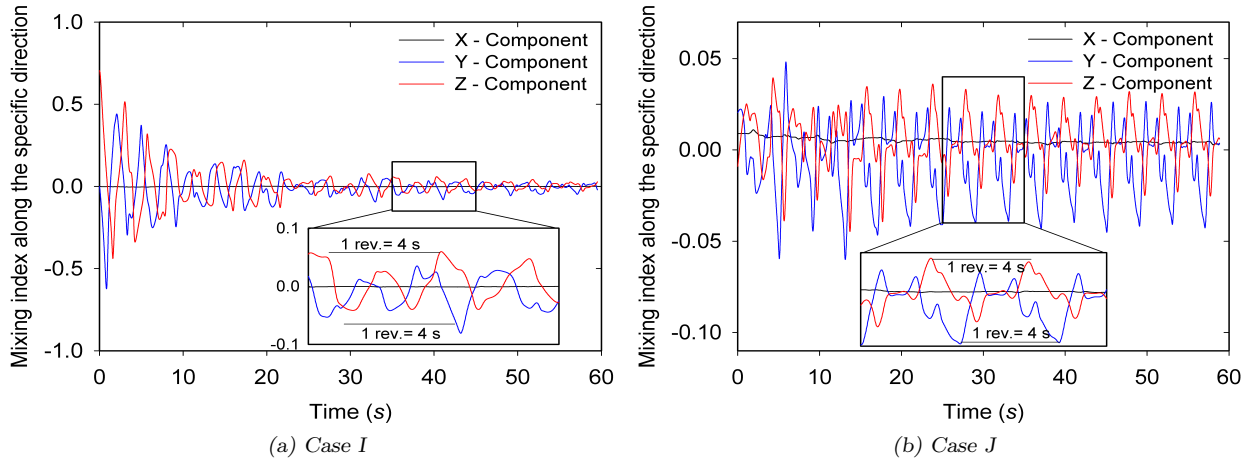


Figure 6.5: Evolution of the strong sense mixing index in the X , Y and Z directions for a bidisperse mixture in the standard tetrapodal blender. The simulations were run from (a) fully segregated (FB loading profile) and (b) fully mixed initial states.

formance of the two blenders. Perhaps the most complete segregation experiments for the V-blender were carried out by Alexander et al. (2003, 2004). In their experiments, after enough revolutions of the blender, specific segregation patterns were visualized for different sized blenders depending on the fill level (30-80%V) and the rotational speed (4-30RPM). Such patterns were captured when the authors did not observe any significant changes for 100 revolutions, thereby indicating that these patterns had converged to a final state. The first state is “small-out”, characterized by a core of the larger particles with the smaller particles at the periphery, next to the shell. In the second segregation profile, a stripe of the smaller particles develops in each of the blender arms. The strongest segregation phenomenon is related to the “left-right” profile and occurs at high enough rotational speeds. In such a case, the smaller and the larger particles are each located on one side of the vertical central plane of the blender. In this pattern, each arm may contain up to 80% of the smaller or larger particles, respectively.

Compared to the segregation patterns observed in the V-blender, the results shown in Fig. 6.5 evidence the superiority of the standard tetrapodal blender. In the next section, the mechanisms that govern the minor segregation inside the standard tetrapodal blender is

discussed.

Mechanisms of segregation in the standard tetrapodal blender

The small oscillations of β_{ss} in Fig. 6.5, which persist with time, indicate the occurrence of small local segregation in the standard tetrapodal blender. Indeed, it can be noticed that these small peaks do not vanish with time and repeat themselves at each revolution of the blender. The corresponding local segregation patterns, as predicted by the DEM, are shown in Fig. 6.6 for angular positions $\theta = 0^\circ$ and $\theta = 180^\circ$. Considering the complicated granular flow inside the blender, several mechanisms govern the formation of these patterns. The rotation of the blender provides inclined surfaces in the blender arms, whereby granules flow downward. For example, note the inclined surface with angle φ in region A of Fig. 6.6b, where the particles flow along the arrows shown. These arrows correspond to the expected velocity profile in such flow (Douady et al., 1999). It should be noticed that, depending on the blender angular position, φ varies. Kinetic sieving is the dominant segregation mechanism in dense granular free-surface flows, which separates large and small particles (Savage and Lun, 1988). If particles slide on the surface of a bulk solid or the inclined surface of a blender, the local void ratio fluctuates. Consequently, there is a higher probability for the smaller particles to percolate through the sufficiently large cavities on the surface. These particles then migrate towards the bottom of the flow thereby pushing the larger particles upwards. As a result, at $\theta = 0$ the large (blue) particles end up close to the free surface, have a higher velocity, and travel a larger distance due to their higher inertia, thus forming region B (Fig. 6.6a). On the other hand, the small (red) particles travel a shorter distance due to smaller inertia and then pour into region C (Fig. 6.6b). Separation of granules when flowing out of an inclined surface due to differences in their velocity is known as “trajectory mechanism” in the literature (Rhodes, 2008). It should be noted that regions B and C are thin layers. For instance, region B cannot be seen from the side view (Fig. 6.6b). Moreover, the occurrence of kinetic sieving in each revolution of the blender does not strengthen the segregation intensity.

This can be explained by the positions of regions with a high concentration of large (I in Fig. 6.6b) and small (II in Fig. 6.6b) particles, corresponding to regions B and C, respectively. As the blender rotates clockwise, region I moves under region II. Consequently, the occurrence of kinetic sieving helps the large particles of layer I to migrate up into layer II, which alleviates segregation and enhances mixing. Such mechanisms involving the movements of regions I and II does not exist in a V-blender. This explains why segregation is problematic in such a blender.

Similar observations can also be made when $\theta = 180^\circ$. When the flowing layer is reduced to a thin layer, the kinetic sieving process is so efficient that the zones with nearly pure large or small particles develop, leading to a sharp concentration jump (regions D and E in Fig. 6.6c). The large particles located in region E (close to the free surface) have a higher velocity (as shown by white arrows in Fig. 6.6c) and then travel a longer distance than the small particles, due to their higher inertia, and end up in region F (Fig. 6.6c).

In the field of kinetic sieving, [Gray and Thornton \(2005\)](#) defined the mean segregation velocity as :

$$q = \frac{\lambda}{c} g \cos(\varphi), \quad (6.11)$$

where g is the gravitational acceleration, c the interparticle drag and λ a dimensionless parameter. This equation indicates there is greater likelihood for segregation in small angled inclined surfaces. However, this can be counterbalanced by increasing the blender rotational speed, which reduces the time spent by the particles along such inclined surfaces. Particles do not, therefore, have sufficient time to separate and less segregation is expected. One could argue that the higher the rotational speed, the more often this mechanism occurs, meaning that segregation remains a priori inevitable. However, this is not the case, thanks to the specific motion of layers of high concentrations of small and large particles, as explained above.

One should keep in mind that this analysis involves a binary mixture and a size ratio of 2.

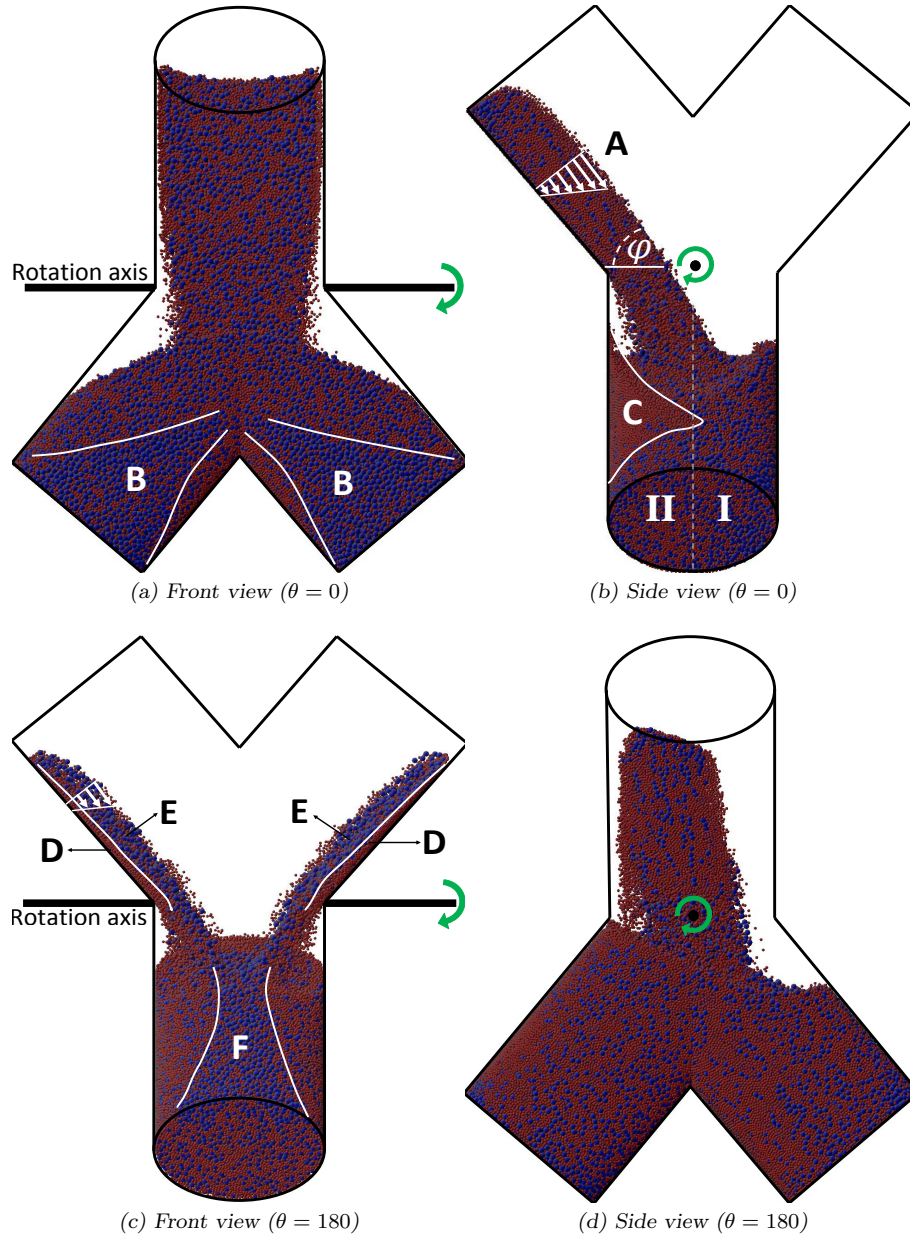


Figure 6.6: Front (a and c) and side (b and d) views of the local segregation patterns in the standard tetrapodal blender (case J). When the granules flow over an inclined surface (region A), kinetic sieving and trajectory mechanisms separate the large (blue) and small (red) granules into regions B and C, respectively. When the flowing layer becomes thin enough, kinetic sieving separates the particles with respect to size into nearly pure layers (D and E). For similar reasons, the larger particles also accumulate in region F.

Segregation may be more significant with larger size or density ratios. In addition to granule properties, operating conditions (*e.g.*, rotational speed and fill level) as well as blender size

and shape may affect the segregation pattern and its intensity. While a similar analysis could in principle be done for all these test cases, this would require many computationally intensive DEM simulations. The idea in this section was to show why the standard tetrapodal blender is efficient in preventing segregation.

In the next section, the effect of particle dynamics on mixing efficiency is investigated for the V-blender and the standard and twisted tetrapodal blenders.

6.3.4 Dynamics of particles

Axial flux of granules

The investigation of the particle dynamics may help understand the mixing mechanisms. Before presenting velocity profiles, it is of interest to look into the axial flux of granules in the different blenders to gain insight into its effect on the axial mixing efficiency. The axial flux is defined as the percentage of particles crossing the axial plane of symmetry of the blender (from left to right and vice versa). Two large peaks can be observed in Fig. 6.7a in the case of the standard tetrapodal blender (P_{T1} and P_{T2}), which are related to the separation of granules between the blender arms in the X and Z directions, respectively. The magnitude of these two peaks is of the same order, confirming that similar amounts of granules cross the axial plane for both cases. The smaller peak P_{T3} corresponds to the position where the second arm of the upper V-shaped part (twisted by 90° with respect to the rotation axis) ends up under the particles that are separating in the Z direction. Also, there are two valleys (V_{T1} and V_{T2}) that belong to the quasi-static positions, as described in Section 6.3.1, where small amounts of granules cross the axial plane. Results for the V-blender (see Fig. 6.7b) show two peaks, one in the separation phase (P_{V1}) and the other in the recombination phase (P_{V2}). Since P_{V1} is larger than P_{V2} , it can be concluded that more mass is transferred during the separation phase than the recombination phase; this was previously reported by Lemieux et al. (2007) and Kuo et al. (2005).

As can be clearly seen from Figs. 6.7a and 6.7b, a higher amount of granules cross the axial

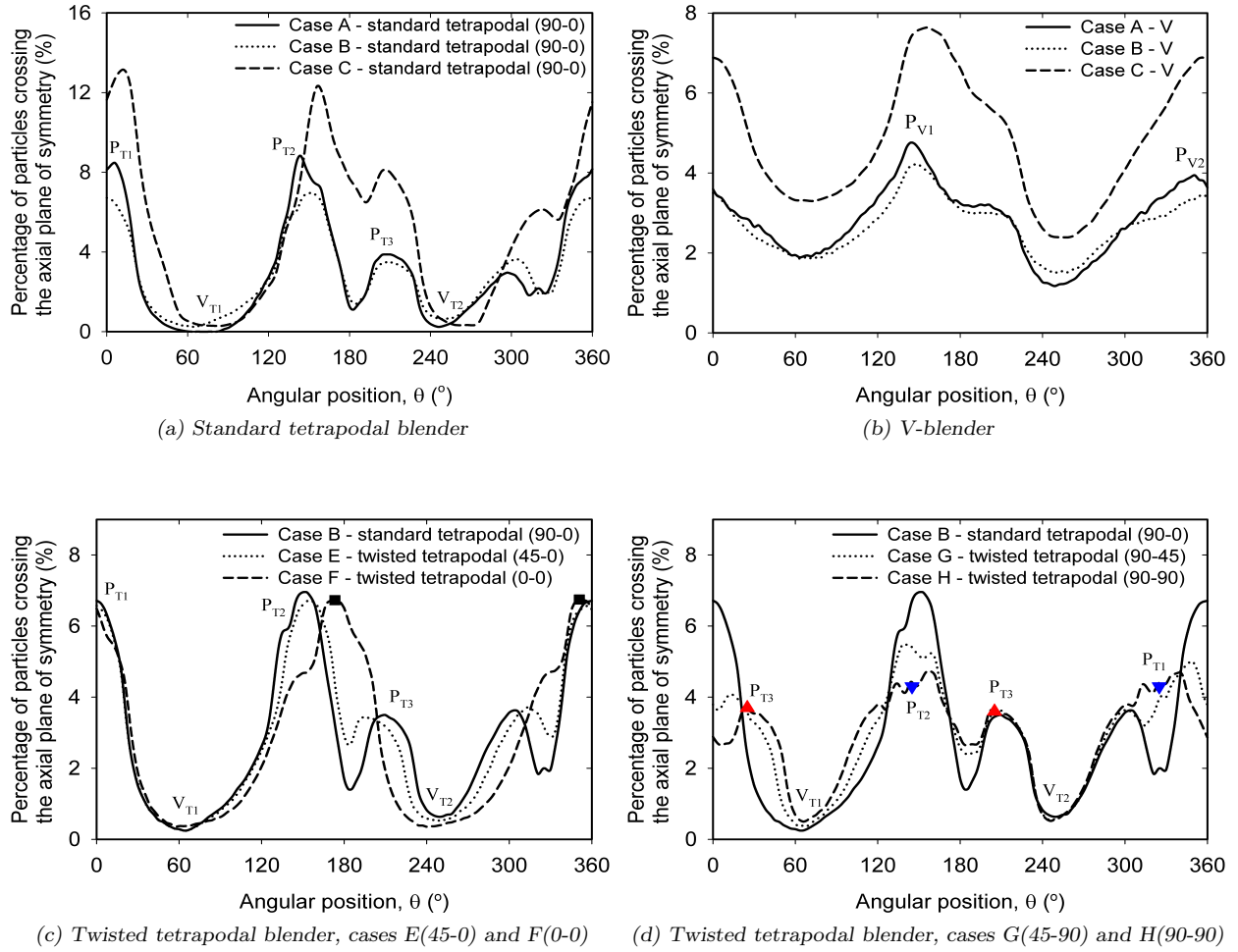


Figure 6.7: Percentage of particles crossing the axial plane of symmetry in a full revolution, for the different blenders and operating conditions.

plane in the standard tetrapodal blender than the V-blender in all cases. The percentage of granules crossing the axial plane is not affected by the fill level (cases A and B) but increases with the rotational speed (cases B and C). The discussion regarding the standard tetrapodal blender also applies to the twisted configurations. Aligning the blender arms in the axial direction from (90-0) to (0-0), as can be observed in Fig. 6.7c, makes P_{T3} smaller in case E and inexistent in case F, while aligning them in the radial direction from (90-0) to (90-90) causes twice the appearance of P_{T3} in cases G and H (for $\theta \in (20^\circ, 30^\circ)$ and $\theta \in (210^\circ, 220^\circ)$ in Fig. 6.7d). In particular, for cases F and H, where the upper and lower parts of the blender

are symmetrical (same twist angle with respect to the rotation axis), similar peaks exist in the first and second phases of the blender operation. Similar peaks are shown with ■ and ▲&▼ symbols for cases F and H, respectively. Despite the similar and smaller percentages of particles crossing the axial plane in cases E and G, respectively, when compared to case B (see Figs. 6.7c and 6.7d), it was shown in previous Section 6.3.2 that these two cases exhibit a more efficient axial mixing mechanism than case B. This suggests that in addition to granules crossing the axial plane, an efficient axial flow is needed to move these granules to regions far from the middle of the blender, and thus guarantee good uniformity throughout the bed. The granular mean radial and axial velocities are investigated next.

Mean granular velocities

Velocity analyses in the V-blender were previously performed by Moakher et al. (2000), Kuo et al. (2005, 2002) and Lemieux et al. (2007, 2008). Fig. 6.8 displays the granular mean radial and axial velocity profiles for the standard tetrapodal blender and the V-blender in the Lagrangian frame of reference over one revolution, the duration of which is 4s and 2s for rotational speeds of 15RPM and 30RPM, respectively. The mean axial and radial velocities are defined as $v_{axial} = v_x$ and $v_{radial} = \sqrt{v_y^2 + v_z^2}$, respectively. Two peaks can be noticed in both cases at 15RPM, the magnitudes of which for the standard tetrapodal blender (P_{T1} and P_{T2}) are significantly larger than those of the V-blender (P_{V1} and P_{V2}). More precisely P_{T1} can be divided into two smaller peaks ($P_{T1,a}$ and $P_{T1,b}$), which are related to the consecutive separations of material in the X direction from one set of two blender arms, twisted by 90° with respect to the rotation axis, into the two opposite arms. This does not happen at higher rotational speed (case C in Figs. 6.8a and 6.8b) because of nearly simultaneous downpours of material within these arms. For both blenders, the velocity profiles increase when the rotational speed increases (case C) and the fill level decreases (case A). The latter can be explained by the volume of free space available for the granules. There are two angular positions ($\sim 45^\circ$ and $\sim 225^\circ$) in the standard tetrapodal blender (V_{T1} and V_{T2}) where the

granules are stagnant in the Lagrangian frame of reference (quasi-static states), while in the V-blender the granules flow in all angular positions. These stagnant regions are wider in lower fill levels (case A). A near zero velocity signifies that the standard tetrapodal blender is without functionality in these zones. To alleviate this limitation, more arms could be added to this blender, though this would make the geometry even more complicated. Twisting the V-shaped parts of the tetrapodal blender affects the velocity profiles. Configurations of cases E(45-0) and F(0-0) have similar (resp. different) lower (resp. upper) V-shaped parts when compared to the standard tetrapodal blender (case B). Therefore, as can be seen from Fig. 6.9a, their radial velocity profiles are similar in the first phase but differ in the second phase. On the other hand, for similar geometrical reasons, the radial velocity profiles of cases B (90-0), G (90-45) and H (90-90) are similar in the second phase but differ in the first phase. Moreover, Fig. 6.9b illustrates that, aligning the arms in the axial direction (from 90-0 to 0-0) increases the mean axial velocity, whereas aligning these arms in the radial direction (from 90-0 to 90-90) decreases it. In particular, for cases F and H, where the upper and lower parts of the blender are symmetrical, two similar profiles are observed in the first and second phases.

While the existence of an axial velocity is necessary for axial mixing, for a given geometry, a higher axial velocity leads to a larger axial mixing rate. This can be inferred from Fig. 6.8b and Table 6.3 for cases B and C of the standard tetrapodal blender. One should however keep in mind that a higher axial velocity does not guarantee more efficient mixing in the axial direction when different blenders are compared. For instance, Fig. 6.9b shows a lower axial velocity for case G (45-90) than for case B of the standard tetrapodal blender (90-0), although axial mixing is more efficient for case G, as shown in Table 6.3. This is mainly due to more efficient granular flow in this twisted configuration of the tetrapodal blender.

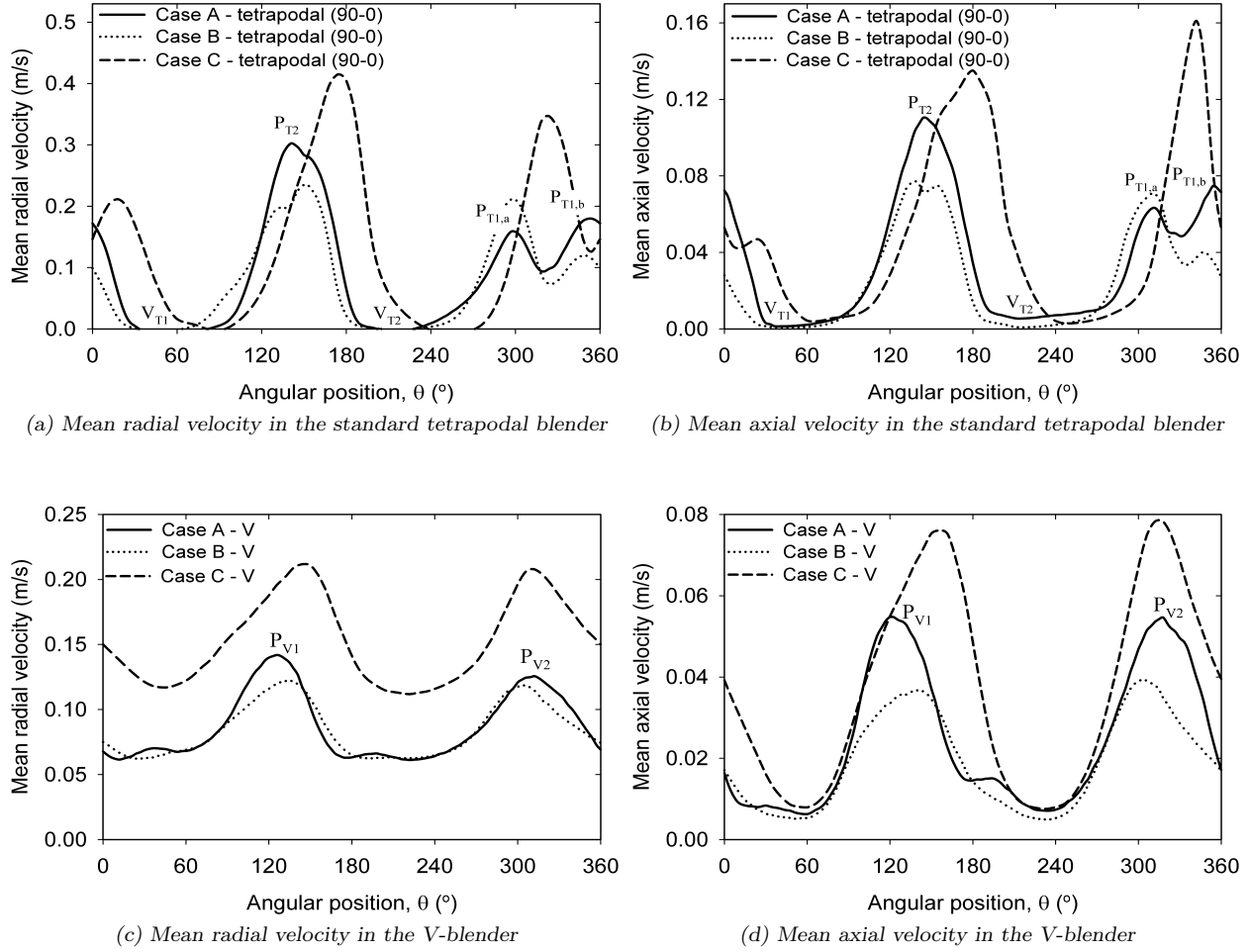


Figure 6.8: Granular mean radial and axial velocities in a full revolution of the different blenders, for operating conditions given in Table 6.2 : (a), (b) standard tetrapodal blender and (c), (d) V-blender.

6.4 Concluding remarks

Limitations of conventional tumbling blenders (weak diffusive axial mixing and segregation of free flowing granules) provided the motivation for investigating the performance of various configurations of the so-called tetrapodal blender with respect to that of a V-blender. Compared to the V-blender, its geometry generates twice the capacity to pour, split and recombine powder material in one revolution. The discrete element method (DEM) was employed to simulate granular flow inside the tetrapodal blender and the V-blender under several

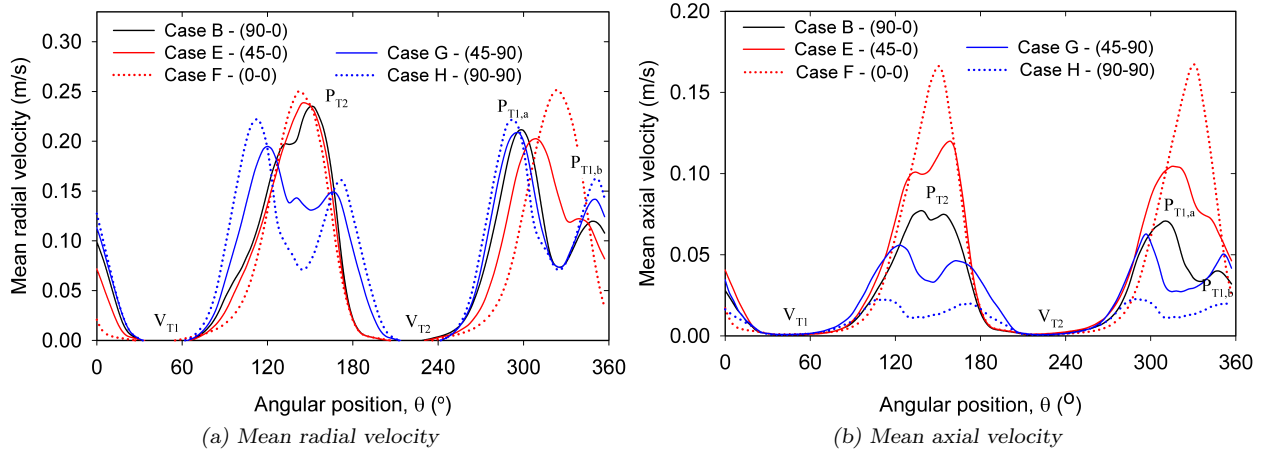


Figure 6.9: Granular (a) mean radial and (b) axial velocities in a full revolution of twisted configurations of the tetrapodal blender, for the operating conditions in Table 6.2.

operating conditions (different loading profiles, fill levels and rotational speeds) with both monodisperse and bidisperse mixtures. The tetrapodal blender showed a shorter mixing time than the V-blender and more efficient convective radial and diffusive axial mixing mechanisms. Moreover, it was demonstrated that if one part (upper or lower V-shaped parts) of the standard tetrapodal blender is twisted by 45° , the axial mixing is significantly enhanced and it becomes likewise efficient as the radial mixing. The particle dynamics inside the blenders were also analyzed to investigate its effect on the overall performance. Higher mean axial and radial velocity profiles were observed for the tetrapodal blender than the V-blender. In addition to a monodisperse mixture, simulations with a binary mixture (size ratio of 2) showed that, contrary to the V-blender, there is no significant segregation in the tetrapodal blender. However, the segregation intensity might be different in situations involving, for instance, large diameter and density ratios. Further investigation could be needed in this field.

Acknowledgments

The financial contribution of Teva Canada, Praxair and the Natural Sciences and Engineering Research Council of Canada (NSERC) is gratefully acknowledged. All simulations

were made possible thanks to the computational resources of Compute Canada.

6.5 References

- Alexander, A., Muzzio, F. J., and Shinbrot, T. (2003). Segregation patterns in V-blenders. *Chemical Engineering Science*, 58(2) :487–496.
- Alexander, A., Shinbrot, T., Johnson, B., and Muzzio, F. J. (2004). V-blender segregation patterns for free-flowing materials : effects of blender capacity and fill level. *International Journal of Pharmaceutics*, 269(1) :19–28.
- Alizadeh, E., Bertrand, F., and Chaouki, J. (2012). Comparison of DEM results and lagrangian experimental data for the mixing and segregation of granules in a rotating drum. *Submitted to AIChE Journal*.
- Alizadeh, E., Bertrand, F., and Chaouki, J. (2013). Development of a granular normal contact force model based on a non-newtonian liquid filled dashpot. *Powder Technology*, 237 :202–212.
- Anderson, M. (1964). Tetrapodal mixing device. US Patent :US 3,134,578.
- Aranson, I. and Tsimring, L. (1999). Dynamics of axial separation in long rotating drums. *Physical Review Letters*, 82(23) :4643–4646.
- Arratia, P., Duong, N.-H., Muzzio, F., Godbole, P., and Reynolds, S. (2006). A study of the mixing and segregation mechanisms in the bohle tote blender via DEM simulations. *Powder Technology*, 164(1) :50–57.
- Baxter, J., Tüzün, U., Burnell, J., and Heyes, D. (1997). Granular dynamics simulations of two-dimensional heap formation. *Physical Review E*, 55(3) :3546–3554.
- Bouffard, J., Bertrand, F., Chaouki, J., and Dumont, H. (2013). Discrete element investigation of flow patterns and segregation in a spheronizer. *Computers and Chemical Engineering*, 49 :170–182.

- Brone, D., Alexander, A., and Muzzio, F. (1998). Quantitative characterization of mixing of dry powders in V-blenders. *AIChE Journal*, 44(2) :271–278.
- Brone, D., Wightman, C., Connor, K., Alexander, A., Muzzio, F. J., and Robinson, P. (1997). Using flow perturbations to enhance mixing of dry powders in V-blenders. *Powder Technology*, 91(3) :165–172.
- Carson, J., Royal, T., and Troxel, T. (1996). Mix dry bulk solids properly and maintain blend integrity. *Chemical Engineering Progress*, 92 :72–80.
- Cundall, P. and Strack, O. (1979). Discrete numerical model for granular assemblies. *Geotechnique*, 29(1) :47–65.
- Douady, S., Andreotti, B., and Daerr, A. (1999). On granular surface flow equations. *European Physical Journal B*, 11(1) :131–142.
- Doucet, J., Bertrand, F., and Chaouki, J. (2008a). Experimental characterization of the chaotic dynamics of cohesionless particles : Application to a V-blender. *Granular Matter*, 10(2) :133–138.
- Doucet, J., Bertrand, F., and Chaouki, J. (2008b). An extended radioactive particle tracking method for systems with irregular moving boundaries. *Powder Technology*, 181(2) :195–204.
- Doucet, J., Bertrand, F., and Chaouki, J. (2008c). A measure of mixing from lagrangian tracking and its application to granular and fluid flow systems. *Chemical Engineering Research and Design*, 86(12) :1313–1321.
- Fischer, J. (1950). Blending or mixing apparatus. US Patent :US 2,514,126.
- Fischer, J. (1983). Dual shell blender with intensifier. US Patent :US 4,368,986.
- Gray, J. and Thornton, A. (2005). A theory for particle size segregation in shallow granular free-surface flows. *Proceedings of the Royal Society of London, Series A (Mathematical, Physical and Engineering Sciences)*, 461(2057) :1447–14473.
- Khakhar, D., McCarthy, J., and Ottino, J. (1997). Radial segregation of granular mixtures in rotating cylinders. *Physics of Fluids*, 9(12) :3600–3614.

- Khakhar, D., Orpe, A. V., and Ottino, J. (2001). Continuum model of mixing and size segregation in a rotating cylinder : Concentration-flow coupling and streak formation. *Powder Technology*, 116(2-3) :232–245.
- Krugger-Emden, H., Simsek, E., Rickelt, S., Wirtz, S., and Scherer, V. (2007). Review and extension of normal force models for the discrete element method. *Powder Technology*, 171(3) :157–173.
- Krugger-Emden, H., Wirtz, S., and Scherer, V. (2008). A study on tangential force laws applicable to the discrete element method (DEM) for materials with viscoelastic or plastic behavior. *Chemical Engineering Science*, 63(6) :1523 – 1541.
- Kuo, H., Knight, P., Parker, D., and Seville, J. (2005). Solids circulation and axial dispersion of cohesionless particles in a V-mixer. *Powder Technology*, 152(1-3) :133–140.
- Kuo, H., Knight, P., Parker, D., Tsuji, Y., Adams, M., and Seville, J. (2002). The influence of DEM simulation parameters on the particle behaviour in a V-mixer. *Chemical Engineering Science*, 57(17) :3621–3638.
- Lacey, P. (1954). Development in the theory of particle mixing. *Journal of Applied Chemistry*, 4 :257–268.
- Langston, P. A., Tüzün, U., and Heyes, D. M. (1995). Discrete element simulation of granular flow in 2D and 3D hoppers : Dependence of discharge rate and wall stress on particle interactions. *Chemical Engineering Science*, 50(6) :967–987.
- Larachi, F., Kennedy, G., and Chaouki, J. (1994). A gamma ray detection system for 3-D particle tracking in multiphase reactors. *Nuclear Instruments & Methods in Physics Research Section A-Accelerators Spectrometers Detectors and Associated Equipment*, A338(2-3) :568–576.
- Lemieux, M., Bertrand, F., Chaouki, J., and Gosselin, P. (2007). Comparative study of the mixing of free-flowing particles in a V-blender and a bin-blender. *Chemical Engineering Science*, 62(6) :1783–1802.

- Lemieux, M., Leonard, G., Doucet, J., Leclaire, L.-A., Viens, F., Chaouki, J., and Bertrand, F. (2008). Large-scale numerical investigation of solids mixing in a V-blender using the discrete element method. *Powder Technology*, 181(2) :205–216.
- Manickam, S., Shah, R., Tomei, J., Bergman, T., and Chaudhuri, B. (2010). Investigating mixing in a multi-dimensional rotary mixer : Experiments and simulations. *Powder Technology*, 201(1) :83–92.
- Mehrotra, A. and Muzzio, F. (2009). Comparing mixing performance of uniaxial and biaxial bin blenders. *Powder Technology*, 196(1) :1–7.
- Mindlin, R. and Deresiewicz, H. (1953). Elastic spheres in contact under varying oblique forces. *Journal of Applied Mechanics*, 20(3) :327–344.
- Moakher, M., Shinbrot, T., and Muzzio, F. J. (2000). Experimentally validated computations of flow, mixing and segregation of non-cohesive grains in 3D tumbling blenders. *Powder Technology*, 109(1-3) :58–71.
- Muzzio, F., Robinson, P., Wightman, C., and Dean, B. (1997). Sampling practices in powder blending. *International Journal of Pharmaceutics*, 26(2) :153–178.
- Muzzio, F. J., Shinbrot, T., and Glasser, B. J. (2002). Powder technology in the pharmaceutical industry : the need to catch up fast. *Powder Technology*, 124(1) :1–7.
- Paul, E., Atiemo-Obeng, V., and Kresta, S. (2004). *Handbook of industrial mixing : science and practice*. John Wiley & Sons.
- Peck, W. C. (1954). Improvements relating to apparatus for mixing discrete particles. GB Patent :GB 709,003.
- Rapaport, D. (2007). Radial and axial segregation of granular matter in a rotating cylinder : a simulation study. *Physical Review E*, 75(3) :31301–1–11.
- Rhodes, M. (2008). *Introduction to particle technology, 2nd edition*. John Wiley and sons.
- Russum, G. (1959). Mixing apparatus. US Patent :US 2,901,227.

- Savage, S. and Lun, C. (1988). Particle size segregation in inclined chute flow of dry cohesionless granular solids. *Journal of Fluid Mechanics*, 189 :311–325.
- Scott, D. M. (2003). Characterizing particle characterization. *Particle and Particle Systems Characterization*, 20(5) :305–310.
- Wonglimpiyarat, J. (2005). Standard competition : Is collaborative strategy necessary in shaping the smart card market ? *Technological Forecasting and Social Change*, 72(8) :1001–1010.
- Zhou, Y., Wright, B., Yang, R., Xu, B., and Yu, A. (1999). Rolling friction in the dynamic simulation of sandpile formation. *Physica A*, 269(2-4) :536–553.
- Zhou, Y., Xu, B., Yu, A., and Zulli, P. (2002). An experimental and numerical study of the angle of repose of coarse spheres. *Powder Technology*, 125(1) :45–54.

CHAPTER 7

Experimental Investigation of Solid Mixing and Segregation in a Tetrapodal Blender

Ebrahim Alizadeh, Habibollah Hajhashemi, François Bertrand, Jamal Chaouki

Department of Chemical Engineering, École Polytechnique de Montréal, C.P. 6079 succ.

Centre-Ville, Montréal, Québec, Canada, H3C 3A7

(Accepted in *Chemical Engineering Science*.)

Presentation of the article : In the previous chapter, using the DEM results, performances of a tetrapodal blender and a V-blender were investigated. Efficiency of tetrapodal blender was observed to be higher than V-blender in the case of free flowing granules regarding the mixing and size segregation. Previously, only one case study was considered for the segregation of granules (bidisperse mixture with size ratio of 2), yet more investigation is needed for unfavorably worst-case scenarios such as granules with large size and/or density ratios. Investigation of all affecting parameters on the segregation intensity with the DEM-based model is time-consuming with current computing facilities. Therefore, it was decided to study the effect of all these parameters experimentally and in addition validate the obtained numerical findings. Obtained results are presented in this chapter.

Abstract : Known limitations of tumbling blenders (weak diffusive axial mixing and segregation of free flowing granules) have provided the motivation to investigate the flow and mixing of granules inside a tetrapodal blender. This blender can be thought of as two V-shaped pairs of arms connected and twisted at their bottom ends. In this work, more than 100 experiments were carried out under a wide set of operating conditions and geometrical configurations. Compared to the conventional V-blender, this geometry is shown to provide shorter mixing times and better axial and radial mixing efficiency, especially when its upper or lower V-shaped part is twisted by 45° with respect to the rotation axis. Segregation of granules with different sizes and densities were investigated for varying rotational speeds ($5\text{-}30\text{RPM}$) and fill levels ($35\text{-}65\%V$). It is observed that the segregation intensity is far less important in the tetrapodal blender than in the V-blender, and that it decreases significantly with an increase in rotational speed, the effect of the fill level being insignificant. It is also shown that kinetic sieving is the main governing mechanism for the segregation of granules. Finally, a criterion is proposed for the scale-up of the tetrapodal blender and the V-blender so that they may operate efficiently, without pronounced segregation.

Keyword : Tetrapodal blender, V-blender, Solid mixing, Segregation, Scale-up, Thief sampling

7.1 Introduction

Tumbling blenders, available for the purpose of granular mixing, have various applications in many industries including ceramic, metallurgical, chemical, food, cosmetics, plastics and pharmaceutical. These blenders are essentially a hollow vessel horizontally attached to a slow rotating shaft, rendering them ideal for shear sensitive materials. Among these types of blenders, rotating drums, V-blenders, double cone and bin blenders (tote and bohle) are the most common. In such blenders, active agents are generally mixed with excipients, and their concentration must be strictly maintained within very small intervals to meet the quality and performance goals.

In tumbling blenders, mixing happens in both axial and radial directions. Axial direction is along the rotation axis of the blender (axis X_1 in Fig. 7.1a) and radial direction is perpendicular to the rotation axis (plane X_2X_3 in Fig. 7.1a). The mixing mechanism is diffusive in the axial direction and a combination of convection and diffusion in the radial direction. Given that diffusive mixing is an order of magnitude slower than convective mixing, tumbling blenders always suffer from weak mixing in the axial direction (Arratia et al., 2006; Brone and Muzzio, 2000; Brone et al., 1997; Lemieux et al., 2007; Moakher et al., 2000). Several attempts have been made to increase axial mixing efficiency (*e.g.* Manickam et al., 2010; Mehrotra and Muzzio, 2009). In addition, these blenders have a tendency to segregate granules differing in size, shape or density into isolated regions. Several studies have been carried out to investigate segregation in a rotating drum (Alizadeh et al., 2013b; Chen et al., 2010), V-blender (Adams and Baker, 1956; Alexander et al., 2003, 2004b; Harnby, 1967; Lemieux et al., 2008; Samyn and Murthy, 1974), double cone blender (Alexander et al., 2001) and bin blender (Arratia et al., 2006). For the most part, these publications concluded that tumbling blenders are inadequate for the mixing of granules which show segregating tendencies.

To alleviate such limitations, we recently undertook an interest in the so-called tetrapodal mixing device. This apparatus was first patented in 1964 (USA patent office, 3,134,578) by Anderson (1964). It can be thought of as two V-shaped pairs of arms connected at their

bottom ends, one of which is twisted by 90° (see Fig. 7.1a). Since its registration as a patent, this blender has not appealed to academia or industry. The only investigation on the performance of this blender was recently performed in our previous work, where it was shown that it is superior to the V-blender (Alizadeh et al., 2013a). There is no application of this blender, despite its technical superiority vis-a-vis conventional tumbling blenders mainly due to the complexity of its geometry and the cleaning step after its operation. In addition to its size and energy required to operate it, the scale-up of this blender for industrial applications might not be straight forward from mechanical point of view. Regardless of such drawbacks, the limitations of conventional tumbling blenders have provided the motivation to investigate solid mixing inside the tetrapodal blender.

Using the discrete element method (DEM), it was shown by Alizadeh et al. (2013a) that the granules separate and recombine twice per each revolution of the tetrapodal blender, yet it occurs but once in the V-blender. Therefore, there is double the ability to pour, split and recombine granular materials in one revolution of the tetrapodal blender. As a result, mixing mechanisms in both axial and radial directions are more efficient than in the V-blender and mixing time is then shorter. Moreover, it was demonstrated that the tetrapodal blender is less prone to segregate different sized granules (size ratio of 2). However, segregation may be more significant with larger size or density ratios. In addition to granule properties, operating conditions (*e.g.*, rotational speed and fill level) as well as blender size and configuration may also affect the segregation pattern and its intensity. Investigating the effect of such parameters on blender efficiency via the DEM-based model would have required many computationally intensive simulations and were not done in that work.

The objective of this study is to experimentally investigate mixing and segregation of free flowing granules in a lab-scale version of the tetrapodal blender. The performance of this blender is compared to that of the V-blender under several operating conditions such as fill level, rotational speed and loading profile. Moreover, the effect of blender configurations on the mixing rate and segregation intensity is studied. Finally, a criterion is given for the

scale-up of this blender.

This article is organized as follows. In Section 7.2, the apparatus, experimental procedure, and materials used are described. In Section 7.3, the observations obtained from experiments are presented and analyzed. Finally, Section 7.4 contains concluding remarks.

7.2 Methodology

7.2.1 Apparatus

Figure 7.1 shows the V-blender and standard tetrapodal blender considered in this study (6.7 liters each in volume). The dimensions of the V-blender were obtained by the scaling-down of typical V-blenders used in the pharmaceutical industry and the dimensions of the tetrapodal blender were designed according to the equivalent volume of this V-blender. In this tetrapodal blender, the joint of the upper and lower V-shaped parts was designed such that the twist angle with respect to the rotation axis can be altered. This enabled the study of the efficiency of various configurations of the tetrapodal blender as will be further described in Section 7.2.3. The tetrapodal blender is made from stainless steel, a common material for the manufacturing of pharmaceutical equipment. There are two sight glasses in each arm of the tetrapodal blender (for a total of 8 windows), allowing the visualization of granular flow throughout the experiments. Note that stainless steel prevents the formation of static forces during the experiments due to its high electrical conductivity. This is of interest, since electrostatic forces were neglected in the DEM simulations conducted in our previous study (Alizadeh et al., 2013a). The V-blender was built with antistatic cast acrylic and its inner layer was covered with a thin aluminum foil to weaken the possibility of occurrence of static forces during the experiments. The rotation of the blenders was guaranteed by a 0.5hp Baldor DC motor coupled to a 50 :1 speed reducer in order to maintain a constant rotational speed.

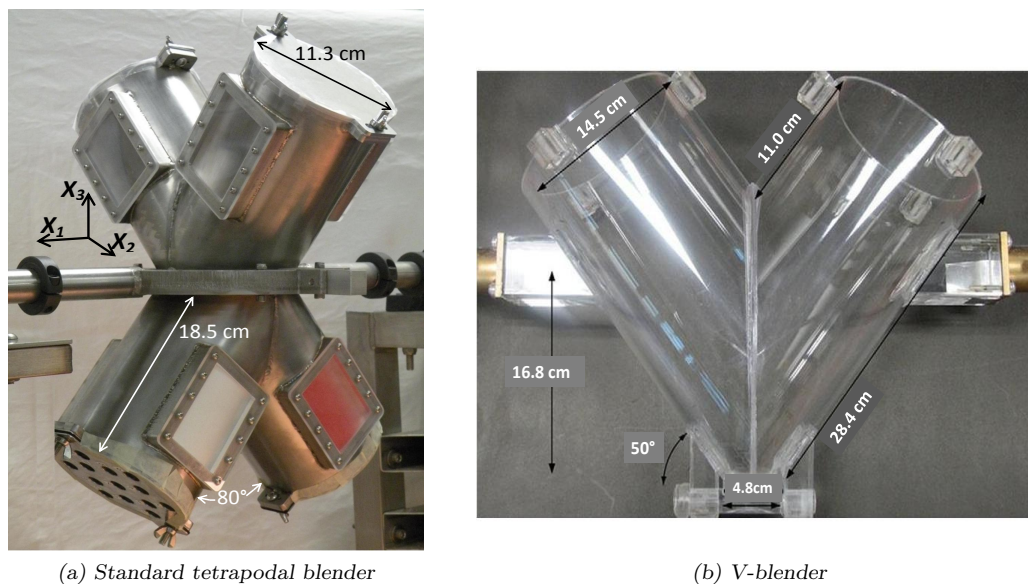


Figure 7.1: Dimension : of the blenders considered in this study ; (a) standard tetrapodal blender, and (b) V-blender.

7.2.2 Materials

The materials involved in this study are spherical free flowing granules and their characteristics are given in Table 7.1. Their size distributions and mean sizes were measured using Beckman LS 13 320 and HORIBA LA-950 particle size analyzers.

To study the mixing efficiency in the tetrapodal blender and V-blender, a red/white mixture of MTL1/MTL2 was employed. MTL1 granules are uniform white spheres (Surespheres from Colorcon) made of sucrose and starch, which are common drug layering pellets in the pharmaceutical industry. To produce the MTL2 granules, white spheres of MTL1 were coated with a red aqueous solution of Opadry II in a fluidized bed and then sieved through 45-mesh ($355\mu m$) and 25-mesh ($710\mu m$) screens prior to the experiments in order to separate broken and agglomerated granules, respectively.

MTL3, MTL4 and MTL5 are commercially available soda lime glass bead spheres. Size and density segregation in the tetrapodal blender were studied in this work using binary mixtures of MTL3/MTL4 and MTL1/MTL5, respectively. Such a size ratio of granules in the MTL3/MTL4 mixture was chosen to accentuate segregation. To make things even worse

Table 7.1: Materials involved in the experiments.

Material	Composition	Size range (mean size) [μm]	Density [g/cm^3]	Color	Supplier
MTL1	Sucrose and starch	450-710 (600)	1.5	White	Colorcon
MTL2	Sucrose and starch	450-710 (600)	1.5	Red	Colorcon
MTL3	Glass bead	750-1000 (875)	2.5	Fushia	SiLi
MTL4	Glass bead	300-430 (365)	2.5	Transparent	Potters
MTL5	Glass bead	500-710 (617)	2.5	Transparent	Potters

as regards segregation, mixtures with different sizes and densities were considered. More precisely, the MTL1/MTL3 mixture consisting of light small and dense big particles was chosen to examine the role of “trajectory” as a segregation mechanism in the tetrapodal blender. In trajectory-governed segregation, if a particle of diameter d_p and density ρ_p , whose drag force is governed by Stokes’ law, is forced to move horizontally with an initial velocity v_o into a fluid of viscosity μ_f and density ρ_f , the distance it can travel horizontally is given by (Rhodes, 2008) :

$$X_d = \frac{v_o \rho_p d_p^2}{18 \mu_f}. \quad (7.1)$$

Therefore, dense big and light small particles have a tendency to travel, respectively, relatively long and short distances and, as a result, segregate from each other.

Finally, a mixture of MTL1/MTL4 (light big and dense small particles) was considered to investigate situations where percolation and kinetic sieving are the governing segregation mechanisms. In kinetic sieving, when particles slide downwards on the surface of a bulk of solids or any inclined surface of a granular bed, there is a higher probability for smaller particles to be caught by sufficiently large cavities. Thus, these smaller particles stay in the cavities and are entrained to the bottom of the flow, whereas the larger particles remain near the free surface and slide down towards the base of the inclined surface. This may also happen for a mixture of granules with different densities, where the denser particles move towards the bottom of the flow and the lighter ones remain near the free surface.

7.2.3 Details of the experiments

The experiments involved three fill levels ($35\%V$, $50\%V$ and $65\%V$ with respect to the total volume of the blenders) and six rotational speeds ω of 5,10,15,20,25 and $30RPM$. These fill levels are within the range of operating conditions of tumbling blenders and rotational speeds yield a tumbling regime suitable for mixing applications (Brone et al., 1998). Raising the fill volume above $70\text{--}80\%V$ would lead to a remarkable reduction in blender efficiency (Sudah et al., 2002).

The experiments are detailed in Table 7.2. Four experiments (cases A-D) were carried out to compare the performance of the tetrapodal blender and the V-blender under several operating conditions. In addition to comparing the performance of these blenders, the effect of tetrapodal blender configurations on mixing efficiency was studied. To do so, experiments E-H were performed, which correspond to the $(45|0)$, $(0|0)$, $(90|45)$ and $(90|90)$ configurations, respectively. These configurations are shown in Fig. 7.2. The first and second numbers correspond to the twist angles of the upper and lower V-shaped parts, respectively, with respect to the blender rotation axis. Based on this definition, the configuration for the standard tetrapodal blender shown in Fig. 7.1a is also denoted $(90|0)$. Throughout the rest of this work, if the twist angles are not mentioned, the tetrapodal blender refers to the standard $(90|0)$ configuration. Cases A-H were carried out for three loading profiles : Top-Bottom (TB, Fig. 7.2a), Front-Back (FB, Fig. 7.2b) and Right-Left (RL, Fig. 7.2c).

Cases I-K were performed to investigate the segregation of different sized granules in three configurations of the tetrapodal blender : $(90|0)$, $(45|0)$ and $(-45|45)$. These experiments were done under several operating conditions, which cover three fill levels (30% , 50% and $65\%V$) and six rotational speeds (5,10,15,20,25 and $30RPM$). Cases L,M and N were performed for one configuration $(-45|45)$, one fill level ($50\%V$) and six rotational speeds. Case L involved a MTL1/MTL5 mixture to examine the effect of different granule densities on the segregation intensity. Note that the granules in this mixture have different densities yet nearly similar mean sizes. Cases M and N correspond to situations, where trajectory and kinetic sieving are

Table 7.2: Characteristics of the experiments.

Case	Fill level [%V]	ω [RPM]	Mixture ¹	Blender(s)	Sample analyzing technique
A	35	15	MTL1/MTL2	Tetrapodal (90 0) and V	Image analysis
B	50	15	MTL1/MTL2	Tetrapodal (90 0) and V	Image analysis
C	50	30	MTL1/MTL2	Tetrapodal (90 0) and V	Image analysis
D	65	15	MTL1/MTL2	Tetrapodal (90 0) and V	Image analysis
E	50	15	MTL1/MTL2	Twisted tetrapodal (45 0)	Image analysis
F	50	15	MTL1/MTL2	Twisted tetrapodal (0 0)	Image analysis
G	50	15	MTL1/MTL2	Twisted tetrapodal (90 45)	Image analysis
H	50	15	MTL1/MTL2	Twisted tetrapodal (90 90)	Image analysis
I	35,50,65	5-30 ²	MTL3/MTL4	Tetrapodal (90 0)	35 US mesh (500 μ m) sieve
J	35,50,65	5-30 ²	MTL3/MTL4	Tetrapodal (45 0)	35 US mesh (500 μ m) sieve
K	35,50,65	5-30 ²	MTL3/MTL4	Tetrapodal (-45 45)	35 US mesh (500 μ m) sieve
L	50	5-30 ²	MTL1/MTL5	Tetrapodal (-45 45)	Washing with water and acetone
M	50	5-30 ²	MTL1/MTL3	Tetrapodal (-45 45)	25 US mesh (710 μ m) sieve
N	50	5-30 ²	MTL1/MTL4	Tetrapodal (-45 45)	35 US mesh (500 μ m) sieve

¹ All mixtures are 50%V-50%V.² Rotational speeds of 5,10,15,20,25 and 30RPM

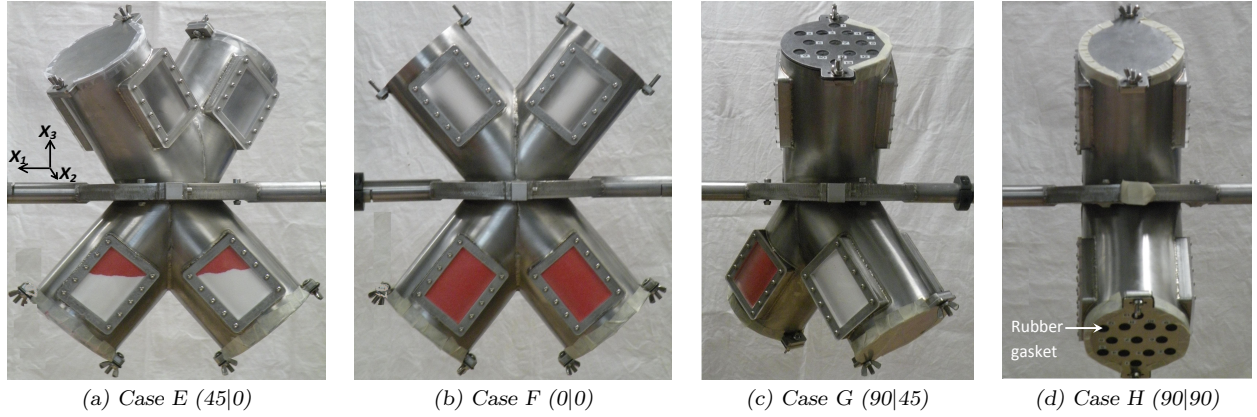


Figure 7.2: Front view of the different configurations and loading profiles of the tetrapodal blender : (a) (45|0) and Top-Bottom (TB), (b) (0|0) and Front-Back (FB), (c) (90|45) and Right-Left (RL), (d) (90|90).

the governing segregation mechanisms, respectively. All the segregation experiments (cases I-N) began from an initially mixed state, following which segregation built up with the rotation of the blender.

A total of 108 experiments were carried out : 36 experiments in cases A-H, 54 experiments in cases I-K, 6 experiments in case L and 12 experiments in cases M-N.

7.2.4 Sampling method

Since the granules are opaque, samples were extracted in order to assess mixture quality. To do so, thief sampling was applied. However, this method disrupts the granular bed, and several studies have been performed to measure its perturbations (Muzzio et al., 1997, 2003). To reduce the perturbations due to sampling, the so-called core sampler (Muzzio et al., 2003) was used in this study to extract samples from the tetrapodal blender (see Fig. 7.3a). It consists of a hollow tube with an internal plugger that can be positioned in different locations to control sample size. Outer and inner diameters of the hollow tube are 9.5 and 6.5 mm, respectively. When the insertion of the sampler is complete, it can be opened by pulling out the plugger to let granules flow inside the sampler. Due to the complex geometry of the tetrapodal blender, sampling was performed solely from the lower V-shaped part. In order to

prevent the flow of granules through sampling holes, a rubber gasket (as seen in Fig. 7.2d) was installed to block these holes after withdrawal of the sampler. Since the granules are free flowing, the extraction of samples with the core sampler from the top of the V-blender is challenging because there is a possibility for the samples to pour out during withdrawal. To avoid such a problem, sampling from the V-blender was carried out using a side sampler. This sampler is similar to the core sampler, but is blind-ended and contains a cavity (see Fig. 7.3b). The dimensions of this cavity are $8mm \times 8mm$, and it can be opened in a controlled manner via an internal plugger. The outer and inner diameters of the hollow tube are $12.7mm$ and $9.5mm$, respectively.

Samples were extracted from different radial and axial positions in each arm of the blenders. The radial locations of the sampling points are shown in Fig. 7.4 and details on the number of samples in each case are given in Table 7.3. Due to the rather large number of sampling holes near the center of each arm in the tetrapodal blender, no samples were extracted from locations 3,5,7,16,18 and 20 in cases A-H (shown by blue circles in Fig. 7.4a). Therefore, up to 20 samples were extracted after fixed numbers of revolutions of the tetrapodal blender. The same number of samples was used in the case of the V-blender; the samples corresponding to the blue circles in Fig. 7.4b were not extracted. For the RL profile of the V-blender, the samples were taken after several more blender revolutions than for

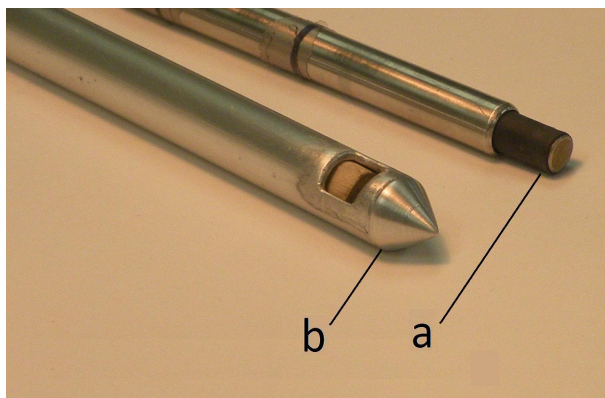


Figure 7.3: Applied (a) core sampler and (b) side sampler in the experiments involving the tetrapodal blender and the V-blender, respectively.

the TB and FB profiles. This is due to the low efficient diffusion mechanism in the case of RL profile, which yields larger mixing times. Note that, all samples for the RL profile were taken from 6 axial locations corresponding to the red circles along the red dashed line of Fig. 7.4b. Sampling from axial locations is enough in such a case since mixing only occurs in the axial direction, as discussed by Muzzio et al. (2003) and Alexander et al. (2004a). Also note that only samples from axial locations (red circles) were extracted after large number of revolutions (20,40,60 and 100) for cases A-H and both blenders to reduce the extent of perturbation due to sampling. This is reasonable given that after a large number of revolutions, axial diffusion becomes the only effective mechanism, radial mixing taking place and completing after the first few revolutions owing to a strong convective mechanism. Finally, in cases I-N, 52 samples were extracted after 1000 blender revolutions. Such a number of revolutions was deemed sufficient because no change in the segregation patterns would be observed from the sight glasses of the tetrapodal blender.

7.2.5 Sample Analysis

The sample analysis techniques used for each case are presented in Table 7.2. The compositions of the extracted samples of cases A-H were determined by means of image analysis. A similar approach was previously applied by Lemieux et al. (2007) and Daumann et al. (2009), where further details about this technique may be found. By resorting to reference samples,

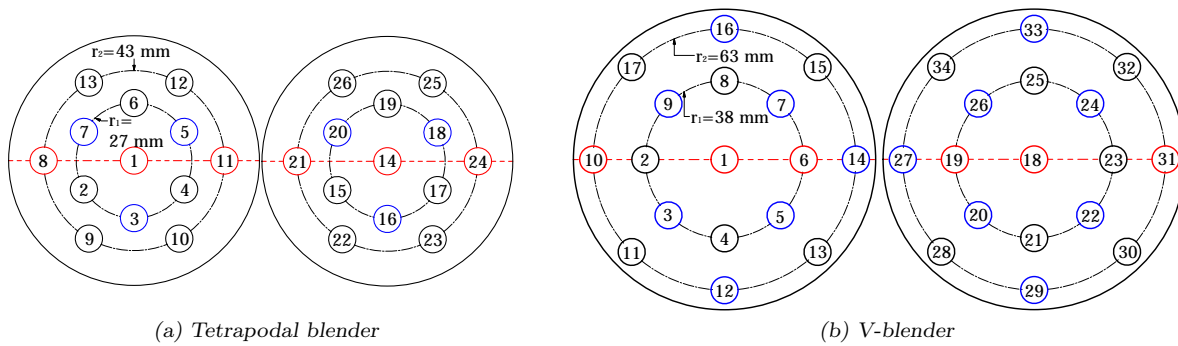


Figure 7.4: Sampling locations for (a) the tetrapodal blender and (b) the V-blender. The red dashed straight lines show the rotation axis of the blenders.

Table 7.3: Number of samples in each case of Table 7.2.

Case	Blender	Loading profile	No. of revolutions (no. of samples)	Total number of samples per experiment
A-D	V	TB, FB	2(20), 5(20), 10(20) 20(6), 40(6), 60(6), 100(6)	84
A-D	V	RL	10(6), 40(6), 90(6) 150(6), 250(6), 400(6)	36
A-H	Tetrapodal	TB, FB, RL	2(20), 5(20), 10(20) 20(6), 40(6), 60(6), 100(6)	84
I-N	Tetrapodal	Initially mixed	1000(52)	52

the image analysis software parameters (Image Processing Toolbox of MATLAB) were first calibrated. The big and small sample granules for cases I-K and N were separated using a 35 US mesh ($500\mu m$) sieve, while a 25 US mesh ($710\mu m$) sieve was used for case M. The weight of each component in each sample was then measured using a scale with an accuracy of $10^{-2}g$. The sample analyses for case L were based on the fact that MTL1 can be washed with water. Therefore, the weight of each sample was first measured, then the sample was washed with hot water, followed by acetone to accelerate the evaporation of water. Finally, the weight of the MTL5 component was measured using a scale, which gave its composition in the sample. Using reference samples, the measurement errors inherent to these methods were observed to be less than 1% for all three techniques.

7.3 Results and discussions

In this section, the performance of the tetrapodal blender is compared to that of the V-blender on the basis of the mixing rate and mixing time. The ability of the tetrapodal blender to obtain a homogenous mixture from granules with segregating tendencies is examined and a criterion is provided for the scale-up of tumbling blenders.

7.3.1 Degree of mixing

The degree of mixing for cases A-H is investigated using relative standard deviation (RSD) curves. The RSD is defined as :

$$RSD = \frac{\sigma}{\bar{x}}, \quad (7.2)$$

with

$$\sigma = \sqrt{\frac{\sum_{i=1}^M (x_i - \bar{x})^2}{M - 1}}, \quad (7.3)$$

where M is the number of samples, x_i the concentration of one specific species in sample i and \bar{x} the mean concentration of this species in the entire blender. Note that the value of this index depends on the number, size and location of the samples. The mixing time is then the time needed to reach RSD value of a randomly mixed blend :

$$RSD_r = \frac{\sigma_r}{\bar{x}}, \quad (7.4)$$

with

$$\sigma_r = \sqrt{\frac{\bar{x}(1 - \bar{x})}{m}}, \quad (7.5)$$

where m is the number of individual granules in one sample. For the cases A-H, the mean number of granules in one sample was ~ 2200 , which gives $RSD_r = 2.1\%$.

To evaluate the sampling procedure and check the reproducibility of the results, the experiments of case B for the tetrapodal blender were repeated for all loading profiles. An average discrepancy of 2.7% on the RSD values was observed illustrating the reproducibility of the data.

The RSD curves of the tetrapodal blender and V-blender are presented in Fig. 7.5 for cases A-D and the TB and FB loading profiles where radial convection is the main mixing mechanism. In all cases, the RSD curves of the tetrapodal blender is observed to decrease more rapidly towards RSD_r . This suggests more efficient radial convective mixing and shorter mixing times in the tetrapodal blender than the V-blender. Likewise, similar behavior is

seen in the case of the RL loading profile in Fig. 7.6, confirming more efficient diffusive axial mixing in the standard tetrapodal blender. Similar results regarding the superiority of the tetrapodal blender to the conventional V-blender were previously obtained using DEM simulations (Alizadeh et al., 2013a). Comparison of the RSD curves in Figs. 7.5 and 7.6 demonstrates that the RL profile is less efficient than the TB and FB profiles, confirming that diffusive mixing is less efficient than convective mixing. This has already been previously reported for other tumbling blenders (Arratia et al., 2006; Brone and Muzzio, 2000; Brone et al., 1997; Lemieux et al., 2007; Moakher et al., 2000). To quantify the mixing rates of cases A-H, the following procedure, which was originally proposed by Lacey (1954), was applied :

$$RSD = RSD_r + (RSD_0 - RSD_r)e^{-kN}, \quad (7.6)$$

where N is the number of blender revolutions, $RSD_0 = \sqrt{\bar{x}(1 - \bar{x})}/\bar{x}$ represents the RSD of a fully segregated mixture and k stands for mixing rate. The k factor in radial (k_r) and axial (k_a) directions are associated to the TB/FB and RL loading profiles, respectively. The values of k are given in Table 7.4 and Fig. 7.7. Note that only the results of the TB profile are used to calculate k_r since they are similar to those of the FB profile.

Fig. 7.7 clearly indicates that the mixing rates in both axial and radial directions are higher for the tetrapodal blender than the V-blender. The mixing rates decrease with an increase in the fill level (cases A,B and D), which can be explained by the decrease in free volume inside the blenders (Arratia et al., 2006). An increase in rotational speed (cases B and C) results in

Table 7.4: Mixing rates ($rev^{-1})(\times 10^{-2})$ for different operating conditions.

Case	V-blender		Standard tetrapodal blender			Twisted tetrapodal blender			
	k_r	k_a	Configuration	k_r	k_a	Case	Configuration	k_r	k_a
A	22	0.8	(90 0)	31	3.0	E	(45 0)	20	20
B	11	0.33	(90 0)	18	2.0	F	(0 0)	10	2.5
C	6.5	0.6	(90 0)	18	2.9	G	(90 45)	31	19
D	3.5	0.15	(90 0)	17	0.95	H	(90 90)	24	0.65

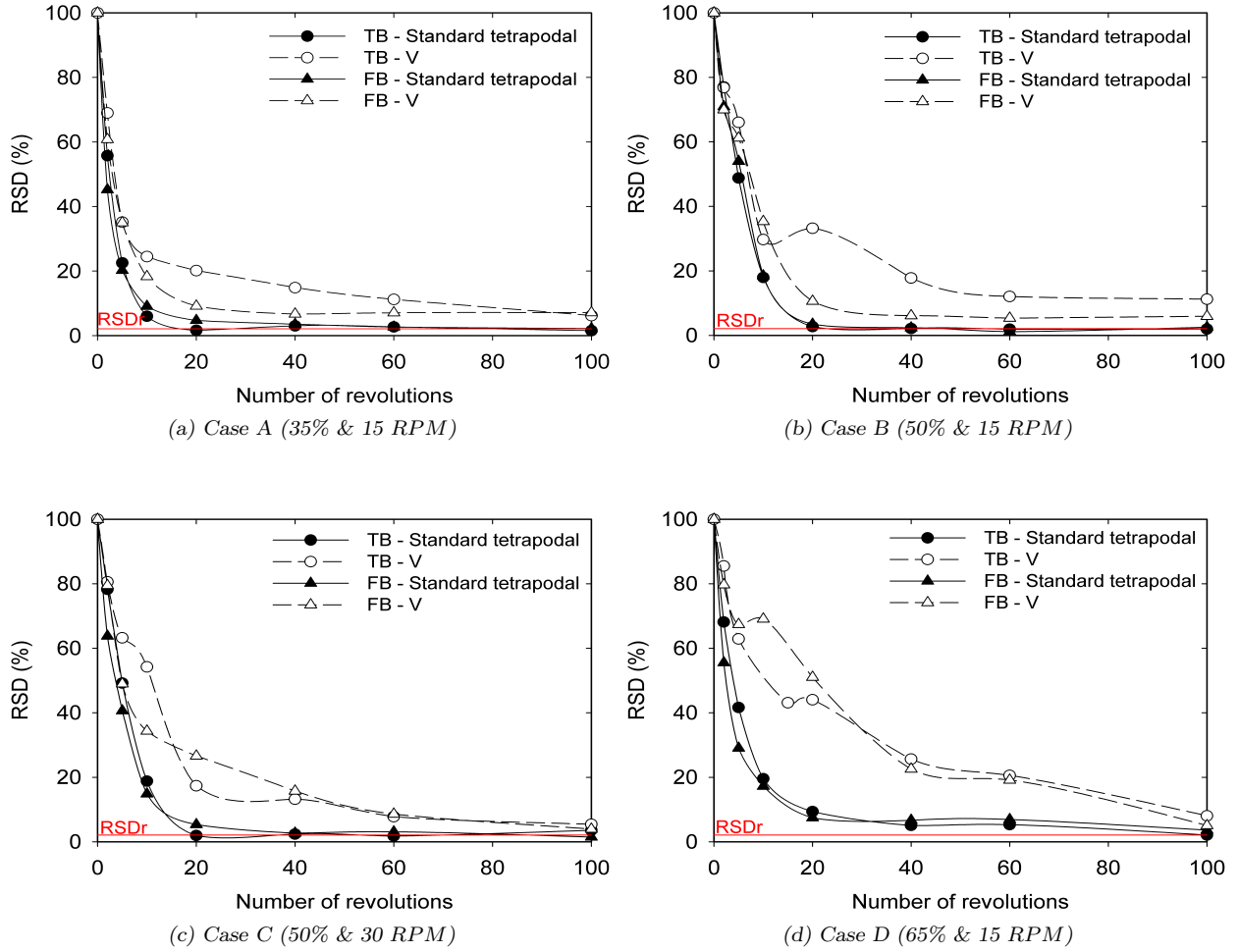


Figure 7.5: Comparison of the RSD curves obtained for the standard tetrapodal blender and the V blender in the case of TB and FB loading profiles under different operating conditions, as summarized in Table 7.2.

particles moving faster, which decreases the time to mix with each other and, consequently, the radial mixing rate. At high rotational speed, some particles stick to the blender wall due to the centrifugal forces, thereby significantly decreasing the radial mixing rate. Such a situation may occur when the Froude number $Fr = \frac{\omega^2 L_{ef}}{g}$ becomes large enough, where L_{ef} is the blender effective length and g stands for the gravitational acceleration (Mellmann, 2001). The effect of the rotational speed on k_a is opposite to that on k_r . This can be explained by the increased percentage of particles crossing the axial plane of symmetry of the blenders and their higher axial velocities, as discussed in Alizadeh et al. (2013a).

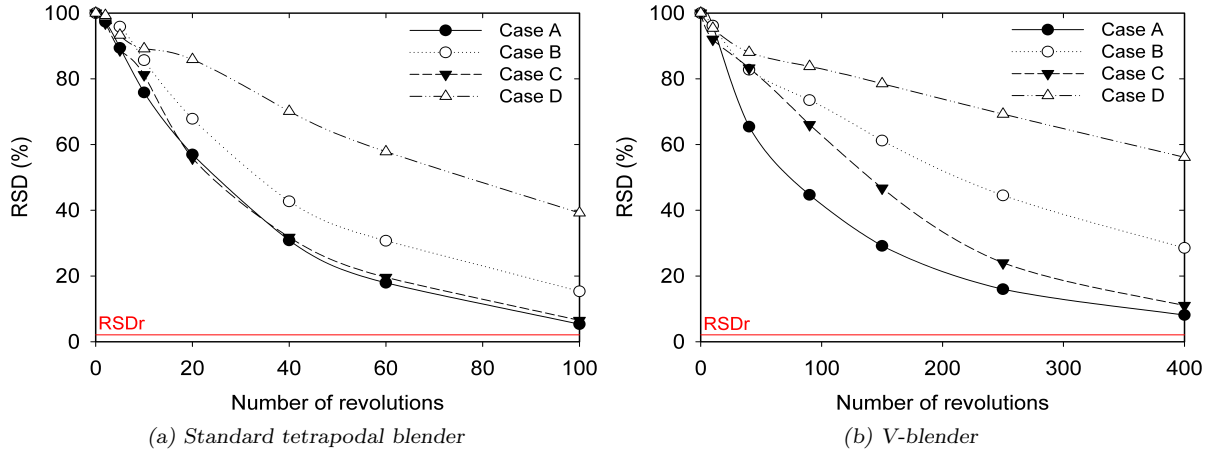


Figure 7.6: Comparison of the RSD curves in the case of RL loading profile under different operating conditions, as summarized in Table 7.2 : (a) standard tetrapodal blender and (b) V-blender.

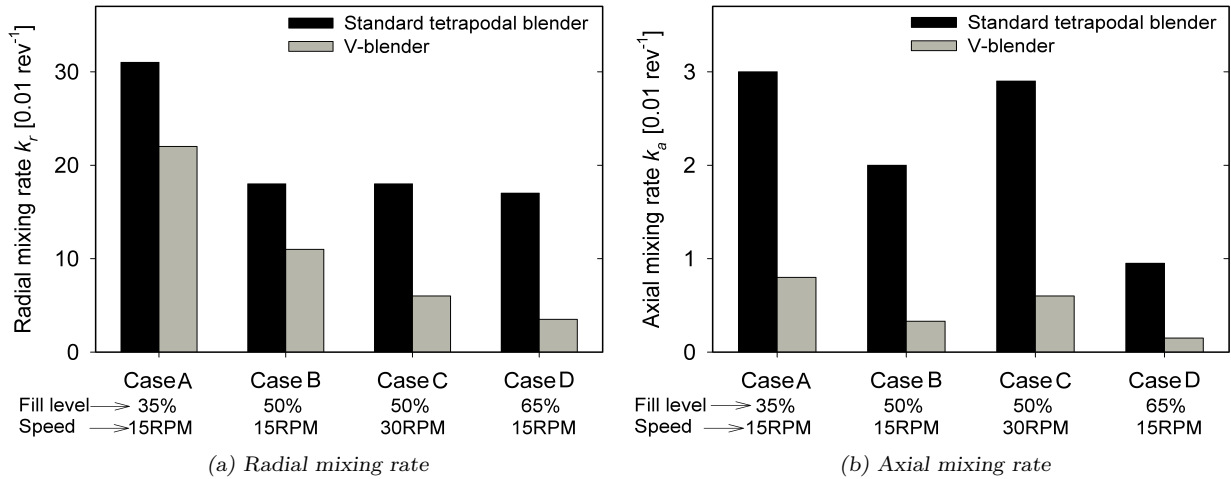


Figure 7.7: (a) Radial k_r and (b) axial k_a mixing rates obtained from the TB and RL loading profiles, respectively. The mixing rates are in $(\text{rev}^{-1})(\times 10^{-2})$.

The higher performance of the tetrapodal blender to the V-blender is largely due to the different granular flow patterns inside the blenders. In the V-blender, all particles exhibit a cascading flow, whereas the rotation of the tetrapodal blender provides larger inclined surfaces within its arms, along which granules may slide (see Fig. 7.10). Flow of granules over

these inclined surfaces provides shear which affects mixing and segregation (Alizadeh et al., 2013a). In fact, it should be noted that both blenders have axial symmetry, which means that granular flow is periodic thereby limiting axial mixing (Adams and Baker, 1956; Alexander et al., 2003). Other configurations of the tetrapodal blender (cases E(45|0) and G(90|45)) do not have axial symmetry and thus granular flow within such equipment is not periodic. Therefore, as can be noticed in Table 7.4, the axial mixing rate for these two configurations are significantly higher than those for the standard tetrapodal blender (case B) and are in the order of the radial mixing rates. Aligning the tetrapodal blender arms in the axial direction (case F, 0|0) allows the granules to flow axially, thus restricting their mobility in the radial direction. Therefore, in comparison with the standard tetrapodal blender (case B, 90|0), k_a increases slightly and k_r reduces to the order of that for the V-blender. In the same manner, when the blender arms are aligned in the radial direction (case H, 90|90), k_r increases and k_a decreases when compared with case B (90|0). As a conclusion, these results show that configurations (45|0) and (90|45) are efficient in improving axial mixing.

7.3.2 Segregation

Segregation index

From a manufacturing viewpoint, it is of importance to identify how segregation influences the performance of blending equipment. RSD curves can be used to investigate segregation from a global viewpoint. Recently, a new index was proposed by Doucet et al. (2008b) to determine the state of a mixture using Lagrangian trajectories to connect the global mixing properties and the local viewpoint of chaotic theory. This index has been applied to assess the quality of mixing in various pharmaceutical equipment (Alizadeh et al., 2012, 2013a; Bouffard et al., 2013; Doucet et al., 2008a). In the literature, one of the most applied criteria to characterize segregation in a system is the intensity of segregation I'_s (Paul et al., 2003). It is defined as :

$$I'_s = \frac{\sigma^2 - \sigma_r^2}{\sigma_0^2 - \sigma_r^2}, \quad (7.7)$$

which describes the ratio of the change in concentration variance to the largest possible change. Here, σ_0^2 corresponds to the variance of a fully segregated state and σ_r^2 is the variance of a randomly mixed blend, which can be obtained from Eq. 7.5. This definition of segregation intensity is normalized so that $I'_s = 1$ and $I'_s = 0$ correspond to completely segregated and randomly mixed states, respectively. However, it appears that it may lack sensitivity when assessing minor segregation phenomena (Rhodes, 2008). For instance, the average index value obtained for case M ($\omega \geq 10RPM$) is 0.005 ± 0.002 , which is very small. Such a small value of I'_s in the range of $I'_s \in (0, 1)$ could mislead a researcher into thinking that the system is fully mixed. However, the mean concentration of MTL1 in these experiments was 0.361 ± 0.036 . Such a large standard deviation (0.036) demonstrates that, despite a low value of I'_s , a considerable amount of segregation occurred inside the tetrapodal blender. Consequently, in this work, a variant of this index is used, where the variance is replaced by the standard deviation :

$$I_s = \frac{\sigma - \sigma_r}{\sigma_0 - \sigma_r}. \quad (7.8)$$

Applying I_s for the experiments of case M ($\omega \geq 10RPM$) results in $\overline{I_s} = 0.059 \pm 0.014$, which we believe reflects more adequately the extent of segregation occurring in the blender.

Comparison of blender performance

Values of I_s for cases I-K are presented in Fig. 7.8, where each graph groups the results of 18 experiments for three fill levels (35,50 and 65%V) and six rotational speeds (5,10,15,20,25 and 30RPM), in the case of a binary mixture of glass beads with two different sizes. As can be seen in this figure, relatively low values of I_s are obtained, particularly when the rotational speed is higher than 10RPM. It should be noted that, due to some minor segregation im-

parted by the sampling procedure, the real values of I_s are in all likelihood even smaller than the reported data. For instance, the mean concentration of big particles if all the samples of cases I-K considered at once (2808 samples) is 0.46, confirming the collection of a larger proportion of small particles in the sampler.

Before going any further, let us mention that segregation in V-blenders have been the topic of a few investigations in the literature. In particular, [Alexander et al. \(2003, 2004b\)](#) used a 50%V-50%V binary mixture of spherical glass beads with two diameters, 780 and 200 μm ,

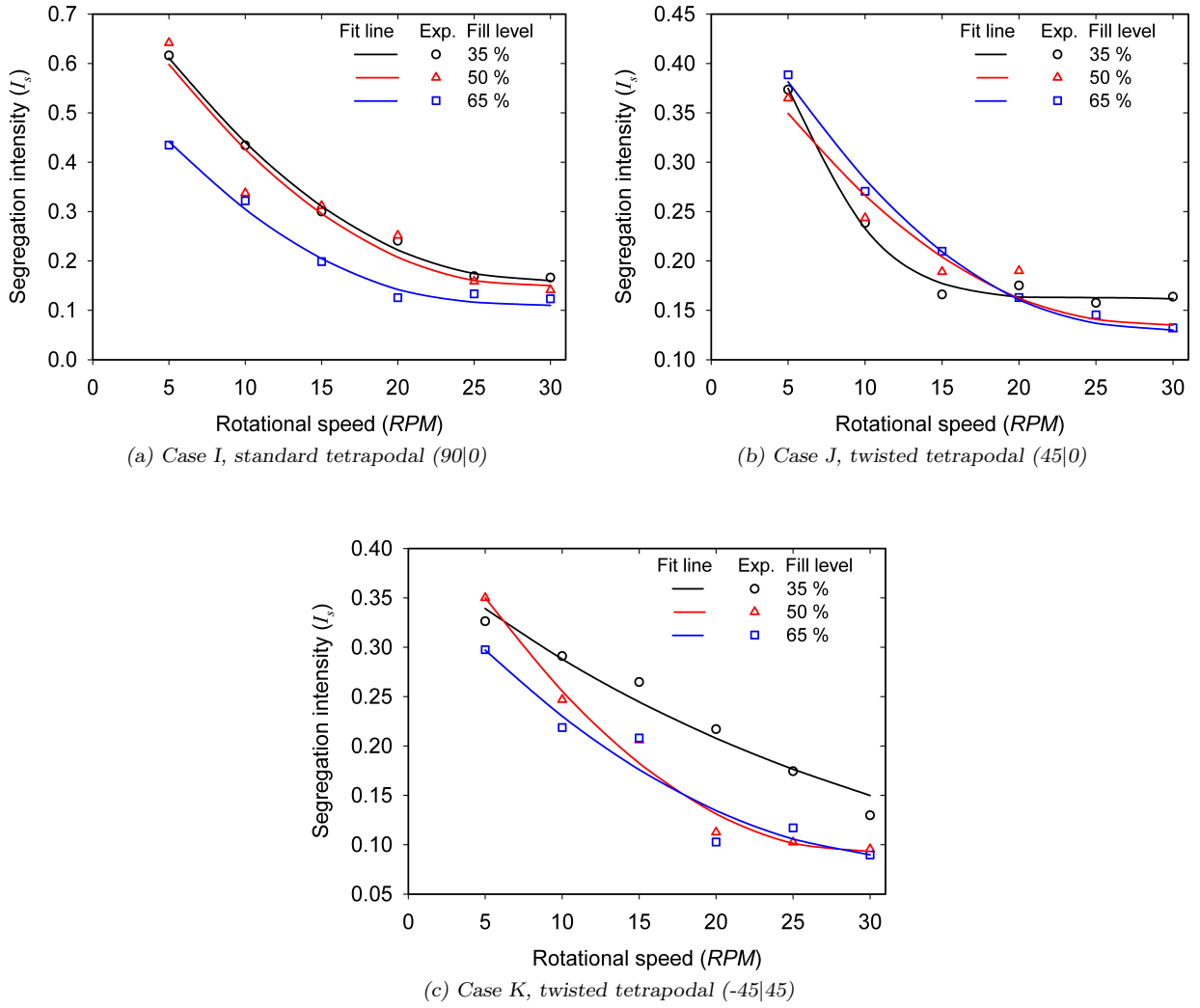


Figure 7.8: Values of I_s for different configurations of the tetrapodal blender under several operating conditions, as summarized in Table 7.2.

which corresponds to nearly similar values of volume fraction, size and size ratio as those used in the current study for cases I-K. In their experiments, significant segregation behaviors were observed for different sized V-blenders depending on the fill level and rotational speed. The first behavior is known as “small-out”, characterize a core of larger particles with smaller particles at the periphery, next to the outer shell. the second segregation pattern, where a stripe of smaller particles develops in each arm of the V-blender, is called “stripes”. The transition between these two patterns is sharp and its rotational speed depends on the size of the blender. This will be examined further later in this paper (see Table 7.6). The third pattern is called “left-right”, where significant segregation happens and a structure is formed with the larger particles on one side of the vertical central plane and the smaller particles on the other side. This pattern occurs at higher rotational speeds and may take hundreds of revolutions to develop. In this pattern, one arm may contain $\sim 80\%$ of the small particles while the other holds $\sim 80\%$ of the large particles. A rough estimation of I_s for such a case, even considering that there is a homogenous mixture of 80% of one size of particles in each arm, results in $I_s = 0.6$, which is remarkably higher than the values reported for the tetrapodal blender, particularly at higher rotational speeds as presented in Fig. 7.8. This demonstrates the higher efficiency of the tetrapodal blender to produce homogenous mixtures and limit segregation.

A left-right pattern was observed in the standard tetrapodal blender (case I). To investigate this phenomenon, average concentrations of big particles (MTL3) in the left and right arms of the tetrapodal blender are given in Table 7.5. These data were obtained by averaging the concentration of samples in each arm. As discussed in detail by Alexander et al. (2003, 2004b), this pattern is not a result of a non-leveled blender, since small (or big) particles appear on either the left or right arm of the blender with nearly equal frequency. To illustrate, for case I and a fill level of $65\%V$ and a rotational speed of $5RPM$, most of the big particles ended in the right arm, whereas for a fill level of $50\%V$ and a rotational speed of $5RPM$, they ended in the left arm. In fact, the left-right pattern disappears with an increase

in rotational speed and, at $30RPM$ nearly the same concentration of big particles is formed in each arm. This is in contrast to the V-blender behavior, where this pattern appears mostly at high rotational speeds. In other words, this behavior of the tetrapodal blender permits proper operation at high rotational speeds. Note that the left-right pattern was not observed in the other configurations of the tetrapodal blender (cases J and K). This may be primarily related to the periodic granular flow in case I (similar to the V-blender), which does not occur in the twisted tetrapodal blenders used for cases J and K. The impact of flow periodicity on segregation was previously reported by [Adams and Baker \(1956\)](#), where they studied the segregation of polyethylene granules inside a V-blender, a double cone and rotocube, and concluded that repeated periodic motions are insufficient in preventing segregation.

Effect of operating conditions on segregation intensity

As can be seen in Fig. 7.8, the segregation intensity slightly decreases in all cases with an increase in the fill level. This is the result of a reduction of the free volume of the blender, in which granules flow, mix and segregate. Contrary to the fill level, the segregation intensity decreases significantly with an increase in the rotational speed. The performance of the blenders is not satisfactory when the rotational speed is very low ($5RPM$) as they yield relatively

Table 7.5: Average concentrations of big particles (MTL3) in the left (white) and right (blue) arms of the tetrapodal blender; these data were obtained by averaging the concentration of samples in each arm.

Case	Fill level [%V]	5 RPM		10 RPM		15 RPM		20 RPM		25 RPM		30 RPM	
I	65	0.26	0.61	0.35	0.59	0.39	0.54	0.45	0.47	0.47	0.46	0.46	0.49
	50	0.69	0.15	0.36	0.54	0.35	0.60	0.36	0.55	0.43	0.51	0.44	0.49
	35	0.23	0.79	0.34	0.65	0.32	0.54	0.37	0.56	0.44	0.52	0.42	0.46
J	65	0.54	0.41	0.50	0.39	0.51	0.41	0.49	0.44	0.47	0.43	0.44	0.45
	50	0.36	0.46	0.40	0.50	0.47	0.49	0.50	0.40	0.48	0.44	0.47	0.44
	35	0.44	0.50	0.42	0.50	0.43	0.49	0.45	0.48	0.45	0.46	0.45	0.48
K	65	0.42	0.47	0.44	0.46	0.44	0.43	0.47	0.49	0.47	0.47	0.46	0.47
	50	0.50	0.44	0.46	0.49	0.46	0.46	0.45	0.46	0.47	0.46	0.49	0.46
	35	0.51	0.43	0.48	0.53	0.51	0.50	0.52	0.47	0.52	0.49	0.49	0.45

high segregation.

The effect of the rotational speed on the segregation intensity may be explained by the mechanisms that govern the segregation inside the tetrapodal blender, which were previously investigated using DEM simulations (Alizadeh et al., 2013a). When the blender is rotating, the angular positions of its arms varies continuously, thereby providing inclined planes along which granules may slide. Kinetic sieving is the dominant segregation mechanism in such dense granular free-surface flows (Savage and Lun, 1988). Using continuum mixture theory and a direct analogy with the percolation of fluids through a porous matrix, Gray and Thornton (2005) showed that the corresponding mean segregation velocity q is larger in horizontally low-angled (α) surfaces. It is defined as :

$$q = \frac{\lambda}{c} g \cos(\alpha), \quad (7.9)$$

where g is the gravitational acceleration, λ a dimensionless parameter and c the interparticle drag coefficient in units of reciprocal seconds. The interparticle drag coefficient depends on the particle size, size ratio and density as well as the surface properties. It has a smaller value for a system containing light big and dense small particles. However, the exact nature of this parameter is poorly understood and, therefore, it is taken as constant in this work (Marks et al., 2012). Higher rotational speeds reduce the time spent by the particles along such low-angled inclined surfaces, which means that these particles do not have enough time to separate so that less segregation happens, as confirmed by the data in Fig. 7.8.

Considering the good performance of the tetrapodal blender at high rotational speed, one may conclude that it comes from the fact that initially fully mixed granules move more or less as a solid body, thereby limiting their segregation. It should be noted that the initial segregation intensity I_{s_0} of the loaded mixture was measured three times for case I and a fill level of 50%V, which gave an average value of 0.24 ± 0.03 . This demonstrates that minor segregation occurred when loading the granules into the blender, meaning that the mixture was not perfectly mixed initially. Note that the value of I_{s_0} is larger than values of I_s obtained

at high rotational speeds. For instance, $I_s < 0.10$ for the twisted (-45|45) tetrapodal blender of case K and fill level larger than 50% V (Fig. 7.8c). To check the ability of the blender to mix initially segregated granules, one experiment was carried out for the TB profile and case I with a 50% V fill level and a rotational speed of 30*RPM*. In such a case, the value of I_s is 0.18, which is indeed close to 0.14 for a fully mixed initial state.

Segregation of granules with different densities

In Fig. 7.8, case K (-45|45) shows the best performance with $I_s < 0.10$ for a rotational speed larger than 20*RPM* and a fill level above 50%. As a result, this configuration was chosen to study the effect of density (case L) and the simultaneous effects of size and density (cases M and N) on the segregation intensity. The experiments for such cases were performed only for the 50% V fill level, since the effect of fill level on the segregation intensity is not significant. The results of these experiments are shown in Fig. 7.9. It can be noticed that the segregation intensity for case L, notably at higher rotational speeds, is relatively small ($I_s < 0.05$). This implies that the effect of the particle density on the segregation is not significant and a reasonably homogenous mixture is obtained.

The goal of cases M and N are to examine the role of the trajectory (case M) and kinetic sieving (case N) mechanisms concerning granular segregation in the tetrapodal blender. From Fig. 7.9, it can be seen that less segregation happens in case M than case N, confirming that trajectory is less important than kinetic sieving as a segregation mechanism.

For cases L-N, the segregation is intense at a rotational speed of 5*RPM* and decreases significantly when the rotational speed increases to 10*RPM*. It seems that there is a transition rotational speed between 5 and 10*RPM*, below which high segregation intensity is observed. As such a speed may vary with the size of the blender, the operating conditions should be set to work away from this point. In the next section, a criterion is provided to help design larger tetrapodal blenders.

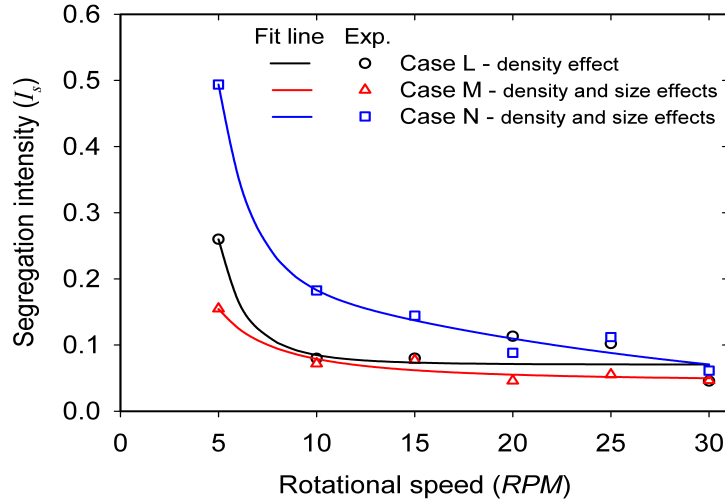


Figure 7.9: Effect of density and simultaneous effects of density and size of granules on the segregation intensity in the twisted tetrapodal blender (-45|45) for various rotational speeds, as summarized in Table 7.2.

Scale-up of tumbling blenders

The scale-up of solid mixing processes from lab- to industrial-scale is of paramount importance for their development. Nonetheless, developing efficient criteria for the scale-up of such processes is challenging due to the complex behavior of granular flow. Generally, there are no accepted rules for determining the operating conditions when equipment size is changed, and most of the recent attempts have focused on the simple geometry of a rotating drum (Ding et al., 2001; Ottino and Khakhar, 2002; Pignatelli et al., 2012). In industrial practice, the two most commonly applied methods are based on matching either the vessel tangential speed (ωL_{ef} , where L_{ef} is blender effective length) or the Froude number. In particular, it was shown by Alexander et al. (2002) that neither of these methods respect kinematic similarity even in the rotating drum. By resorting to dimensionless analysis, Alexander et al. (2002) showed that the quantity $\omega^{2/3} L_{ef} (g/d_p)^{1/6}$ effectively scales the particle velocity in a rotating drum when the rotational speed is below 30 RPM whereas $\omega^{1/2} L_{ef} (g/d_p)^{1/4}$ can be applied for rotational speeds above 30 RPM, where d_p is the particle size. Although these terms are effective in correlating the blender size and operating conditions, trusting such criteria when

granules made of different materials are used in the lab- and industrial-scale equipments is risky. In such a case, it should be noted that in addition to particle size, other properties (*e.g.* density and surface roughness) may also be different, which may affect the equipment performance. If the same material is used but the particle sizes varies, the driving force for granular motion may change owing for instance to a variation of interparticle forces. In particular, the term $\omega^{2/3} L_{ef}(g/d_p)^{1/6}$ was experimentally shown by [Alexander et al. \(2004b\)](#) to be efficient for the scale-up of V-blenders, and made them infer that the segregation patterns may be governed by the magnitude of the particle velocities. However, they did not theoretically investigate the role of the particle velocity on the segregation in V-blenders. It should be noted that the term $\omega^{2/3} L_{ef}(g/d_p)^{1/6}$ has been developed for rotating drums and its utilization for other blenders may be precarious. The aim of this section is to provide a theoretical study on the scale-up of the tetrapodal blender based on the segregation mechanisms prevailing in such a blender. The findings of such an investigation could be extended to the V-blender in that, in both blenders, particles slide on inclined surfaces of their arms, which may lead to segregation.

To provide a criterion for scale-up, the so-called segregation number introduced by [Gray and Thornton \(2005\)](#) for kinetic sieving over inclined surfaces is used, which is the ratio of the mean segregation velocity (q) to the average magnitude of the bulk velocity :

$$S_r = \frac{ql}{h\bar{u}}, \quad (7.10)$$

where l is the length of the inclined surface and h and \bar{u} denote respectively the thickness of the flowing layer and the average velocity of the particles across the thickness of this flowing layer ($\bar{u} = \frac{1}{h} \int_0^h u \, dr$). Substituting the segregation velocity q from Eq. 7.9 into Eq. 7.10 gives :

$$S_r = \frac{g\lambda l \cos(\alpha)}{c \, h \, \bar{u}}. \quad (7.11)$$

Recall that c is the interparticle drag coefficient and λ a dimensionless parameter. The va-

riables of this equation may be associated to the tetrapodal blender, as shown in Fig. 7.10a. This figure comes from results of DEM simulations which were performed in our previous work (Alizadeh et al., 2013a). The value of $\cos(\alpha)$ depends on the angular position of the blender (θ), l can be thought of as the length of each arm, \bar{u} is a function of the rotational speed, the blender size as well as the blender angular position, and h depends on the blender angular position, the radius R of the blender arms and the fill level. Therefore, it follows that in addition to the blender dimensions and operating conditions, S_r also varies with the blender angular position. For this reason, the mean time value of the segregation number over the period within which granules slide on the blender arms and segregation happens, is introduced and denoted by $\overline{S_r}$. Accordingly, expressions for the mean time values of $\cos(\alpha)$ and \bar{u} can be obtained by varying α from α_i to α_f , where α_i corresponds to the angle when granules start sliding along the surface of the blender wall and α_f to that when these granules have terminated their descent :

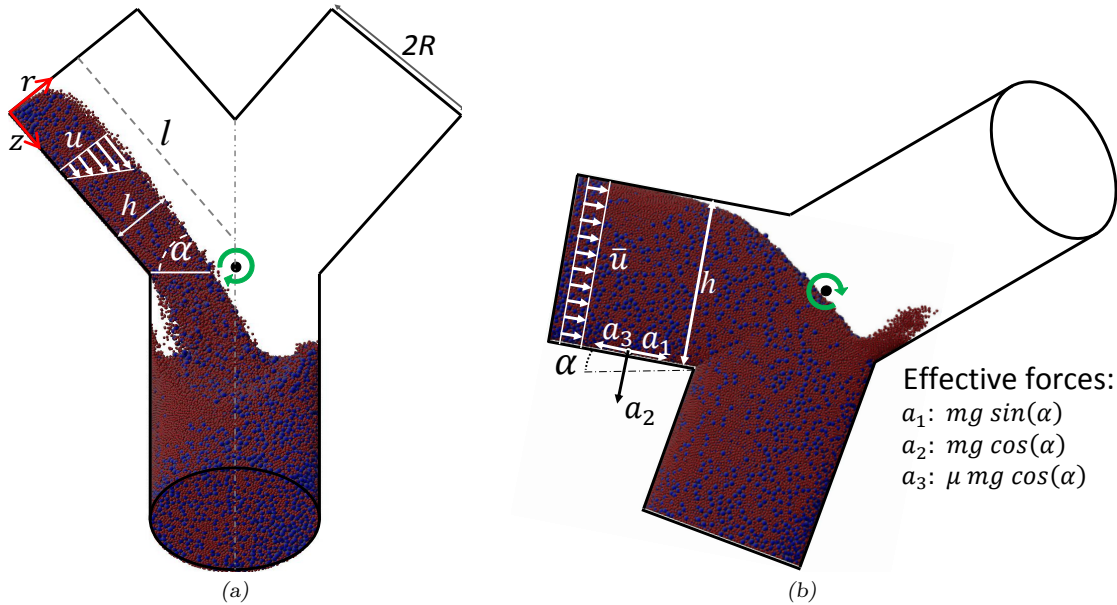


Figure 7.10: (a) Regular granular flow in the tetrapodal blender, (b) granular flow in the simplified model of this work for the scale-up of the blender. The red and blue colors correspond to the two types of particles in the system.

$$\overline{\cos(\alpha)} = \frac{1}{\Delta\alpha} \int_{\alpha_i}^{\alpha_f} \cos(\alpha) d\alpha = \frac{\sin(\alpha_f) - \sin(\alpha_i)}{\Delta\alpha}, \quad (7.12)$$

$$\overline{\overline{u}} = \frac{1}{\Delta\alpha} \int_{\alpha_i}^{\alpha_f} \overline{u} d\alpha. \quad (7.13)$$

where $\Delta\alpha = \alpha_f - \alpha_i$.

To approximate \overline{u} , α_i and α_f , a simplified model of granular flow over the blender arms can be used, as shown in Fig. 7.10b. In this model, it is assumed that all granules flow with a uniform velocity \overline{u} so that the thickness of the flowing layer h is constant ($h = 2R$). Combining Newton's second law of motion and the effective forces illustrated in Fig. 7.10b gives the following expression for the granule acceleration a :

$$a = g \sin(\alpha) - \mu g \cos(\alpha), \quad (7.14)$$

where the second term ($\mu g \cos(\alpha)$) comes from the Coulomb friction law and μ is the friction coefficient. It can then be inferred that granules start to slide along the blender arm when this acceleration becomes positive ($a > 0$), which yielded :

$$\alpha_i = \tan^{-1} \mu. \quad (7.15)$$

Integrating the acceleration (Eq. 7.14) once and twice with respect to time t , yields the velocity \overline{u} of the granules and the distance z that they travel along the blender arm, respectively. By correlating t to the angle α of the inclined surface, the integration can be performed with respect to α :

$$t = \left[(2m + 1) \frac{\pi}{2} + \alpha \right] \frac{60}{2\pi\omega}, \quad (7.16)$$

where even values of m correspond to the first phase of the blender operation ($\theta = 0^\circ - 180^\circ$) and odd values refer to its second phase ($\theta = 180^\circ - 360^\circ$). It follows from $dt = \frac{60}{2\pi\omega} d\alpha$ that :

$$\bar{u} = \frac{60}{2\pi\omega} \int a \, d\alpha = \frac{60}{2\pi\omega} (-g \cos(\alpha) - \mu g \sin(\alpha) + \bar{u}_o), \quad (7.17)$$

$$z = \frac{60}{2\pi\omega} \int \bar{u} \, d\alpha = \left(\frac{60}{2\pi\omega} \right)^2 (-g \sin(\alpha) + \mu g \cos(\alpha) + \bar{u}_o \alpha + z_o), \quad (7.18)$$

where \bar{u}_o and z_o are obtained by applying $\bar{u}|_{\alpha_i} = 0$ and $z|_{\alpha_i} = 0$, which leads to :

$$\bar{u}_o = g \cos(\alpha_i) + \mu g \sin(\alpha_i), \quad (7.19)$$

$$z_o = g \sin(\alpha_i) - \mu g \cos(\alpha_i) - \bar{u}_o \alpha_i. \quad (7.20)$$

An expression for α_f can be obtained by applying $z|_{\alpha_f} = l$ in Eq. 7.18, which gives :

$$l = \frac{60}{2\pi\omega} \int_{\alpha_i}^{\alpha_f} \bar{u} \, d\alpha = \left(\frac{60}{2\pi\omega} \right)^2 (-g \sin(\alpha_f) + \mu g \cos(\alpha_f) + \bar{u}_o \alpha_f + z_o), \quad (7.21)$$

From this equation :

$$\int_{\alpha_i}^{\alpha_f} \bar{u} \, d\alpha = \frac{2\pi\omega l}{60}. \quad (7.22)$$

The substitution of this equation into Eq. 7.13 yields :

$$\bar{\bar{u}} = \frac{2\pi\omega l}{60\Delta\alpha}. \quad (7.23)$$

Finally, substituting $\overline{\cos(\alpha)}$ from Eq. 7.12, $\bar{\bar{u}}$ from Eq. 7.23 and $h = 2R$ into Eq. 7.11 provides a mean time value for the segregation number :

$$\overline{S_r} = \frac{15g\lambda}{\pi c} \left[\frac{\sin(\alpha_f) - \sin(\alpha_i)}{R\omega} \right]. \quad (7.24)$$

The first term $k = \frac{15g\lambda}{\pi c}$ in this equation is related to the segregating tendency of the mixture through the interparticle drag coefficient c . Angles α_i and α_f in the second term $(\frac{\sin(\alpha_f) - \sin(\alpha_i)}{R\omega})$ depend on the blender/granules friction coefficient μ as well as the blender size and rotational

speed.

Getting back to Fig. 7.9, there is a transition in the segregation intensity of the tetrapodal blender for a rotational speed between 5 and 10 *RPM*, below which there is notable segregation and above which the segregation intensity is not significant. When the same material is used for the scale-up, it is claimed that the quantity $\overline{S_{r,t}}/k$, where $\overline{S_{r,t}}$ denotes the value of $\overline{S_r}$ corresponding to the transition rotational speed ω_t , does not depend on the blender size. To verify this, the experimental data of different sized V-blenders, as reported by Alexander et al. (2004b), can be used. One may note that Eq. 7.24 was developed for the tetrapodal blender, yet it is examined via experimental data for the V-blender. This is justified because segregation in both blenders comes from granular flow over inclined surfaces in their arms and the governing mechanisms are similar. Table 7.6 displays values of $\overline{S_{r,t}}/k$ calculated from these experimental data and Eqs. 7.15, 7.21 and 7.24, where each blender is named according to the volume of material corresponding to a 60% fill level, and ω_t refers to the transition rotational speed between the small-out and stripe patterns. More precisely, the value of $\overline{S_{r,t}}/k$ was calculated according to the following algorithm :

1. α_i was obtained from Eq. 7.15. μ was taken as 0.135 ± 0.01 , as reported by Alizadeh et al. (2012) for the motion of glass beads on a Plexiglas sheet, which is the material used for the construction of V-blenders in Table 7.6;
2. By substituting the blender arm length l and transition rotational speed ω_t into Eq. 7.21, α_f was calculated;
3. $\overline{S_{r,t}}/k$ was calculated from Eq. 7.24.

As can be seen in Table 7.6, the value of $\overline{S_{r,t}}/k$ is indeed almost constant (1.04 ± 0.08). It then follows from Eq. 7.24 that $\overline{S_{r,t}}/k$ is inversely proportional to ω_t . This means that the transition between the segregation patterns becomes less important as the blender size increases. This implies that the operation of industrial-scale V-blenders is less problematic since ω_t decreases as the blender size is increased. In practice, appropriate values for ω should be larger than ω_t , which can be determined from Eq. 7.24 using the constant value of $\overline{S_{r,t}}/k$.

Table 7.6: Calculated values of $\overline{S_{r,t}}/k$ for different sized V-blenders. The blender sizes and experimental transition speeds were extracted from [Alexander et al. \(2004b\)](#).

Nominal capacity [quart]	l [cm]	$2R$ [cm]	ω_t [RPM]	$\overline{S_{r,t}}/k$ [(RPM.m) ⁻¹] Eqs. 7.15, 7.21 and 7.24
0.5	10.5	6.7	9.5	1.17
1	13.9	9.2	7.7	1.01
4	21.2	13.8	3.5	1.03
8	24.7	17.6	2.5	0.96
16	33.0	21.2	1.7	1.00

Finally, a similar analysis could be performed for the tetrapodal blender. In particular, the results of Fig. 7.9, which correspond to the twisted (-45|45) configuration, indicate that ω_t is somewhere between 5 and 7.5RPM. These values and the algorithm described above yield values of $\overline{S_{r,t}}/k$ in the range [0.9,1.1], which are close to the values calculated for the V-blender. More experimental data measured on different sizes of the tetrapodal blender would be needed to provide a detailed analysis.

7.4 Concluding remarks

Mixing and segregation of free flowing granules inside a tetrapodal blender were investigated and its efficiency was compared to that of the V-blender. More than 100 experiments were carried out and characterized using thief sampling. For a wide range of operating conditions, the tetrapodal blender demonstrated more efficient radial and axial mixing mechanisms than the V-blender. In twisted configurations of the tetrapodal blender, it was shown that axial mixing is as efficient as radial mixing. Both the radial and axial mixing rates were shown to decrease with an increase in the fill level, while the effect of the increase in rotational speed on these mixing rates was not significant, the axial (resp. radial) mixing rate increasing (resp. decreasing) slightly.

Size segregation was investigated in different configurations of the tetrapodal blender under a wide range of rotational speeds and fill levels. The segregation intensity was observed

to decrease rather slightly with the fill level, but significantly with the rotational speed, in the standard and twisted configurations of the tetrapodal blender. Compared to the reported data in the literature for the V-blender, the tetrapodal blender revealed less prone to segregate granules. Next, the effect on the segregation intensity of granule density and the simultaneous effects of granule density and size were investigated. It was shown that the size effect is more important than the density effect in all cases. Finally, kinetic sieving was observed to be the main governing mechanism for segregation and, based on this mechanism, a criterion was introduced for the scale-up of tumbling blenders.

Acknowledgments

The financial contribution of Teva Canada, Praxair and the Natural Sciences and Engineering Research Council of Canada (NSERC) is gratefully acknowledged. The coating of MTL2 granules was performed in the R&D laboratories of Ratiopharm operations (Mirabel, Québec). The authors are grateful to Olivier Dubé and Jonathan Bouffard for their help in designing the tetrapodal blender, and JSALEX regarding the building of the blender. We would also like to thank Amin Esmaeili for his help during the experiments and Jaber Shabanian for providing the size distribution of the sugar beads.

7.5 References

- Adams, J. and Baker, A. (1956). An assessment of dry blending equipment. *Transactions of the Institution of Chemical Engineers*, 34 :91–97.
- Alexander, A., Arratia, P., Goodridge, C., Sudah, O., Brone, D., and Muzzio, F. (2004a). Characterization of the performance of bin blenders : Part 1 of 3 : Methodology. *Pharmaceutical Technology*, 28(5) :70–86.
- Alexander, A., Muzzio, F. J., and Shinbrot, T. (2003). Segregation patterns in V-blenders. *Chemical Engineering Science*, 58(2) :487–496.

- Alexander, A., Shinbrot, T., Johnson, B., and Muzzio, F. J. (2004b). V-blender segregation patterns for free-flowing materials : effects of blender capacity and fill level. *International Journal of Pharmaceutics*, 269(1) :19–28.
- Alexander, A., Shinbrot, T., and Muzzio, F. (2001). Granular segregation in the double-cone blender : Transitions and mechanisms. *Physics of Fluids*, 13(3) :578–587.
- Alexander, A., Shinbrot, T., and Muzzio, F. J. (2002). Scaling surface velocities in rotating cylinders as a function of vessel radius, rotation rate, and particle size. *Powder Technology*, 126(2) :174–190.
- Alizadeh, E., Bertrand, F., and Chaouki, J. (2012). Comparison of DEM results and lagrangian experimental data for the mixing and segregation of granules in a rotating drum. page Submitted to AIChE Journal.
- Alizadeh, E., Bertrand, F., and Chaouki, J. (2013a). Discrete element simulation of particle mixing and segregation in a tetrapodal blender. page Submitted to Computers and Chemical Engineering.
- Alizadeh, E., Dubé, O., Bertrand, F., and Chaouki, J. (2013b). Characterization of mixing and size segregation in a rotating drum by a particle tracking method. *Accepted in AIChE Journal*, DOI 10.1002/aic.13982.
- Anderson, M. (1964). Tetrapodal mixing device,. US Patent :US 3,134,578.
- Arratia, P., Duong, N.-H., Muzzio, F., Godbole, P., and Reynolds, S. (2006). A study of the mixing and segregation mechanisms in the Bohle Tote blender via DEM simulations. *Powder Technology*, 164(1) :50–57.
- Bouffard, J., Bertrand, F., Chaouki, J., and Dumont, H. (2013). Discrete element investigation of flow patterns and segregation in a spheronizer. *Computers and Chemical Engineering*, 49 :170–182.
- Brone, D., Alexander, A., and Muzzio, F. (1998). Quantitative characterization of mixing of dry powders in V-blenders. *AIChE Journal*, 44(2) :271–278.

- Brone, D. and Muzzio, F. (2000). Enhanced mixing in double-cone blenders. *Powder Technology*, 110(3) :179–189.
- Brone, D., Wightman, C., Connor, K., Alexander, A., Muzzio, F. J., and Robinson, P. (1997). Using flow perturbations to enhance mixing of dry powders in V-blenders. *Powder Technology*, 91(3) :165–172.
- Chen, P., Ottino, J. M., and Lueptow, R. M. (2010). Onset mechanism for granular axial band formation in rotating tumblers. *Physical Review Letters*, 104(18) :188002.
- Daumann, B., Fath, A., Anlauf, H., and Nirschl, H. (2009). Determination of the mixing time in a discontinuous powder mixer by using image analysis. *Chemical Engineering Science*, 64(10) :2320–2331.
- Ding, Y., Forster, R., Seville, J., and Parker, D. (2001). Scaling relationships for rotating drums. *Chemical Engineering Science*, 56(12) :3737–3750.
- Doucet, J., Bertrand, F., and Chaouki, J. (2008a). Experimental characterization of the chaotic dynamics of cohesionless particles : Application to a V-blender. *Granular Matter*, 10(2) :133–138.
- Doucet, J., Bertrand, F., and Chaouki, J. (2008b). A measure of mixing from lagrangian tracking and its application to granular and fluid flow systems. *Chemical Engineering Research and Design*, 86(12) :1313–1321.
- Gray, J. and Thornton, A. (2005). A theory for particle size segregation in shallow granular free-surface flows. *Proceedings of the Royal Society of London, Series A (Mathematical, Physical and Engineering Sciences)*, 461(2057) :1447–14473.
- Harnby, N. (1967). A comparison of the performance of industrial solids mixers using segregating materials. *Powder Technology*, 1(2) :94–102.
- Lacey, P. (1954). Development in the theory of particle mixing. *Journal of Applied Chemistry*, 4 :257–268.

- Lemieux, M., Bertrand, F., Chaouki, J., and Gosselin, P. (2007). Comparative study of the mixing of free-flowing particles in a V-blender and a bin-blender. *Chemical Engineering Science*, 62(6) :1783–1802.
- Lemieux, M., Leonard, G., Doucet, J., Leclaire, L.-A., Viens, F., Chaouki, J., and Bertrand, F. (2008). Large-scale numerical investigation of solids mixing in a V-blender using the discrete element method. *Powder Technology*, 181(2) :205–216.
- Manickam, S., Shah, R., Tomei, J., Bergman, T., and Chaudhuri, B. (2010). Investigating mixing in a multi-dimensional rotary mixer : Experiments and simulations. *Powder Technology*, 201(1) :83–92.
- Marks, B., Rognon, P., and Einav, I. (2012). Grainsize dynamics of polydisperse granular segregation down inclined planes. *Journal of Fluid Mechanics*, 690 :499–511.
- Mehrotra, A. and Muzzio, F. (2009). Comparing mixing performance of uniaxial and biaxial bin blenders. *Powder Technology*, 196(1) :1–7.
- Mellmann, J. (2001). The transverse motion of solids in rotating cylinders - forms of motion and transition behavior. *Powder Technology*, 118(3) :251–270.
- Moakher, M., Shinbrot, T., and Muzzio, F. J. (2000). Experimentally validated computations of flow, mixing and segregation of non-cohesive grains in 3D tumbling blenders. *Powder Technology*, 109(1-3) :58–71.
- Muzzio, F., Robinson, P., Wightman, C., and Dean, B. (1997). Sampling practices in powder blending. *International Journal of Pharmaceutics*, 26(2) :153–178.
- Muzzio, F. J., Goodridge, C. L., Alexander, A., Arratia, P., Yang, H., Sudah, O., and Mergen, G. (2003). Sampling and characterization of pharmaceutical powders and granular blends. *International Journal of Pharmaceutics*, 250(1) :51–64.
- Ottino, J. M. and Khakhar, D. V. (2002). Scaling of granular flow processes : From surface flows to design rules. *AIChE Journal*, 48(10) :2157–2166.

- Paul, E., Atiemo-Obeng, V., and Kresta, S. (2003). *Handbook of Industrial Mixing, Science and Practice*. John Wiley & Sons, Hoboken, NJ.
- Pignatel, F., Asselin, C., Krieger, L., Christov, I. C., Ottino, J. M., and Lueptow, R. M. (2012). Parameters and scalings for dry and immersed granular flowing layers in rotating tumblers. *Phys. Rev. E*, 86 :011304.
- Rhodes, M. (2008). *Introduction to particle technology, 2nd edition*. John Wiley and sons.
- Samyn, J. C. and Murthy, K. S. (1974). Experiments in powder blending and unblending. *Journal of Pharmaceutical Sciences*, 63(3) :370–375.
- Savage, S. and Lun, C. (1988). Particle size segregation in inclined chute flow of dry cohesionless granular solids. *Journal of Fluid Mechanics*, 189 :311–325.
- Sudah, O., Arratia, P., Coffin-Beach, D., and Muzzio, F. (2002). Mixing of cohesive pharmaceutical formulations in tote (bin) blenders. *Drug Development and Industrial Pharmacy*, 28(8) :905–918.

CHAPTER 8

Development of a granular normal contact force model based on a non-Newtonian liquid filled dashpot

Ebrahim Alizadeh, François Bertrand, Jamal Chaouki

Department of Chemical Engineering, École Polytechnique de Montréal, C.P. 6079 succ.

Centre-Ville, Montréal, Québec, Canada, H3C 3A7

Powder Technology 237 (2013) 202-212

Presentation of the article : Although, good agreements were observed between DEM results and experimental data especially when the dynamics of granules were considered (*e.g.* Figs. 5.1 and 5.2), there were some discrepancies, particularly in terms of mixing rates. This was shown in the case of a rotating drum in Fig. 5.7 and for a tetrapodal blender in Fig. 8.1 for mentioned operating conditions. Most of such errors arise mainly from inappropriate simulation parameters as well as weak predictions of contact force models. The former was discussed in Chapter 5, but the latter indeed requires more investigation. Therefore, in this chapter, a new normal contact force model is developed and its ability to predict a single collision property is examined against the experimental data as well as other conventional models.

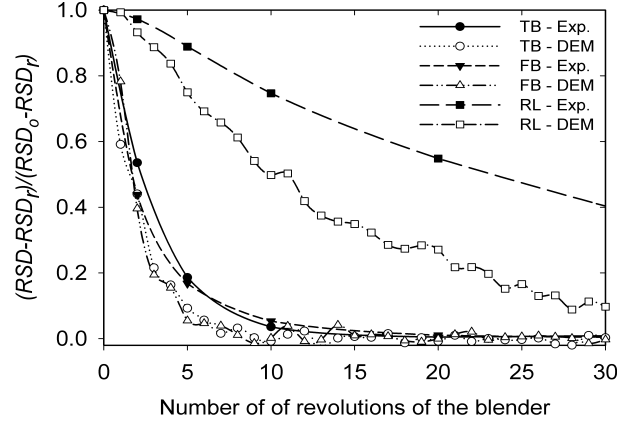


Figure 8.1: Normalized RSD curves obtained from DEM simulations (Chapter 6) and thief sampling (Chapter 7) for a tetrapodal blender (fill level 35%V and rotating at 15RPM).

Abstract : Normal contact force models often suffer from a weak prediction of collisions between particles. They regularly fail to predict an adequate energy restitution behavior with increasing normal impact velocity. In particular, most non-linear models predict a net attraction force between two impacting particles near the end of a collision, which is unrealistic according to reported results. Such limitations have provided the impetus for the development of a normal contact force model that better predicts the unfolding of a collision between two particles. This model comprises a Hertz elastic force and a dissipative force that is evaluated by the motion of a non-Newtonian liquid in a dashpot. The model parameters are set using experimental restitution data for particle/particle and particle/wall contacts. In the current work, the measurement of energy restitution for particle/wall collision was carried out using several materials over a wide range of impact velocities, whereas particle/particle collision data were obtained from the literature. Model predictions for microscopic (*e.g.* particle velocity) and macroscopic (*e.g.* collision time) quantities are presented and compared with those from other non-linear models and experimental data. The model is observed to adequately predict the coefficient of restitution and to decrease the attraction force at the end of a collision.

Keyword : Normal contact force model, Coefficient of restitution, Collision time, Discrete element method, Non-Newtonian fluid

8.1 Introduction

Due to the importance of processes involving solids, a high percentage of recent research activities has focused on the flow of particles ([Di Renzo and Di Maio, 2004](#)), which in many cases is governed by the collisions among them. A better understanding of particle impact in the granular bed facilitates the design of more efficient unit operations, thus improving the throughput and the quality of the final product ([Doucet et al., 2008](#)). A typical example of this can be seen in the pharmaceutical industry, with for instance mixing systems such as tumbling blenders, where improved knowledge of the particle behavior as these particles collide with their neighbors and the blender wall is known to help design systems that have greater throughput, consume less power and have smaller failure rate. Beside experimental efforts to investigate particulate material beds (*e.g.* [Ding et al., 2002](#); [Nakagawa et al., 1993](#)), numerical investigations have progressed due to advances in high performance computing ([Yamane et al., 1998](#)). In these studies, both continuum and discrete models have been developed. The first is a Eulerian approach that considers powder as a fluid (*e.g.* [Aranson and Tsimring, 1999](#); [Khakhar et al., 1997, 2001](#)), and the second is a Lagrangian approach that treats particles as discrete entities. Among the discrete models, the discrete element method (DEM), initially introduced by [Cundall and Strack \(1979\)](#), has been widely applied to investigate solids motion (*e.g.* [Dury and Ristow, 1997](#); [Rapaport, 2007](#); [Taberlet et al., 2004](#); [Yamane et al., 1998](#); [Zhu et al., 2008](#)). It has been shown to provide valuable insight into phenomena occurring in the granular bed by modeling each particle and its interaction with the neighboring particles and the solid parts of the equipment.

In the DEM, the motion of each particle is subjected to Newton's second law of motion. It is a time-driven soft-particle method that allows any two colliding particles to interpenetrate so as to mimic their deformation upon impact. The total applied force may take into account gravity, drag, buoyancy, particle/particle and particle/wall contact, and cohesive terms such as the electrostatic, Van der Waals and capillary forces. Given the particle size in DEM simulations (generally in the order of one millimeter), the non-contact cohesive forces are

often neglected so that only gravity and contact forces are considered. Particle contacts can be described via contact mechanics and modeled by the finite element method (FEM) (Li et al., 2000; Wu et al., 2005, 2009). Considering there can be millions and possibly billions of particles in a small rig, the FEM approach remains too computationally intensive. To overcome this problem, several simplified force models have been proposed, some of which will be described in Section 8.2.

Although these simplified force models decrease the simulation time, they are nonetheless subject to limitations. For instance, most of the current models require input parameters that can hardly be measured directly (*e.g.* spring and damping coefficients) (Stevens and Hrenya, 2005). In addition, some normal contact force models cannot yield accurate values of the normal coefficient of restitution (CoR) when the particle impact velocity changes. The CoR is defined as the ratio of the relative velocities after and before collision. The models that are able to predict the correct behavior of the CoR fails to approximate it accurately in comparison with experimental data. Furthermore, many of these models predict a net attraction force at the end of a collision, which is unrealistic. The details of such drawbacks will be described and further discussed in Section 8.2.

The aim of this work is to develop a normal contact force model that alleviates the stated shortcomings. The model parameters are adjusted to accurately predict particle/particle as well as particle/wall interactions. A wide range of experiments were carried out to measure the normal impact on a flat metal plate of spherical particles made from a wide variety of materials. These experiments enabled the estimation of the parameters inherent to the proposed model. Experimental data from the literature (Goldsmith, 1960; Kruggel-Emden et al., 2007; Stevens and Hrenya, 2005) were also used to assess the quality of the model in the case of two particles collisions.

The paper is organized as follows. In Section 8.2, the most common contact force models are reviewed and their limitations are discussed. In Section 8.3, the experimental procedure and materials used for the particle/wall contact experiments are described. In Section 8.4,

the proposed collision model is introduced and model parameters are obtained for several materials in the case of particle/particle and particle/wall collisions. In Section 8.5, the model is assessed by means of experimental data and results obtained with other non-linear models. Finally, Section 8.6 provides concluding remarks.

8.2 Contact forces

The way particle collisions are taken into account in the DEM is recalled. Next, the most common contact force models are presented and their limitations are discussed.

8.2.1 Collision of particles

Most DEM simulations involve spheres. A collision between two spheres with this model is schematized in Fig. 8.2. The contact force acting between them can be decomposed into normal and tangential components. In this study, we focus on normal contact forces.

In the DEM, the particle deformation during contact is characterized by a small particle overlap δ :

$$\delta = \max\{0, (R_i + R_j) - (\vec{x}_i - \vec{x}_j) \cdot \vec{n}\}, \quad (8.1)$$

where R_i and R_j are the radii of contacting particles i and j , \vec{x}_i and \vec{x}_j are their positions, and \vec{n} is the normal unit vector, which is perpendicular to the tangent unit vector \vec{t} . The relative velocity, \vec{v}_{ij} , is related to the displacement rate of the particles :

$$\vec{v}_{ij} = \dot{\delta} = (\vec{v}_j - \vec{v}_i), \quad (8.2)$$

in which \vec{v}_i and \vec{v}_j are the velocities of particles i and j , respectively. In Fig. 8.2, $\vec{\omega}_i$ and $\vec{\omega}_j$ are the angular velocities of these particles, although particle rotation is not relevant in this work. Note that \vec{v}_{ij} will be subsequently denoted by v_{ij} .

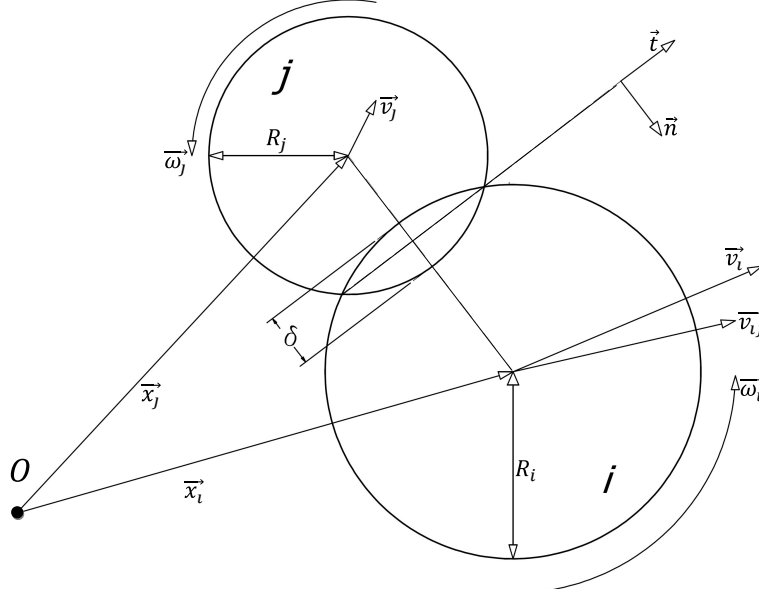


Figure 8.2: Collision of two spheres.

8.2.2 Normal contact force models

Normal force schemes can be divided into several groups depending on the way the impact of the normal force on the particle overlap and the relative particle velocities is modeled. Four main groups are defined : the *continuous potential models* (Aoki and Akiyama, 1995; Langston et al., 1994), the *linear viscoelastic models* (Walton, 1983), the *non-linear viscoelastic models* (Brilliantov et al., 1996; Kuwabara and Kono, 1987; Lee and Herrmann, 1993; Tsuji et al., 1992) and the *hysteretic models* (Sadd et al., 1993; Thornton, 1997; Thornton and Ning, 1998; Walton and Braun, 1986). Further details on force models can be found in Kruggel-Emden et al. (2007). Note that contact force models based on FEM simulation results have also been developed (Li et al., 2002). However, due to their relative complexity, their potential utilization within DEM has been limited (Stevens and Hrenya, 2005). Because of their widespread use in DEM simulations and the relatively good predictions they can generally provide, we focus here on the viscoelastic models that are found in the literature. The continuous potential models are known to be inefficient for DEM simulations, whereas the accuracy of hysteric models have been observed to depend on the material (Kruggel-Emden

et al., 2007; Stevens and Hrenya, 2005; Wojtkowski et al., 2010). In the viscoelastic models, the contact force between two colliding particles includes two parts, one for the elastic repulsion modeled by a spring and the other for the viscous dissipation via a dashpot (Ji and Shen, 2006) :

$$F^n = F_{el}^n + F_{diss}^n = -K_n \delta^\alpha - C_n \delta^\beta v_{ij}^\gamma, \quad (8.3)$$

where K_n is the constant of a Hookean spring and C_n is the damping coefficient. When $\alpha = 1$, $\beta = 0$ and $\gamma = 1$, the model is referred to as the linear spring dashpot (LSD) model. In a linear contact force model, the damping coefficient is given by :

$$C_n = 2\xi_n \sqrt{m_{eff} K_n}, \quad (8.4)$$

where m_{eff} is the mean mass of particles i and j ($\frac{1}{m_{eff}} = \frac{1}{m_i} + \frac{1}{m_j}$) and ξ_n depends on the CoR (Thornton et al., 2013) :

$$\ln(CoR) = -\sqrt{\frac{K_n}{m_{eff}}} \xi_n t_c, \quad (8.5)$$

in which t_c is the contact duration. For the LSD model, the following equation has been commonly used to obtain ξ_n (Ji and Shen, 2006; Mishra and Murty, 2001) :

$$\xi_n = \frac{-\ln(CoR)}{\sqrt{\pi^2 + \ln^2(CoR)}}. \quad (8.6)$$

Note that this equation is inappropriate for DEM simulations since it assumes that the contact ends when the displacement first returns to zero, at which point the normal force is attractive (Schwager and Poschel, 2007; Thornton et al., 2013). The use of a linear contact model in Newton's second law of motion leads to a differential equation that has an analytical solution with constant CoR and collision time (independent of the initial impact velocity) (Schäfer et al., 1996), whereas experimental and theoretical studies have shown that the CoR and

the contact duration depend sensitively on the impact velocity (Bridges et al., 1984; Gorham and Kharaz, 2000; Kuwabara and Kono, 1987; Ramirez et al., 1999; Stevens and Hrenya, 2005). In the case of LSD, the damping force is independent of the overlap and depends linearly on the particle relative velocities. In such a model, the initial force is not zero despite the absence of the particle overlap δ , which is non-physical (Zhang and Whiten, 1996). To overcome this limitation of LSD, particle overlap δ can be added to the dissipative term, which is the case for most of the non-linear viscoelastic models that have been developed based on the *Hertz* theory. Hertzian contacts are pure elastic ($C_n = 0$ in Eq. 8.3) and the spring constant (K_n) with this model ($\alpha = 3/2$) is a function of the particle geometry and its mechanical properties :

$$K_n = \frac{4}{3} E^* \sqrt{R^*}, \quad (8.7)$$

where R^* is the reduced radius ($\frac{1}{R^*} = \frac{1}{R_i} + \frac{1}{R_j}$) and E^* is the effective Young's modulus ($\frac{1}{E^*} = \frac{1-\nu_i^2}{E_i} + \frac{1-\nu_j^2}{E_j}$). ν_i and ν_j are the Poisson's ratios and E_i and E_j the Young's modulus of particles i and j , respectively. The drawback of such model is that it cannot resolve adequately inelastic collisions because of the absence of a damping term. Lee and Herrmann (1993) (LH) proposed a non-linear viscoelastic model ($\alpha = 3/2$, $\beta = 0$ and $\gamma = 1$) in which the elastic term is based on the Hertz theory and the damping term depends linearly on the particle velocities. However, due to the absence of the overlap δ in the dissipative term, this model yields a non zero force at the beginning of the contact between two particles. Kuwabara and Kono (1987) (KK) proposed a non-linear viscoelastic model with $\alpha = 3/2$, $\beta = 1/2$, and $\gamma = 1$. This model was also independently derived by Brilliantov et al. (1996). In the KK model, C_n is an adjustable parameter. Results have shown that it leads to a decrease of the CoR and collision time when there is an increase in the impact velocity. Another non-linear model was derived heuristically by Tsuji et al. (1992) (TS) ($\alpha = 3/2$, $\beta = 1/4$, and $\gamma = 1$). This model gives a constant CoR and a velocity-dependent collision time. It appears that all these non-linear models for normal contact forces only differ in the exponent β in the

dissipative term. Moreover, this exponent has a strong effect on the behavior of the model. [Ramirez et al. \(1999\)](#) proved that the dependency of the terminal velocity on the initial velocity vanishes if

$$2(\beta - \alpha) + \gamma(1 + \alpha) = 0. \quad (8.8)$$

This is the case for the LSD and the TS models. In practice, it appears that this dependency of the terminal velocity on the initial velocity has often been overlooked or ignored.

Another drawback of the non-linear viscoelastic models is encountered when there is an inelastic impact between two particles. Fig. 8.3 shows the variation of the normal contact force versus the contact duration both numerically (Figs. 8.3a and 8.3b) and experimentally (Fig. 8.3c). The numerical data are typical results that have been obtained for stainless steel spheres using a MATLAB implementation of the KK and TS models. One may notice that the repulsive contact force decreases from zero to a minimum, then increases back to zero. For nearly elastic collisions (CoR=1), the contact force profile is symmetric, whereas for inelastic collisions it is not (CoR< 1). In this latter case, the numerical models fail to predict accurately the contact force at the end of the collision. This can be seen in Figs. 8.3a and 8.3b where the force switches from repulsive to attractive, whereby pulling the particles back towards each other instead of forcing them to split. Indeed, this attractive force at the end of the collision is unrealistic as shown in Fig. 8.3c ([Zhang and Whiten, 1996](#)) and discussed in the literature ([Ji and Shen, 2006](#); [Schwager and Poschel, 2007](#); [Stevens and Hrenya, 2005](#)). To overcome this limitation, some researchers have suggested that particles should be forced to separate when the force goes to zero, even though this corresponds to a non-zero overlap ([Goldenberg and Goldhirsch, 2004](#); [Ji and Shen, 2006](#); [Schäfer et al., 1996](#)).

The limitations of the non-linear models have provided the impetus for this work. A new non-linear contact force model is introduced; it is based on CoR experimental data for the calibration of its parameters. This model is based on the Hertz theory ($\alpha = 3/2$) and uses $\beta = 1$ and a variable value of γ for the damping term.

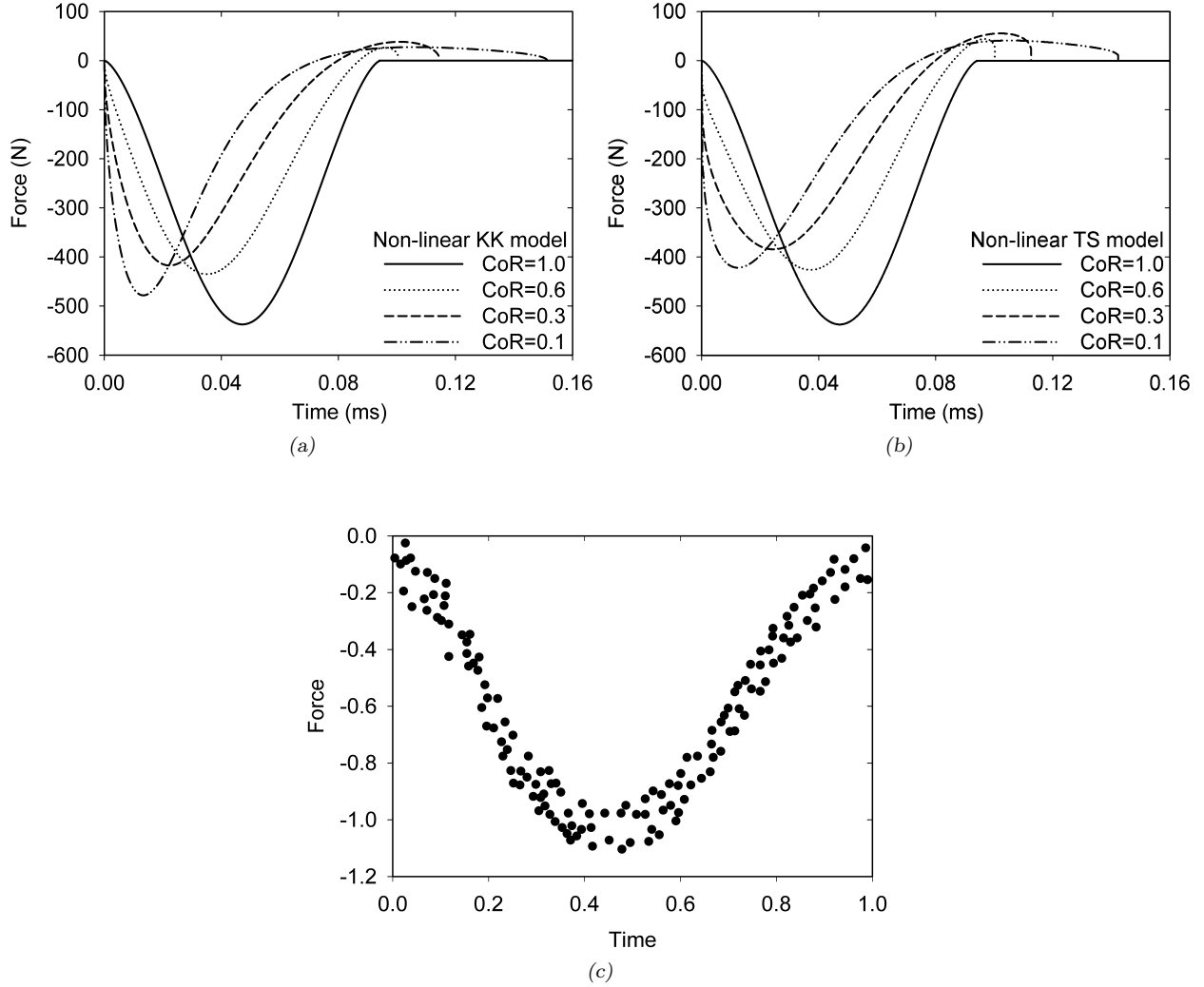


Figure 8.3: Nonlinear contact force model predictions for normal impact with different coefficients of restitution : (a) Kuwabara and Kono (KK) model, (b) Tsuji (TS) model and (c) normalized experimental results (Zhang and Whiten, 1996).

8.3 Experimental setup and materials

In this study, we have chosen to investigate the fall of single particles when they are launched from specific heights toward a metal plate, thus providing adequate control over the experiments. The use of a similar procedure has been reported in the literature (Kharaz et al., 1999). In particular, the effect on the CoR of the material type (Brauer, 1980) and plate thickness (Sondergaard et al., 1990) has been investigated.

A schematic of the setup is shown in Fig. 8.4. Spherical particles (McMaster-Carr) made from a wide range of materials were used in order to study their impact on the CoR. The mechanical and geometrical properties of these particles and materials are summarized in Table 8.1. Given that the processing equipment found in the industry is often made from stainless steel, the plate is a 6-*mm* thick stainless steel 304 slab. Various heights above the plate were considered to impart different impact velocities. The particles were initially held in place by means of a 1-*mm* nozzle connected to a vacuum pump. When a particle was released, it then fell toward the plate without spinning at a zero initial velocity. A high speed camera (frame rate $\simeq 200$ frames/sec) was used to record the displacement of the particles. The images (480×640 pixels) were transferred to a PC and converted to RGB format using the image processing toolbox in MATLAB.

Particles were dropped from six different heights, covering a velocity range of 0.8 to 2.6 *m/s*. The values for the impact velocity were derived from the initial position of these particles and the conservation of mechanical energy. Each test was repeated five times under the same conditions and the results were averaged out.

Note that no experiments were carried out in this work for the calibration of the particle/particle collision parameters. Instead, we used particle/particle impact data from the

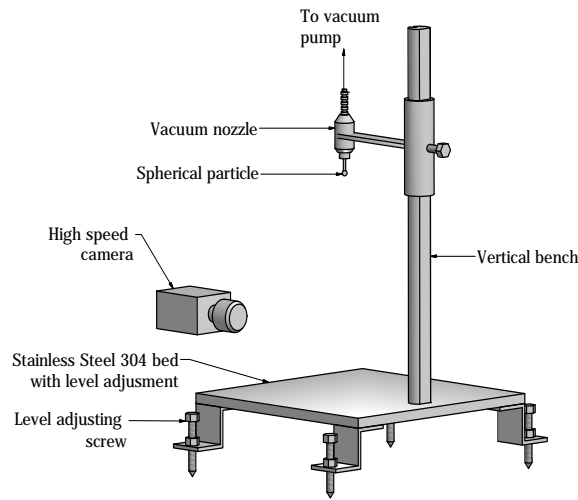


Figure 8.4: The main components of the experimental setup.

Table 8.1: Mechanical and geometrical properties of the spheres used in the particle/wall normal impact experiments. These properties were provided by the supplier (McMaster-Carr) and the literature (Bolz and Tuve, 1970; Gale, 2004; Kschinka et al., 1986).

Material	Abbr.	<i>Hardness</i> [<i>vickers</i>]	Young's modulus [N/m^2]	Poisson's ratio	Density [kg/m^3]	Diam. [mm]
Stainless steel	SS	324	1.93×10^{11}	0.29	8000	4.00
Low carbon steel (alloy 1010-1020)	LCS	697	1.93×10^{11}	0.29	7850	4.00
Formable brass (alloy 260)	BR	153	1.01×10^{11}	0.35	8550	4.00
E52100 alloy steel	CS	800	2.07×10^{11}	0.29	7860	4.00
Titanium	Ti	319	1.16×10^{11}	0.32	4500	4.00
Aluminum (alloy 2017)	Al	112	7.24×10^{10}	0.33	2800	3.18
Borosilicate glass	GB	982	6.89×10^{10}	0.21	2500	4.00
Nylon 6/6	NY	50	3.30×10^9	0.39	1140	4.00
Clear extruded acrylic	AC	52	3.20×10^9	0.37	1190	4.00
White delrin	DE	52	3.10×10^9	0.35	1420	4.00
Silicon nitride ceramic	CE	1150	3.24×10^{11}	0.23	3200	4.00

literature to calibrate these parameters (Goldsmith, 1960; Kruggel-Emden et al., 2007; Stevens and Hrenya, 2005). Different approaches have been used to investigate the impact of two particles. For instance, Stevens and Hrenya (2005) used a pendulum-based experiment for the simultaneous measurements of the CoR and collision duration of two identical spheres undergoing a normal contact. Details of the impact between two spheres have also been analyzed with a high speed video camera (Foerster et al., 1994; Labous et al., 1997; Lorenz et al., 1997).

8.4 Model development

The relative velocity of two colliding particles at the contact point in the normal direction is given by Eq. 8.2. We recall that, in the DEM, the particles are allowed to overlap. We propose here to predict the extent of the related normal force by means of an elastic spring and a viscous dashpot. This method of modeling the dynamic response of a viscoelastic material is known as the Kelvin-Voigt model. The elastic force is predicted using the non-linear Hertz law as described in the previous section. The dashpot contains of a cylinder

filled with a liquid in which a piston operates. To add flexibility to our model, we propose to consider a non-Newtonian liquid that obeys a power law equation of state :

$$\tau_{rz} = -K_l \left(\frac{\partial v_z}{\partial r} \right)^{n_l}, \quad (8.9)$$

where v_z is the liquid velocity in the axial direction z , τ_{rz} is the shear stress, K_l the consistency index and n_l the power-law index. Its density is denoted by ρ_l . The piston and the cylinder have arbitrary radii denoted by kR_D and R_D (k slightly less than 1), respectively. In a conventional dashpot, the piston is fully immersed in the liquid, and as a result, the damping force is proportional to the particle relative velocity. Following along the lines of [Kuwabara and Kono \(1987\)](#) and [Tsuji et al. \(1992\)](#), the damping force in our model should also depend on the particle overlap. For this reason, the piston is located at the surface of the non-Newtonian liquid prior to a particle/particle collision (Fig. 8.5a). As the particles begin to overlap, the piston moves along the axial direction and penetrates into the liquid. The depth of penetration is equal to δ , the particle overlap (Fig. 8.5b). Such a displacement of the piston results in the flow of the liquid in the annulus between the piston and the cylinder. The non-Newtonian liquid exerts a viscous force on the surface of the piston and the inner surface of the cylinder. This force is related to the dissipative force in the DEM force balance and can be calculated through a momentum balance.

First, the velocity profile of the non-Newtonian liquid when the piston is immersed into the non-Newtonian liquid at a velocity v_{ij} must be obtained. It is assumed, as an approximation, that :

1. There is no velocity in the azimuthal direction, $v_\theta = 0$;
2. Because the liquid velocity is small and the annulus is narrow (k is slightly less than 1), the flow on a $r - z$ cross section resembles a plane couette flow, $v_z = v_z(r)$ ([Bird et al., 2001](#)).

A momentum balance on an element of fluid yields :

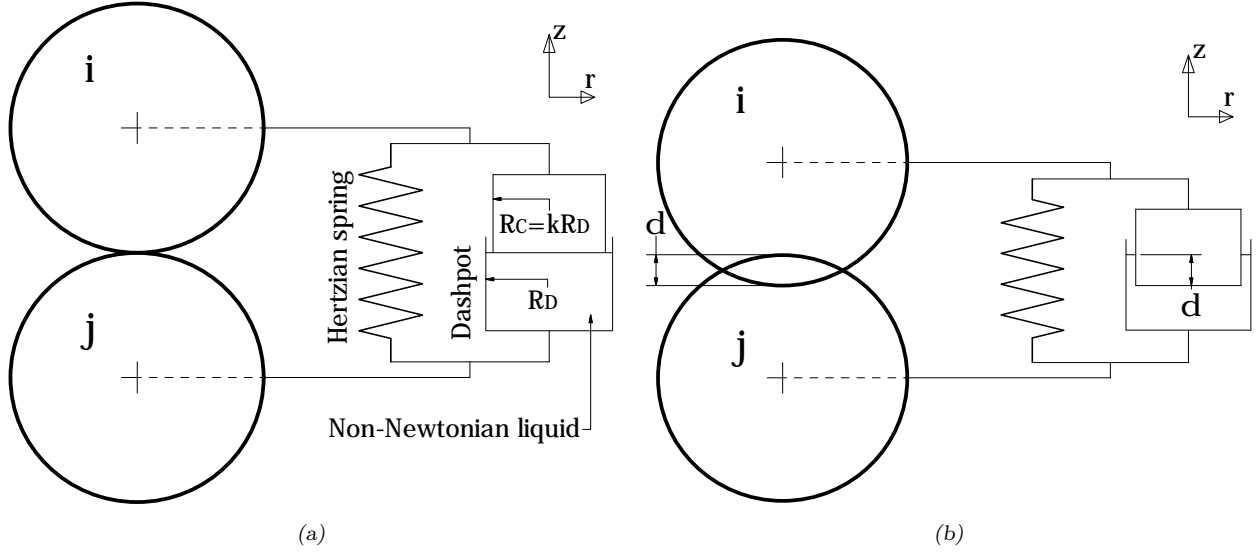


Figure 8.5: Model proposed for the normal contact of two particles : (a) just before the collision, and (b) during the collision. The piston is partially immersed in the non-Newtonian liquid of the dashpot, and kR_D and R_D are the radii of the piston and cylinder, respectively.

$$\rho_l \left(\frac{\partial v_z}{\partial t} \right) + \frac{1}{r} \frac{\partial}{\partial r} (r \tau_{rz}) = 0. \quad (8.10)$$

In that the time step in DEM simulations is quite small (of the order of $1\mu s$ in this work), this equation can be treated as a quasi-steady state problem. Thus, the first term can be neglected, and an integration yields

$$r \tau_{rz} = C_1. \quad (8.11)$$

Substituting the power-law rheological model (Eq. 8.9) into Eq. 8.11 and integrating give ($n_l \neq 1$) :

$$\frac{\partial v_z}{\partial r} = \left(-\frac{C_1}{K_l} \right)^{\frac{1}{n_l}} r^{\frac{-1}{n_l}}, \quad (8.12)$$

$$v_z = \left(-\frac{C_1}{K_l} \right)^{\frac{1}{n_l}} \frac{n_l r^{\frac{n_l-1}{n_l}}}{n_l - 1} + C_2. \quad (8.13)$$

From the boundary conditions

$$v_z|_{r=kR_D} = v_{ij}, \quad (8.14)$$

$$v_z|_{r=R_D} = 0, \quad (8.15)$$

the following expressions for the constants C_1 and C_2 can be deduced :

$$C_1 = K_l \left(v_{ij} \frac{n_l - 1}{n_l} \frac{1}{R_D^{\frac{n_l-1}{n_l}} - (kR_D)^{\frac{n_l-1}{n_l}}} \right)^{n_l}, \quad (8.16)$$

$$C_2 = \frac{v_{ij}}{1 - k^{\frac{n_l-1}{n_l}}}. \quad (8.17)$$

The dissipative force related to the damping term in the DEM is then the sum of the viscous forces on the outer surface of the piston and the inner surface of the cylinder :

$$\begin{aligned} F_{diss}^n &= \tau_{rz}|_{r=kR_D} A_{kR_D} + \tau_{rz}|_{r=R_D} A_{R_D}, \\ &= \frac{C_1}{kR_D} A_{kR_D} + \frac{C_1}{R_D} A_{R_D}, \end{aligned} \quad (8.18)$$

where $A_{R_D} = 2\pi R_D \delta$ and $A_{kR_D} = 2\pi kR_D \delta$ denote the area of the corresponding surfaces.

Hence, from Eq. 8.16 :

$$F_{diss}^n = 4\pi K_l \left(\frac{n_l - 1}{n_l} \frac{1}{R_D^{\frac{n_l-1}{n_l}} - (kR_D)^{\frac{n_l-1}{n_l}}} \right)^{n_l} v_{ij}^{n_l} \delta. \quad (8.19)$$

Finally, introducing $\mu = K_l \left(\frac{n_l-1}{n_l} \frac{1}{R_D^{\frac{n_l-1}{n_l}} - (kR_D)^{\frac{n_l-1}{n_l}}} \right)^{n_l}$ yields :

$$F_{diss}^n = 4\pi\mu v_{ij}^{n_l}\delta, \quad (8.20)$$

This model is similar to those of KK and TS with the difference that $\beta = 1$, $\gamma = n_l$ and $C_n = 4\pi\mu$ in Eq. 8.3.

Values of parameters μ and n_l must be determined for each material considered in this work. To do so, we used CoR data obtained from our experimental setup for particle/wall collisions and from the literature for particle/particle collisions. Values of these parameter were corrected in a way to minimize the error between the simulated terminal velocity and that obtained from CoR experimental data. The values of these parameters are presented for the particle/particle and particle/wall collisions in Tables 8.2 and 8.3, respectively. They were used in this work and can be used by researchers for DEM simulations involving particle/particle and particle/wall collisions. As can be noticed, parameters μ and n_l do depend on the materials involved in the particle/particle (Table 8.2) and particle/wall (Table 8.3) interactions. This is why there are differences in the values reported in these two tables. In Table 8.2, the two colliding particles are made of the same material, whereas, in Table 8.3, one particle impacts a stainless steel plate. Note that these model parameters may also depend on the particle size. Actually, the effect of the particle size on the CoR has not been studied a lot despite the fact that its value may have a significant impact on DEM results (Antypov et al., 2011; Sondergaard et al., 1990). In this work, a few additional experiments with different sized low carbon steel spheres were carried out, which revealed that the particle size does affect the value of μ but barely that of n_l . We will get back to this in Section 8.5.1. Note that the model parameters could also be set so that the collision time is well predicted. However, collision times are much harder to measure in practice.

8.5 Results and discussion

During the collision of two particles, both microscopic (local) and macroscopic (global) quantities can be measured. Microscopic quantities such as force, overlap, and particle velo-

Table 8.2: Model parameters for various materials in the case of particle/particle collisions. Mechanical and geometrical properties of these materials can be found in [Kruggel-Emden et al. \(2007\)](#).

Material	μ	n_l	Velocity range (m/s)
Aluminium (Al)	1.26×10^6	1.01	0.05 – 0.5
Brass (BR)	2.75×10^6	0.96	0.02 – 0.5
Lead (LE)	1.14×10^6	0.66	< 0.5
Marble (MR)	4.56×10^5	0.57	0.05 – 0.5
Stainless steel (SS)	3.77×10^5	0.98	0.4 – 1.5
Chrome steel (ChS)	3.90×10^4	1.09	0.6 – 2.0

Table 8.3: Model parameters for various materials in the case of particle/wall collisions. For abbreviations and material properties, see Table 8.1.

Material	μ	n_l	Velocity range (m/s)
SS	1.74×10^5	1.48	0.8 – 2.6
LCS	1.35×10^5	1.72	0.8 – 2.6
BR	1.62×10^5	1.30	0.8 – 2.6
CS	1.36×10^5	1.76	0.8 – 2.6
Ti	9.38×10^4	1.41	0.8 – 2.6
Al	8.86×10^4	0.71	0.8 – 2.6
GB	2.31×10^4	1.72	0.8 – 2.6
NY	5.06×10^3	0.66	0.8 – 2.6
AC	3.26×10^3	0.71	0.8 – 2.6
DE	3.39×10^3	0.88	0.8 – 2.6
CE	1.53×10^5	1.75	0.8 – 2.6

city, require a detailed record of the contact between the two colliding particles. This explains why only a few such experimental studies can be found in the literature (*e.g.* [Goldsmith, 1960](#); [Stevens and Hrenya, 2005](#)). Macroscopic quantities such as the CoR are generally easier to evaluate.

From the view point of macroscopic quantities, the numerical results obtained with the proposed model are compared to the particle/wall experimental data. An analysis is done on model parameters n_l and μ . For particle/particle collisions, values of the CoR and collision time are predicted by our model are compared to experimental data from the literature and results obtained with other non-linear models. Finally, microscopic quantities determined

with our model are compared to results from other non-linear models. Note that all the simulations were run using MATLAB implementations of the models considered.

8.5.1 Macroscopic quantities

Particle/particle collision

Values of the CoR and contact time obtained with the proposed model are compared to other predicted results and experimental data from the literature in Figs. 8.6 and 8.7, respectively, for different materials (see Table 8.2). The experimental data for stainless steel come from [Stevens and Hrenya \(2005\)](#) and those for the other materials from [Goldsmith \(1960\)](#). The model parameters for the KK and TS models can be found in [Kruggel-Emden et al. \(2007\)](#) and those of the proposed model are summarized in Table 8.2. Note that these authors adjusted the parameters of the KK and TS models by means of CoR experimental data. This was done carefully by resorting to least-square fitting to minimize the discrepancy between numerical results obtained with these models and experimental data. From a qualitative point of view, the TS model fails to predict the CoR trend and the KK model does not fit well with the experimental data, whereas there is very good agreement between the experimental data and the values predicted with our model. As expected, the collision time decreases with the impact velocity ([Goldsmith, 1960](#); [Stevens and Hrenya, 2005](#)). It takes up infinite time when this velocity goes to zero, whereas it goes to zero for high collision velocities.

The contact time in Fig. 8.7 is defined as the time during which the contact force is repulsive. As can be seen, there is good agreement between the experimental data and the predictions of the current model, while the KK and TS models underpredict the collision durations for these three materials. Such underpredictions are due to the large fractions of time for which an attractive force is predicted by these two models. As will be further discussed in Section 8.5.2, such fraction of time is smaller with the proposed model. Note that in the case where the contact time also includes the time during which there is an

attractive force, as done by [Kruggel-Emden et al. \(2007\)](#), the performance of all three models is very good.

Particle/wall collision

Values of the CoR predicted with the proposed model in the case of the collision of various metallic and non-metallic spheres on a flat plate are compared in Fig. 8.8 to experimental data obtained with the apparatus described in Section 8.3. Values of the standard deviation

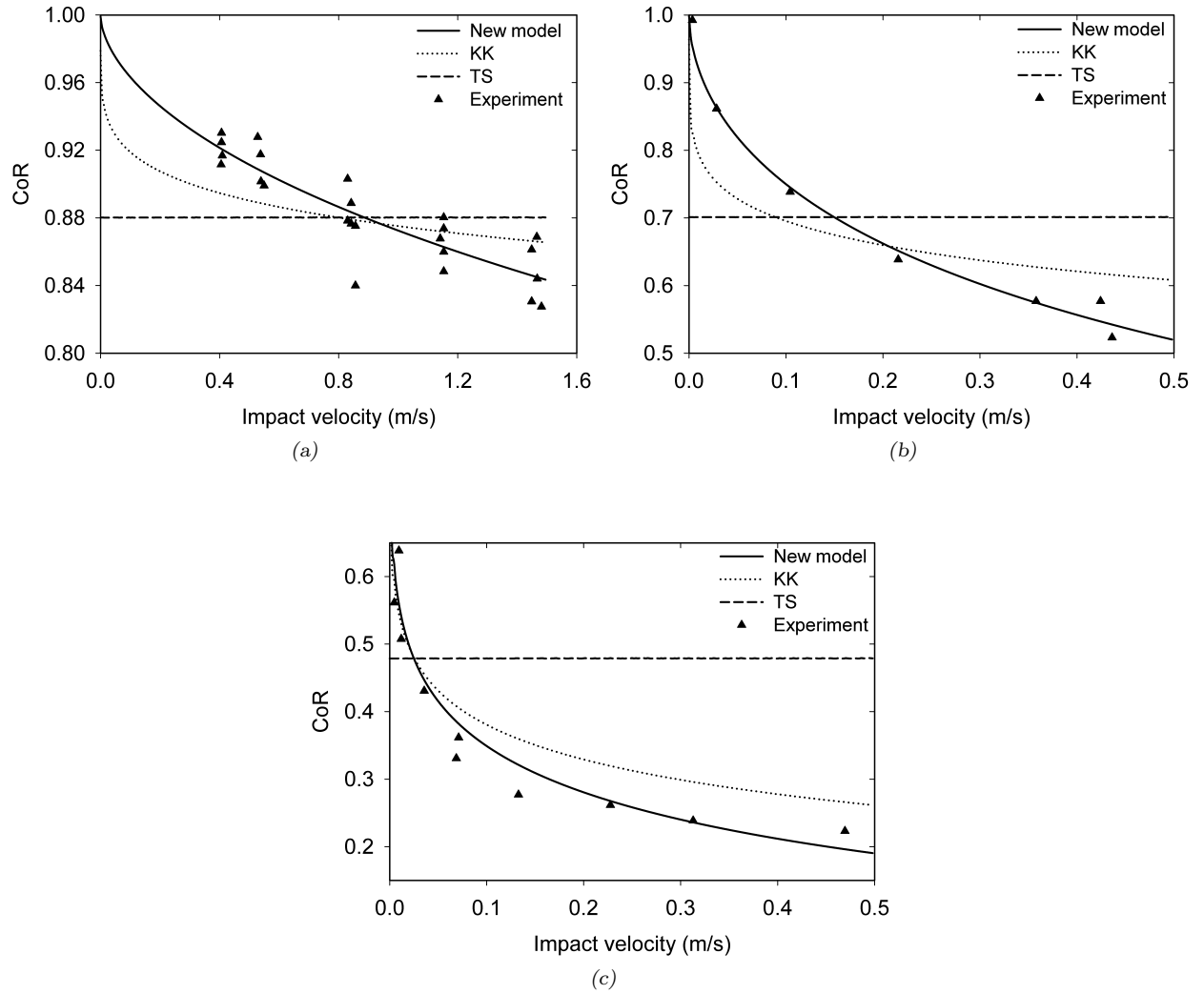


Figure 8.6: Coefficient of restitution versus the impact velocity for different materials in the case of particle/particle collisions : (a) stainless steel (SS), (b) brass (BR) and (c) lead (LE).

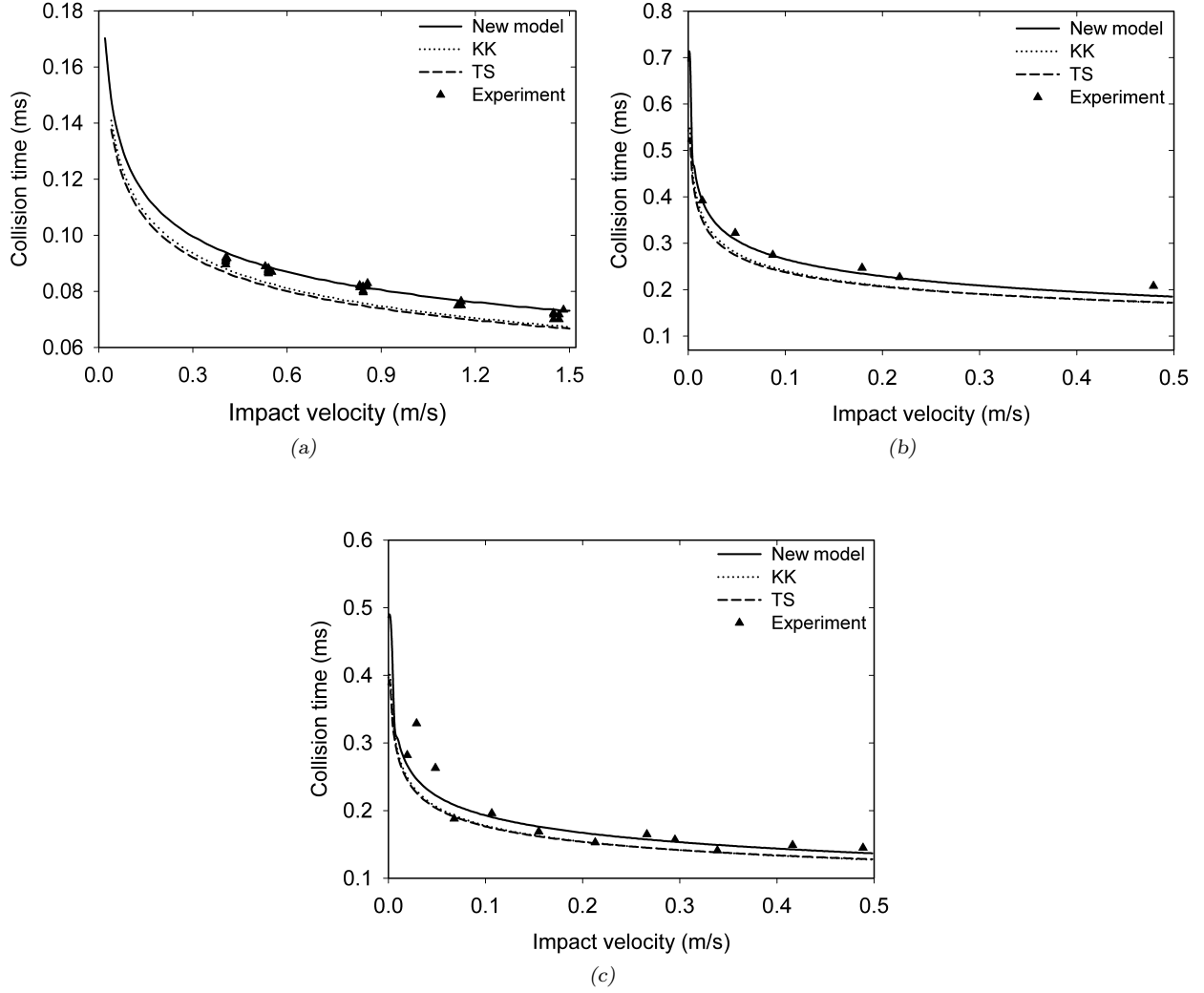


Figure 8.7: Collision time versus the impact velocity for different materials in the case of particle/particle collisions : (a) stainless steel (SS), (b) brass (BR) and (c) aluminum (Al).

(S.D.) for the experimental data were also calculated for each point and the averaged value is given in Fig. 8.8 for each material. One may notice that there is a good agreement between the numerical results and these experimental data. In both cases, the CoR decreases with an increase of the normal impact velocity. Most models from the literature do not predict this behavior. The LH model predicts an upward trend whereas the Hertz, the TS and the LSD models predict a CoR that is independent of the impact velocity.

To understand the effect of the parameters of the model on particle collisions, the variation

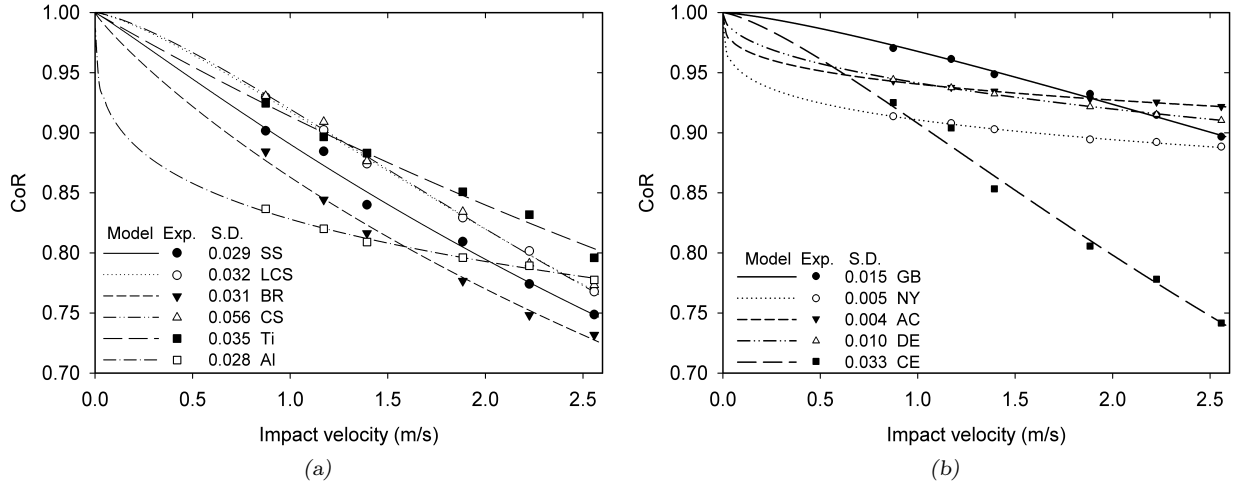


Figure 8.8: Coefficient of restitution versus the impact velocity for different materials in the case of particle/wall collisions : (a) metallic spheres and (b) non metallic spheres.

of the CoR versus the impact velocity is given for low carbon steel spheres (LCS) in Fig. 8.9, where one of the parameters is kept constant while the other one is varied. More precisely, the power law index is kept constant ($n_l = 1.72$) and μ varies in Fig. 8.9a, while μ is kept constant ($\mu = 1.35 \times 10^5$) and the power law index varies in Fig. 8.9b (based on the values in Table 8.3). In Fig. 8.9a, one can see that there is less dissipation of energy and the collision becomes more elastic, that is the curves flatten out, when μ approaches zero. On the other hand, the energy dissipation increases and the collisions get more and more viscoelastic when μ is increased. In such cases, the curves become steeper at low impact velocities and flatten out at high impact velocities. Experimental data of CoR for different particle sizes are also shown on this figure. It can be noticed that increasing the particle size leads to an increase of μ and a decrease of the CoR for a given impact velocity. As mentioned in Section 8.4, no significant impact of the particle size on the value of n_l was observed for LCS particles.

Fig. 8.9b shows that the CoR is not dependent on the impact velocity when $n_l = 0.4$ (blue line), as can be deduced from Eq. 8.8 (by substituting $\alpha = 3/2$, $\beta = 1$ and $\gamma = n_l$). Below and above this value, the model predicts respectively increasing and decreasing behaviors of the CoR curves when the normal impact velocity increases. For instance, for a value of n_l around

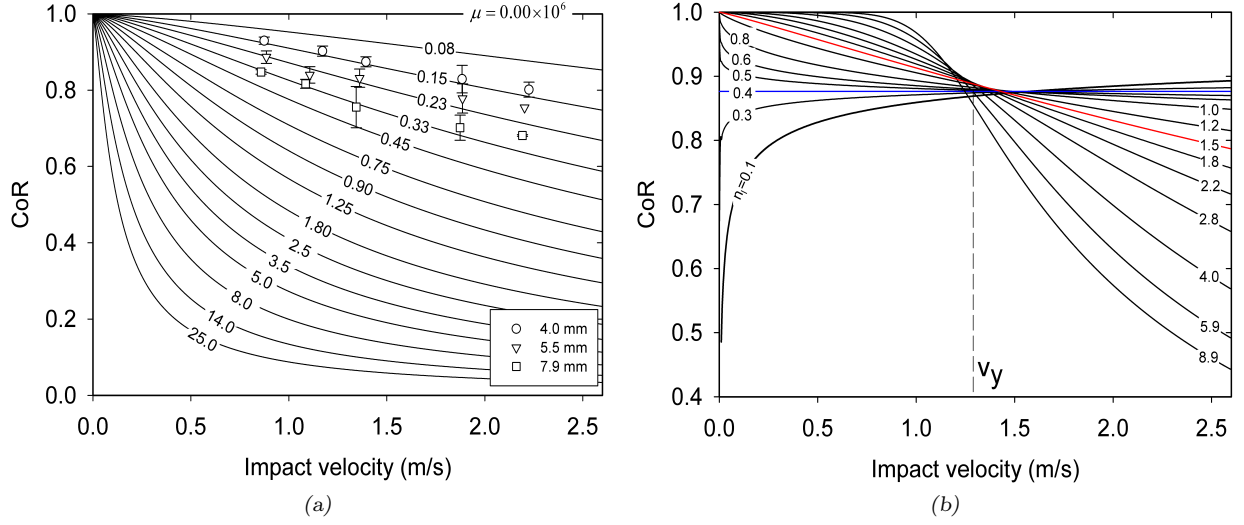


Figure 8.9: Variation of the coefficient of restitution for low carbon steel spheres when (a) the power law index is constant ($n_l = 1.72$) and μ varies, and (b) μ is constant ($\mu = 1.35 \times 10^5$) and n_l varies. The symbols in (a) refer to particle size.

1.5 (red line), the curve is linearly decreasing for the range of impact velocities considered. This behavior is in fact true for all the materials considered in this work (not shown here). As n_l increases to larger values, the collisions are close to pure elastic at low impact velocities, and the CoR then decreases sharply when this velocity becomes large enough. As can be seen on the graph, there is in fact a velocity v_y of about 1.3 m/s for large values of n_l , below which collisions are nearly elastic and above which they become viscoelastic.

A graph of n_l versus the hardness of the materials is presented in Fig. 8.10 in order to highlight the dependency of n_l on the material. It can be noticed that the dashpot liquid for hard materials is shear thickening (hardness > 90 vickers), whereas it is shear-thinning for soft materials (hardness < 90 vickers). When the particle hardness is ~ 90 vickers, the dashpot liquid is Newtonian. As evidenced in the figure, the value of n_l should be less than 0.4 for very soft materials (hardness < 50 vickers), indicating that the CoR for such materials should show an increasing trend when the impact velocity is increased, as shown in Fig 8.9b. To validate this, 4-mm polypropylene (PP) particles (hardness $\simeq 48$ vickers) were dropped

against the horizontal plate of the apparatus described in Section 8.3. The corresponding CoR versus impact velocity curve is depicted in Fig. 8.11. The best fit for this curve is $\mu = 5.39 \times 10^3$ and $n_l = 0.21$. It may be readily noticed that the CoR does increase with the impact velocity. It decreases significantly when the impact velocity tends toward zero and levels off to a fixed value at high impact velocities. This result contradicts what is common belief in the literature, let alone that the CoR decreases when the impact velocity is increased.

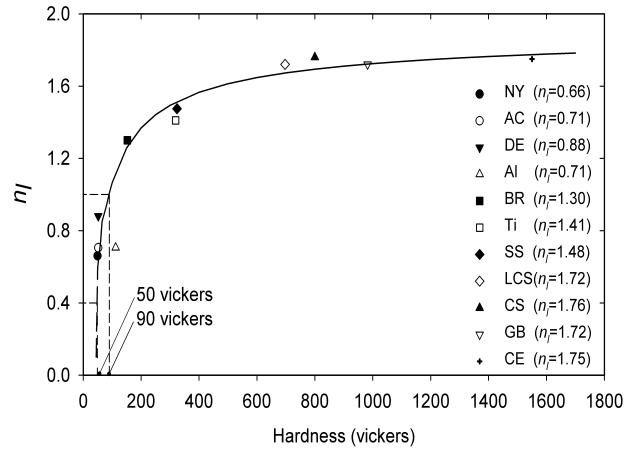


Figure 8.10: Experimental variation of the power law index (n_l) versus the hardness of the materials.

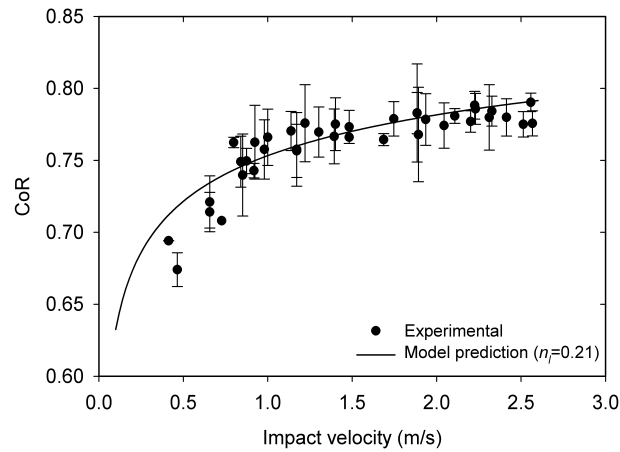


Figure 8.11: Experimental variation of the coefficient of restitution with respect to the impact velocity for 4-mm polypropylene spheres. Error bars have been added to show the uncertainty for this type of measurements

8.5.2 Microscopic quantities

For the model introduced in this work, which involves a non-linear Hertz spring and a dissipative damping force, the equation of motion for impacting particles is

$$m_{eff}\ddot{\delta} + 4\pi\mu\dot{\delta}^{n_l}\delta + \frac{4}{3}E^*\sqrt{R^*}\delta^{\frac{3}{2}} = 0. \quad (8.21)$$

A particle/particle (or particle/wall) contact implies a positive overlap ($\delta > 0$), and the eventual separation happens when this overlap goes to zero ($\delta = 0$). Adequate initial conditions for Eq. 8.21 are $\delta(0) = 0$ and $\dot{\delta}(0) = v_{ij}^\circ$, where v_{ij}° is the impact velocity. There is no analytical solution for this equation. It was solved here using the sixth-order Runge-Kutta method and MATLAB. The time step was chosen to be 10^{-2} times the characteristic time τ_c that corresponds to a typical contact time. Such a characteristic time can be evaluated as (Lemieux et al., 2008) :

$$\tau_c = R^* \sqrt{\frac{8\rho\pi^3}{E^*}}. \quad (8.22)$$

Variations of the particle overlap, the normalized velocity, and the contact force during a particle/particle collision are given in Fig. 8.12 for stainless steel, brass and lead spheres, which correspond to nearly elastic, viscoelastic and very viscoelastic collisions, respectively, in the context of the proposed model. These results show that the particle overlap and the absolute value of the contact force increase from zero to a maximum and then decrease to zero. Given that the non-linear models only differ in dissipative terms, they predict similar values for the elastic collision (stainless steel), yet deviate from one another when the collision is viscoelastic (brass and lead). In all cases, the initial contact force is zero while some of the other models from the literature (*e.g.* the LSD model in Section 8.2.2) suffer from a non-zero initial force. The presence of the overlap δ in the dissipative term of the current model and those of the KK and TS models eliminates this non-physical behavior (Ji and Shen, 2006; Zhang and Whiten, 1996).

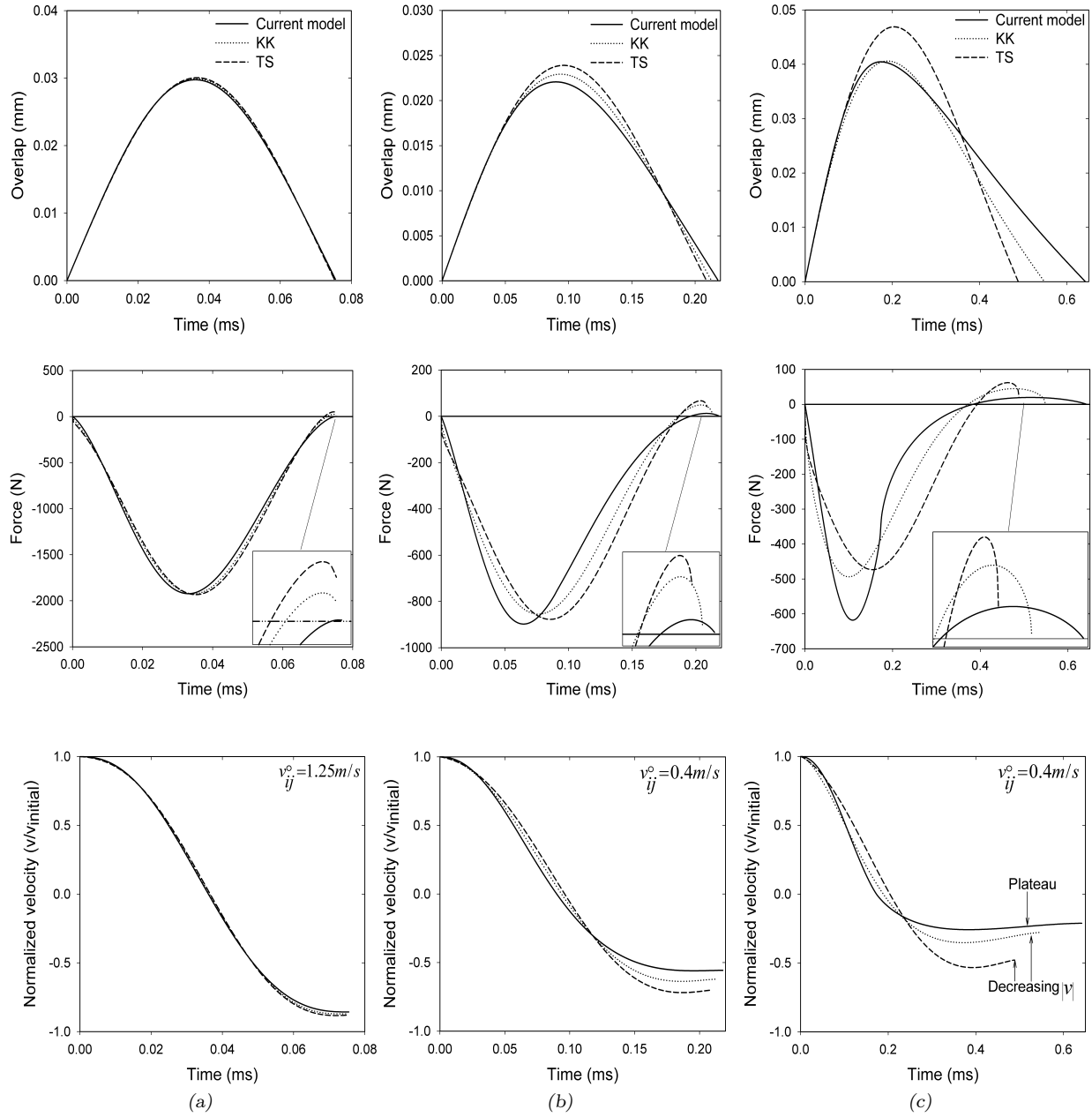


Figure 8.12: Comparison of non-linear models in the case of a particle/particle collision : (a) nearly elastic collision (stainless steel), (b) viscoelastic collision (brass) and (c) very viscoelastic collision (lead).

The KK and TS models exhibit a dissipative term that surpasses the repulsive elastic force at the end of a collision, resulting in an attractive net force that subsequently leads to a decrease of the absolute value of the particle velocity. As mentioned in Section 8.2.2, this

is unphysical. As shown in Fig. 8.12, the current model alleviates this shortcoming and, as a result, the particle velocity levels off to a plateau at the end of the collision. Moreover, the occurrence of a short duration for the attractive force in the case of stainless steel and brass particles leads to predicted collision times that are closer to the experimental data, as can be observed in Fig. 8.7. In the case of the lead particles, the duration of the repulsive force is similar for all models. However, it can be seen in the Fig. 8.12 that the maximum value of the attractive force is significantly lower for the proposed model than for the KK and TS models. To compare the performance of the non-linear models, the normal impulse, P^n , was computed during a collision, when the contact force is repulsive or attractive :

$$P_{rep}^n = \int_{t=0}^{t_{F^n=0}} F^n(t) dt \quad (\text{repulsive}), \quad (8.23)$$

$$P_{att}^n = \int_{t_{F^n=0}}^{t_{\delta=0}} F^n(t) dt \quad (\text{attractive}). \quad (8.24)$$

As an illustration, the P^n versus impact velocity curve for brass spheres is shown in Fig. 8.13. One may notice that the values of P_{rep}^n are similar for all models, while the values of P_{att}^n are much smaller with the proposed model than with the KK and TS models : A similar behavior was observed for all the materials considered in this work.

8.6 Conclusion

The objective of this work was to develop a contact force model that alleviates some of the limitations characteristic of existing models. For instance, some of the common models fail to predict the correct behavior of the CoR with respect to the impact velocity. They can predict an increase (LH model) or a decrease (KK model) of the CoR, or even constant value of this coefficient (LSD and TS models). Some models (KK model) do predict a correct trend yet they are not sufficiently accurate. Another drawback of most existing models is the

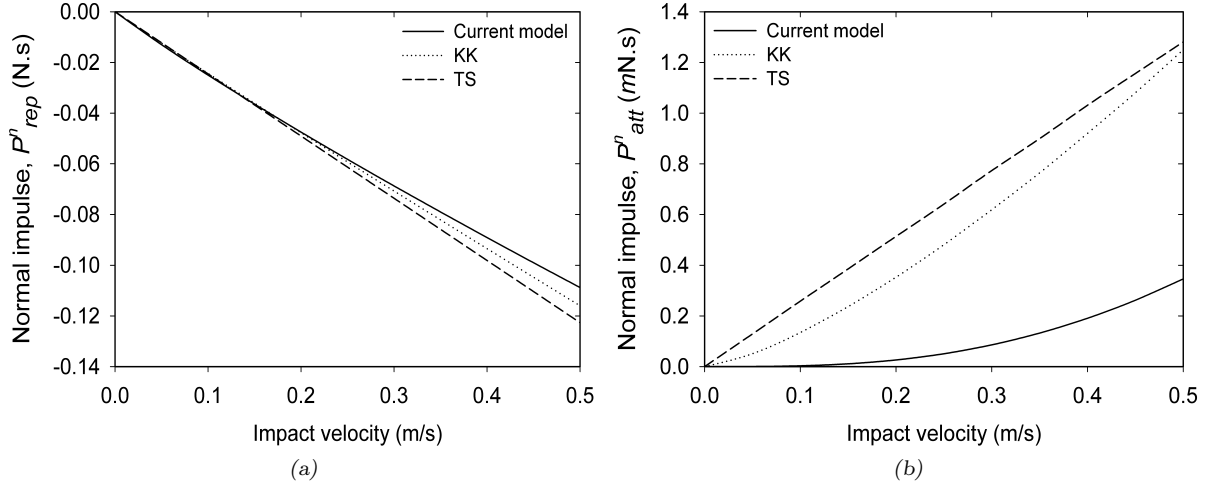


Figure 8.13: Graph of the normal impulse P^n versus the impact velocity when (a) repulsive and (b) attractive forces are considered for the collision of two brass spheres.

occurrence of an attractive force at the end of a particle collision, which reduces the absolute value of the particle velocity.

The model proposed in this work uses the Hertz theory to evaluate the elastic force and a dashpot filled with a non-Newtonian liquid to dissipate energy. More precisely, when two particles collide, the extent of the overlap is predicted by the depth of penetration of a piston in this non-Newtonian liquid that obeys a 2-parameter power law model. The values of these two parameters were evaluated for various materials by means of experimental CoR data obtained from an apparatus that we built for particle/wall collisions and from the literature for particle/particle collisions. It was observed that the power-law index of the non-Newtonian liquid depends on the hardness of the impacting particles, and that this liquid is shear-thickening and shear-thinning for hard and soft materials, respectively. For very soft materials, the model predicts an increase of the CoR with an increase of the impact velocity, which was confirmed by experimental measurements involving polypropylene spheres. Overall, it was shown that the results obtained with the new model agree well with experimental data. In particular, it was observed that, contrary to existing models, this model predicts a smaller attractive force at the end of a collision.

Finally, although the proposed model is simple to calibrate, its use is restricted to the normal impact between two particles. Future work will focus on the extension and use of this model in the more general case of collisions involving multiple particles.

Acknowledgments

The authors would like to thank Dr. Harald Kruggel-Emden for providing the experimental data for the particle/particle collisions. This research was supported by the Research and Development Center of Ratiopharm operations (Mirabel, Québec) and NSERC (Canada).

8.7 References

- Antypov, D., Elliott, J. A., and Hancock, B. C. (2011). Effect of particle size on energy dissipation in viscoelastic granular collisions. *Physical Review E*, 84 :021303.
- Aoki, K. and Akiyama, T. (1995). Simulation studies of pressure and density wave propagations in vertically vibrated beds of granules. *Physical Review E*, 52(3) :3288–3291.
- Aranson, I. and Tsimring, L. (1999). Dynamics of axial separation in long rotating drums. *Physical Review Letters*, 82(23) :4643–4646.
- Bird, R., Stewart, W., and Lightfoot, E. (2001). *Transport phenomena*. John Wiley & Sons, Inc.
- Bolz, R. and Tuve, G. (1970). *CRC handbook of tables for applied engineering science*. CRC Press, Boca Raton.
- Brauer, H. (1980). Report on investigations on particle movement in straight horizontal tubes, particle/wall collision and erosion of tubes and tube bends. *Journal of powder & bulk solids technology*, 4(2-3) :3–12.
- Bridges, F., Hatzes, A., and Lin, D. (1984). Structure, stability and evolution of saturn's rings. *Nature*, 309(5966) :333–335.
- Brillantov, N., Spahn, F., Hertzsch, J.-M., and Poschel, T. (1996). Model for collisions in granular gases. *Physical Review E*, 53(5) :5382–5392.

- Cundall, P. and Strack, O. (1979). Discrete numerical model for granular assemblies. *Geotechnique*, 29(1) :47–65.
- Di Renzo, A. and Di Maio, F. P. (2004). Comparison of contact-force models for the simulation of collisions in DEM-based granular flow codes. *Chemical Engineering Science*, 59(3) :525–541.
- Ding, Y., Forster, R., Seville, J., and Parker, D. (2002). Segregation of granular flow in the transverse plane of a rolling mode rotating drum. *International Journal of Multiphase Flow*, 28(4) :635–663.
- Doucet, J., Bertrand, F., and Chaouki, J. (2008). An extended radioactive particle tracking method for systems with irregular moving boundaries. *Powder Technology*, 181(2) :195–204.
- Dury, C. M. and Ristow, G. H. (1997). Radial segregation in a two-dimensional rotating drum. *Journal de physique I*, 7(5) :737–745.
- Foerster, S., Louge, M., Chang, H., and Allia, K. (1994). Measurements of the collision properties of small spheres. *Physics of Fluids*, 6(3) :1108–1115.
- Gale, W.F. and Totemeier, T. (2004). *Smithells Metals Reference Book (8th Edition)*. Elsevier.
- Goldenberg, C. and Goldhirsch, I. (2004). Small and large scale granular statics. *Granular Matter*, 6(2-3) :87–96.
- Goldsmith, W. (1960). *Impact*. Edward Arnold Ltd.
- Gorham, D. and Kharaz, A. (2000). The measurement of particle rebound characteristics. *Powder Technology*, 112(3) :193–202.
- Ji, S. and Shen, H. H. (2006). Effect of contact force models on granular flow dynamics. *Journal of Engineering Mechanics*, 132(11) :1252–1259.
- Khakhar, D., McCarthy, J., and Ottino, J. (1997). Radial segregation of granular mixtures in rotating cylinders. *Physics of Fluids*, 9(12) :3600–3614.

- Khakhar, D., Orpe, A. V., and Ottino, J. (2001). Continuum model of mixing and size segregation in a rotating cylinder : Concentration-flow coupling and streak formation. *Powder Technology*, 116(2-3) :232–245.
- Kharaz, A., Gorham, D., and Salman, A. (1999). Accurate measurement of particle impact parameters. *Measurement Science and Technology*, 10(1) :31–35.
- Krugel-Emden, H., Simsek, E., Rickelt, S., Wirtz, S., and Scherer, V. (2007). Review and extension of normal force models for the discrete element method. *Powder Technology*, 171(3) :157–173.
- Kschinka, B., Perrella, S., Nguyen, H., and Bradt, R. (1986). Strengths of glass spheres in compression. *Journal of the American Ceramic Society*, 69(6) :467–472.
- Kuwabara, G. and Kono, K. (1987). Restitution coefficient in a collision between two spheres. *Japanese Journal of Applied Physics*, 26(8) :1230–1233.
- Labous, L., Rosato, A. D., and Dave, R. N. (1997). Measurements of collisional properties of spheres using high-speed video analysis. *Physical Review E*, 56(5-B pt B) :5717–5717.
- Langston, P., Tüzün, U., and Heyes, D. (1994). Continuous potential discrete particle simulations of stress and velocity fields in hoppers : transition from fluid to granular flow. *Chemical Engineering Science*, 49(8) :1259–1275.
- Lee, J. and Herrmann, H. (1993). Angle of repose and angle of marginal stability : molecular dynamics of granular particles. *Journal of Physics A*, 26(2) :373–83.
- Lemieux, M., Leonard, G., Doucet, J., Leclaire, L.-A., Viens, F., Chaouki, J., and Bertrand, F. (2008). Large-scale numerical investigation of solids mixing in a V-blender using the discrete element method. *Powder Technology*, 181(2) :205–216.
- Li, L., Thornton, C., and Wu, C. (2000). Impact behaviour of elastoplastic spheres with a rigid wall. *Proceedings of the Institution of Mechanical Engineers, Part C : Journal of Mechanical Engineering Science*, 214(8) :1107–1114.

- Li, L.-Y., Wu, C.-Y., and Thornton, C. (2002). A theoretical model for the contact of elastoplastic bodies. *Proceedings of the Institution of Mechanical Engineers, Part C (Journal of Mechanical Engineering Science)*, 216(C4) :421–431.
- Lorenz, A., Tuozzolo, C., and Louge, M. (1997). Measurements of impact properties of small, nearly spherical particles. *Experimental Mechanics*, 37(3) :292–298.
- Mishra, B. and Murty, C. (2001). On the determination of contact parameters for realistic DEM simulations of ball mills. *Powder Technology*, 115(3) :290–297.
- Nakagawa, M., Altobelli, S., Caprihan, A., Fukushima, E., and Jeong, E.-K. (1993). Non-invasive measurements of granular flows by magnetic resonance imaging. *Experiments in Fluids*, 16(1) :54–60.
- Ramirez, R., Poschel, T., Brilliantov, N., and Schwager, T. (1999). Coefficient of restitution of colliding viscoelastic spheres. *Physical Review E*, 60(4) :4465–4472.
- Rapaport, D. (2007). Radial and axial segregation of granular matter in a rotating cylinder : a simulation study. *Physical Review E*, 75(3) :31301–1–11.
- Sadd, M. H., Tai, Q., and Shukla, A. (1993). Contact law effects on wave propagation in particulate materials using distinct element modeling. *International Journal of Non-Linear Mechanics*, 28(2) :251–265.
- Schäfer, J., Dippel, S., and Wolf, D. (1996). Force schemes in simulations of granular materials. *Journal De Physique, I*, 6(1) :5–20.
- Schwager, T. and Poschel, T. (2007). Coefficient of restitution and linear-dashpot model revisited. *Granular Matter*, 9(6) :465–469.
- Sondergaard, R., Chaney, K., and Brennen, C. (1990). Measurements of solid spheres bouncing off flat plates. *Journal of Applied Mechanics, Transactions ASME*, 57(3) :694–699.
- Stevens, A. and Hrenya, C. (2005). Comparison of soft-sphere models to measurements of collision properties during normal impacts. *Powder Technology*, 154(2-3) :99–109.

- Taberlet, N., Losert, W., and Richard, P. (2004). Understanding the dynamics of segregation bands of simulated granular material in a rotating drum. *Europhysics Letters*, 68(4) :522–528.
- Thornton, C. (1997). Coefficient of restitution for collinear collisions of elastic-perfectly plastic spheres. *Journal of Applied Mechanics, Transactions ASME*, 64(2) :383–386.
- Thornton, C., Cummins, S. J., and Cleary, P. W. (2013). An investigation of the comparative behaviour of alternative contact force models during inelastic collisions. *Powder Technology*, 233(0) :30–46.
- Thornton, C. and Ning, Z. (1998). A theoretical model for the stick/bounce behaviour of adhesive, elastic-plastic spheres. *Powder Technology*, 99(2) :154–162.
- Tsuji, Y., Tanaka, T., and Ishida, T. (1992). Lagrangian numerical simulation of plug flow of cohesionless particles in a horizontal pipe. *Powder Technology*, 71(3) :239–250.
- Walton, O. and Braun, R. (1986). Viscosity, granular-temperature, and stress calculations for shearing assemblies of inelastic, frictional disks. *Journal of Rheology*, 30(5) :949–980.
- Walton, O. R. (1983). Application of molecular dynamics to macroscopic particles. *International Journal of Engineering Science*, 22(8-10) :1097–1107.
- Wojtkowski, M., Pecen, J., Horabik, J., and Molenda, M. (2010). Rapeseed impact against a flat surface : Physical testing and DEM simulation with two contact models. *Powder Technology*, 198(1) :61–68.
- Wu, C.-Y., Li, L.-Y., and Thornton, C. (2005). Energy dissipation during normal impact of elastic and elastic-plastic spheres. *International Journal of Impact Engineering*, 32(1-4) :593–604.
- Wu, C.-Y., Thornton, C., and Li, L.-Y. (2009). A semi-analytical model for oblique impacts of elastoplastic spheres. *Proceedings of the Royal Society of London, Series A (Mathematical, Physical and Engineering Sciences)*, 465(2103) :937–960.

- Yamane, K., Nakagawa, M., Altobelli, S., Tanaka, T., and Tsuji, Y. (1998). Steady particulate flows in a horizontal rotating cylinder. *Physics of Fluids*, 10(6) :1419–27.
- Zhang, D. and Whiten, W. (1996). Calculation of contact forces between particles using spring and damping models. *Powder Technology*, 88(1) :59–64.
- Zhu, H., Zhou, Z., Yang, R., and Yu, A. (2008). Discrete particle simulation of particulate systems : a review of major applications and findings. *Chemical Engineering Science*, 63(23) :5728–5770.

CHAPTER 9

GENERAL DISCUSSION

The main objective of this work was to shed light on the mixing and segregation behavior inside tumbling blenders. Among the conventional blenders, the V-blender and the rotating drum were chosen because they have many applications in a wide range of industries. However, known limitations of tumbling blenders (weak diffusive axial mixing and segregation of free flowing granules) provided the motivation to investigate the performance of the so-called tetrapodal blender and compare it to conventional V-blenders. Before investing in manufacturing a lab-scale version of the tetrapodal blender to investigate its performance experimentally, it is of interest to characterize the efficiency of the blender via numerical tools to verify its superiority against conventional tumbling blenders and obtain design parameters. Discrete element method (DEM) was chosen to investigate granule mixing and segregation inside these blenders. This technique suffers from some limitations that one should be vigilant when using its results. Therefore, in the first step of this work, the accuracy of DEM-based model was assessed by comparing its results against Lagrangian experimental data, obtained by radioactive particle tracking (RPT), and new criteria were provided to choose simulation parameters. Next, considering the results of first step, appropriate DEM parameters were chosen to investigate the mixing and segregation of non-adhesive granules inside the tetrapodal blender and the V-blender. Finally, the numerical findings of mixing and segregation inside these blenders were validated through experimental data of thief sampling and more investigations were performed to characterize the effect of operating conditions on the blender efficiency. The above mentioned three steps corresponded to the specific objectives of this work :

1. To validate the DEM-based model and conduct a sensitivity analysis with respect to simulation parameters ;

2. To introduce the tetrapodal blender and compare its performance to that of the V-blender ;
3. To validate the numerical simulation results of solid mixing and segregation in the tetrapodal blender and the V-blender, and investigate the effect of operating parameters on their efficiencies.

The main findings of these steps are described next.

First specific objective :

Validation of the DEM-based model was on the basis of experimental RPT data for mixing and size segregation behavior of a polydisperse mixture of glass beads inside a rotating drum. Both techniques (DEM and RPT) provide Lagrangian particle trajectories. Sodium was used for the first time as irradiating isotope in RPT experiments. All the properties of glass beads were measured experimentally or extracted from the literature and used in the DEM simulations excluding the Young's modulus and the friction coefficients, where smaller and higher values were applied, respectively. A comparison of RPT and DEM results was performed based on the velocity profile and residence time of the granules in the active and passive layers as well as their axial dispersion and mixing/segregation behavior. A good agreement was obtained in terms of the velocity profile and residence time. The DEM prediction for the axial dispersion along the radial direction was observed to comply with the RPT data, although with smaller axial dispersion coefficients. In the case of mixing and segregation, the DEM simulations predicted axial segregation, a phenomenon that was not observed in the experiments. This can be explained by the large friction coefficients used in these simulations.

A sensitivity analysis of the DEM-based model was then performed with respect to the particle physical parameters. Dimensionless equations of motion were derived and analyzed in both the normal and tangential directions. These equations indicate that when the gravity force on the particles can be neglected against the contact forces, the particle dynamics and the dimensionless motion equations are not affected by the Young's modulus. In the other

situations, where the gravity force on the particles is non-negligible, a correlation was derived, which may be used to set the values of the static friction coefficients $\mu_{w,s}$ for DEM simulations when a smaller value of the Young's modulus E is used :

$$\frac{A^t}{C^t} = K\mu_{w,s}E^{0.4}. \quad (9.1)$$

Second specific objective :

Considering the findings from the first specific objective, DEM-based model was employed to simulate the granular flow inside the tetrapodal blender and the V-blender underlying several operating conditions (different loading profiles, fill levels and rotational speeds) with monodisperse and bidisperse mixtures. The tetrapodal blender indicated a shorter mixing time than the V-blender and its radial convective and axial diffusive mixing mechanisms were more efficient. It was also demonstrated that if one part (upper or lower V-shaped parts) of the standard tetrapodal blender is twisted by 45° , the geometry significantly enhances the axial mixing rendering it as efficient as the radial mixing. Higher mean axial and radial velocity profiles were observed for the tetrapodal blender than the V-blender. In addition to a monodisperse mixture, simulations with a binary mixture showed that there is not significant segregation in the tetrapodal blender. Segregation mechanisms were investigated and it was shown that kinetic sieving is the dominant segregation mechanism in the tetrapodal blender.

Third specific objective :

In the second step only one case study was considered for the segregation of granules (bidisperse mixture with size ratio of 2), yet more investigation is needed for unfavorably worst-case scenarios such as granules with large size and/or density ratios. Investigation of all affecting parameters on the segregation intensity with DEM-based model is time-consuming with current computing facilities. Therefore, it was decided to study the effect of all these parameters experimentally and, in addition, validate the obtained numerical findings. More

than 100 experiments were carried out and characterized using thief sampling. Under several operating conditions, tetrapodal blender showed more efficient radial and axial mixing mechanisms than the V-blender. In especial configurations of the tetrapodal blender, it was shown that axial mixing is as efficient as radial mixing. Both radial and axial mixing rates decreased with an increase in the fill level, whereas the effect of increasing of rotational speed was not significant and axial (resp. radial) mixing rates increased (resp. decreased) slightly. Size segregation was investigated in different configurations of the tetrapodal blender underlying a wide range of rotational speeds ($5\text{-}30\text{RPM}$) and fill levels ($35\text{-}65\%V$). Segregation intensity decreased slightly with fill level, but significantly with rotational speed. Comparing these results with the reported data in the literature for V-blenders, it was shown that the tetrapodal blender is less prone to segregate granules than the V-blender. Finally, the effect of granules density and simultaneous effects of granules density and size on the segregation intensity were investigated. A criterion was given for the scale-up of this blender to operate away from the situations, where significant segregation occurs.

New contact force model :

Though good agreements were observed between DEM results and experimental data of RPT in the case of the rotating drum and thief sampling in the case of the tetrapodal blender and the V-blender, there were some discrepancies. We believe that such errors arise mainly from inappropriate simulation parameters as well as weak predictions of contact force models. The former was discussed in the first step of this work, but the latter indeed requires more investigation. Therefore, in the last part of this study, a model was developed, thus alleviating certain limitations of existing models.

The model proposed in this work uses the Hertz theory to evaluate the elastic force and a dashpot filled with a non-Newtonian liquid to dissipate energy. More precisely, when two particles collide, the extent of the overlap is approximated by the depth of penetration of a piston in this non-Newtonian liquid that obeys a 2-parameter power law model. The values

of these two parameters were evaluated for various materials by means of the experimental coefficient of restitution (CoR) data obtained from an apparatus that we built for particle/wall collisions and from the literature for particle/particle collisions. It was observed that the power-law index of the non-Newtonian liquid depends on the hardness of the impacting particles, and the liquid is shear-thickening and shear-thinning for hard and soft materials, respectively. For very soft materials, the model predicts an increase in the CoR with an increase in impact velocity, which was confirmed by experimental measurements involving polypropylene spheres. Overall, it was shown that the results obtained with the new model agree well with experimental data. In particular, it was observed that, contrary to the existing models, this model predicts a smaller attractive force at the end of a collision.

In Chapter 8, the predictions of this model were only compared with those of non-linear viscoelastic models in order to keep this chapter straightforward and aligned with the viscoelastic models. It is also of interest to compare the predictions of the proposed model with hysteric models. According to the discussion that has been provided in Kruggel-Emden et al. (2007), among hysteretic models those given by Thornton (1997); Thornton and Ning (1998) (TH) and Tomas (2003) (TO) perform well for predicting CoR, and the model given by Walton and Braun (1986) (WB) performs less accurate. These models are not very accurate to predict collision time. For example, the WB model that performs acceptably for CoR behavior of metallic spheres, yet utterly fails in the case of collision time (Kruggel-Emden et al., 2007).

In general, hysteric models perform well for some material, but fail for others. For instance, in the case of collision of two brass spheres, TO has very good prediction, TH is acceptable, while WB has low accuracy and KK fails (see Fig. 9.1a). For marble spheres, none of the hysteric models have good performance, but KK works well (Fig. 9.1b). Therefore, while viscoelastic and hysteric models have good predictions for some materials and fail for others, our model performs quite well for a wide range of materials.

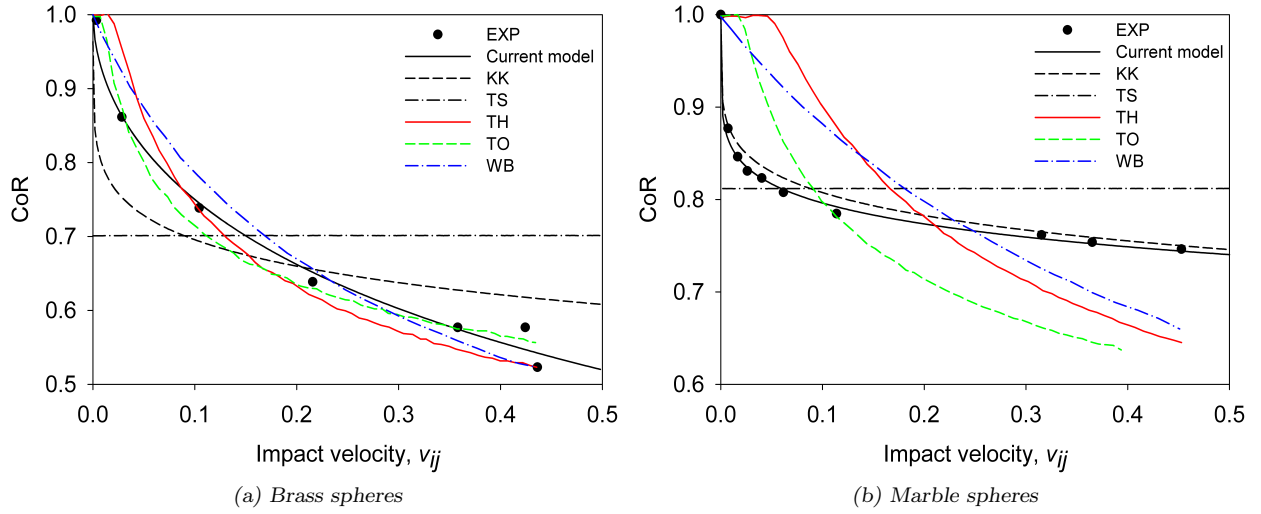


Figure 9.1: Prediction of CoR for (a) brass spheres and (b) marble spheres using viscoelastic, hysteretic and proposed models. The symbols refer to the experimental data from (Goldsmith, 1960) and the predictions of hysteretic models are extracted from Kruggel-Emden et al. (2007).

9.1 References

Goldsmith, W. (1960). *Impact*. Edward Arnold Ltd.

Kruggel-Emden, H., Simsek, E., Rickelt, S., Wirtz, S., and Scherer, V. (2007). Review and extension of normal force models for the discrete element method. *Powder Technology*, 171(3) :157–173.

Thornton, C. (1997). Coefficient of restitution for collinear collisions of elastic-perfectly plastic spheres. *Journal of Applied Mechanics, Transactions ASME*, 64(2) :383–386.

Thornton, C. and Ning, Z. (1998). A theoretical model for the stick/bounce behaviour of adhesive, elastic-plastic spheres. *Powder Technology*, 99(2) :154–162.

Tomas, J. (2003). Mechanics of nanoparticle adhesion - A continuum approach. *Particles on Surfaces 8 : Detection, Adhesion and Removal*, pages 1–47.

Walton, O. and Braun, R. (1986). Viscosity, granular-temperature, and stress calculations for shearing assemblies of inelastic, frictional disks. *Journal of Rheology*, 30(5) :949–980.

CHAPTER 10

CONCLUSION AND RECOMMENDATIONS

10.1 Summary of the thesis

In this work, mixing and segregation behavior of free-flowing spherical granules were investigated in a rotating drum, a V-blender and a tetrapodal blender. A detailed study was performed on granular flow inside the rotating drum using radioactive particle tracking (RPT) data. Such an analysis was used to verify our DEM-based model (discrete element method) and a sensitivity analysis of this model with respect to its parameters was carried out.

A comparison was performed between the performances of the tetrapodal blender and the V-blender (both numerically and experimentally). It was shown that the axial and radial mixing mechanisms are more efficient in the tetrapodal blender and this blender is less prone to segregation of granules with different properties. Therefore, it is suggested to replace conventional tumbling blenders with this blender when the following conditions are encountered :

- Significant segregation is observed in the final product ;
- The final product is not homogeneous due to weak mixing mechanisms ;
- The mixing time is long.

10.2 Contributions of the thesis

The scientific contributions of this work belong to four categories. First, the deep findings of this work in the case of tumbling blenders may facilitate the design and scale-up of more efficient solid mixing processes. Secondly, mixing and segregation inside the tetrapodal blender were studied for the first time. It is recommended to use a tetrapodal blender, where there

are issues with conventional mixers regarding mixing time or non-homogenous products that may be a result of less efficient mixing mechanisms or segregation. Thirdly, it was originally shown : “why a DEM-based model yields acceptable results even with wrong physical parameters”. Finally, our accurate contact force model can be applied in DEM-based simulations to obtain more reliable results.

10.3 Limitations of the tetrapodal blender

Although the tetrapodal blender is technical superior to common tumbling blenders, it nonetheless suffers from some limitations :

- Complexity of the geometry generates some issues regarding the construction of the blender as well as its cleaning after operation ;
- Larger dimensions of this blender than the conventional V-blender necessitate additional space and energy for its operation ;
- There are trends in the industry which rely on the blenders that can also be used as a storage bin. This blender does not satisfy this requirement ;
- Standardization of the blender has not been carried out to fit industrial applications.

10.4 Future work and recommendations

1. Further investigation is needed to characterize the ability of the tetrapodal blender regarding the mixing of cohesive granules ;
2. Numerically obtained granular dynamics inside the tetrapodal blender should be verified through Lagrangian experimental data ;
3. The new contact force model, developed in Chapter 8, needs to be applied in DEM simulations with many particles and the results should be verified through experimental data ;
4. The tangential contact force models in DEM simulations suffer from many limitations. It is recommended to perform a thorough investigation in this regard ;

5. In this study, only spherical particles have been considered. Investigation of non-spherical granules (both numerically and experimentally) is of high interest.

APPENDIX A

Dynamics of Non-Spherical Particles in a Rotating Drum

Olivier Dubé, Ebrahim Alizadeh, Jamal Chaouki, François Bertrand

Department of Chemical Engineering, École Polytechnique de Montréal, C.P. 6079 succ.

Centre-Ville, Montréal, Québec, Canada, H3C 3A7

(Submitted to *Chemical Engineering Science*)

Presentation of the appendix : The granular flow, solid mixing and segregation behavior in several tumbling blenders have been studied for spherical particles. However, investigation of non-spherical granules (both numerically and experimentally) is of high interest. In this appendix, the flow of non-spherical particles in a rotating drum will be studied.

Abstract : Considerable amount of experimental work has been performed to elucidate the behavior of granular flow inside a rotating drum and it has yet to be clearly understood. However, a majority of these investigations have involved spherical or nearly spherical particles. The extent of the experiments involving non-spherical particles previously carried out was limited by the experimental technique used for the investigation or the inability to single out the effect of the particle shape. In this work, the radioactive particle tracking technique (RPT) is adapted to follow large non-spherical particles inside a rotating drum. The particles consist of pharmaceutical tablets containing a suitable compound, thus enabling their use as a tracer particle. Three crucial aspects of particle dynamics inside a rotating drum are studied : residence time in the active and passive layers, mixing and segregation, as well as axial dispersion. The results obtained for non-spherical particles are compared to those which would be predicted using models developed for spherical or nearly spherical particles. For the different shapes studied in this work, it is found that particles having an aspect ratio greater than two can lead to significant deviations in velocity profile and residence time. In addition, the mixing of different shaped particles is observed to lead to unexpected core segregation patterns. Lastly, it is found that the non-spherical particle higher degree of spatial orientation in the active layer leads to a lower axial dispersion coefficient than the ones obtained with spherical particles.

Keyword : Rotating drum, Non-spherical particles, Dynamics, Mixing, Segregation, Radioactive Particle Tracking

A.1 Introduction

Rotating drums are widely used to process granular materials in a great variety of industries such as pharmaceutical, food processing, polymer, ceramic, chemical, metallurgical, solid waste treatment, etc. Due to their adequate mixing and heat transfer efficiency (Descoins et al., 2005) as well as their ability to handle heterogeneous feedstock (Boateng, 1998), they are used in a broad range of processes which involves, for example, size reduction, sintering, mixing, drying, heating, cooling, chemical reactions or solid thermal decomposition (*e.g.* incineration, pyrolysis, combustion) operations. Heat and mass transfer, determined by solid transport and particulate mixing, control and/or limit these operations (Heydenrych et al., 2002; Liu et al., 2006; Mellmann et al., 2004). The rotating drums are usually operated in the so-called rolling regime since it provides superior particle mixing, resulting in enhanced heat transfer (Fantozzi et al., 2007; Li et al., 2002; Liu et al., 2006). This regime is characterized by two regions : a passive layer found near the cylinder wall, where particles move as a solid body, and an active layer, where the particles avalanche and cascade downward. It is widely accepted that mixing, segregation, heat transfer or other transport phenomena mainly occur in the active layer (Cheng et al., 2011; Ding et al., 2001; Ingram et al., 2005; Liu and Specht, 2010; Liu et al., 2006). Understanding the phenomena occurring inside rotating drums on a fundamental level is essential for optimal design and operation of this equipment (Heydenrych et al., 2002; Khakhar et al., 1997b; Mellmann, 2001). In particular, characterizing the transverse flow of particles is of primary importance. Although rotating drums represent a relatively simple geometry, the granular flow occurring inside them is rather complex (Boateng, 1998; Ding et al., 2002a; Ndiaye et al., 2010). If the particles are reagents and/or change size or shape over the course of the process, like in incineration, pyrolysis, sintering, combustion or size reduction operations, the problem becomes much more complex as new phenomena affecting the particle dynamics may occur.

Experimental studies of granular flow are tedious mainly because of the opaque nature of such materials. Nevertheless, a considerable amount of experimental work has been performed

in order to elucidate the behavior of granular flow inside a rotating drum. To perform these investigations, a wide selection of experimental techniques, such as in situ bed freeze ([Wightman and Muzzio, 1998](#)), magnetic resonance imaging (MRI) ([Hill et al., 1997](#); [Kawaguchi, 2010](#); [Nakagawa et al., 1993](#)), fiber optics probe ([Boateng and Barr, 1997](#)), positron emission particle tracking (PEPT) ([Ding et al., 2001](#); [Ingram et al., 2005](#); [Parker et al., 1997](#)), particle image velocimetry (PIV) and particle tracking velocimetry (PTV) ([Alexander et al., 2002](#); [Felix et al., 2002, 2007](#); [Jain et al., 2002, 2004](#); [Mellmann et al., 2004](#); [Thomas, 2000](#)) and radioactive particle tracking (RPT) ([Alizadeh et al., 2013](#); [Sherritt et al., 2003](#)), have been used. However, a majority of these investigations have involved spherical or nearly spherical particles. As it was previously mentioned, one advantage of rotating drums is their ability to handle varied feedstock, *i.e.* granular material having a wide distribution of size, density, shape, roughness or else. It has been known for quite some time now that the particle shape affects the dynamical properties ([Ridgway and Rupp, 1971](#)). The behavior of non-spherical particles differs from that of spherical particles in terms of their compaction efficiency, resistance to shear, dilation under shear, transfer of momentum between translational and angular motions as well as their ability to form arches and block the flow ([Cleary, 2010](#)). Experimental investigations of granular flow in rotating drums involving non-spherical particles drums are rather limited : [Boateng and Barr \(1997\)](#) used limestone and rice grains, [Van Puyvelde et al. \(2000\)](#) used shale, [Woodle and Munro \(1993\)](#) used particles made from and with ovoid, shell and tube shapes, [Henein et al. \(1983, 1985\)](#) used sand, limestone and gravel, and [Ingram et al. \(2005\)](#) used sand. In the pharmaceutical field, the dynamics of non-spherical particles is particularly of interest for particle and tablet coating applications, which are generally conveyed in a pan coater consisting of a rotating drum. [Wilson and Crossman \(1997\)](#) as well as [Tobiska and Kleinebudde \(2003\)](#) studied the effect of the tablet shape and size on the tablet film coating uniformity and efficiency. While useful, the results and extent of these studies involving non-spherical particles were restricted by either the experimental technique used, the inability to single out the effect of the particle shape or the objectives of the study.

This work aims at investigating three crucial aspects of the particle dynamic inside a rotating drum containing non-spherical particles : the residence time in the active and passive layers, the mixing and segregation of these particles, and the axial dispersion. To do so, the radioactive particle tracking (RPT) technique was adapted to follow the motion of non-spherical particles, which are in fact non-spherical tablets suitably built to become radioactive tracer particles. The results obtained for the non-spherical particles are compared to models previously developed for spherical or nearly spherical particles.

A.2 Methodology

As previously mentioned, numerous non-intrusive experimental techniques have been used to study granular flow. In particular, PIV and/or PTV can solely provide information on flow at the bed surface or, if the rotating drum has a transparent side, flow under the surface. In the latter case, the flow measured is affected by the presence of the end wall as well as the material constituting it, and may not represent what is going on inside the particle bed. Using PIV and/or PTV is then limited to two-dimensional systems and properties like axial dispersion can hardly be quantified. MRI and PEPT can also be used though they present limitations on the size and constitution of the system that can be studied, not to mention they are also expensive. On the other hand, RPT does not present any limitations on the system size and is much cheaper than these two methods. However, its extension to a system having irregular moving boundaries is not trivial ([Doucet et al., 2008](#)). This technique was used to carry out the investigations of this work since the rotating drum possesses simple moving boundaries. The next section briefly describes the RPT technique and the adaptations performed to apply it to this work.

A.2.1 RPT

RPT is a non-invasive experimental velocimetry and tomography technique that can be used to study the hydrodynamics inside a variety of systems. In this technique, the trajectory

of a single tracer particle emitting isotropic γ -rays can be reconstructed using a phenomenological model relating the number of γ -rays received and effectively counted by an array of scintillation detectors strategically placed around the system. Assuming a nonparalyzable counting RPT setup, the phenomenological relation linking the number of γ -rays C counted by a scintillation detector to the position (\vec{r}) of the tracer particle is given by :

$$C(\vec{r}) = \frac{T\nu A\zeta(\vec{r})}{1 + \tau\nu A\phi\zeta(\vec{r})}, \quad (\text{A.1})$$

where T is the sampling period (s), ν the number of distinct energy γ -rays emitted by the source, A the activity of the source (Bq), τ the detector dead-time (s), ζ the detector absolute efficiency and ϕ the fraction of the energy spectrum captured by the detector. ζ is rigorously evaluated using a Monte Carlo technique developed by [Beam et al. \(1978\)](#). Following a calibration procedure, Eq. [A.1](#) is used to compute the detector count dictionaries, corresponding to theoretical count rates associated with specific positions inside the system.

In this study, the detectors were positioned according to guidelines coming from an optimization strategy to find an optimal configuration for detectors given specific experimental conditions, as developed by [Dubé et al. \(2013\)](#). Further details on the traditional application of the RPT technique can be found in [Larachi et al. \(1994\)](#); [Roy et al. \(2002\)](#) and [Dubé et al. \(2013\)](#).

Similar to [Alizadeh et al. \(2013\)](#), this work uses a tracer particle containing the isotope ^{24}Na . This isotope emits two γ -rays at energy levels of 1.368 and 2.754 MeV, and has a relatively short half-life (14.95 hours). Explanations on why this particular isotope is used are provided in Section [A.2.2](#). To account for the short half-life, [Alizadeh et al. \(2013\)](#) suggested using a second tracer particle having the same activity as the first tracer particle, placed outside of the vessel, to monitor the source loss of activity throughout experiments. This method yielded satisfactory results when the tracer particle consisted of a 3mm to 6mm radius glass bead. However, since the count dictionaries with this strategy are corrected according to count values obtained from an emitting sentinel having a different specific absolute effi-

ciency because it does not take into account the particle bed, the error in the tracer particle trajectory reconstruction increases with the experimental time. In this work, the decrease in activity is instead accounted for by introducing the equation for the isotope half-life in the phenomenological model (Eq. A.1) :

$$A = A(t) = A_o \exp\left(-\frac{t \ln(2)}{t_{1/2}}\right), \quad (\text{A.2})$$

where t is the time elapsed since the beginning of the experiment, $t_{1/2}$ the half-life of the isotope and A_o the activity of the tracer particle at the beginning of the experiment. The quality of each RPT experiment was assessed and, under the conditions of this work, the RPT technique was shown to be able to reconstruct a given tracer particle position with an accuracy of 2.5mm and a precision of 2.0mm.

A.2.2 Experiments

Material

One of the biggest challenges encountered when applying the RPT technique is how build a tracer particle which has the exact same physical properties (*e.g.* density, mass, shape, etc.) as the material under study. When studying the effect of the particle shape on the hydrodynamics, the shape of the tracer particle is all the more important. In this study, pharmaceutical tablets were used to investigate non-spherical particle dynamics in a rotating drum. Pharmaceutical tablets were chosen for three main reasons. First, their composition can be controlled to some extent. Consequently, an isotope suitable for the RPT technique can easily be introduced in the powder mixture used for manufacturing. Second, the mass and size of a given pharmaceutical tablet can be carefully controlled during the manufacturing process, thus ensuring that tablets are nearly identical. Finally, punches and dies of a broad range of shapes and sizes are readily available for tablet manufacturing.

The composition of the pharmaceutical tablets is presented in Table A.1. The sodium

contained in the sodium bicarbonate was used as the suitable isotope for the RPT technique. More precisely, the isotope ^{24}Na was produced from the sodium bicarbonate by means of the Slowpoke reactor of École Polytechnique de Montréal. Sodium bicarbonate is the ideal choice for a sodium-based compound in that it possesses adequate flow and compression properties for the tableting process. The amount of sodium bicarbonate needed inside the tablets was dictated by a single criterion : the smallest tablet produced needs to reach an activity of $60\mu\text{Ci}$ (2.22MBq) in less than 20 minutes when activated in the Slowpoke nuclear reactor. This time limit is extremely relevant in order to avoid any changes in the physical properties of the tablets during the activation process. Computations revealed that a 40% concentration of sodium bicarbonate is sufficient to respect this criterion. Ultimately, it was decided to use an activity of $45\mu\text{Ci}$ (1.665MBq) for the experiments, therefore all tablets needed less than 12 minutes to complete their activation.

Five different pharmaceutical tablets were produced using a fully instrumented 10-station small-scale rotary tablet press KORSCH XL100 (KORSCH America Inc., South Easton, MA). Their shapes and dimensions are shown in Fig. A.1, and their properties are presented in Table A.2. These shapes were chosen so as to cover various sphericities and aspect ratios, but also to have tablets with similar shapes yet different sizes in order to study mixing and segregation. For the purpose of improving the shear resistance of the pharmaceutical tablets, a 2% weight Opadry® II-red coating (Colorcon®, West Point, PA) was applied on all tablets using a Vector LDCS pan coater (Freund-Vector Corporation, Marion, IA).

Table A.1: Tablet composition

Components	Mass %
Sodium bicarbonate (NaHCO_3)	40%
Mannitol 100	29.75%
Avicel PH-200	29.75%
Magnesium stearate (MgSt)	0.5%

Table A.2: Tablet properties

Tablet	Mass M (mg)	Volume V (mm ³)	Surface S (mm ²)	Particle density ρ_p (mg/mm ³)	Bulk density ρ_b (kg/m ³)	Sphericity	Aspect ratio
A	206.8 ± 2.1	147.2 ± 0.4	162.6 ± 0.5	1.40 ± 0.01	1072 ± 3	0.83	1.84
B	219.8 ± 3.0	139.0 ± 0.8	143.2 ± 0.6	1.58 ± 0.02	1035 ± 3	0.91	1.02
C	276.1 ± 3.7	169.0 ± 1.6	157.6 ± 1.1	1.63 ± 0.02	1029 ± 2	0.94	1.07
D	280.1 ± 3.3	181.9 ± 1.3	176.1 ± 0.7	1.54 ± 0.02	968 ± 2	0.88	2.48
E	284.4 ± 3.1	220.9 ± 1.6	195.5 ± 1.3	1.29 ± 0.01	1031 ± 6	0.90	1.84

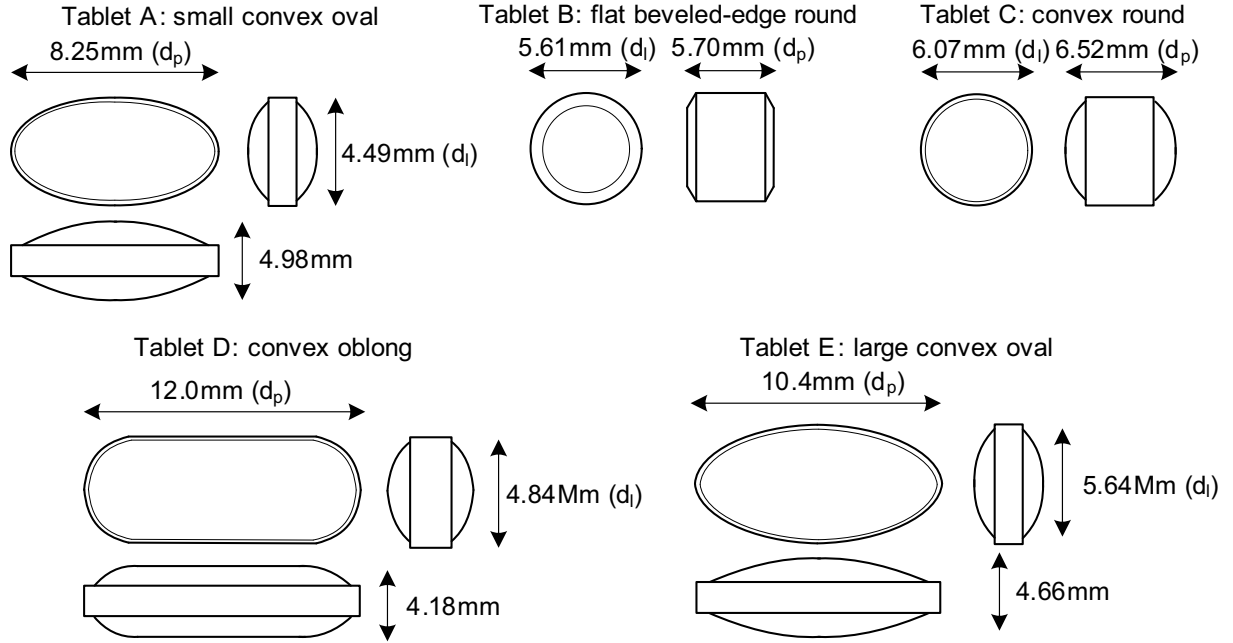


Figure A.1: Schematic representation of the five tablets used in this study.

Design of experiments

The experiments performed for this study used a 16.8L rotating drum made from acrylic with a 0.3556m internal length and a 0.2413m internal diameter. A single filling fraction (35vol%) was used for all experiments. The mass of material put inside the rotating drum was based on the bulk density of the individual tablets. The design of experiments applied is presented in Table A.3. The five different tablet shapes were tested individually and bi-disperse blends of tablets were also tested. The blends were chosen so as to study bi-disperse mixtures of mono-shaped tablets (*i.e.* mixtures made from tablets A-E and B-C), and bi-

disperse mixtures of bi-shaped tablets (*i.e.* mixtures made from tablets C-D and C-E). These two kinds of mixture were chosen to represent cases when a varied feedstock is used or when changes in size (mono-shaped mixture) or shape (bi-shaped mixtures) occur over the course of the rotating drum operation. The blend compositions were chosen to represent situations where only a small fraction of the particle bed changes size or shape. Hence, these blends were composed of 85vol% of the bigger tablet and 15vol% of the smaller tablet. Moreover, in order to compare the non-spherical particle dynamics to the spherical one, three experiments involving spherical glass beads were performed. One experiment involved mono-disperse 6mm glass beads (GB6 in Table A.3) while the other two were a blend of 5mm and 6mm glass beads (GB56.5 and GB56.6 in Table A.3). All the experiments were performed in the rolling regime given that it is the one used in most applications. Because of the tracer particle half-life (~ 15 hours), a 10RPM drum rotational speed was used to gather as much data as possible within one single experiment. Only one experiment was performed with at 5RPM to verify the effect of the drum rotational speed on the particle dynamics. Each experiment used a 10ms sampling period T and lasted at least 180 minutes, resulting in a total of 1,080,000 tracer particle positions. A total of eighteen experiments were performed.

A.3 Results and discussion

Three important characteristics of granular flow inside a rotating drum are presented and analyzed in this section : the residence time in the active and passive layers, the mixing and segregation of the particles and finally, the axial dispersion. The results of this study were obtained using the tracer particle trajectories acquired from the RPT experiments. Using such a trajectory, the tracer particle velocity was computed and projected onto an Eulerian grid. Given that the granular flow inside a rotating drum is essentially two-dimensional, a two-dimensional grid with a $2.5 \times 2.5\text{mm}^2$ cell size was used. To avoid any interference of the drum axial end walls, only the part of the tracer particle trajectory axially located in a 20cm region around the drum center was considered. It is believed that statistically reliable data

Table A.3: Design of experiments

Type	Experiment	Blend specification	Rotational speed Ω (RPM)	Tracer Particle
Mono-disperse	A	100vol% A	10	A
	B	100vol% B	10	B
	C	100vol% C	10	C
	D	100vol% D	10	D
	E	100vol% E	10	E
	GB6	100vol% 6mm	10	6mm
Bi-disperse	AE.A	15vol% A, 85vol% E	10	A
	AE.E	15vol% A, 85vol% E		E
	AE.A*	15vol% A, 85vol% E	5	A
	AE.E*	15vol% A, 85vol% E		E
	BC.B	15vol% B, 85vol% C	10	B
	BC.C	15vol% B, 85vol% C		C
	CD.C	15vol% C, 85vol% D	10	C
	CD.D	15vol% C, 85vol% D		D
	CE.C	15vol% C, 85vol% E	10	C
	CE.E	15vol% C, 85vol% E		E
	GB56.5	15vol% 5mm, 85vol% 6mm	10	5mm
	GB56.6	15vol% 5mm, 85vol% 6mm		6mm

* Indicates a rotational speed of 5 RPM.

was obtained since the tracer particle was found to pass anywhere between 200 and 1200 times in each cell.

Before going any further, the variables used subsequently must be defined. Fig. A.2 presents a schematic cross-section view of the drum. In this figure, it can be seen that the bed is composed of two different layers : a passive layer found near the cylinder wall, where the particles move as a solid body, and an active layer, where the particles avalanche and cascade downward. The interface between the two layers is defined as the yield line (Boateng and Barr, 1997) and is represented in Fig. A.2b by the $\delta(x)$ curve. The turning point line, found above the yield line and denoted by the $\alpha(x)$ curve in Fig. A.2b, is where the streamwise $u(x, y)$ velocity changes direction ($u(x, y) = 0$). The space between the yield and turning point lines is known as the transition region and is sometimes neglected due to its relatively small size (Khakhar et al., 1997a). In such a case, the active layer boundary is singularly

Table A.4: Definition of the variables used

Variable	Definition
x	Streamwise direction (m)
y	Transverse direction (m)
u	Streamwise velocity (m/s)
v	Transverse velocity (m/s)
R	Drum radius
h	Normal distance between the bed surface center and the drum center of rotation (m)
L_s	Half-length of the bed surface (m)
L	Half-length of a streamline in the active layer (m)
β	Angle between the horizontal axis x' and the yield line
ν_A	Inclination angle of the yield line at the top of the material bed
θ	Dynamic repose angle
ω	Angular velocity (rad/s), $\omega < 0$ since the rotation is clockwise
B_H	Bed height

The experimental measurement of these quantities are of great importance since the models developed for the granular flow inside a rotating drum frequently use one or all of them (see Sections A.3.1 to A.3.1).

The static repose angle corresponds to the angle made by the stationary free surface of the particles once the cylinder operating under steady flow conditions stops rotating. The dynamic repose angles were computed using the velocity field. Fig. A.3 displays a typical velocity field obtained from the RPT experiments. The reported values of the dynamic repose angle correspond to the mean angle between the velocity vectors and the horizontal axis, for vectors belonging to the range $-0.05 \leq x \leq 0.05$ and $-(h + 0.005) \leq y \leq -h$. For the bi-dispersed mixtures, the dynamic repose angles were obtained from the combination of the two tracer particle velocity fields. Note that the reported values match the visual measurements made in the laboratory but are more accurate and not affected by end wall effects. The rotational speed was computed using the mean streamwise velocity u at $x = 0$ and $-R < y < -R + 0.015$. Finally the filling fraction f was measured using the bed height at $x = 0$, as inferred by the velocity field (Fig. A.3).

It can be readily noticed that the use of tablets B, C and D resulted in a significantly

Table A.5: Primary observations

Case	Static repose angle $\theta_s(^{\circ})$	Dynamic repose angle $\theta(^{\circ})$	Rotational speed Ω (RPM)	Filling fraction $f(\%)$
A	29.1 ± 4.1	32.24 ± 0.95	8.83 ± 0.38	35.9
B	32.8 ± 4.6	34.00 ± 1.72	8.82 ± 0.39	39.0
C	33.2 ± 5.0	35.01 ± 1.11	8.36 ± 0.13	40.0
D	30.6 ± 2.2	35.55 ± 1.93	8.38 ± 0.19	37.4
E	27.4 ± 4.2	29.27 ± 1.59	8.78 ± 0.15	36.9
AE	28.4 ± 2.8	30.40 ± 1.24	8.84 ± 0.17	38.5
BC	33.0 ± 3.6	34.39 ± 1.64	8.23 ± 0.18	38.5
CD	33.2 ± 1.8	35.34 ± 1.25	8.73 ± 0.05	41.6
CE	32.5 ± 2.3	35.23 ± 0.92	8.55 ± 0.13	41.6

higher dynamic repose angle than tablets A and E. This can be explained by the shape of the tablets (Fig. A.1). Tablets B, C and D all exhibit a longer straight side which enables them to form stable structures upstream, near the wall of the cylinder, thus yielding higher dynamic repose angles. It can be noticed that even if the aspect ratio of tablet D is 2.5 times greater than those of tablets B and C (Table A.2), similar dynamic repose angles were measured. When tablets having similar dynamic repose angles are mixed, the resulting repose angle is the same as the individual ones. However, in the case of the binary mixture made from tablets C and E, even though tablets C only represent 15% of the whole volume, they nonetheless dictate the resulting dynamic repose angle.

All the experiments presented in Table A.5 were performed at 10RPM. Even though the experimental setup encoder confirmed that the cylinder rotational speed was 10 ± 0.5 RPM, the one experienced by the particles was approximately 1.5RPM lower. This confirms the experimental observation that the particles seemed to slip against the cylinder wall. Slipping of the particles is attributed to the friction between the bulk of the particles and the acrylic of the cylinder. Given that the tablets were all coated using the same substance, it is not surprising that all individual tablets and blends experienced approximately the same rotational speed.

As it was specified in Section A.2.2, all the experiments involved a 35vol% filled cylinder.

From Table A.5, it can be noticed that bed dilation occurred in all cases. More precisely, a bed dilation of more than 5% was measured in four cases (B, C, CD and CE). This phenomenon, which was not observed with the spherical glass beads used by Alizadeh et al. (2013), is a characteristic of non-spherical granular flow (Cleary, 2010).

Velocity profiles

The computation of the active layer boundary essentially relies on the velocity profiles. Fig. A.3 displays the velocity fields in the case of experiments E and AE. At the exception of the bed dilation which can be appreciated by comparing these two pictures, every experiment presented a qualitatively similar velocity field.

To make an efficient comparison and observe the effect of the shape on the velocity fields, one has to analyze the streamwise and transverse components of the velocity at specific x positions and along the surface bed.

Streamwise and transverse velocity profiles at specific x positions :

Fig. A.4 shows the streamwise and transverse velocity profiles for the individual tablets as well as for the different blends, at $x = 0$. As representative examples of the individual

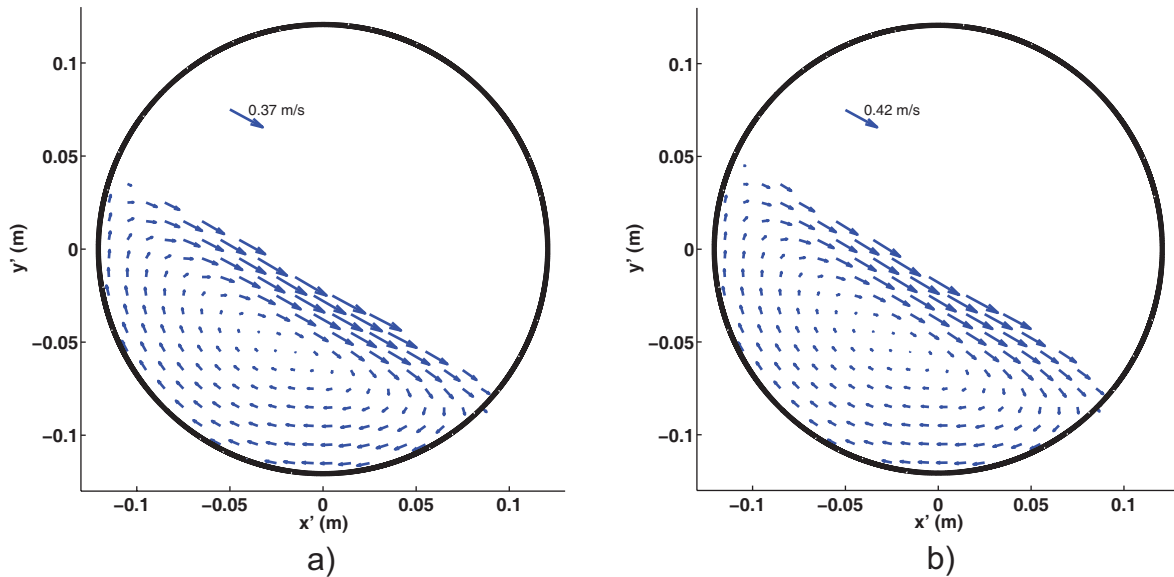


Figure A.3: Typical velocity field for (a) tablet E and (b) blend AE (at 10RPM).

tablets and blends, Fig. A.5 presents the same profiles for tablet C and blend AE, but at various x positions.

In the passive layer ($-R \leq y \leq -(\delta(x) + h)$), since the particles are moving according to a solid body rotation (SBR), the streamwise ($u_{passive}$) and transverse ($v_{passive}$) velocity profiles follow :

$$u_{passive}(x, y) = \omega y, \quad (\text{A.3})$$

$$v_{passive}(x, y) = -\omega x. \quad (\text{A.4})$$

The linear variation of the streamwise and transverse velocities in the passive layer predicted by the previous equations can be appreciated in Figs. A.4 and A.5.

In the active layer ($-(\delta(x) + h) \leq y \leq -h$), the streamwise and transverse velocities likewise display a linear profile except in the transition region ($-(\delta(x) + h) \leq y \leq -(\alpha(x) + h)$), where a non-linear variation of the streamwise velocity (*i.e.* a non-constant shear rate ($\dot{\gamma} = \dot{\gamma}(y)$) can be observed (Figs. A.4a and c, Figs. A.5a and c). However, most models consider a constant shear rate ($\dot{\gamma} \neq \dot{\gamma}(y)$) in the active layer (Khakhar et al., 2001b; Makse, 1999; Meier et al., 2007). Figs. A.5a and c also suggests that the shear rate depends on the streamwise position ($\dot{\gamma} = \dot{\gamma}(x)$). Again, for modeling purposes, it is often assumed that ($\dot{\gamma} \neq \dot{\gamma}(x)$). Knowing that $u(x, y) = 0$ at $y = -(\alpha(x) + h)$, the streamwise velocity in the active layer can be modeled by (Alizadeh et al., 2013) :

$$u_{active}(y)|_x = u_{surf}(x)(1 + \xi(x, y)), \quad (\text{A.5})$$

where $u_{surf}(x)$ is the streamwise velocity at the surface and $\xi(x, y) = \frac{y+h}{\alpha(x)}$ represents a dimensionless depth in the active layer based on the turning point line. An expression for $u_{surf}(x)$ will be presented later. Letting $v = 0$ at $y = -h$ and knowing that $v = -\omega x$ at $y = -(\delta(x) + h)$, the transverse velocity in the active layer can be written as (Meier et al., 2007) :

$$v_{active}(x, y) = -\frac{\omega x(y + h)}{\delta(x)}. \quad (\text{A.6})$$

As mentioned by Alizadeh et al. (2013), the linear behavior of the streamwise velocity profiles has been extensively reported in the literature. Furthermore, Alizadeh et al. (2013) and Jain et al. (2004) showed that the transverse velocity profiles at $x = 0$ oscillate around zero in the active layer. The same phenomenon was observed here for all the tablets and blends tested (Figs. A.4b and d). In Fig. A.5c, it can be noticed that the streamwise velocity profile near the surface seems to be more parabolic than linear. The development of a parabolic velocity profile for non-spherical particles has been observed before by Boateng and Barr (1997) for long-grain rice. This parabolic velocity profile suggests that the shear rate near the surface is close to zero, which means that the particles at the surface and a few millimeters under move together (at the same velocity). It can be observed in Figs. A.5a and c that the streamwise velocity profiles in the active layer are not symmetric with respect to the y axis. In other words, the $x = \pm 0.04$ profiles are different as well as those corresponding at $x = \pm 0.08$. This is more evident when looking at the streamwise velocity evolution along the bed surface. Finally, it can be observed in Figs. A.5b and d that the transverse velocity profiles in the passive layer are in agreement with what is predicted by Eq. A.4. Fig. A.5 also highlights the fact that the active layer boundary as defined by the turning point line ($u = 0$) can easily be identified using the RPT results, unlike the one based on the yield line (dashed line), especially when $x \neq 0$.

Streamwise velocity profile along the bed surface

The evolution of the streamwise velocity along the bed free surface is another significant feature of granular flow inside the rotating drum that needs to be analyzed thoroughly. This particular profile is essential to evaluate the residence time on the surface as well as in the active layer.

Figures A.6a and b display the streamwise velocity profiles on the bed surface for the individual tablets and all the blends. The results obtained using 6mm glass beads and a mix

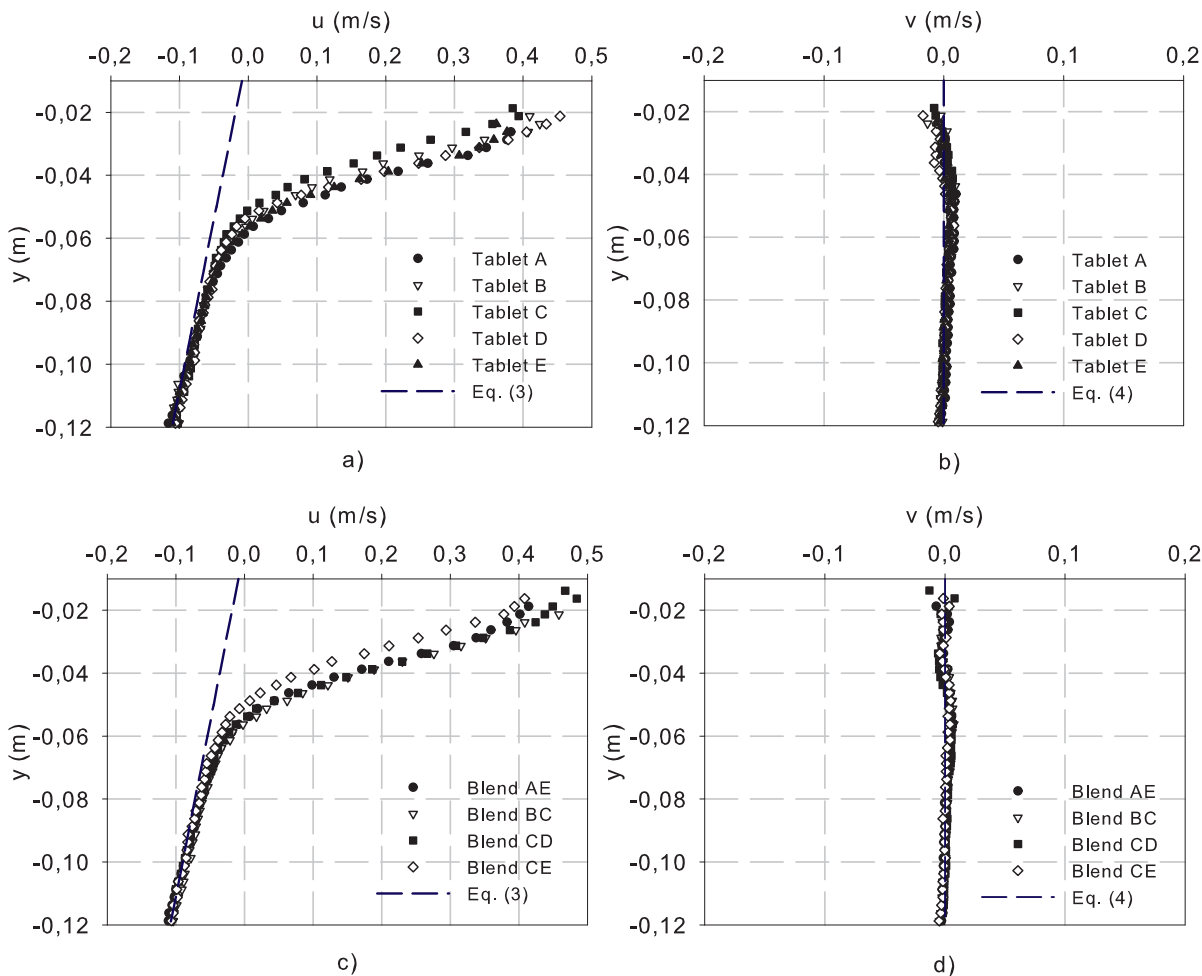


Figure A.4: Streamwise velocity profiles at $x=0$ for (a) the individual tablets and (c) the different blends, and transverse velocity profiles at $x=0$ for (b) the individual tablets and (d) the different blends.

of 5mm (15vol%) and 6mm (85vol%) glass beads are also included to allow a comparison between spherical and non-spherical particles. It must be noted that the mass of a 6mm glass bead is approximately the same as that of tablets C, D or E (*i.e.* $\sim 280\text{mg}$). It can be noticed that the individual tablets B and D as well as the blends made from either of these tablets present the highest velocity peaks in comparison to the other shapes and blends. All the individual tablets and blends exhibit a higher velocity profile than the glass beads. [Suzzi et al. \(2012\)](#) and [Wilson and Crossman \(1997\)](#) mentioned that, if the shape of a tablet is relatively flat, this tablet is likely to have a preferred spatial orientation on the surface and inside the

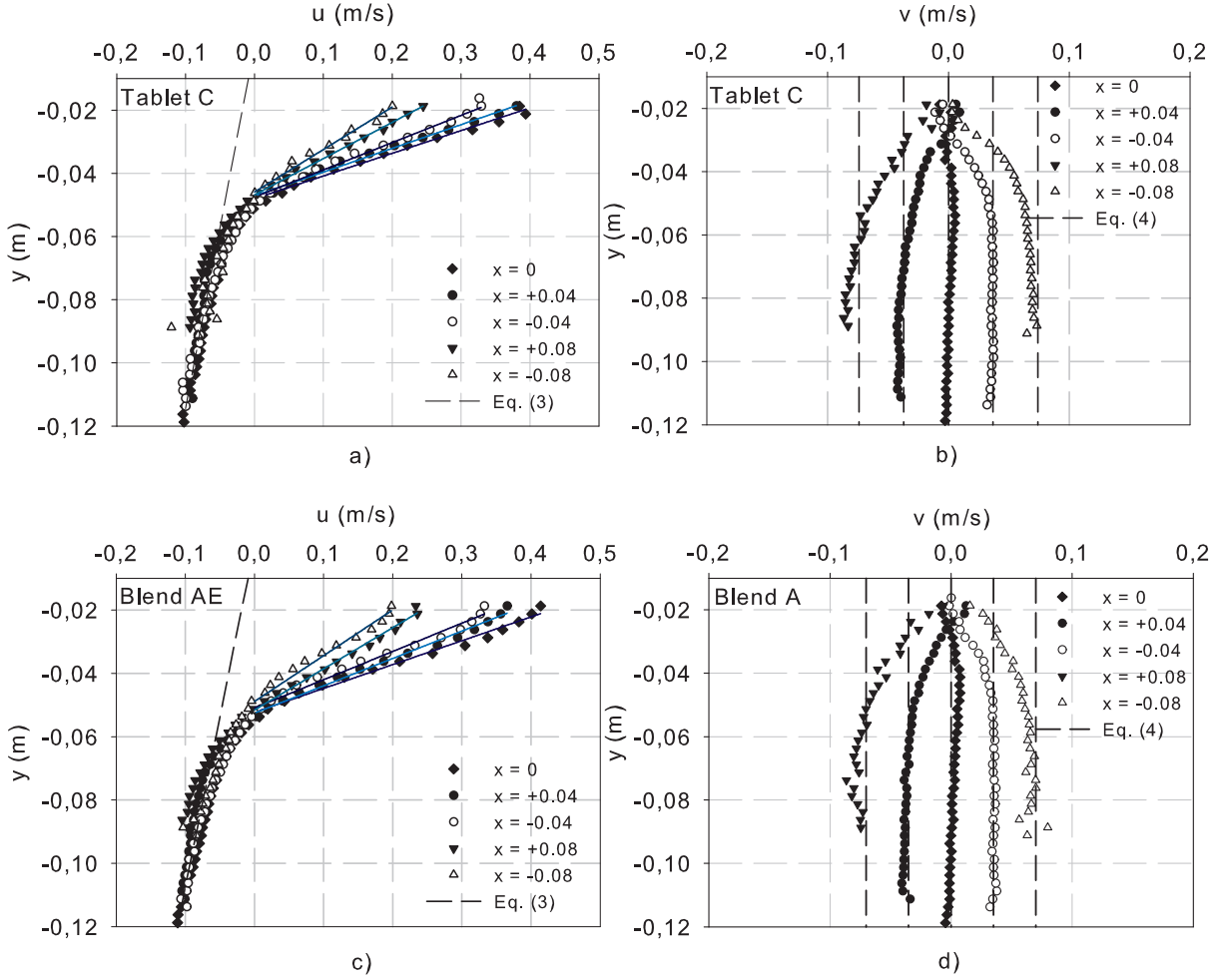


Figure A.5: Streamwise velocity profiles for (a) tablet C and (c) blend AE, and transverse velocity profiles for (b) tablet C and (d) blend AE, at $x = 0\text{m}$, $\pm 0.04\text{m}$ and $\pm 0.08\text{m}$.

bed, thereby causing to slide rather than rotate. Even though the RPT technique used in this study did not measure the angular velocity, the larger streamwise velocities observed in Figs. A.6a and b for the non-spherical tablets seem to corroborate these findings. Unfortunately, the comparison of these profiles cannot be made directly as each experiment used different particle sizes and resulted in different effective rotational speeds and dynamic repose angles (Table A.5). On the one hand, the increase in the streamwise velocity peak could potentially simply be attributed to the difference in the dynamic repose angle. Indeed, the dynamic repose angle of the glass beads was measured at 27° , which is lower than those measured in involving tablets. On the other hand, the fact that no slipping between the glass beads and

the wall of the cylinder was observed suggests that the glass beads have a higher velocity than the non-spherical tablets in the passive layer, which means that these spherical particles should start cascading down the bed free surface with a larger momentum. Alexander et al. (2002) found that, for a rotational speed below 30RPM, the streamwise velocity of spherical particles at the bed surface scales as :

$$u \propto R\omega^{2/3} \left(\frac{g}{d_p} \right)^{1/6}, \quad (\text{A.7})$$

where g is the gravitational acceleration and d_p is the particle diameter. Since this relation incorporates the particle diameter as well as the rotational speed, the streamwise velocity profiles were normalized by the expression on the right-hand side of Eq. A.7 using for d_p the values of Fig. A.1. The new profiles are presented in Figs. A.6c and d. They indicate that tablet D and the 6mm glass bead have a behavior significantly different than that of the other tablets. The same phenomenon can be observed in Fig. A.6d, where the profiles of the mixture containing tablet D and the mixture of 5mm and 6mm glass beads differ from the other profiles. These results further confirm that tablets D, which exhibit the highest aspect ratio (Table A.5) and the flatter shape, have a tendency to slide on the bed surface, whereas the glass beads have a tendency to rotate. The other shapes behave somewhere in between, combining translational and rotational motion.

According to Khakhar et al. (1997a), the streamwise velocity along the bed surface $u_{surf}(x)$ can be expressed as :

$$u_{surf}(x) = u_{max} \left(1 - \frac{x^2}{L_s^2} \right), \quad (\text{A.8})$$

with

$$u_{max} = \frac{\omega L_s^2}{\alpha_o}, \quad (\text{A.9})$$

where the distance α_o , shown in Fig. A.2b, corresponds to $y = -(\alpha(x=0) + h)$.

Figures A.7a and b confirms that this equation correctly models the streamwise velocity

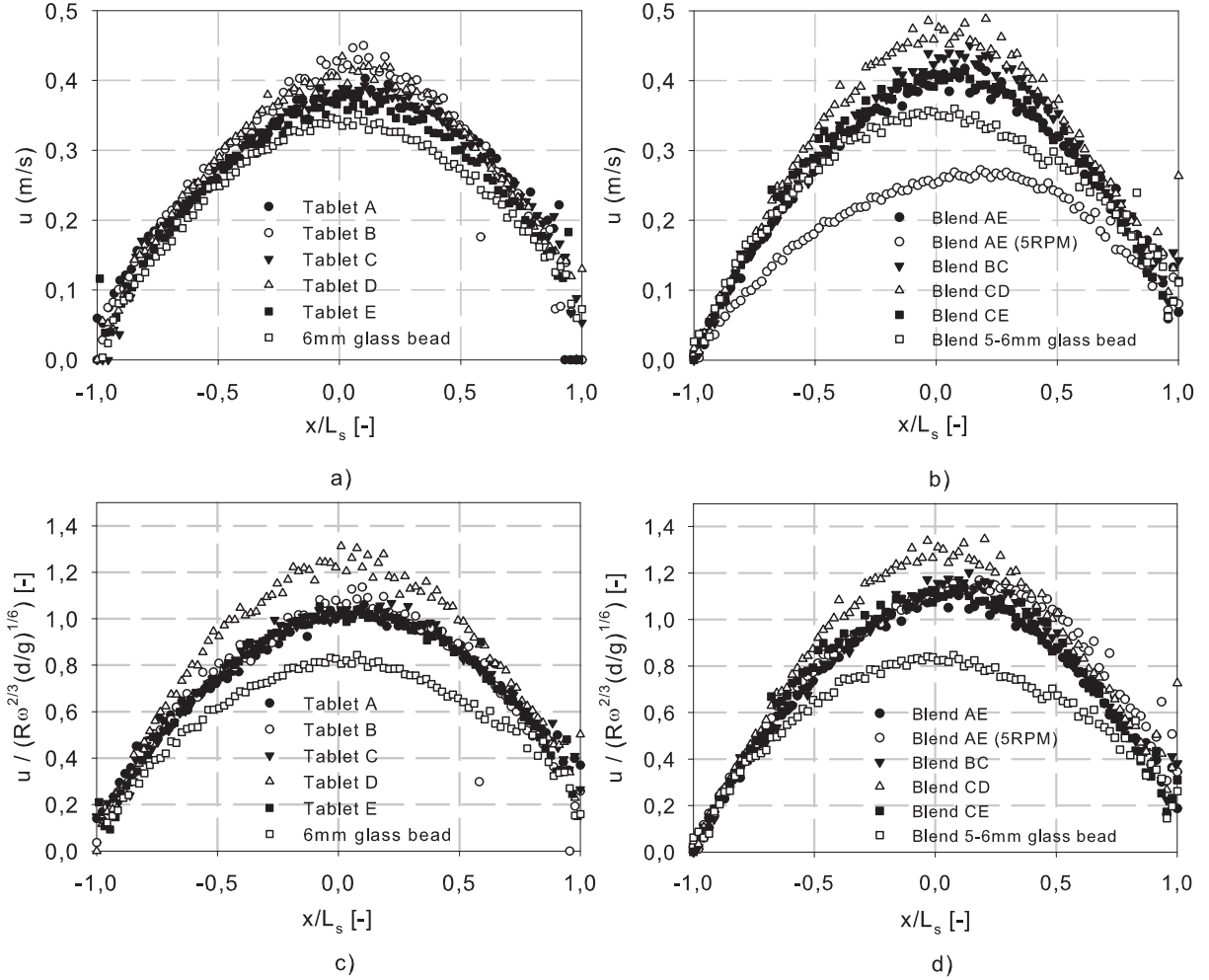


Figure A.6: Streamwise velocity profiles along the bed free surface for (a) the individual tablets and (b) the different blends, and the scaled streamwise velocity profiles along the bed free surface for (c) the individual tablets and (d) the different blends.

profiles for both the individual tablets and the different blends, at the exception of the blend AE with a 5RPM rotational speed. As was observed by [Ding et al. \(2002b\)](#) and [Alizadeh et al. \(2013\)](#), the downstream part of the flow is better modeled by adding $2/3$ as an exponent to Eq. A.8, which complies with the asymmetry noticed in Section A.3.1 and presented in Fig. A.5.

The blend AE with a rotational speed of 5RPM displays a skewed streamwise velocity profile with a peak velocity attained past the mid-chord position ($x/L_s = 0$), whereas its profile at 10RPM is symmetric. The occurrence of an asymmetric profile for a smaller rotational

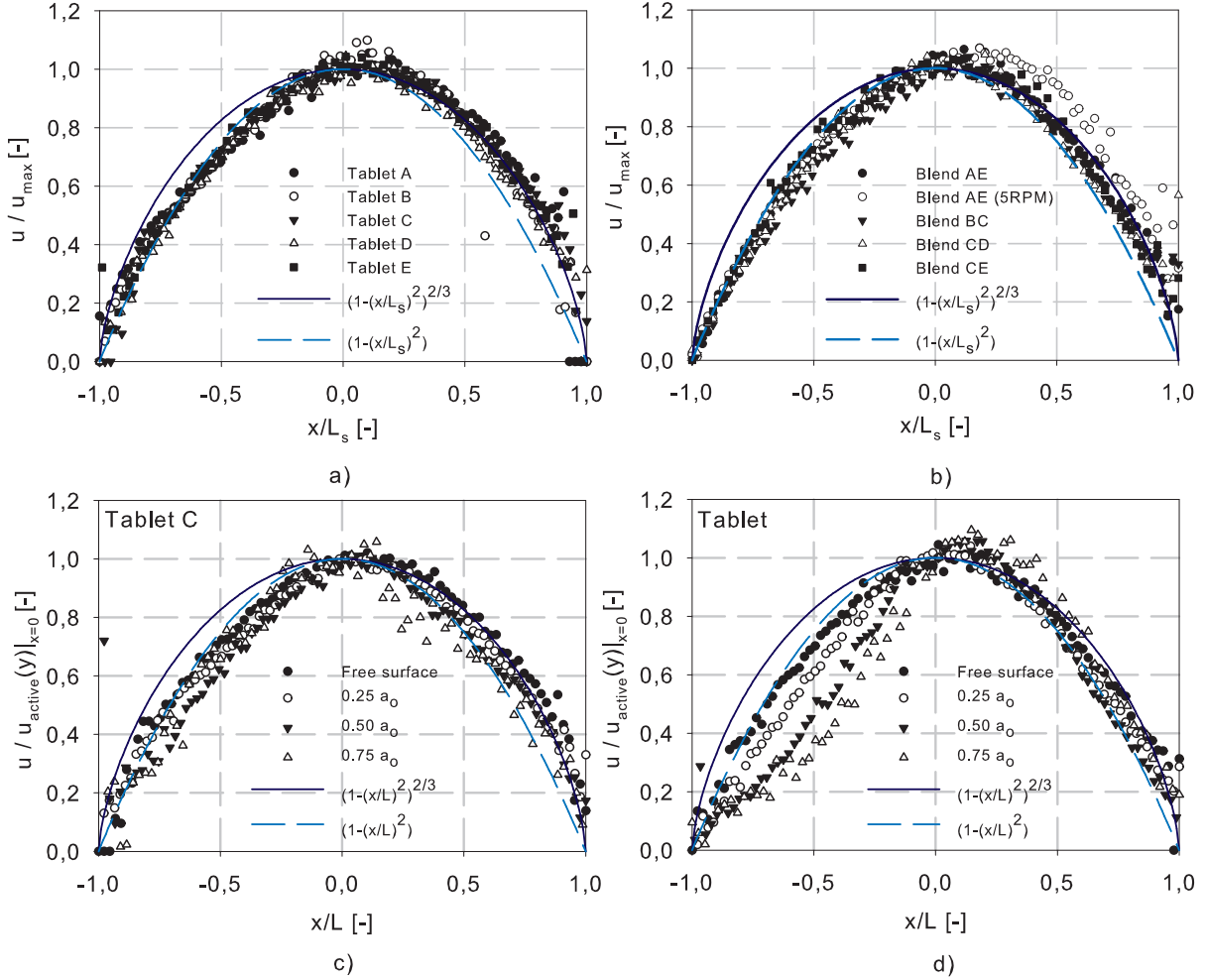


Figure A.7: Normalized streamwise velocity profiles at the bed surface for (a) the individual tablets and (b) the different blends, and under the bed surface for (c) tablet C and (d) tablet D.

speed has been observed previously by [Alexander et al. \(2002\)](#); [Boateng and Barr \(1997\)](#) and [Nakagawa et al. \(1993\)](#). In particular, [Alexander et al. \(2002\)](#) mentioned that the asymmetry in the profile may be due to the fact that the frictional/collisional losses within the cascade do not balance, before the particles reach the mid-chord position, the particle kinetic energies imparted by the rotational speed of the blender, thereby allowing these particles to accelerate beyond this point.

Finally, the streamwise velocity profile under the bed surface is analyzed. For this purpose, the evolution of the profile with respect to the bed depth for tablets C and D is provided in

Fig. A.7c and d, respectively. Note that tablets A, D, E as well as blends AE, BC and CE all follow the same trend as the one shown for tablet C, whereas blend CD and tablet D exhibit similar profiles. For all these cases, the velocity profile can be approximated by :

$$u_{us}(x) = u_{active}(y)|_{x=0} \left(1 - \frac{x^2}{L^2}\right). \quad (\text{A.10})$$

This expression is similar to the one obtained using spherical particles by Alizadeh et al. (2013). However, as can be seen in Fig. A.7d, the profile for tablet D deviates from Eq. A.10 as it becomes more asymmetric as the distance under the free surface increases. Nevertheless, the downstream portion of the flow follows the profile predicted by Eq. A.10. The deviation of the upstream portion can be explained by the shape of the particles. The long flat side of tablet D enables it to form a stable structure near the cylinder wall. By doing so, only the tablets at or near the surface will easily cascade downstream. This creates an asymmetric profile under the surface, much more pronounced than for tablet C, whereby the tablets accelerate past the mid-chord position. As Weir et al. (2005) mentioned, complex repositioning within the shear layer is expected for particles having a large aspect ratio.

The results presented in this section showed that the particle shape can have a significant impact on the velocity profile. They also evidenced that more complicated structures can form within the bulk of particles. At the exception of tablet D as well as blends CD and AE (at 5RPM), the models previously developed could adequately represent the streamwise and transverse velocities of the non-spherical systems considered in this work.

Active layer thickness

The active layer thickness is a key parameter as mixing, segregation, heat transfer or other phenomena mainly occur in this region. Many correlations can be found in the literature to predict the thickness of the active layer, based either on the turning point or yield line. These correlations often use parameters that are difficult to measure experimentally (*e.g.* the surface velocity profile or the angle between the active layer boundary at its extremities and

the horizontal plane (ν_A in Fig. A.7b), operating conditions, material properties, geometrical characteristics of the rotating drum, fitting parameters, or a combination of any of these). In this section, some of these correlations are compared to evaluate their performance in predicting the active layer thickness for the non-spherical particles and blends used in this study.

Active layer thickness based on the turning point line :

The active layer thickness based on the turning point line can easily be identified using the results from the RPT experiments. The profiles for tablets D, E, and for the 6mm glass beads are displayed in Fig. A.8. Note that tablets A, B and C, and blends AE, CB and CE all present profiles similar to that of tablet E, while the profile for the blend CD is similar to that of tablet D.

It can be observed that, at the exception of tablet D (look at the results downstream from $x = 0$), the active layer can be properly modeled by :

$$\alpha(x) = \alpha_o \sqrt{1 - \frac{x^2}{L^2}}. \quad (\text{A.11})$$

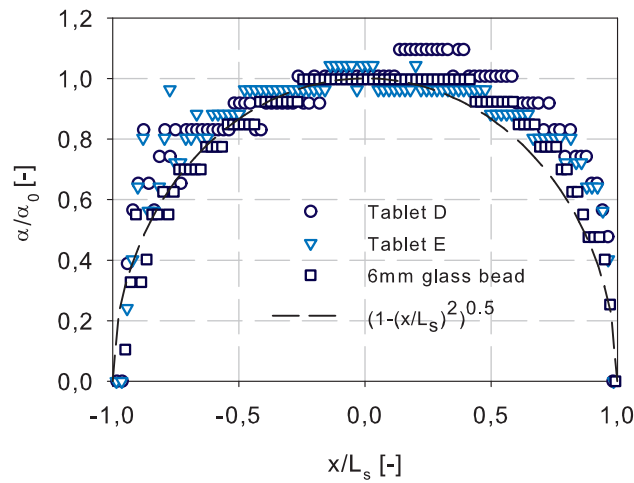


Figure A.8: Normalized active layer depth profile $\alpha(x)/\alpha_o$ for tablets D and E, and 6mm glass bead.

As noted by [Sturman et al. \(2008\)](#), although the square root in Eq. [A.11](#) appears in some models and not in others, both forms yield comparable results. However, as will be discussed in Section [A.3.1](#), the model used for $\alpha(x)$ has an impact on the prediction of the residence time along streamlines in the active layer. The asymmetric active layer profile of tablet D is compliant with the corresponding streamwise velocity profiles under the bed surface (Fig. [A.7d](#)).

The experimental values obtained for α_o are presented in Table [A.6](#) and are compared to those which would be obtained using the models developed by [Liu et al. \(2006\)](#); [Weir et al. \(2005\)](#) and [Ding et al. \(2001\)](#). The reader is referred to these references for the detailed description of these models.

The model derived by [Liu et al. \(2006\)](#) is based on a previous one developed by [Mellmann et al. \(2004\)](#), which uses mass and momentum balances to evaluate the transverse solids motion in a rotating drum. In order to compute the active layer thickness, this model requires the particle diameter d_p (identified in Fig. [A.1](#)), the drum diameter D , the dynamic angle of repose θ as well as the inclination angle of the active layer boundary line at the top of the material bed (*i.e.* the angle ν_A in Fig. [A.2](#)). This angle is difficult to measure ([Mellmann et al., 2004](#)) and could not be backed out with adequate accuracy from the RPT data. To overcome this limitation, a correlation between ν_A and θ , developed by [Mellmann et al. \(2004\)](#), was used. This correlation was experimentally derived using 15 different materials, including both spherical and non-spherical particles, with $25^\circ < \theta < 50^\circ$, which matches the properties of the tablets used for the current work. The correlation needs θ , f , R as well as ω to compute ν_A .

[Weir et al. \(2005\)](#) developed a regression model using experimental results obtained by various authors. Their model requires d_p , R , ω , f as well as an author- and particle-dependent fitting parameter λ . This parameter depends on particle properties, geometrical characteristics of the rotating drum and operating conditions.

Finally, [Ding et al. \(2002b, 2001\)](#) proposed a model based on mass and momentum ba-

lances. They also considered a quadratic polynomial to model the streamwise velocity in the active layer along the axis perpendicular to the bed surface, $u_{active}(y)|_x$. Let us recall that this velocity was introduced as a linear polynomial in y for a given x in Eq. A.5. Their model, which can be used to compute both active layer boundaries ($\alpha(x)$ and $\delta(x)$), requires the knowledge of ω , f and the streamwise velocity along the bed surface, $u_{surf}(x)$. Note that only $u_{active}(0)|_{x=0}$ is needed to compute α_o and δ_o . Ding et al. (2002a) provided a correlation to evaluate this value for nearly spherically shaped particles having high restitution coefficients, yet it was found to be inadequate for the tablets used in this work. In fact, the use of this correlation resulted in values for $u_{active}(0)|_{x=0}$ that are 40% lower than the experimental ones. For this reason, experimental values measured by the RPT technique were used instead.

Previous studies reported an increase in the active layer thickness with an increase of the drum rotational speed and polydispersity (Alizadeh et al., 2013; Boateng and Barr, 1997; Henein et al., 1983; Van Puyvelde et al., 2000; Woodle and Munro, 1993). From Table A.6, it can be noticed that the polydispersity does not increase α_o except in the case of blend CD. In addition, no change in α_o can be noticed when the drum rotational speed is increased in the case of blend AE. The model from Liu et al. (2006) invariably underpredicts α_o and presents a high average errors. This model best predicts the value of tablet D yet it fails to predict the high increase in α_o observed in blend CD. The errors may be attributed to the angle ν_A , which was obtained using a correlation, as explained above. In fact, it was found that, to adequately predict α_o using this model, ν_A has to be 6° higher than that predicted by the correlation. The model proposed by Ding et al. (2001) also underpredicts α_o and presents an even higher average errors than the previous model. It is believed that the errors may be partially attributed to the quadratic polynomial used to model $u_{active}(y)|_x$. A closer look at the results presented in Ding et al. (2001) reveals that their model does underpredict $\alpha(x)$ and that a linear approximation model for $u_{active}(y)|_x$ would reduce this under-prediction. Moreover, the results presented previously, indicate that, for the solid particles of this work, a linear profile can accurately model $u_{active}(y)|_x$. Finally, the model of Weir et al. (2005) results

Table A.6: Values of the active layer thickness α_o based on the turning point line

Case	Measured α_o cm[% ¹]	Liu et al. (2006) cm[% ¹]	Weir et al. (2005) cm[% ¹]	Ding et al. (2001) cm[% ¹]
A	3.1[33]	2.2[24]	3.1[33]	2.2[23]
B	3.4[34]	2.3[23]	3.5[35]	2.1[21]
C	3.2[31]	2.4[23]	3.3[33]	2.1[21]
D	2.8[29]	2.6[27]	2.8[29]	1.8[19]
E	3.1[33]	2.2[23]	3.0[32]	2.2[23]
Average error (%)	-	25	2	33
AE	3.3[33]	2.2[23]	3.2[32]	2.1[22]
AE*	3.3[33]	2.0[20]	2.7[26]	1.8[18]
BC	3.3[34]	2.3[23]	3.3[34]	1.8[18]
CD	3.8[36]	2.6[25]	3.3[31]	1.9[18]
CE	3.4[32]	2.5[24]	3.3[32]	2.1[20]
Average error (%)	-	32	8	43

1 percentage of bed depth

in the smallest average errors. This is not surprising as this model uses a particle-dependent fitting parameter λ . Its value had to be set at 1 for tablets B and C (just as for spherical particles), 0.8 for tablets A and E, and 0.7 for tablet D. In other words, rather close values for λ were found for tablets of similar shapes.

Active layer thickness based on the yield line :

The experimental values for δ_o are presented in Table A.7 and are compared to those obtained using the models of Alizadeh et al. (2013); Orpe and Khakhar (2001) and Ding et al. (2001).

The model proposed by Orpe and Khakhar (2001) is based on a model developed by Makse (1999), and obtained using a mass balance and the assumption of constant shear rate $\dot{\gamma}$ along the y direction in the active layer. In this model, the active layer thickness based on the yield line is expressed as :

$$\delta(x) = \sqrt{\frac{\omega}{\dot{\gamma}(x)}(L_s^2 - x^2)}, \quad (\text{A.12})$$

with $\dot{\gamma}(x)$ given by (Khakhar et al., 2001a,b; Meier et al., 2007; Orpe and Khakhar, 2001) :

$$\dot{\gamma}(x) = \sqrt{\frac{g \cos \beta(x) \sin(\theta - \theta_s)}{c d_p \cos \theta \cos \theta_s}}, \quad (\text{A.13})$$

where θ_s the static angle of repose, $\beta(x)$ the angle between the horizontal and the boundary of the active layer, and c a fitting parameter. It can be noticed that $\dot{\gamma}(x)$ depends mainly on particle properties. Previous studies reported a value of for two-dimensional systems (Khakhar et al., 2001b; Meier et al., 2007; Orpe and Khakhar, 2001).

Alizadeh et al. (2013) proposed a model based on the intersection between the linear streamwise velocity profiles in the passive and active layers. This model gives a relation between α_o and δ_o . They suggested using it to compute α_o using the value of δ_o obtained from Eq. A.12. Since this equation requires an a priori unknown fitting parameter c and $\delta(x)$ is harder to identify experimentally, it was instead decided to use the experimental value of α_o to obtain δ_o . Aside from α_o , this model only requires f to compute δ_o .

Table A.7 shows a slight increase of the experimental values of δ_o with an increasing drum rotational speed for blend AE. Furthermore, polydispersity seems to increase δ_o in the case of blends AE and CD. The model from Orpe and Khakhar (2001) adequately predicts δ_o in all cases, with a very low average error. However, it must be mentioned that, as in Alizadeh et al. (2013), $c = 1$ was used to match the experimental results. Moreover, it was noticed that this model is strongly dependent on the values of θ and θ_s . As can be seen in Table A.5, the θ_s values present an uncertainty of approximately 4° . Interestingly, a different value of θ_s , lying in the range of uncertainty, used in combination with $c = 1.5$, could be found in each case so that the model matches the experimental results. Thus, it is believed that a more precise value of θ_s should be obtained before concluding on the value of c . The model of Alizadeh et al. (2013) always underpredicts δ_o . The underprediction is due to the fact that this model computes δ_o as the intersection between the two linear velocity profiles of the active and passive layers and does not consider the varying shear rate characteristic of the transition region. Nevertheless, its application results in acceptable discrepancies, presenting average errors of 13% and 12% for individual tablets and blends, respectively. Unfortunately,

Table A.7: Values of the active layer thickness δ_o based on the yield line

Case	Measured δ_o cm[% ¹]	Orpe and Khakhar cm[% ¹]	Alizadeh et al. cm[% ¹]	Ding et al. cm[% ¹]
A	3.8[40]	3.8[41]	3.5[37]	2.3[25]
B	4.4[44]	4.4[45]	3.9[39]	2.2[22]
C	4.2[41]	4.1[40]	3.6[35]	2.2[22]
D	3.7[39]	3.7[38]	3.1[33]	1.9[20]
E	4.2[44]	4.6[48]	3.5[37]	2.4[25]
Average error (%)	-	4	13	45
AE	4.6[46]	4.5[46]	3.7[38]	2.2[23]
AE*	4.4[44]	4.5[45]	3.8[38]	1.8[18]
BC	4.1[41]	4.2[43]	3.8[38]	1.9[19]
CD	4.7[45]	4.4[42]	4.4[42]	1.9[19]
CE	4.5[43]	4.4[42]	3.8[27]	2.2[21]
Average error (%)	-	3	12	55

¹ percentage of bed depth

the model does not capture the increase in δ_o with an increasing drum rotational speed. This can be attributed to the experimental data used for δ_o . Finally, the results obtained using the model of Ding et al. (2001) are completely off the mark, presenting average errors between 45% and 55%. Reasons for these large discrepancies have already been provided before.

The results of this work indicate that there does not seem to be a significant effect of the tablet shape on the values of α_o and δ_o , contrary to what has been previously reported, for other non-spherical particles. At the exception of the models by Ding et al. (2001) and Liu et al. (2006), most of them could predict with reasonable accuracy the size of the active layer depth. However, they all needed at some point a fitting parameter, the value of which is a priori unknown.

Residence time

Knowing the residence time in the active layer of a rotation drum is important for many applications such as those involving rotary kilns since the material renewal occurs mainly in this region. Fig. A.9 presents the mean residence time spent by the tracer particle in each

cell of the Eulerian grid, for tablets B and D. It can be readily observed that the shape of tablet D disrupts the expected profile symmetry observed for spherical particles.

Using the results presented in Sections A.3.1 to A.3.1, it is possible to compute the residence times spent by the particles in the active and passive layers. In order to extract these residence times from the RPT results, streamlines must be identified. To do so, massless tracers are launched in the velocity fields of each experiment, along the line $x = 0$ and $-(\alpha_o + h) < y < -h$. The time spent in the active and passive layers can then be computed using these massless tracer trajectories. Two criteria can be used to define the boundary between the active and passive layers : the turning point and yield line. As was previously mentioned, the former can easily be identified through the RPT data whereas the latter cannot be identified with enough accuracy. To overcome this limitation, it is assumed that the ratio $\Lambda(x) = \alpha(x)/\delta(x)$ is constant, even though the velocity profiles from Fig. A.5 and Ding et al. (2001) suggest it does vary. Consequently, the yield line is defined as :

$$\Lambda = \frac{\alpha_o}{\delta_o} \Rightarrow \delta(x) = \frac{\alpha(x)}{\Lambda}. \quad (\text{A.14})$$

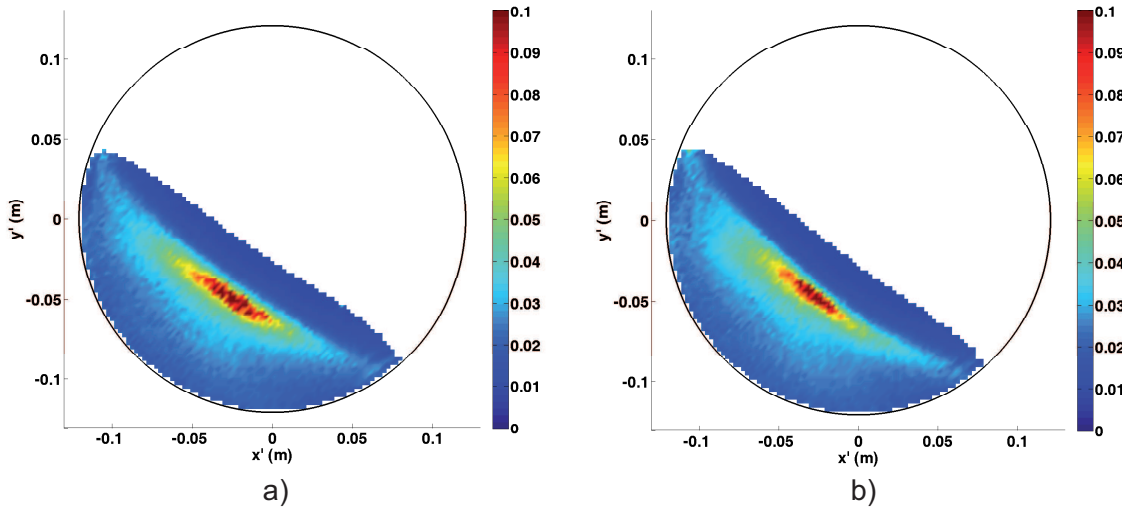


Figure A.9: Mean residence time in cells of the Eulerian grid used for (a) tablet B and (b) tablet D.

The residence time in the passive layer (t_p) is modeled using the angle of the streamlines (ε , see Fig. A.2) and the angular velocity (ω) (Alizadeh et al., 2013) :

$$t_p = \frac{\varepsilon}{\omega}. \quad (\text{A.15})$$

For this equation to hold, the angle of the streamline must be associated with the yield line boundary and not the turning point boundary. Alizadeh et al. (2013) modeled the residence time in the active layer t_a by neglecting the curvature at the beginning and the end of the streamlines and assuming that :

- the streamlines in the active layer are parallel to the bed surface ;
- the streamwise velocity profile in the active layer obeys Eqs. A.5 and A.10 ;
- the active layer boundary $\alpha(x)$ is symmetric and follows :

$$\alpha(x) = \alpha_o \left(1 - \frac{x^2}{L_s^2} \right). \quad (\text{A.16})$$

Given that it was shown that Eq. A.11 adequately models $\alpha(x)$, the model proposed by Alizadeh et al. (2013) can be adapted to yield :

$$t_a = \frac{3\alpha_o}{\omega L_s} \frac{\sqrt{1 - \xi_o^2}}{1 + \xi_o}, \quad (\text{A.17})$$

where $\xi_o = \frac{y+h}{\alpha_o}$, and y represents the height of the streamline in the active layer. Equation A.17 holds only when the active layer is defined by the turning point line. It is proposed here to modify this model so that it takes into account the transition region and thus brings into play the yield line. Since Λ is assumed constant, it then comes from Eqs. A.11 and A.14 that :

$$\delta(x) = \frac{\alpha(x)}{\Lambda} = \frac{\alpha_o}{\Lambda} \sqrt{1 - \frac{x^2}{L_s^2}}. \quad (\text{A.18})$$

It is also assumed that, in the transition region (*i.e.* for $-(\delta(x) + h) < y < -(\alpha(x) + h)$), the streamlines are oriented along the y axis. It can then be deduced from Fig. A.9b that the

time spent by a streamline in the transition region ($t_{\alpha-\delta}$) can be approximated by :

$$t_{\alpha-\delta} = 2 \frac{(\delta(x) - \alpha(x))}{|\overline{v(x, y)}|}, \quad (\text{A.19})$$

where $\overline{v(x, y)}$ is the mean transverse velocity between $\alpha(x)$ and $\delta(x)$ which can be obtained by Eq. A.6. By letting $x = L$, it can be shown that :

$$\overline{v(x, y)} = \frac{1}{2} \omega (\Lambda + 1) L, \quad (\text{A.20})$$

where, from Eq. A.11,

$$L = L_s \sqrt{1 - \xi_o^2}, \quad (\text{A.21})$$

Finally, using the fact that the numerator of Eq. A.19 can be expressed as :

$$\delta(x) - \alpha(x) = \xi_o (\alpha_o - \delta_o). \quad (\text{A.22})$$

It comes from Eqs. A.19, A.20 and A.21 that :

$$t_{\alpha-\delta} = \frac{4\xi_o(\alpha_o - \delta_o)}{\omega(\Lambda + 1)L_s\sqrt{1 + \xi_o^2}}. \quad (\text{A.23})$$

The total residence time in the active layer is then given by summing Eqs. A.17 and A.23 :

$$t_{\alpha-\delta} = \frac{3\alpha_o}{\omega L_s} \frac{\sqrt{1 - \xi_o^2}}{1 + \xi_o} + \frac{4\xi_o(\alpha_o - \delta_o)}{\omega(\Lambda + 1)L_s\sqrt{1 + \xi_o^2}}, \quad (\text{A.24})$$

and the total residence time along a specific streamline ($t_a + t_p$) is simply the sum of Eqs. A.15 and A.24. Fig. A.10 displays the experimental and predicted residence times in the active and passive layers as well as the total residence time along streamlines for all tablets and blends tested in this work. It must be mentioned that the model developed for the residence time in the active layer is not expected to work in the case of tablet D and blends AE (at 5RPM)

and CD as their velocity profiles were shown in Fig. A.7 to deviate from Eq. A.10. This is confirmed in Fig. A.10, where a large deviation between the model and the experimental data can be noticed.

In all cases, a good agreement is found between the values of t_p predicted by Eq. A.15 and the experimental data. The small discrepancies that can be observed for $\xi_o < -0.4$ can be attributed to the way $\delta(x)$ was defined (*i.e.* Eq. A.14) for the experimental data. As was already mentioned, only $\alpha(x)$ could be identified experimentally. A constant Λ was assumed in order to evaluate $\delta(x)$. Since the experimental values of t_p are greater than the ones predicted by Eq. A.15, it seems that Eq. A.14 underestimates $\delta(x)$, thus confirming the findings of Ding et al. (2001) who observed that Λ decreases as the distance from the center of the flow increases. As for the residence time in the active layer, a good agreement is obtained between the experimental results and Eq. A.24, except for the three cases previously mentioned. In fact, it can be readily noticed that the model generally overestimates t_a . Again, this can be attributed to the identification of $\delta(x)$ through Eq. A.24. An even better agreement is obtained for the total residence time along the streamline. This is expected as the total experimental time does not need the identification of $\delta(x)$. Finally, a comparison of the curves of Fig. A.10 for all tablets and blends with a rotational speed of 10RPM reveals that the tablet shape has little effect on the residence times in both layers with the exception of tablet D that shows slight differences.

The good quality of the model developed here means that it could be used to predict the total residence time along streamlines for any situations. It simply needs the filling fraction f to compute L , the drum rotational speed ω , Eq. A.12 to evaluate δ_o , the model of Alizadeh et al. (2013) to evaluate α_o from δ_o , and finally, Eq. A.11 to link L to ε .

A.3.2 Mixing and segregation

The mixing and segregation of non-spherical particles were investigated using the tablet blends presented in Table A.3. As already discussed, the mixtures were chosen to represent

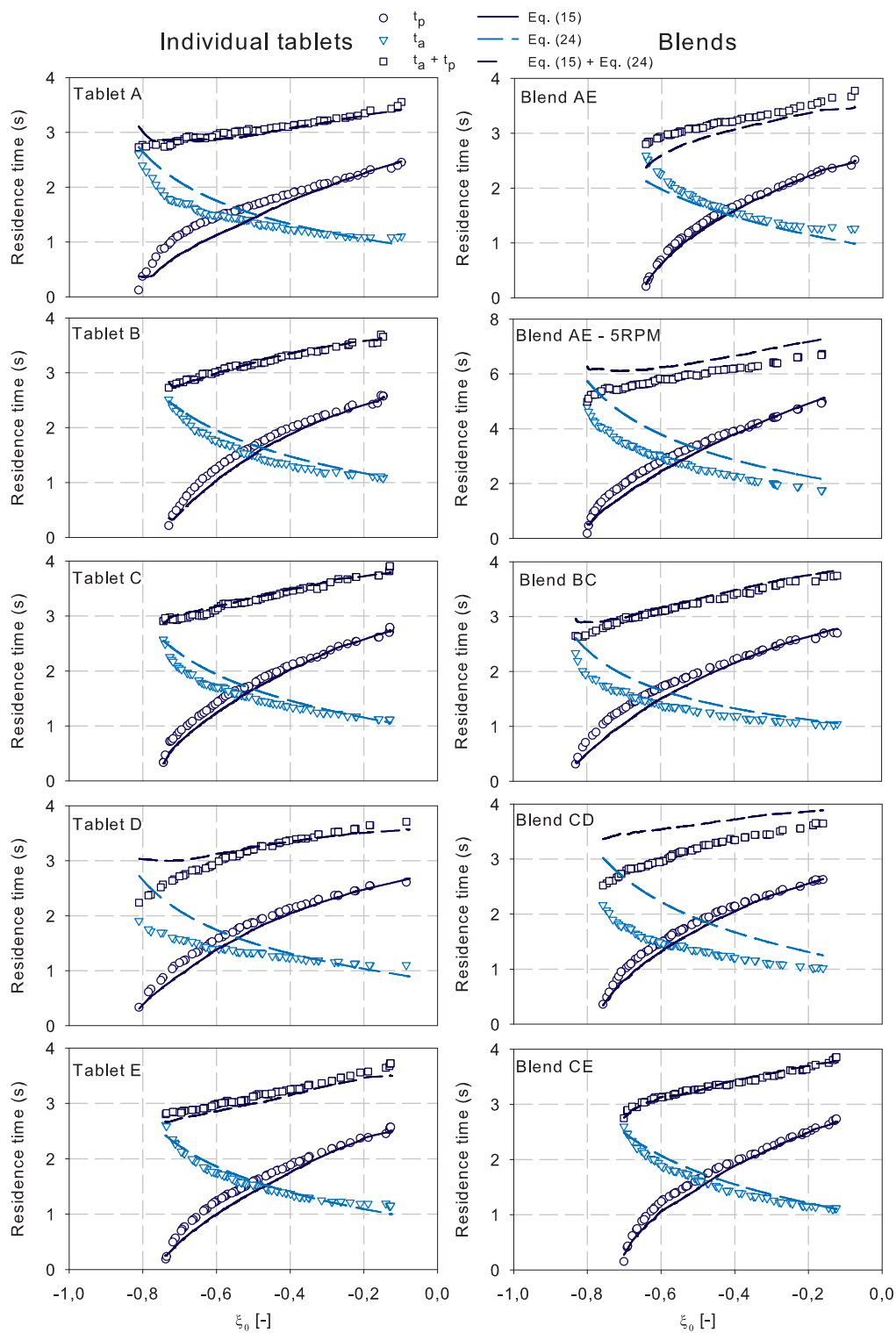


Figure A.10: Residence times in the active and passive layers for all the tablets and blends tested. The symbols correspond to experimental data.

cases when a varied feedstock is used or when changes in size (mono-shaped mixture) or shape (bi-shaped mixtures) occur over the course of the rotating drum operation. The study of segregation inside rotating drums is important as it can greatly affect the heat and mass transfer efficiency occurring in the active layer. In order to compare the segregation of non-spherical particles to that of spherical particles, an experiment using 5mm (15vol%) and 6mm (85vol%) glass beads with a 10RPM drum rotational speed was realized. The volume, density as well as the particle diameter ratios of each blend are presented in Table A.8.

Jain et al. (2005) conducted an impressive and thorough study of the combined size and density effect on mixing and segregation inside a rotating drum. They limited their study to cohesionless spherical particles. Depending on the size or density ratios of the mixtures, percolation (*i.e.* size) and/or buoyancy (*i.e.* density) driven segregation could be observed. In the case where buoyancy and percolation acted in the same direction, the smaller/denser particles were always found in the center of the bed (core segregation), unless the size ratio of the small particle to the large particle was lower than 0.5, in which case radial streaks of particles of the same size would be observed. In this work, it can be seen from Table A.8 that both percolation and buoyancy are expected to act in the same direction : the particle with the smaller volume, invariably has a higher (or nearly equal) density. Thus, traditional core segregation is expected in all cases.

To quantify the extent of segregation, the occupancy and the location probability were computed. The occupancy is simply the ratio of the number of times the tracer particle was found in a specific cell of the Eulerian grid to the maximum number of times it was detected

Table A.8: Blend characteristic ratios

Blend (ratio)	V ratio	ρ_p ratio	d_p ratio	d_l ratio
AE (E/A)	1.5	0.92	1.26	1.26
BC (C/B)	1.2	1.02	1.14	1.08
CD (D/C)	1.1	0.94	1.84	0.80
CE (E/C)	1.3	0.79	1.60	0.87
5-6mm glass beads	1.7	1	1.2	-

in a single cell. The location probability is computed as the number of times a tracer particle was found in a specific cell to the total number of times that both tracer particles (one for each tablet type) were found in that same specific cell. The occupancy and location probability for blends AE, AE*, BC and the 5-6mm glass beads are presented as a function of the normalized bed depth ($|y+h|/B_H$) in Fig. A.11, while those for blends CD and CE can be found in Fig. A.12. It must be noted that only the values of the occupancy and location probability along the y axis at $x = 0$ are presented. In these two figures, the notation AB.C signifies blend AB and the use of Tablet C as a tracer in the experiments.

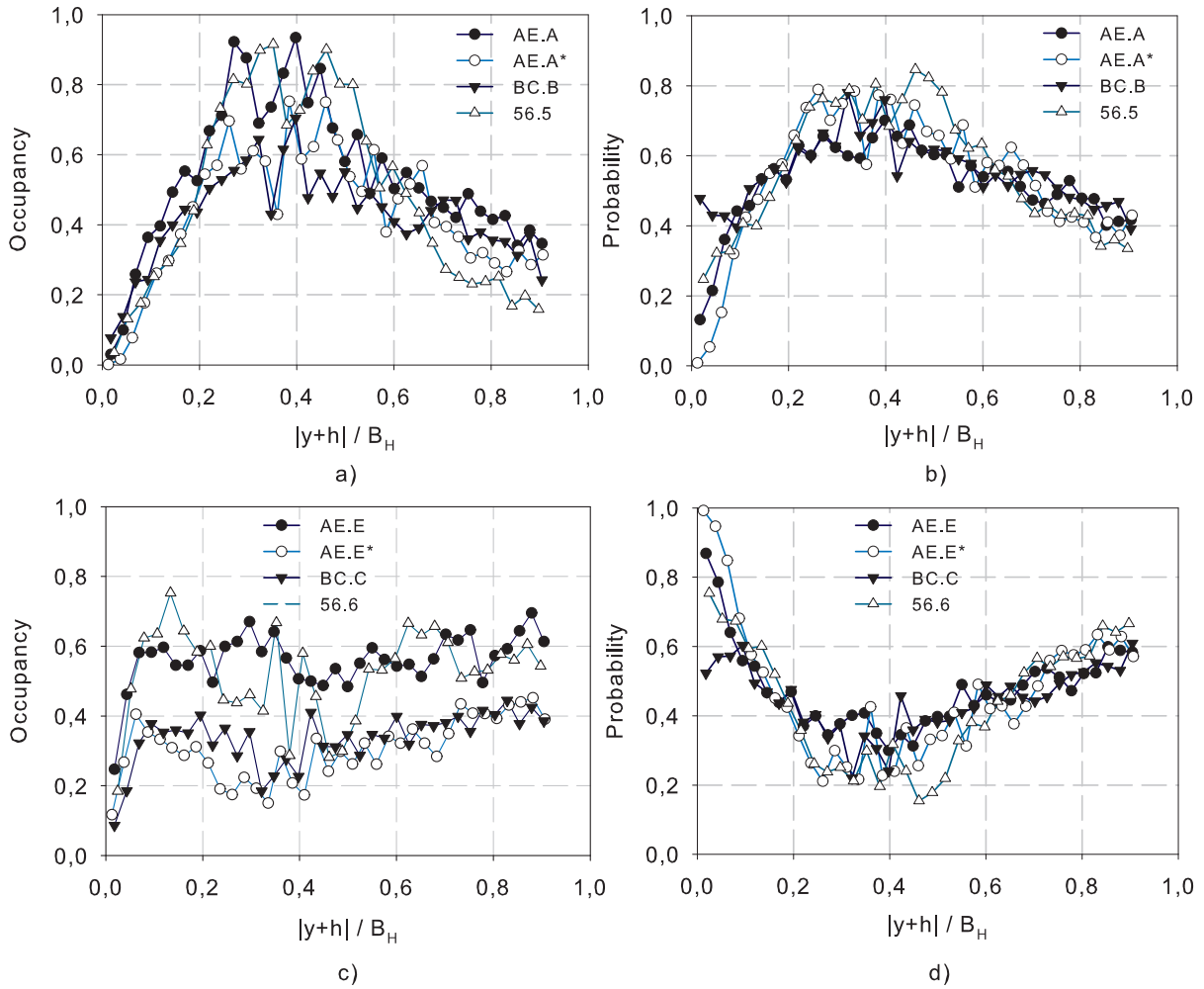


Figure A.11: Values of (a and c) the occupancy and (b and d) the location probability for blends AE, AE*, BC and the 5-6 mm glass beads. For (a) and (b), the smaller particle was used as a tracer. For (c) and (d), the larger particle was used as a tracer.

The location probabilities of Fig. A.11b show that the smaller particles (*i.e.* tablets A, B and the 5mm glass bead) have a higher probability of being found in the center of the bed rather than on the outside. The occupancy plot for the smaller particles (Fig. A.11a) also confirms this trend. These results indicate the occurrence of traditional core segregation. However, one may notice that the occupancy curves of the larger particles (Fig. A.11c) are nearly uniform in all cases. Similar occupancy profiles were obtained in mono-disperse experiments (not shown here), suggesting that even though the core of the bed is more likely to contain a greater concentration of smaller particles, this does not seem to affect the flow pattern of larger particles. A similar result was obtained for a 4mm glass tracer in a blend of 3, 4, 5 and 6mm glass beads (Alizadeh et al., 2013). From Fig. A.12, it can be seen that completely different results were obtained for blends CD and CE. The smaller and denser particle (*i.e.* tablet C) is never found in the core of the bed as its occupancy and location probability both approach zero in this zone. This is an indication of a counter-intuitive phenomenon.

Two points of view can be provided to explain these results. First, it is probable that the buoyancy and percolation mechanisms are hampered by the effect of the particle shape. The preferred orientation taken by tablets D and E when flowing in the active layer may result in a lack of the space required for tablet C to segregate between them. In fact, it was observed experimentally that the preferred orientation taken by tablets D and E enabled them to slide along their longest edge. Second, perhaps the volume ratio does not dictate the observed segregation patterns. Indeed, given that tablets D and E slide along their longest edge (d_p in Fig. A.1), it is plausible that the width (d_l in Fig. A.1) or the height of the tablets would be a better criterion. For instance, tablet C has a smaller volume but a bigger width (d_l ratio) than tablets D and E, which may explain the reverse core segregation phenomenon described above. Further investigations would be required to fully understand the segregation mechanisms observed in this work. Nevertheless, the results presented here are of interest in that they highlight for the first time the effect that the shape of a particle may have on

mixing and segregation inside a rotating drum.

A.3.3 Axial dispersion

It is well known that tumbling blenders used without intensifier bars or baffles suffer from weak axial mixing ([Lemieux et al., 2007](#)). Nevertheless, it is best to have efficient mixing in both the radial and axial directions. In this section, a comparison of the axial motion of the non-spherical tablets and the spherical glass beads is performed. To quantify the extent of axial displacement occurring in each experiment, the axial dispersion coefficient was computed using Einstein's law ([Einstein, 1905](#)) :

$$D_{axial} = \frac{\sum_i^N (\Delta z_i - \overline{\Delta z})^2 / \Delta t_i}{2(N-1)}, \quad (\text{A.25})$$

where Δz_i is the axial displacement of the tracer particle during the i th cycle, $\overline{\Delta z}$ the mean axial displacement of the tracer particle for the N cycles and Δt_i the time interval. To reduce the effect of the measurement error on the computation of the dispersion coefficient, the time interval for cycle i was taken as the residence time of the tracer particle along the corresponding streamline ([Alizadeh et al., 2013](#); [Sherritt et al., 2003](#)). The residence time

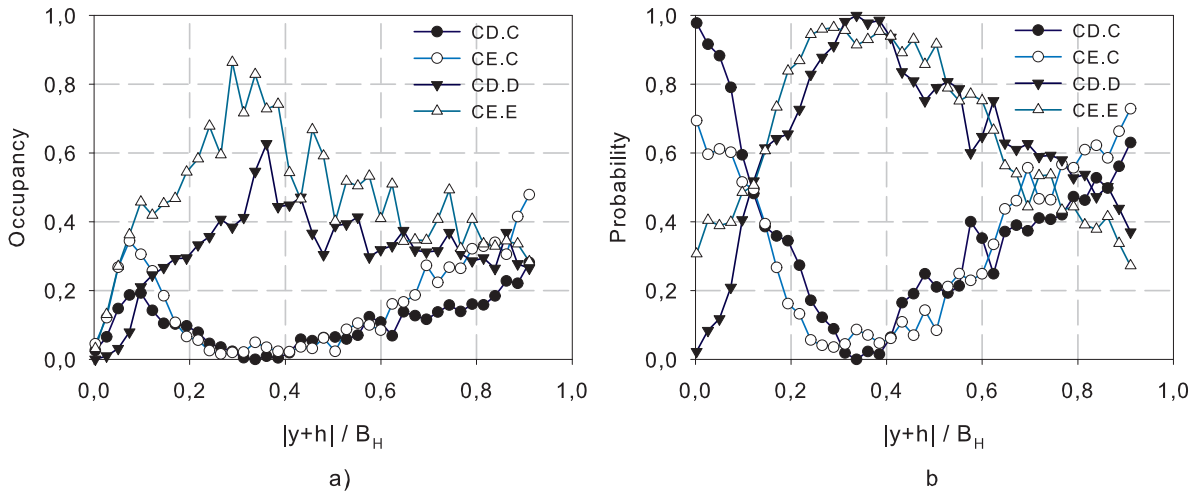


Figure A.12: Values of (a) the occupancy and (b) the location probability for blends CD and CE.

was approximated using the model presented in Section A.3.1 (*i.e.* Eqs. A.24 and A.15). Fig. A.13 displays the evolution of D_{axial} with respect to the active layer depth (ξ_0) and Table A.9 contains the value of D_{axial} measured for all experiments.

As was reported by Alizadeh et al. (2013), Fig. A.13 shows an increase in the axial dispersion coefficient as the depth in the active layer decreases. This behavior is expected as the particles found at or near the bed surface have more freedom to move and are in fact more likely to move axially. There does not seem to be a noteworthy difference between the D_{axial} profiles of the blends tested (Fig. A.13b), but a significant difference can be noticed between the D_{axial} profile of the 6mm glass beads and the ones obtained for the non-spherical tablets (Fig. A.13a).

Previous studies using polydisperse mixtures of particles have reported an increase in the dispersion coefficient with the increase of the particle size, except when large particles occupy the center of the bed (Alizadeh et al., 2013; Ingram et al., 2005). A similar trend is expected here for the non-spherical tablets composing a specific blend. In other words, a higher axial dispersion should be obtained for the particles most likely to be at or near the surface of the bed : $D_{axial,AE.A} < D_{axial,AE.E}$, $D_{axial,BC.B} < D_{axial,BC.C}$, $D_{axial,CD.D} < D_{axial,CD.C}$, $D_{axial,CE.E} < D_{axial,CE.C}$ and $D_{axial,GB56.5} < D_{axial,GB56.6}$). In the case of the mono-disperse

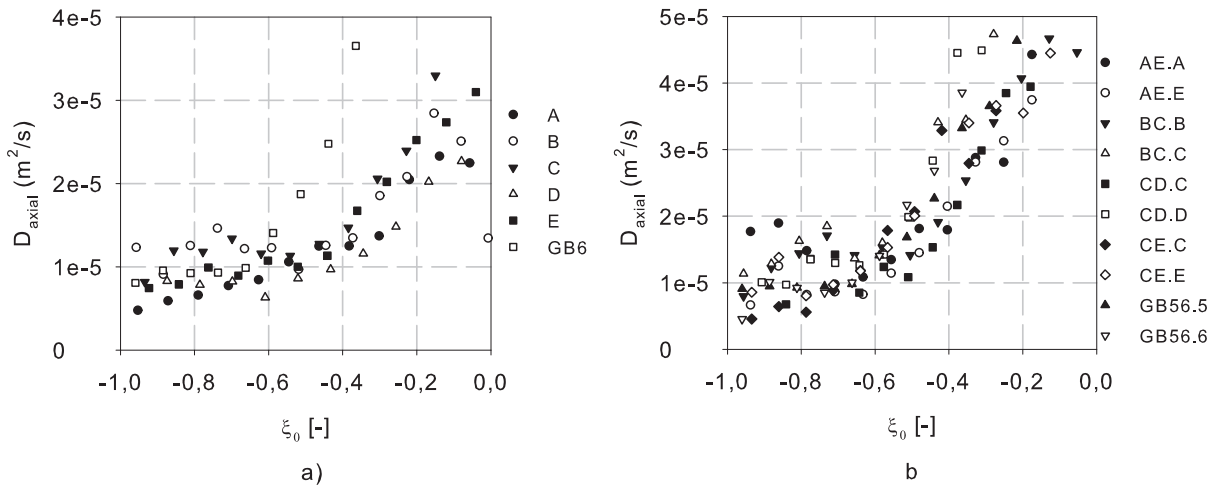


Figure A.13: Evolution of D_{axial} with respect to the active layer depth (ξ_0).

experiments, when comparing similar shapes, it is expected that the largest tablet should present a slightly higher dispersion coefficient : $D_{axial,A} < D_{axial,E}$ and $D_{axial,B} < D_{axial,C}$). Moreover, it is likely that a higher degree of preferred spatial orientation in the active layer will lead to a lower axial dispersion coefficient. This means that a higher dispersion coefficient for the glass bead is expected. For the same reason, tablet D should present a slightly lower coefficient than the other shapes. The results presented in Table A.9 confirm all these expectations. However, the differences in axial dispersion are not significant in all cases. Experiments E, BC.B, and CD.C were repeated. The results obtainment suggest that the uncertainty on D_{axial} is approximately $5 \times 10^{-6} \text{ m}^2/\text{s}$. It must be noted that the values reported for the 6mm glass beads and the blend containing 5mm and 6mm glass beads are comparable to those reported by Alizadeh et al. (2013).

Table A.9: Axial dispersion coefficient

Type	Experiment ID	$D_{axial} \times 10^{-6} [\text{m}^2/\text{s}]$
Mono-disperse	A	15.3
	B	15.9
	C	20.0
	D	12.9
	E	17.4
	GB6	34.2
Bi-disperse	AE.A	13.4
	AE.E	27.6
	AE.A*	8.0
	AE.E*	20.8
	BC.B	17.8
	BC.C	19.5
	CD.C	25.2
	CD.D	17.9
	CE.C	27.1
	CE.E	13.0
	GB56.5	14.3
	GB56.6	45.3

A.4 Conclusion

In this work, the dynamics of non-spherical particles in a rotating drum was investigated using pharmaceutical tablets. The tablets were composed of sodium bicarbonate, making them suitable tracer particles for the RPT technique. Three important aspects of the particle dynamics in rotating drums were investigated : the active and passive layer residence times, the mixing and segregation as well as the axial dispersion. It was shown that models previously developed using spherical or nearly spherical particles could adequately predict the velocity profile and the active layer thickness, except when the non-spherical particles have a high aspect ratio (*i.e.* greater than two). In this case, significant deviations in the velocity profile were found under the bed surface. A model for the residence times in the active and passive layers was developed and good agreement was obtained with the RPT experimental data for most of the non-spherical tablets tested. It was observed that the mixing of non-spherical particles having different shapes led to unexpected reverse core segregation where the smaller and denser tablets were found on the outside of the bed and larger and lighter tablets in the bed core. Lastly, the non-spherical tablets displayed a lower axial dispersion coefficient than the spherical particles which can partially be attributed to the higher degree of spatial orientation of these non-spherical tablets in the active and passive layers.

Acknowledgments

The financial support of the Natural Sciences and Engineering Council of Canada (NSERC), the Research and Development Center of Teva (Mirabel, Quebec) and PRAXAIR Inc. is gratefully acknowledged. The authors are thankful to Cornelia Chilian and RahmaKada from the SLOWPOKE Neutron Activation Analysis laboratory for the precise activations of the tracer particles.

A.5 References

- Alexander, A., Shinbrot, T., and Muzzio, F. J. (2002). Scaling surface velocities in rotating cylinders as a function of vessel radius, rotation rate, and particle size. *Powder Technology*, 126(2) :174–190.
- Alizadeh, E., Dubé, O., Bertrand, F., and Chaouki, J. (2013). Characterization of mixing and size segregation in a rotating drum by a particle tracking method. *Accepted in AIChE Journal*, page DOI 10.1002/aic.13982.
- Beam, G. B., Wielopolski, L., Gardner, R. P., and Verghese, K. (1978). Monte carlo calculation of efficiencies of right-circular cylindrical NaI detectors for arbitrarily located point sources. *Nuclear Instruments and Methods*, 154,(3) :501–508.
- Boateng, A. and Barr, P. (1997). Granular flow behaviour in the transverse plane of a partially filled rotating cylinder. *Journal of Engineering and Applied Science*, 330 :233–249.
- Boateng, A. A. (1998). Boundary layer modeling of granular flow in the transverse plane of a partially filled rotating cylinder. *International Journal of Multiphase Flow*, 24(3) :499–521.
- Cheng, N.-S., Zhou, Q., Tan, S. K., and Zhao, K. (2011). Application of incomplete similarity theory for estimating maximum shear layer thickness of granular flows in rotating drums. *Chemical Engineering Science*, 66(12) :2872–2878.
- Cleary, P. W. (2010). DEM prediction of industrial and geophysical particle flows. *Particuology*, 8(2) :106–118.
- Descoins, N., Dirion, J.-L., and Howes, T. (2005). Solid transport in a pyrolysis pilot-scale rotary kiln : Preliminary results - stationary and dynamic results. volume 44, pages 315–321.
- Ding, Y., Forster, R., Seville, J., and Parker, D. (2002a). Granular motion in rotating drums : bed turnover time and slumping-rolling transition. *Powder Technology*, 124(1-2) :18–27.
- Ding, Y., Forster, R., Seville, J., and Parker, D. (2002b). Segregation of granular flow in the transverse plane of a rolling mode rotating drum. *International Journal of Multiphase Flow*, 28(4) :635–663.

- Ding, Y., Seville, J., Forster, R., and Parker, D. (2001). Solids motion in rolling mode rotating drums operated at low to medium rotational speeds. *Chemical Engineering Science*, 56(5) :1769–1780.
- Doucet, J., Bertrand, F., and Chaouki, J. (2008). An extended radioactive particle tracking method for systems with irregular moving boundaries. *Powder Technology*, 181(2) :195–204.
- Dubé, O., Dubé, D., Chaouki, J., and Bertrand, F. (2013). Optimization of detector positioning in the radioactive particle tracking technique. page Submitted to Applied Radiation and Isotopes.
- Einstein, A. (1905). Über die von der molekularkinetischen theorie der wärme geforderte bewegung von in ruhenden flüssigkeiten suspendierten teilchen (on the movement of small particles suspended in a stationary liquid demanded by the molecular-kinetic theory of heat). *Annalen der Physik*, 322(8) :549–560.
- Fantozzi, F., Colantoni, S., Bartocci, P., and Desideri, U. (2007). Rotary kiln slow pyrolysis for syngas and char production from biomass and waste. part I. working envelope of the reactor. *Journal of Engineering for Gas Turbines and Power*, 129(4) :901–907.
- Felix, G., Falk, V., and D’Ortona, U. (2002). Segregation of dry granular material in rotating drum : Experimental study of the flowing zone thickness. *Powder Technology*, 128(2-3) :314–319.
- Felix, G., Falk, V., and D’Ortona, U. (2007). Granular flows in a rotating drum : the scaling law between velocity and thickness of the flow. *European Physical Journal E*, 22(1) :25–31.
- Henein, H., Brimacombe, J., and Watkinson, A. (1983). Experimental study of transverse bed motion in rotary kilns. *Metallurgical Transactions B (Process Metallurgy)*, 14 B(2) :191–205.
- Henein, H., Brimacombe, J., and Watkinson, A. (1985). Experimental study of segregation in rotary kilns. *Metallurgical transactions. B, Process metallurgy*, 16B(4) :763–774.

- Heydenrych, M., Greeff, P., Heesink, A., and Versteeg, G. (2002). Mass transfer in rolling rotary kilns : A novel approach. *Chemical Engineering Science*, 57(18) :3851–3859.
- Hill, K., Caprihan, A., and Kakalios, J. (1997). Bulk segregation in rotated granular material measured by magnetic resonance imaging. *Physical Review Letters*, 78(1) :50–53.
- Ingram, A., Seville, J., Parker, D., Fan, X., and Forster, R. (2005). Axial and radial dispersion in rolling mode rotating drums. *Powder Technology*, 158(1-3) :76–91.
- Jain, N., Ottino, J., and Lueptow, R. (2002). An experimental study of the flowing granular layer in a rotating tumbler. *Physics of Fluids*, 14(2) :572–582.
- Jain, N., Ottino, J., and Lueptow, R. (2004). Effect of interstitial fluid on a granular flowing layer. *Journal of Fluid Mechanics*, 508 :23–44.
- Jain, N., Ottino, J. M., and Lueptow, R. M. (2005). Regimes of segregation and mixing in combined size and density granular systems : An experimental study. *Granular Matter*, 7(2-3) :69–81.
- Kawaguchi, T. (2010). MRI measurement of granular flows and fluid-particle flows. *Advanced Powder Technology*, 21(3) :235–241.
- Khakhar, D., McCarthy, J., and Ottino, J. (1997a). Radial segregation of granular mixtures in rotating cylinders. *Physics of Fluids*, 9(12) :3600–3614.
- Khakhar, D., McCarthy, J., Shinbrot, T., and Ottino, J. (1997b). Transverse flow and mixing of granular materials in a rotating cylinder. *Physics of Fluids*, 9(1) :31–43.
- Khakhar, D., Orpe, A., Andresen, P., and Ottino, J. (2001a). Surface flow of granular materials : model and experiments in heap formation. *Journal of Fluid Mechanics*, 441 :255–264.
- Khakhar, D., Orpe, A. V., and Ottino, J. (2001b). Surface granular flows : two related examples. *Advances in Complex Systems*, 64(4) :407–417.
- Larachi, F., Kennedy, G., and Chaouki, J. (1994). A gamma ray detection system for 3-D particle tracking in multiphase reactors. *Nuclear Instruments & Methods in Physics Research*

Section a-Accelerators Spectrometers Detectors and Associated Equipment, A338(2-3) :568–576.

Lemieux, M., Bertrand, F., Chaouki, J., and Gosselin, P. (2007). Comparative study of the mixing of free-flowing particles in a V-blender and a bin-blender. *Chemical Engineering Science*, 62(6) :1783–1802.

Li, S.-Q., Yan, J.-H., Li, R.-D., Chi, Y., and Cen, K.-F. (2002). Axial transport and residence time of MSW in rotary kilns - part i. experimental. *Powder Technology*, 126(3) :217–227.

Liu, X. Y. and Specht, E. (2010). Predicting the fraction of the mixing zone of a rolling bed in rotary kilns. *Chemical Engineering Science*, 65(10) :3059–3063.

Liu, X. Y., Specht, E., Gonzalez, O., and Walzel, P. (2006). Analytical solution for the rolling-mode granular motion in rotary kilns. *Chemical Engineering and Processing*, 45(6) :515–521.

Makse, H. (1999). Continuous avalanche segregation of granular mixtures in thin rotating drums. *Physical Review Letters*, 83(16) :3186–3189.

Meier, S., Lueptow, R., and Ottino, J. (2007). A dynamical systems approach to mixing and segregation of granular materials in tumblers. *Advances in Physics*, 56(5-6) :757–827.

Mellmann, J. (2001). The transverse motion of solids in rotating cylinders - forms of motion and transition behavior. *Powder Technology*, 118(3) :251–270.

Mellmann, J., Specht, E., and Liu, X. (2004). Prediction of rolling bed motion in rotating cylinders. *AIChE Journal*, 50(11) :2783–2793.

Nakagawa, M., Altobelli, S., Caprihan, A., Fukushima, E., and Jeong, E.-K. (1993). Non-invasive measurements of granular flows by magnetic resonance imaging. *Experiments in Fluids*, 16(1) :54–60.

Ndiaye, L., Caillat, S., Chinnayya, A., Gambier, D., and Baudoin, B. (2010). Application of the dynamic model of saeman to an industrial rotary kiln incinerator : Numerical and experimental results. *Waste Management*, 30(7) :1188–1195.

- Orpe, A. V. and Khakhar, D. V. (2001). Scaling relations for granular flow in quasi-two-dimensional rotating cylinders. *Physical Review E*, 64 :031302.
- Parker, D., Dijkstra, A., Martin, T., and Seville, J. (1997). Positron emission particle tracking studies of spherical particle motion in rotating drums. *Chemical Engineering Science*, 52(13) :2011–2022.
- Ridgway, K. and Rupp, R. (1971). Mixing of powder layers on a chute. the effect of particle size and shape. *Powder Technology*, 4(4) :195–202.
- Roy, S., Larachi, F., Al-Dahhan, M., and Dudukovic, M. (2002). Optimal design of radioactive particle tracking experiments for flow mapping in opaque multiphase reactors. *Applied Radiation and Isotopes*, 56(3) :485–503.
- Sherritt, R., Chaouki, J., Mehrotra, A., and Behie, L. (2003). Axial dispersion in the three-dimensional mixing of particles in a rotating drum reactor. *Chemical Engineering Science*, 58(2) :401–415.
- Sturman, R., Meier, S., Ottino, J., and Wiggins, S. (2008). Linked twist map formalism in two and three dimensions applied to mixing in tumbled granular flows. *Journal of Fluid Mechanics*, 602 :129–174.
- Suzzi, D., Toschkoff, G., Radl, S., Machold, D., Fraser, S., Glasser, B., and Khinast, J. (2012). DEM simulation of continuous tablet coating : effects of tablet shape and fill level on inter-tablet coating variability. *Chemical Engineering Science*, 69(1) :107–121.
- Thomas, N. (2000). Reverse and intermediate segregation of large beads in dry granular media. *Physical Review E*, 62(1) :961–974.
- Tobiska, S. and Kleinebudde, P. (2003). Coating uniformity and coating efficiency in a Bohle lab-coater using oval tablets. *European Journal of Pharmaceutics and Biopharmaceutics*, 56(1) :3–9.

- Van Puyvelde, D., Young, B., Wilson, M., and Schmidt, S. (2000). Modelling transverse segregation of particulate solids in a rolling drum. *Chemical Engineering Research and Design*, 78(4) :643–650.
- Weir, G., Krouse, D., and McGavin, P. (2005). The maximum thickness of upper shear layers of granular materials in rotating cylinders. *Chemical Engineering Science*, 60(7) :2027–2035.
- Wightman, C. and Muzzio, F. J. (1998). Mixing of granular material in a drum mixer undergoing rotational and rocking motions II. segregating particles. *Powder Technology*, 98(2) :125–134.
- Wilson, K. and Crossman, E. (1997). The influence of tablet shape and pan speed on intra-tablet film coating uniformity. *Drug Development and Industrial Pharmacy*, 23(12) :1239–1243.
- Woodle, G. R. and Munro, J. M. (1993). Particle motion and mixing in a rotary kiln. *Powder Technology*, 76(3) :241–245.